Structural Dynamics of Smart Laminated Composite Cylindrical Shells

By

Hossein Kheirollahi Nataj Bisheh

A Thesis submitted to the Faculty of Graduate Studies of
the University of Manitoba
in partial fulfilment of the requirements for the degree of

Doctor of Philosophy

Department of Mechanical Engineering
Faculty of Engineering
University of Manitoba
Winnipeg, Manitoba, Canada

April 2020

Abstract

Smart laminated composite cylindrical shells are widely used in many engineering applications such as aerospace, mechanical, civil, and marine structures. Dynamics (wave propagation and vibration) analysis of smart laminated composite shell structures plays an important role in design and fabrication of such structures. Understanding the dynamic characteristics of composite structures can be used for detecting possible defects in a structure and monitoring its structural integrity. Proper dynamics analysis of composite cylindrical shells has significant importance in accurate determination of wave propagation and vibration characteristics. In this thesis, a set of mathematical models is developed to model wave propagation and free vibration in smart laminated composite cylindrical shells reinforced with fibers with different sizes and arrangements based on different shell theories. The resulting effective material properties for composite structures reinforced with carbon nanotubes are estimated using the Mori-Tanaka micromechanics model. The hygrothermal environmental conditions are also considered in the proposed models. Wave dispersion and free vibration analyses are performed by solving an eigenvalue problem and finding the wave phase velocities and natural frequencies for different wave and vibration modes. Through numerical simulations, the effects of various parameters such as hygrothermal environmental conditions, axial and circumferential wavenumbers, arrangement and distribution of reinforcing fibers and carbon nanotubes, stacking sequence of the laminate, shell geometry parameters, piezoelectricity, and mechanical boundary conditions on the dynamic characteristics of different composites are examined. It is concluded that the shear effects on wave dynamics of smart laminated composite cylindrical shells are much more noticeable than its effects on wave dynamics of smart isotropic cylindrical shells. Furthermore, the effects of reinforcing fibers and carbon nanotubes and their volume fraction and geometrical distribution within the structure on

wave propagation characteristics are significant and must be carefully considered in the analyses of such structures. The hygrothermal environmental conditions have a moderate impact on the wave propagation and vibration characteristics. Shell geometry and boundary conditions have noticeable effects on dynamic characteristics of smart composite cylindrical shells. The theoretical and mathematical framework developed in this thesis can be used by designers and manufacturers for the analyses of structural integrity and health monitoring of smart laminated composite cylindrical shell structures. It can also be used for energy harvesting through the piezoelectric materials embedded in such structures under different environmental conditions.

Acknowledgements

I would like to express my sincerest thanks to my supervisor, Dr. Nan Wu, for offering me the opportunity to study at the University of Manitoba and participate in this research project, and for his motivating guidance, support, and encouragement throughout this research work and the completion of my dissertation. I also would like to show gratitude to my advisory committee members, Dr. Mohammad Javad Hosseini Kahsari, Dr. Pooneh Maghoul, and Dr. Chuang Deng, for their efforts put into reviewing my thesis and their valuable comments and suggestions.

I am thankful to Prof. Timon Rabczuk from the Bauhaus University Weimar, Germany and Prof. David Hui from the University of New Orleans, USA for their kind support, advice, and collaboration on my Ph.D. research.

I appreciate the University of Manitoba for providing me the circumstance to perform my doctoral research. I acknowledge the funding received from the Natural Sciences and Engineering Research Council of Canada (NSERC), the University of Manitoba Graduate Fellowships (UMGF), Graduate Enhancement of Tri-Council Stipends (GETS) Fellowship, the Mitacs Globalink Research Award, and other awards from the University of Manitoba to support my Ph.D. research.

My thanks also go to my colleagues in the Sound and Vibration Laboratory for all the academic discussions and happy time working with them. I am really grateful to my all friends in Winnipeg for providing me so many merry moments and encouragement.

I would like to express my deep love and appreciation to my parents, parents-in-law, sister, brother, sister-in-law, brothers-in-law, and my cute nieces for their consistent and unconditional love and support through my all life. Finally, my special appreciation and gratitude to my lovely wife, Shima, for her love, support, encouragement, and patience during this difficult journey.

Dedication

To my wife and parents

Declaration of the Academic Achievement

Findings of this Ph.D. research have been disseminated in eight peer-reviewed journal papers and presented in one international conference. Hossein Kheirollahi Nataj Bisheh is the first author and the major contributor in all papers. The contributions of Hossein Kheirollahi Nataj Bisheh in all papers are listed as follows: initiating and developing the research ideas, developing the mathematical models and numerical analyses, data analysis, preparing the figures, writing all the manuscripts, and responding to reviewers' comments.

Contents

List of Figures

List of Tables

List of Abbreviations

NDE	Non-Destructive Evaluation
CNT	Carbon nanotube
SWCNT	Single-walled carbon nanotubes
DWCNT	Double-walled carbon nanotubes
MWCNT	Multi-walled carbon nanotubes
IDT	Interdigital transducer
SAW	Surface acoustic wave
MEMS	Microelectromechanical systems
PZT	Piezo lead zirconate titanate
FCC	Face-centered cubic
Hz	Hertz
FSDT	First-order shear deformation shell theory
FEM	Finite element method
FEA	Finite element analysis
FGM	Functionally graded material
PFRC	Piezoelectric fiber-reinforced composite
CLPT	Classical laminated plate theory

GDQ	Generalized differential quadrature
LW-DQ	Layer wise - differential quadrature
RVE	Representative Volume Element
CTE	Coefficient of thermal expansion
CME	Coefficient of moisture expansion
C-C	Clamped-Clamped
C-SS	Clamped-Simply Supported
SS-SS	Simply Supported-Simply Supported
C-SL	Clamped-Sliding
C-F	Clamped-Free

List of Copyrighted Materials

- Parc olympique de Montréal, Parc Olymp. (n.d.). https://parcolympique.qc.ca. Figure 1.1 is adapted from this website.
- Boeing: 777, (n.d.). https://www.boeing.com/commercial/777. Figure 1.2 is adapted from this website.
- Carnival Corporation & plc, Carnival Corp. Plc. (n.d.). https://www.carnivalcorp.com/index. Figure 1.3 is adapted from this website.
- I.M. Daniel, O. Ishai, Engineering Mechanics of Composite Materials, Second Edition, Oxford University Press, New York, 2006. Figures 1.4, 1.7, and 1.9 and Tables 1.1 and 2.1 are adapted from this book.
- S. Iijima, Helical microtubules of graphitic carbon, Nature. 354 (1991) 56. https://doi.org/10.1038/354056a0. Figure 1.5 is adapted from this paper.
- M. Giulianini, N. Motta, Polymer Self-assembly on Carbon Nanotubes, in: S. Bellucci (Ed.), Self-Assem. Nanostructures INFN Lect. Vol III, Springer New York, New York, NY, 2012: pp. 1–72. https://doi.org/10.1007/978-1-4614-0742-3_1. Figure 1.6 is adapted from this book chapter.
- J.N. Reddy, Mechanics of Laminated Composite Plates and Shells: Theory and Analysis, Second Edition, CRC Press, Boca Raton, 2003. Figure 1.8 is adapted from this book.
- Interdigital transducer, Wikipedia. (2019). https://en.wikipedia.org/w/index.php?title=Interdigital_transducer&oldid=884499375. Figure 1.10 is adapted from this website.

- E. Carrera, S. Brischetto, P. Nali, Plates and Shells for Smart Structures, Wiley, New Delhi, India, 2011. Figure 1.11 is adapted from this book.
- T. Hehn, Y. Manoli, Piezoelectricity and Energy Harvester Modelling, in: T. Hehn, Y. Manoli (Eds.), CMOS Circuits Piezoelectric Energy Harvest. Effic. Power Extr. Interface Model. Loss Anal., Springer Netherlands, Dordrecht, 2015: pp. 21–40. https://doi.org/10.1007/978-94-017-9288-2_2. Figures 1.12 and 1.13 are adapted from this book chapter.
- G.R. Liu, Z.C. Xi, Elastic Waves in Anisotropic Laminates, CRC Press, Boca Raton, Florida, 2002. Figures 1.14, 1.15, 1.16, and Table 1.2 are adapted from this book.
- Wavelength, Wikipedia. (2020). https://en.wikipedia.org/w/index.php?title=Wavelength&oldid=953748107. Figure 1.17 is adapted from this website.
- H. Bisheh, T. Rabczuk, N. Wu, Effects of nanotube agglomeration on wave dynamics of carbon nanotube-reinforced piezocomposite cylindrical shells, Compos. Part B Eng. 187 (2020) 107739. https://doi.org/10.1016/j.compositesb.2019.107739. Some contents of this paper are included in Chapters 1– 4.
- H. Bisheh, N. Wu, T. Rabczuk, Free vibration analysis of smart laminated carbon nanotube-reinforced composite cylindrical shells with various boundary conditions in hygrothermal environments, Thin-Walled Struct. 149 (2020) 106500. https://doi.org/10.1016/j.tws.2019.106500. Some contents of this paper are included in Chapters 1– 4.
- H. Bisheh, N. Wu, D. Hui, Polarization effects on wave propagation characteristics of piezoelectric coupled laminated fiber-reinforced composite cylindrical shells, Int. J. Mech.

Sci. 161–162 (2019) 105028. https://doi.org/10.1016/j.ijmecsci.2019.105028. Some contents of this paper are included in Chapters 1– 4.

- H. Bisheh, N. Wu, Wave propagation in smart laminated composite cylindrical shells reinforced with carbon nanotubes in hygrothermal environments, Compos. Part B Eng. 162 (2019) 219–241. https://doi.org/10.1016/j.compositesb.2018.10.064. Some contents of this paper are included in Chapters 1– 4.
- H. Bisheh, N. Wu, Wave propagation in piezoelectric cylindrical composite shells reinforced with angled and randomly oriented carbon nanotubes, Compos. Part B Eng. 160 (2019) 10–30. https://doi.org/10.1016/j.compositesb.2018.10.001. Some contents of this paper are included in Chapters 1– 4.
- H. Bisheh, N. Wu, On dispersion relations in smart laminated fiber-reinforced composite membranes considering different piezoelectric coupling effects, J. Low Freq. Noise Vib. Act. Control. 38 (2019) 487–509. https://doi.org/10.1177/1461348418821773. Some contents of this paper are included in Chapters 1– 4.
- H.Kh. Bisheh, N. Wu, Analysis of wave propagation characteristics in piezoelectric cylindrical composite shells reinforced with carbon nanotubes, Int. J. Mech. Sci. 145 (2018) 200–220. https://doi.org/10.1016/j.ijmecsci.2018.07.002. Some contents of this paper are included in Chapters 1– 4.
- H. Bisheh, N. Wu, Wave propagation characteristics in a piezoelectric coupled laminated composite cylindrical shell by considering transverse shear effects and rotary inertia, Compos. Struct. 191 (2018) 123–144. https://doi.org/10.1016/j.compstruct.2018.02.010. Some contents of this paper are included in Chapters 1– 4.

Chapter 1

Introduction

1.1. Background and Scope

Due to outstanding material properties of advanced composite materials superior to the material properties of traditional materials such as steel, aluminium, etc., they are widely used in many engineering applications such as mechanical, aerospace, civil, marine, and offshore structures. A study on wave propagation and vibration of composite structures helps us to understand their dynamic characteristics and failure mechanism. An analysis of wave propagation behavior is a perquisite to seismic and/or acoustic Non-Destructive Evaluation (NDE) techniques. Analysis of elastic waves in smart anisotropic materials is much more complicated than that for smart isotropic materials. Hence, to accurately predict the dynamic behaviors of such media, it is of significant importance to develop appropriate analytical and numerical models considering all the anisotropic properties. In the following subsections, a brief introduction of shell structures, composite structures, and smart structures with their applications is presented.

1.1.1. Shell Structures

A shell structure is a three-dimensional structure which is thin in one direction (thickness direction) and long in the other two directions. Shell structures' curvature plays an important role in their structural behavior. Shell structures are abundantly present in the nature, for example sea-shells. Indeed, due to the curvature of the middle surface, shells are very strong and stiff under both in-plane and bending loadings; hence, they can span over relatively large areas and hold applied loads in a very effective way with a minimum amount of material [1].

Shells are largely employed in engineering designs and applications mainly due to their light weight and mechanical properties. In automotive engineering, the bodies of cars are shell structures; in aeronautical engineering, the airplane bodies are shell structures; in naval engineering, the ship hulls are made of shells; in civil engineering, shells are used for roofs, bridges, silos, tanks, cooling towers, and aesthetic and architectural structures; and in biomechanics, arteries conveying flow can be considered as shell structures. Some examples of shell structures are: the roof of the Montreal Olympic stadium shown in Fig. 1.1, the fuselage and wing panel of the huge Boeing 777 aircraft shown in Fig. 1.2, and the hull of the Queen Mary 2 transatlantic boat shown in Fig. 1.3.

Figure 1.1. Olympic stadium, Montreal, Canada. Used with permission [2].

In the design of shell structures, one of the main objectives is to make the thickness as thin as possible to reduce the material usage and consequently provide a lighter structure. The difficulty in the analysis of shell structures is related to their spatial form, e.g. curvature. Curvature, which is the reason for a higher carrying load capacity, causes different failure modes as well as often unknown behaviors. Hence, these features of shells make their analysis more difficult than other structural element such as conventional bars, beams, and plates. In reality, the strength properties of shell structures depend on their spatial curvature form [1]. The analytical formulae for shell structures are very complicated in comparison with other structural elements. Due to an optimum distribution of materials, shell structures may collapse due to buckling, which may occur much before the failure strength of the material. Because shell structures are thin, large displacements usually happen with respect to the shell thickness, which is related to small strains before collapse. Shell structures are often exposed to dynamic loads which lead to their vibrations [3].

Figure 1.2. Boeing 777. Used with permission [4].

Figure 1.3. The Queen Mary 2 transatlantic boat. Used with permission [5].

1.1.2. Composite Materials and Structures

1.1.2.1. Definition and Characteristics

A composite material is made up of two or more phases on a macroscopic scale, whose mechanical properties and performance are superior of those of the constituent materials alone. The discontinuous, stiffer, and stronger phase is called the reinforcement, while the continuous, less stiff, and weaker phase is called the matrix (Fig. 1.4). In some cases, due to chemical interactions or other processing effects, an additional phase is created between the reinforcement and the matrix which is called the interface phase. The properties of a composite material is function of the properties of constituents, their geometry, and spatial distribution. One of the most important parameters affecting on the properties of a composite material is the volume (or weight) fraction of the reinforcement or the fiber volume ratio. The distribution of the reinforcement in the matrix specifies the homogeneity or the uniformity of a composite martial system. More non-uniform distribution of the reinforcement in a composite material leads to more heterogeneity. The orientation and geometry of the reinforcement also influence on the anisotropy of a composite material. Different materials are used for the reinforcement and the matrix phases [6]. The most common reinforcing fibers are Carbon, Kevlar, E-Glass, S-Glass, Boron, and Silicon Carbide. The matrix can be made of polymers, ceramics, and metals. Typical polymer matrices are Epoxy, Polyesters, Vinylester, Polyimides, and Poly-ether-ether-ketone.

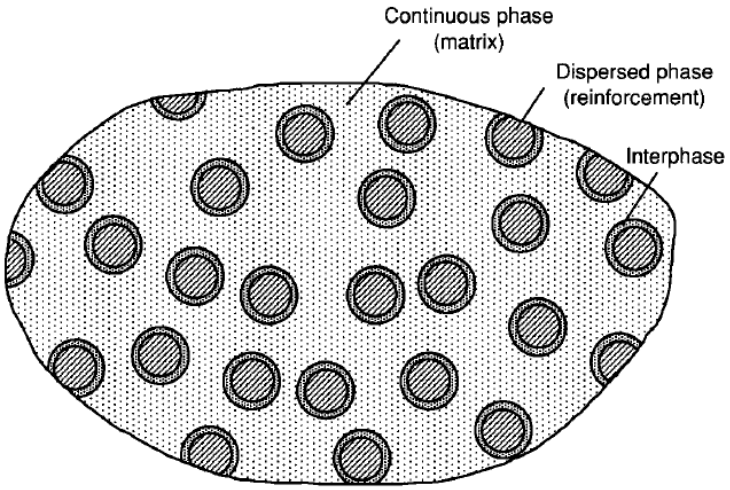

Figure 1.4. Phases of a composite material. Used with permission [6].

1.1.2.2. Nanocomposites

Nanocomposite is a multiphase solid material where one of the phases has one, two or three dimensions of less than 100 nanometers (nm). In mechanical terms, nanocomposites differ from conventional composite materials due to the exceptionally high surface to volume ratio of the reinforcing phase and/or its exceptionally high aspect ratio. The reinforcing material can be made up of particles (e.g. minerals), sheets (e.g. exfoliated clay stacks) or fibres (e.g. carbon nanotubes or electrospun fibres). The area of the interface between the matrix and reinforcement phases is typically an order of magnitude greater than the one for conventional composite materials. The matrix material properties are significantly affected in the vicinity of the reinforcement.

Since their discovery by Iijima [7], carbon nanotubes (CNTs) have attracted much attention of researchers because of their extraordinary enhanced material properties. Fig. 1.5 displays CNTs originally reported by Iijima [7]. CNTs are a class of nanomaterials that consist of a two-dimensional hexagonal lattice of carbon atoms, bent and joined in one direction so as to form a hollow cylinder. CNTs can be found as single individual cylinders, as a single-walled carbon nanotubes (SWCNTs), or as coaxial cylindrical structures bonded by van der Waals forces called

multi-walled carbon nanotubes (MWCNTs). Carbon nanotubes can also be found as double-walled carbon nanotubes (DWCNTs) with particular properties. Fig. 1.6 presents single-, double- and multi-walled carbon nanotubes [8].

As reported in the literature [9–13], the material properties of SWCNTs are anisotropic, chirality- and size – dependent and temperature – dependent . It is noted that the effective wall thickness obtained for the SWCNT (10, 10) is 0.067 nm which satisfies the Vodenitcharova–Zhang criterion [14], and the wide used value of 0.34 nm for tube wall thickness is thoroughly inappropriate for SWCNTs. Radius of the SWCNT (10, 10) is considered 0.68 nm [15,16]. While micro-sized fibers have larger diameter; for example, the diameter of carbon and E-glass fibers are, respectively, 7 μm and 8 μm [6].

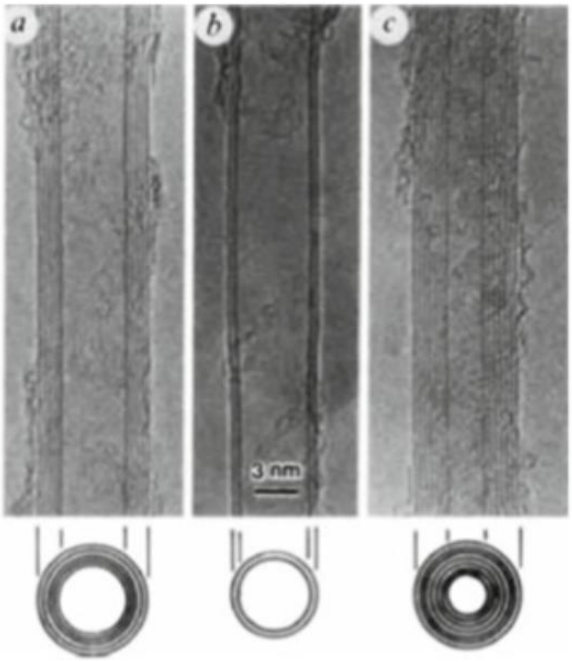

Figure 1.5. Carbon nanotubes as originally reported by Iijima in 1991. Used with permission [7].

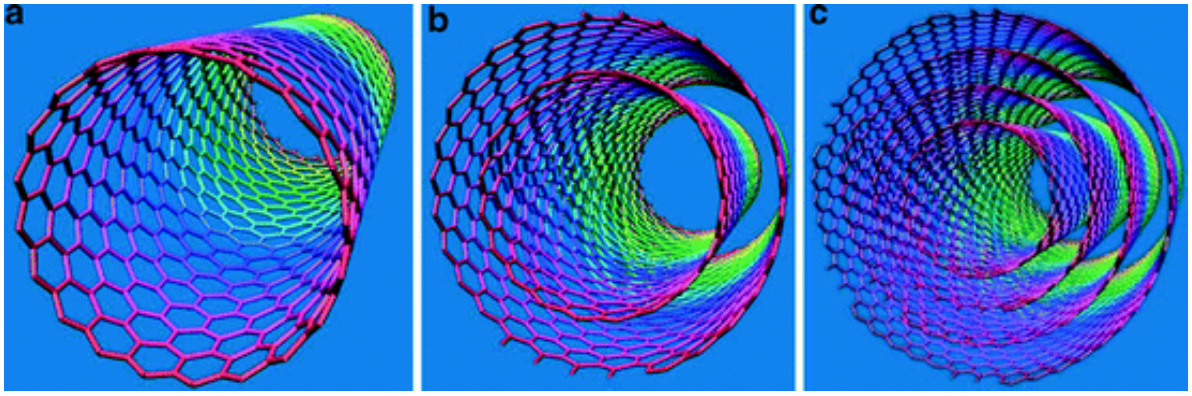

Figure 1.6. (a) Single-walled carbon nanotube, (b) Double-walled carbon nanotube, and (c) multi-walled carbon nanotube. Used with permission [8].

The outstanding mechanical, electrical, and thermal properties of CNTs made them as a potential reinforcing constituent in polymer matrices. The most important properties of CNTs are their extraordinary high strength-to-weight and stiffness-to-weight ratios. Among the most remarkable properties, it is interesting to report that the tensile strength of SWCNTs and MWCNTs is in the range from 13 to $52\,GPa$ and from 11 to $63\,GPa$, respectively [17,18], and both SWCNTs and MWCNTs have Young's modulus about $1TPa$ [17–20]. According to molecular mechanics and molecular dynamics, CNTs have high tensile strength, much higher than that of carbon fibers and steels [20–22]. At the same time, CNTs exhibit high flexibility [23], high thermal conductivity [24], and low density [25]. Due to their outstanding material properties, CNTs have been proposed in many applications such as material reinforcing [26,27], gas sensing [28–30], field emission emitters [31,32], nanomechanics [33], atomic force microscopy tips [34], membranes [35], etc.

1.1.2.3. Types and Classification of Composite Materials

Two-phase composite materials are usually classified in three categories based on the type, geometry, and orientation of the reinforcement phase in the matrix as explained in the chart of Fig. 1.7 [6]:

- Particulate composites contain particles of various sizes and shapes randomly dispersed in the matrix. This group of composites may consist of non-metallic particles in a non-metallic matrix, metallic particles in non-metallic matrices, metallic particles in metallic matrices, and non-metallic particles in metallic matrices.
- Discontinuous or short – fiber composites consist of short fibers, nanotubes, or whiskers as the reinforcing phase. Short fibers can be either all along a specific direction or randomly oriented. Nanocomposites reinforced with carbon nanotubes (approximately $1\ nm$ in diameter and $1000\ nm$ in length) are an example of this type of composites.
- Continuous – fiber composites are reinforced by long continuous fibers and are the most efficient form in term of strength and stiffness. The continuous fibers in the matrix can be all parallel in as unidirectional continuous-fiber composites, oriented at right angles to each other as cross-ply or woven fabric continuous-fiber composite, or oriented along several directions as multidirectional continuous-fiber composite. For some cases of fiber orientation and distribution, the composite can be classified as a quasi-isotropic material.

In addition to the above – discussed types of matrix, there are laminated composites made up of thin layers of different materials bonded together, such as clad metals, bimetals, Formica, plywood, and so on [6]. Continuous fiber – reinforced composites have higher strength and elastic moduli than discontinuous fiber – reinforced composites [36].

1.1.2.4. Lamina and Laminate

Composite structures in engineering applications are commonly made up of a stack of plies called laminate and each ply is called lamina. A lamina (or ply, or layer) is a typical sheet of composite material representing a fundamental building block. A fiber – reinforced lamina consists of many fibers embedded in a matrix material. Unidirectional fiber-reinforced laminae have the

highest strength and modulus in the direction of the fibers, but they show very low strength and elastic modulus in the transverse direction to the fibers. A weak bonding between a fiber and matrix leads to poor transverse properties and failures due to fiber breakage, fiber pull out, and fiber buckling.

A laminate is a collection of stacked laminae (or plies, or layers) to obtain the desired thickness and stiffness. For example, unidirectional fiber-reinforced laminae can be stacked with various fiber orientation in each lamina (see Fig. 1.8). The sequence of various orientations of a fiber-reinforced composite lamina in a laminate is expressed the lamination scheme or stacking sequence. The stacking sequence and the material properties of individual lamina provide the possibility of various designs with tailored stiffness and strength of the laminate to satisfy the structural stiffness and strength requirements [36].

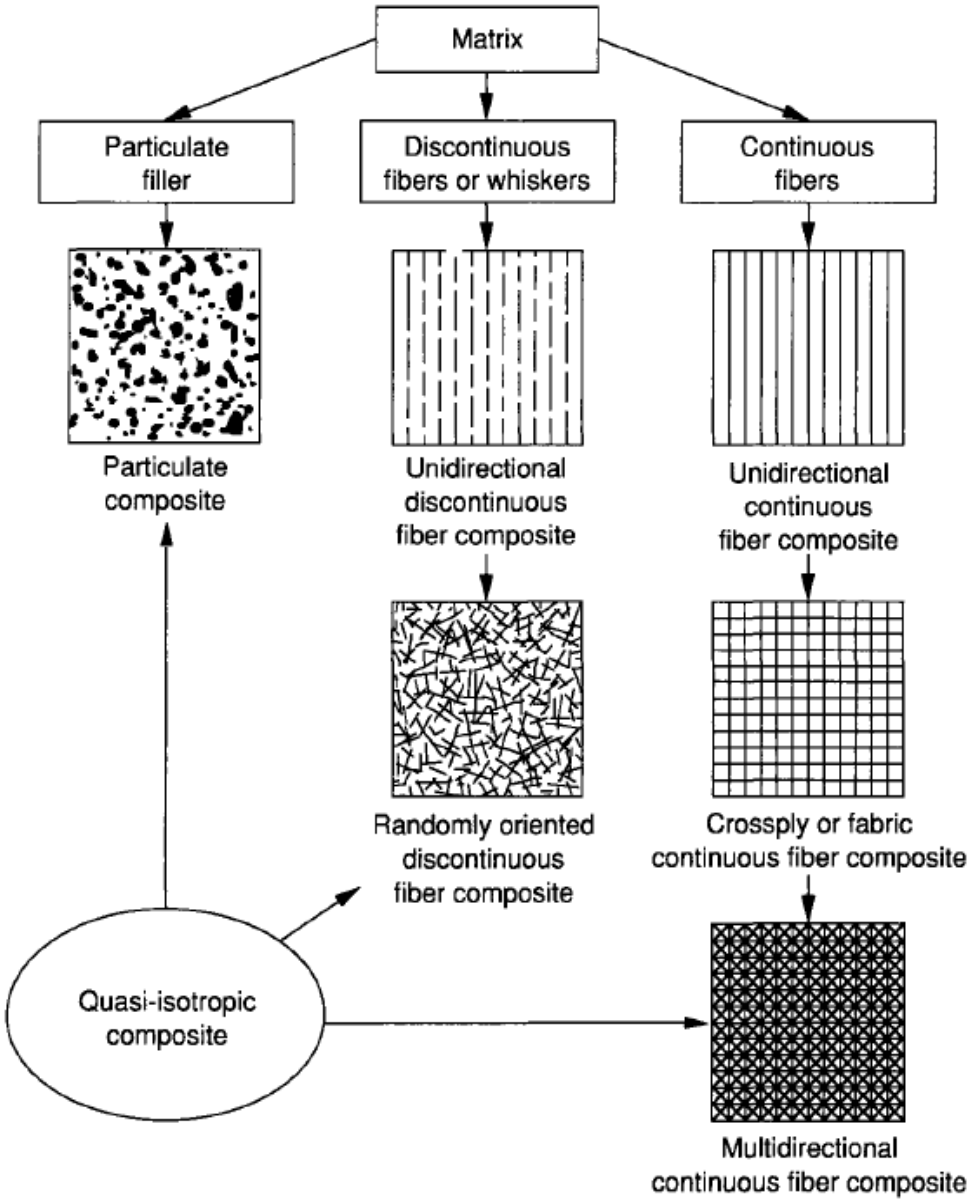

Figure 1.7. Classification of composite material systems. Used with permission [6].

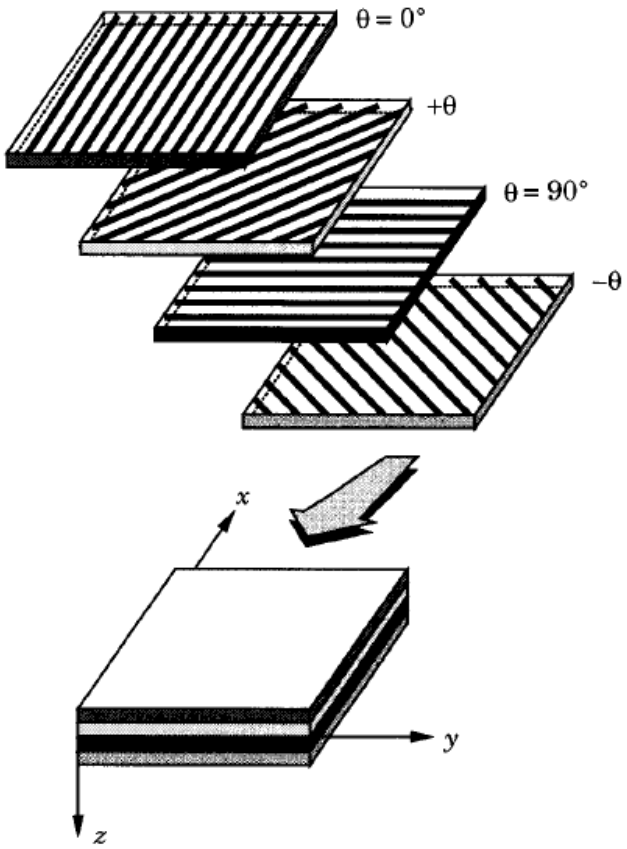

Figure 1.8. A laminate made up of laminae with different fiber orientations. Used with permission [36].

1.1.2.5. Scales of Analysis of Composite Materials

Composite materials can be investigated and analyzed at different scales. A schematic diagram of different levels of analysis and consideration is shown in Fig. 1.9 [6].

Micromechanics is related to the study of the interaction of the constituents at the microscopic level. This scale considers the state of deformation and stress in the constituents and local failures such as fiber failure (tensile, buckling, and splitting), matrix failure (tensile, compressive, and shear), and interface/interphase failure (debonding). Micromechanics is very important when studying properties such as failure mechanism and strength, fracture toughness, and fatigue life.

Micromechanics also provides the estimation of average behavior of the lamina as a function of its constituent material properties and local conditions. The objective of micromechanics methods is to characterize the elastic response of a Representative Volume Element (RVE) of the lamina as a function of the material and geometric properties of the constituents. Average properties of a composite lamina are determined in response of the RVE under simple loadings, such as longitudinal, transverse, in-plane shear, and transverse shear. The relevant engineering elastic properties are Young's moduli (E_{11}, E_{22}, and E_{33}), shear moduli (G_{12}, G_{23}, and G_{13}), and Poisson's ratio (v_{12}, v_{23}, and v_{13}).

Macromechanics scale considers the unidirectional lamina as a quasi-homogenous anisotropic material with its own average stiffness and strength properties. This method, assuming material continuity, is considered to study the elastic, viscoelastic, or hygrothermal behavior of composite laminates and structures. At the laminate level, the macromechanical analysis is used in the form of lamination theory considering overall behavior as a function of lamina properties and stacking sequence.

Finally, at the structure level, methods such as analytical approach or finite element analysis coupled with lamination theory are able to predict the overall behavior of the structure under static and dynamic conditions as well as the state of stress in each lamina.

1.1.2.6. Constitutive Equations of a Lamina

In formulating the constitutive equations of a lamina, it is assumed that: (i) a lamina is a continuum with no gaps or empty spaces, and (ii) a lamina is a linear elastic material. From the microscopic point of view, composite materials are inherently heterogeneous. While, composite materials are assumed to be homogenous from the macroscopic point of view, in which the

effective material properties of a composite are estimated from a weighted average of its constituent materials (fiber and matrix) [36].

The generalized Hooke's law for an anisotropic material is given in contracted notation by,

$$\sigma_{ij} = C_{ij}\varepsilon_{ij} \tag{1.1}$$

where σ_{ij} represent the stress components, ε_{ij} stand for the strain components, and C_{ij} are the elastic constants or the material properties coefficients. Table 1.1 shows the independent elastic constants for various types of materials.

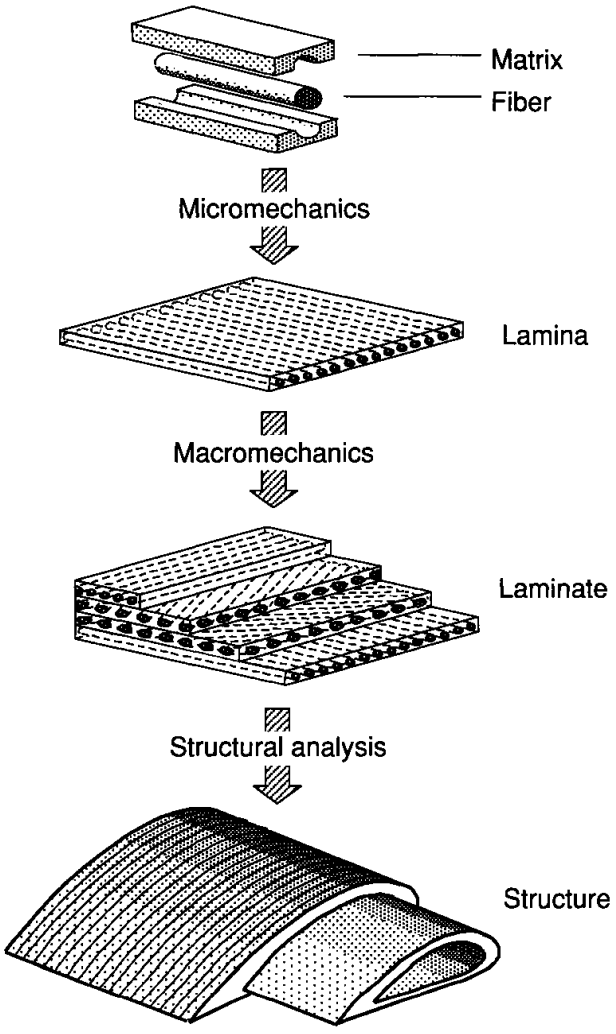

Figure 1.9. Levels of consideration and types of analysis for composite materials. Used with permission [6].

Table 1.1. Independent elastic constants for various types of materials [6].

Material	Number of independent elastic constants
General anisotropic material	81
Anisotropic material considering symmetry of stress and strain tensors ($\sigma_{ij} = \sigma_{ji}, \varepsilon_{ij} = \varepsilon_{ji}$)	36
Anisotropic material with elastic energy considerations	21
General orthotropic material	9
Orthotropic material with transverse isotropy	5
Isotropic material	2

1.1.3. Smart Structures and Their Application

Nowadays, developments in aeronautical and space industries, advanced structures, and automotive and shipbuilding industries are significantly affected by the development of so-called smart structures. Since late 1970s, the definition of smart structures has been discussed extensively. Based on a workshop organized by the US Army Research Office in 1988, the definition of smart system/structures was adopted by the scientific community [37] as: "A system or material which has built-in or intrinsic sensor(s), actuator(s) and control mechanism(s) whereby it is capable of sensing a stimulus, responding to it in a predetermined manner and extent, in a short/appropriate time, and reverting to its original state as soon as the stimulus is removed".

Early damage and delamination detection in composite structures using health monitoring techniques leads to prevention of catastrophic failures. To detect any damage in a composite structure, we need to first make a smart structure system. Based on the design practice, smart structures and systems are able to sense or react to their environment using the integration of sensors and actuators. Smart structures are capable to change their shape to very high precision and without using classical mechanical actuators, diminish vibrations and acoustic noise, and even monitor their own structural health.

Piezoelectric, piezomagnetic, electrostrictive, and magnetostrictive materials, due to their self-actuating electro-mechanical coupling properties, are of interest in design of smart structures, where they are bonded on the surface of the structure or embedded in the structure. With the advantage of piezoelectricity, mechanical energy can be transformed into electrical energy and vice versa. In piezoelectric materials, an electrical charge is generated when mechanical pressure is applied; which is so-called direct effect (sensor configuration). Conversely, the material shape changes when an electrical charge is applied; that is, the inverse effect (actuator configuration). With such reciprocal energy transforming characteristics, piezoelectric materials can be used at the same time as sensors and actuators, called self-sensing piezoelectric actuator [38]. As an actuator, the input voltage is transformed to mechanical strains, and the high frequency input signal is transformed into mechanical wave. While, as a sensor, when the input mechanical signal is applied, electrical signals are produced.

To apply wave propagation in a smart structure, an interdigital transducer (IDT) is used. An IDT is a device that consists of two interlocking comb-shaped arrays of metallic electrodes (in the fashion of zipper). These metallic electrodes are deposited on the surface of a piezoelectric substrate as shown in Fig. 1.10. IDTs convert electric signals to surface acoustic waves (SAW) by generating periodically distributed mechanical forces via piezoelectric effect (an input transducer). Based on the same principle, SAW is converted to electric signals (an output transducer). Hence, IDTs made up of piezoelectric materials can also be used as both actuators and sensors in a smart structure (piezoelectric coupled structure) for the analysis of wave signal for the purpose of damage detection [39].

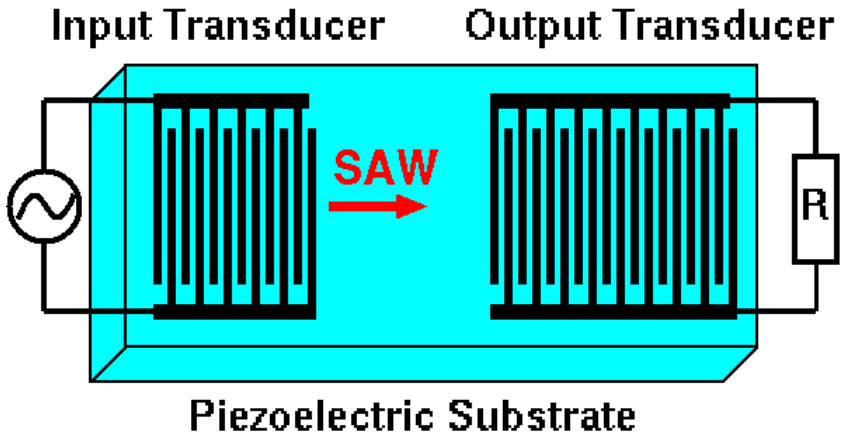

Figure 1.10. Schematic picture of a typical SAW signal processing device containing two interdigital transducers. Used with permission [40].

Nowadays, smart structures are applied in many different applications such as structural health monitoring, vibration control, shape morphing, active optics, and microelectromechanical systems (MEMS). A typical example of a smart structure is displayed in Fig. 1.11, where a network of sensors and actuators is embedded in a plate to control the deformation and apply corrections.

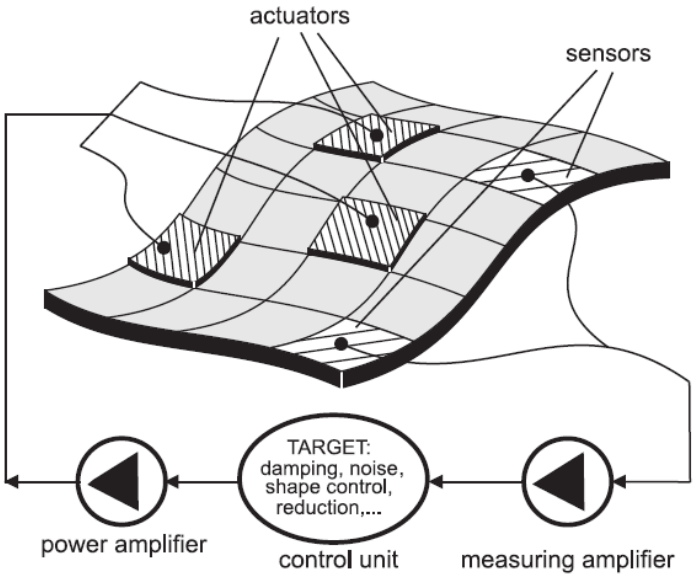

Figure 1.11. Example of a smart structure: the sensor–actuator network for a plate. Used with permission [41].

Piezoelectricity can be found in some natural crystals (such as quartz and tourmaline) or synthetic crystals (lithium sulfate), and some polymers and polarized ceramics. Piezoceramic barium titanate (BaTiO3) and piezo lead zirconate titanate (PZT) are the most common piezoelectric materials. The crystal lattice of piezoelectric materials is of the face-centered cubic (FCC) type. Oxygen atoms are at the center of the cube's faces, while metallic atoms are placed at the vortex of the cube as shown in Fig. 1.12. Heavier atom located at the center of the cube can move slightly to locations with less energy leading to the deformation of the crystal lattice. When an electric field is applied to the structure, because the central atom can exceed the potential energy threshold, it can move to a lower energy position. This causes the rupture of symmetry and an electric dipole (Fig. 1.12). This phenomenon occurs only below the so-called Curie temperature (T_C). Above this temperature ($T > T_C$), due to high thermal agitation, the piezoelectric effect disappears. We can obtain polarized piezoceramics by heating them above their Curie temperature and subjecting to a sever electric field during thermal cooling. By this process, all the dipoles can be oriented in the same direction and a stable polarization can be obtained for the material. After the polarization process, a temporary deformation is obtained by a very small electric potential and vice versa [41].

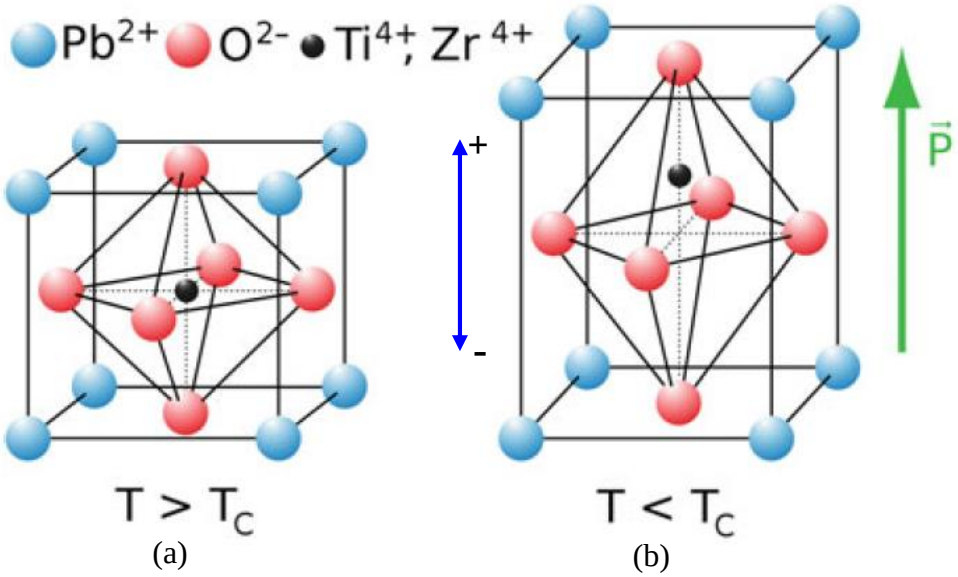

Figure 1.12. Intrinsic piezoelectric effect in piezo lead zirconate titanate (PZT), showing a crystallite (a) above and (b) below the Curie temperature T_C, where the charged zirconium or titanium ion moves relative to the center position. Used with permission [42].

Therefore, to impart piezoelectric properties and effects, piezoelectric materials must be subjected to a process called poling or polarization. Group of dipoles with the same alignments are called Weiss domains. Because of the random distribution of Weiss domains with various directions and alignments inside the ceramics as displayed in Fig. 1.13a, macroscopic piezoelectric effect is negligible. Applying a strong electric field leads to an arrangement of the Weiss domains (as depicted in Fig. 1.13b), and then the ceramics can be polarized. The ceramics are now ready to use and present piezoelectric properties, i.e. converting electrical signals to mechanical strains, or converting mechanical strains to electrical voltages. As shown in Fig. 1.13c, after poling, Weiss

domains are slightly misaligned compared to the case shown in Fig. 1.13b due to aging which leads to a reduction in piezoelectric effects [42].

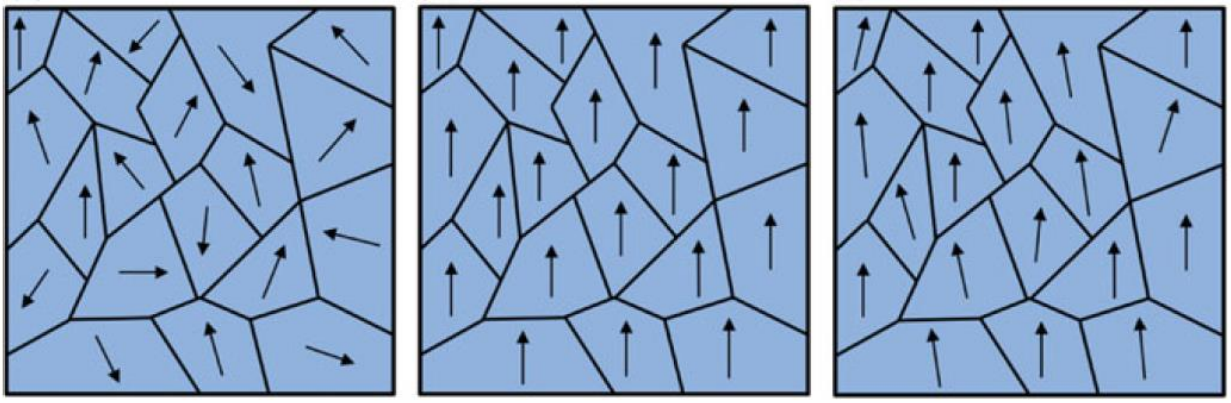

Figure 1.13. Polarization of polycrystalline piezoelectric ceramic causes (a) the as-fired random domain polarity to align to (b) a net positive polarity, which (c) relaxes or ages over time. Used with permission [42].

For piezoelectric materials in the shell structures, different polarization directions may be considered and they can be polarized in the axial, circumferential, and radial (thickness) directions and or a combination of different directions.

It is very important to accurately study and analyze the dynamics of smart laminated composite cylindrical shells by considering the shear effects with the stacked plies and piezoelectric coupling, advanced nanocomposite materials, hygrothermal environmental conditions, and electrical and mechanical boundary conditions. This investigation helps us to clearly understand the dynamic behaviors of smart laminated composite shells integrated with the piezoelectric materials and build a theoretical framework for the composites NDE. The research development in this field is reviewed in the following section.

1.1.4. Waves in Elastic Solids

1.1.4.1. Definition and Characteristics

Waves are a disturbance propagating in a medium such as water, air, or solid. Waves in solids are inaudible to human ears and invisible to human eyes, while acoustic waves in air is audible and surface waves in water is visible. Waves in solids are physical, real, and very important to engineering applications. Mathematical and numerical approaches are needed to analyze and simulate the wave phenomena in solids. These approaches can provide virtual views of waves in our mind. When solids are subjected to external forces, they are stressed. The stresses produce strains observed in form of deformation or displacement. In solid mechanics and structural mechanics, relationship between stresses and strains, displacements and forces, and stresses (strains) and forces are investigated for given boundary conditions applied on solids. These relationships are required to analyze wave motion in solids.

Under dynamic forces varying with time, solids will experience dynamic motion. The stress, strain, and the displacement due to dynamic forces will also be functions of time, and theories of dynamics must be applied. The dynamic motion is often observed in form of wave motion or vibration. We cannot draw a clear line between wave motion and vibration, but, in general, wave is a localized vibration and a vibration is a motion of waves with very long wavelength. When talking regarding waves, one is concerned with the motion or propagation of a localized mechanical disturbance, while in vibration, one usually consider the global motion of the entire structure. Mathematically, both wave motion and vibration are governed by the same dynamic motion equations, which are derived based on the Newton's Law.

Free wave motion is related to wave motion in media free of external excitation. Our aim is to study what could be happening in the media under its natural status, rather than what will be

happening under a special loading condition. In free wave motion analysis, one needs to find the velocity, natural frequency, and wave modes in relation to wavelength or wavenumber. In contrast, forced wave motion refers to waves in media excited by an external excitation. The excitation can be harmonic or transient. The response of the media to a harmonic excitation is presented in the form of frequency spectrum of displacement response. Analysis of waves generated by harmonic excitation is called frequency analysis or wave analysis in frequency domain. Transient response is related to the response of the media under a transient excitation where the results are presented in form of time history of displacement response. Analysis of transient waves is called transient analysis which is also referred to as wave analysis in time domain [43]. The complexity of wave propagation problem is also dependent on the complexity of the geometry of the domain where waves are propagating.

Materials are elastic if they are stressed below the limit called yield stress, while they are plastic if stress beyond this certain limit is applied. Waves propagating in elastic material are expressed elastic waves. One of the major applications of elastic waves is in the field of NDE. In this application, stress level is kept as low as possible and within the elastic range. Otherwise, it could be destructive. Hence, damage detection in structures can be destructive or non-destructive. In NDE, the defect is detected without causing any damage to the structure components and materials through investigation. Elastic wave propagation in solids is one of the NDE techniques serving as a convenient, flexible, and safe method for damage detection developed since 1960s. Hence, wave propagation in solids are usually divided into three categories. The first one is the elastic waves, in which stress relations follow the Hooke's law. The second type of waves is the visco-elastic waves, where viscosity as well as elasticity is applied in the governing equations. The next type of waves is the plastic waves, in which the material yield stress is exceeded. Elastic wave propagation

is the most commonly studied wave due to its simplicity relative to other two waves, used for damage detection aim considering the required low strain/stress level. Hence, elastic wave propagation will be investigated in the present research work.

Studies on wave propagation and vibration of laminated composite shells with different reinforcing materials and under different working conditions are very helpful to understand their dynamic characteristics and failure mechanism. In addition, ultrasonic-based NDE is used to determine the material properties and detect defects (cracks and flaws) in composites. An analysis of wave behaviors, especially the high frequency analysis, is prerequisite in applying NDE techniques effectively using ultrasonic and elastic waves as the theoretical foundation [43]. Analysis of wave propagation in smart laminated composite structures as laminated anisotropic media is much more complicated than the one for isotropic media because of complexity in piezoelectric coupling, boundary condition modeling, micromechanical modeling, and solving procedure.

1.1.4.2. Motion Equation for a Free Wave Motion

To explain how the equation of motion for a free wave motion can be derived, consider a uniform and isotropic thin bar or rod, whose lateral dimension is much smaller than its longitudinal, as shown in Fig. 1.14. The bar is subjected to a uniform traction, $p(x)$, at its cross-section at point x and in the x (axial) direction. As the traction p is applied uniformly in the x direction, the displacement u in the x direction will be dominant. Therefore, the problem can be considered as one dimensional and variables are only function of x and independent of y and z. The governing equation for the one-dimensional wave motion problem can be derived as follows [43].

Consider a representative cell (shaded portion) as shown in Fig. 1.15 isolated from a uniform, isotropic and elastic bar. Let to introduce the linear strain-displacement relation as,

$$\varepsilon = \frac{\partial u}{\partial x} \tag{1.2}$$

where ε is the strain in the material and u is the displacement at point x in the bar.

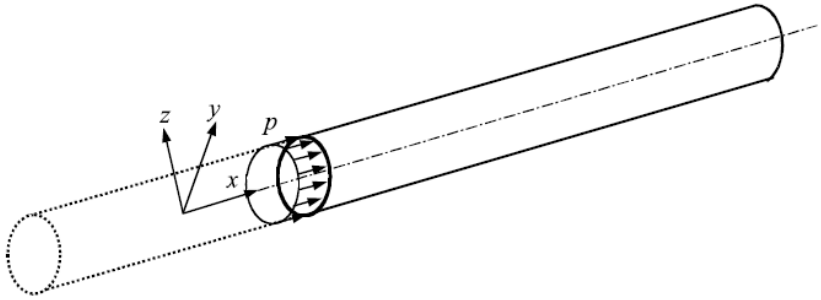

Figure 1.14. Thin bar subjected to axial dynamic force. Used with permission [43].

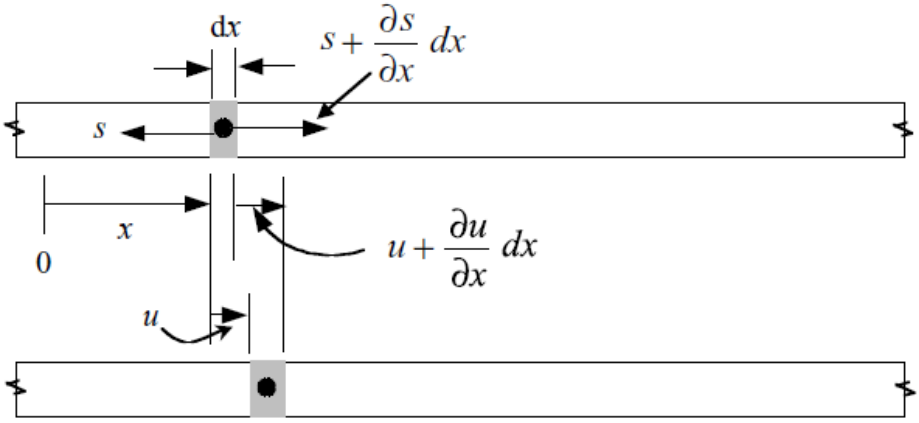

Figure 1.15. Motion of a representative cell in a bar. Used with permission [43].

Using Hooke's law of linear elastic material of the bar, the linear stress-strain relation can be written as,

$$\sigma = E\varepsilon \tag{1.3}$$

where σ is the stress in the material, and E is Young's modulus of the material of the bar. Hook's law for higher dimensional problem is often termed as constitutive equation. By substituting Eq. (1.2) into Eq. (1.3), we obtain,

$$\frac{\partial u}{\partial x} = \frac{\sigma}{E} = \frac{s}{AE} \tag{1.4}$$

where $s = \sigma A$ is the total axial internal force acting on the cross-section. By differentiating Eq. (1.4) with respect to x, we have,

$$AE\frac{\partial^2 u}{\partial x^2} = \frac{\partial s}{\partial x} \tag{1.5}$$

The motion equation of the representative cell can be obtained by Newton's law, indicating that the summation of all unbalanced forces is equal to the product of the mass and acceleration of the cell, i.e.,

$$\frac{\partial s}{\partial x}dx = \rho A dx\frac{\partial^2 u}{\partial t^2} \tag{1.6}$$

where ρ is the mass density of the material of the cell. Using Eq. (1.5), Eq. (1.6) is reduced to,

$$\frac{\partial^2 u}{\partial t^2} = \left(\frac{E}{\rho}\right)\frac{\partial^2 u}{\partial x^2} \tag{1.7}$$

or

$$\frac{\partial^2 u}{\partial x^2} = \frac{1}{c^2}\frac{\partial^2 u}{\partial t^2} \tag{1.8}$$

where

$$c = \sqrt{\frac{E}{\rho}} \tag{1.9}$$

Eq. (1.8) is the so-called wave motion equation, which governs the free wave motion in the bar and c represents the wave velocity.

1.1.4.3. Solution of a Free Wave Motion

The solution of Eq. (1.8) can be considered as,

$$u = F_1(x - ct) + F_2(x + ct) \tag{1.10}$$

where F_1 and F_2 are arbitrary functions representing the shape of propagating waves. Function F_1 represents the shape of waves propagating in the positive x direction and function F_2 demonstrates the shape of waves propagating in the negative x direction. According to Eq. (1.10), c is the velocity of the shape of waves propagating along the bar. Eq. (1.9) indicates that the wave velocity is only dependent on the material properties, Young's modulus, and mass density, and is independent of the excitation frequency. Waves with constant velocity are called nondispersive waves. While for dispersive waves, the velocity is frequency (or wavelength and or wavenumber) dependent. As illustrated in Fig. 1.16, functions F_1 and F_2 are not necessarily the same, but they propagate at the same velocity, and keep the same shape during the propagation in the bar. Eq. (1.10) is often called D'Alembert's solution. In the following, the procedure to determine the explicit solution of functions F_1 and F_2 are explained.

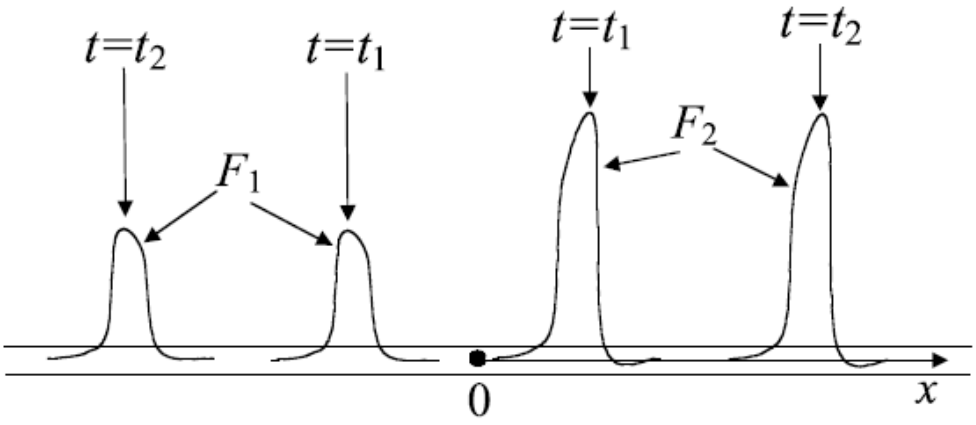

Figure 1.16. Wave propagation in a bar. Used with permission [43].

Let to first consider the harmonic motion of waves generating by a harmonic force. The harmonic force varies with time harmonically. The harmonic force can be expressed mathematically in one of the following sine, cosine, and exponential forms of excitation,

$$p(x,t) = P(x)\sin(\omega t) \tag{1.11}$$

$$p(x,t) = P(x)\cos(\omega t) \tag{1.12}$$

$$p(x,t) = P(x)\exp(-i\omega t) \tag{1.13}$$

where $i = \sqrt{-1}$. In Eqs. (1.11) - (1.13), P is a given function of x, and ω is the angular frequency of the force related to the frequency f, as $\omega = 2\pi f$.

Although the three expressions given in Eqs. (1.11) - (1.13) have different forms, but all can represent a harmonic force. Eq. (1.13) is used commonly because it is the most convenient form in deriving analytical solutions for wave propagation problems. In addition, Eq. (1.13) can be rewritten as,

$$p(x,t) = P(x)\exp(-i\omega t) = P(x)(cos\omega t - isin\omega t) = P(x)cos\omega t - iP(x)sin\omega t \tag{1.14}$$

where the real part represents the cosine excitation and the imaginary part corresponds for the sine excitation. Therefore, the response of the system to an exponential excitation includes real and imaginary parts.

Under the excitation of a harmonic force, the particles in the solid undergo a harmonic motion. Hence, if the wave motion is due to a harmonic excitation, the displacement u must also be harmonic. Therefore, it can be rewritten as,

$$u(x,t) = U_c(x)\exp(-i\omega t) \tag{1.15}$$

where U_c is a function of x, and ω is the angular frequency of the wave. Substituting Eq. (1.15) into Eq. (1.8) gives,

$$\frac{\partial^2 U_c}{\partial x^2} = \frac{-\omega^2}{c^2} U_c \tag{1.16}$$

or

$$\frac{\partial^2 U_c}{\partial x^2} + \gamma^2 U_c = 0 \tag{1.17}$$

where

$$\gamma = \frac{\omega}{c} \tag{1.18}$$

is expressed as wavenumber. $c - \gamma$ and $\omega - \gamma$ curves are called, respectively, dispersion curve and frequency curve. For nondispersive waves with constant velocity c, the wavenumber γ is proportional to the angular frequency ω, and $\omega - \gamma$ curve will be a straight line with slope of c. For dispersive waves with frequency dependent velocity, the relation between c (or ω) and γ is much more complicated.

Solution of Eq. (1.17), as a homogenous differential equation of the second order, can be assumed by,

$$U_c(x) = C \exp(i\alpha x) \tag{1.19}$$

where C is an arbitrary constant. By substituting Eq. (1.19) into Eq. (1.17), we obtain,

$$-\alpha^2 + \gamma^2 = 0 \tag{1.20}$$

This polynomial equation of α has two roots of

$$\alpha = \pm\gamma \tag{1.21}$$

which indicates that U_c has two possible solutions in the form of Eq. (1.19). By superimposing these two possible solutions, the solution of Eq. (1.17) is obtained as,

$$U_c = C_1 \exp(i\gamma x) + C_2 \exp(-i\gamma x) \tag{1.22}$$

where C_1 and C_2 are arbitrary constants to be determined. By substituting Eq. (1.22) into Eq. (1.17), this solution can be verified. U_c, as a function of coordinate x, represents the shape of

propagating waves. Substituting Eq. (1.22) into Eq. (1.15), we obtain the complete solution for harmonic wave motion in a bar as,

$$u(x,t) = C_1 \exp[i\gamma(x - ct)] + C_2 \exp[-i\gamma(x + ct)] \quad (1.23)$$

It is noted that Eq. (1.23) has the same form of Eq. (1.10). Eq. (1.22) is called a complementary solution for free wave motion in infinite bars, where C_1 and C_2 are determined based on the boundary conditions at the two ends of the bar [43].

Therefore, based on the above logic and procedure, analytical models can be developed to derive the governing equations of wave motion and solve the wave propagation problem for various geometries and material properties with the effects of different parameters by combining appropriate theories.

1.1.4.4. Definition of Important Terms

Definitions of some important terms commonly used in structural dynamics and wave propagation analysis are given in the following:

Frequency (f): is the number of occurrences of a repeating event per unit of time. For cyclical processes, such as rotation, oscillations, or waves, frequency is defined as a number of cycles per unit time [44].

Period (T): is the duration of time of one cycle in a repeating event, so the period is the reciprocal of the frequency. The relation between the frequency and the period of a repeating event or oscillation is given by [44],

$$f = \frac{1}{T} \quad (1.24)$$

The SI derived unit of frequency f is Hertz (Hz). One Hz means that an event repeats once per second.

Angular frequency (ω): is defined as the rate of change of angular displacement, θ, (during rotation), or the rate of change of the phase of a sinusoidal waveform (notably in oscillations and waves). Angular frequency ω is commonly measured in radian per second (rad/s) and relates to frequency f by [45],

$$\omega = 2\pi f \tag{1.25}$$

Wavelength (λ): is the spatial period of a periodic wave and the distance over which the wave's shape repeats. It is usually determined by considering the distance between consecutive corresponding points of the same phase, such as crests, troughs, or zero crossings (see Fig. 1.17). The SI unit of wavelength is meter (m) [46].

Assuming a sinusoidal wave moving at a fixed wave speed, wavelength is inversely proportional to the frequency of the wave. Waves with higher frequencies have shorter wavelengths (or higher wavenumbers), and lower frequencies have longer wavelengths (or lower wavenumbers).

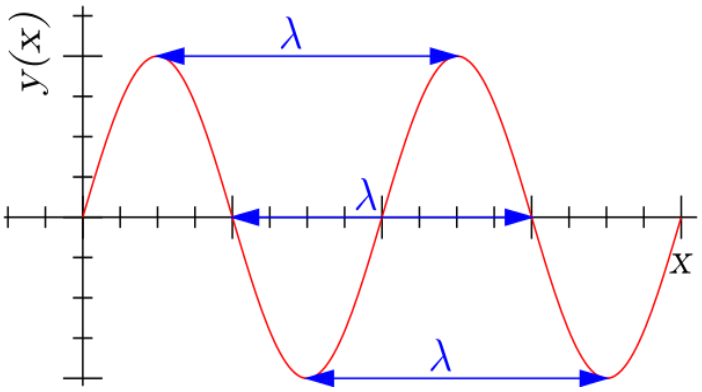

Figure 1.17. Wavelength of a sine wave. Used with permission [46].

Wavenumber (γ): is the spatial frequency of a periodic wave, defined as the number of radians per unit distance. In general, wavenumber in the axial direction (x) is given by [47],

$$\gamma = \frac{2\pi}{\lambda} = \frac{\omega}{c} \tag{1.26}$$

Wavenumber equation in the circumferential direction (θ) is given by,

$$\gamma\theta_0 = n(2\pi) \tag{1.27}$$

where for a complete cylinder $\theta_0 = 2\pi$, so $\gamma = n$.

Wave phase velocity (c): The phase velocity of a wave is the rate at which the phase of the wave propagates in space. For such a component, any given phase of the wave (for example, the crest) will appear to travel at the phase velocity. The phase velocity is given in term of the wavelength λ and period T as [48],

$$c = \frac{\lambda}{T} \tag{1.28}$$

Wavenumber γ is related to wavelength λ, frequency f, angular frequency ω, and phase velocity c as [43],

$$\gamma = \frac{2\pi}{\lambda} = \frac{\omega}{c} = \frac{2\pi f}{c} \tag{1.29}$$

Important fundamental relations are listed in Table 1.2.

Table 1.2. Fundamental relations [43].

Parameter	f	ω	T	λ	γ	c
Frequency f	1	$\omega/2\pi$	$1/T$	c/λ	$c\gamma/2\pi$	c/λ
Angular frequency ω	$2\pi f$	1	$2\pi/T$	$2\pi c/\lambda$	$c\gamma$	$2\pi c/\lambda$
Period T	$1/f$	$2\pi/\omega$	1	λ/c	$2\pi/c\gamma$	λ/c
Wavelength λ	c/f	$2\pi c/\omega$	cT	1	$2\pi/\gamma$	c/f
Wavenumber γ	$2\pi f/c$	ω/c	$2\pi/Tc$	$2\pi/\lambda$	1	ω/c
Velocity c	λf	ω/γ	λ/T	λ/T	ω/γ	1

1.2. Literature Review

This section presents a comprehensive literature review with the basics to reviewing research works which have been done in the research field with the existing gaps.

1.2.1. Wave Propagation and Vibration of Smart Composites

In this section, a review is presented regarding the methods used for modeling and analysis of structural dynamics of smart composites as well as related research works in this field.

1.2.1.1. Brief History of Shell Theories

Different shell theories were developed over the past decades, which can help to model and understand dynamics of shell structures. The lowest-order shell theory, i.e. the membrane shell theory, was developed by Love [49], in which transverse or out-of-plane shear forces (V_{xz} and $V_{\theta z}$), bending and twisting moments (M_{xx}, $M_{\theta\theta}$, and $M_{x\theta}$) are assumed to be negligibly small. Such model is applicable to very thin shell structures in which only the in-plane normal and shear forces (N_{xx}, $N_{\theta\theta}$, and $N_{x\theta}$) applying in the midsurface of the shell are considered. This lower-order shell model presents the essential features of the shell and is used as a fundamental model for higher-order shell theories. Some notable works based on this simplified model were presented by Donnel [50], Flügge [51], Vlasov [52], and Sanders [53].

The classical shell theory, proposed by Love [49] and Reissner [54] as the first approximation to thin shell theory, is based on the following assumptions: (a) the laminate is thin compared to its lateral dimension; (b) the deflection of shell is small; (c) straight lines normal to the middle surface remain straight and normal to that surface after deformation; and (d) the transverse shear stresses (τ_{xz}, $\tau_{\theta z}$) are zero. Usually, the model developed based on the above assumptions is referred as the Love's bending shell theory or the classical shell theory. Many studies were performed on shell

structures based on the Membrane and the Love's bending shell theories. However, the above assumptions are not valid for thicker shells and shells with low stiffness central plies undergoing significant transverse shear deformation. Mirsky and Hermmann [55] considered the shear effects in both axial and circumferential directions and the rotary inertia effects for cylindrical shells with moderate thickness. Lin and Morgan [56] developed equations for axillary symmetric motions considering shear effects and rotary inertia. Cooper and Naghdi [57] developed a theory including both transverse shear effects and rotary inertia for non-axillary symmetric motion of shell structures. Greenspon [58] showed that the Cooper-Naghdi shell theory [57], considering both transverse shear effect and rotary inertia, is sufficient for wave propagation analysis in thicker cylindrical shells. The Cooper-Naghdi shell theory is also known as the first-order shear deformation shell theory (FSDT). Based on the first-order shear deformation shell theory, the assumption of normality of straight lines is removed, that is, straight lines normal to the middle surface remain straight but not normal to that surface after deformation.

Therefore, in the membrane and bending shell theories, concentration is only on the displacement of the middle surface of the shell, while in the theories including shear and rotary inertia, such as the first-order shear deformation shell theory, the slopes of the shell element are also considered. Hence, for moderately thick shells, theories including shear deformation and rotary inertia would be desirable. However, for very thick shells such as pipes, three-dimensional theory of elasticity is more appropriate and reliable than thin shell theories. According to this theory, normal stress in thickness direction as well as other stresses is considered in the constitutive relations.

The shear effects should be considered and studied properly for smart laminated composites and piezoelectric materials with significant shear piezoelectric coefficients considering different poling directions.

1.2.1.2. Finite Element Method in Wave Propagation and Vibration Applications

The finite element method (FEM) is an effective numerical approach for solving boundary value problems on complex domains [59]. However, standard FEM is not much effective to solve wave propagation and frequency problems [59,60]. Some errors occur in wave propagation and vibration analysis using piecewise polynomial approximations of standard FEM [61,62]. It was reported that in the case of time harmonic wave propagation and vibration solution, the accuracy of numerical solution decreases rapidly with the increase of wavenumber [63–65]. Thus, for short wavelength problem, fine meshes are required to attain reasonable solutions considering the high frequency wave motions with large wavenumbers. In the case of transient wave propagation and frequency problem, the numerical wave propagation velocity and natural frequency may be noticeably different from the physical velocity and frequency, due to the numerical period elongation leading to the dispersion errors [59,66]. When a wave travels in a long distance, larger errors occur and more inaccurate numerical solutions are obtained. So, whenever high frequency is required, considerable errors happen in the numerical solutions unless the mesh is fine enough to reduce the errors and variations.

The spectral FEM is a formulation of the FEM that uses high degree piecewise polynomials as basic functions. This method is a numerical approach that can provide numerical solutions very close to the exact solutions because of high degree piecewise polynomials (harmonic functions) used as basic functions, where the solutions of wave equations are basically harmonic functions. However, the spectral finite element method is difficult to be utilized for complicated geometries

as used in a real case, since it uses global basic functions. Thus, this method has some limitations to be used in practical cases for analysis of structures. The spectral element method has lower numerical errors in comparison to the standard finite element method. Moreover, this method has been developed to solve effectively wave propagation and vibration problems by approximating the solutions with trigonometric polynomials [67–69]. However, the spectral finite element method is an expensive approach and also difficult to develop and extend for general nonlinear analysis.

It is difficult or even impossible to assign various distributions of CNTs in a composite based on the finite element methods, and a combination of micromechanics models and numerical approaches is needed for this purpose. Hence, developing an analytical approach for solving wave propagation and vibration problem in composites is more beneficial, while it will not have the limitation and drawbacks of finite element methods.

Mazuch [70] obtained wave dispersion solutions for anisotropic shells and rods using the finite element method where the results were compared with those obtained based on the lower order theories. Datta and Kishore [71] used a two-dimensional plane strain finite element model to investigate the features of ultrasonic wave propagation to identify defects in composite materials. Chakraborty et al. [72] performed a finite element analysis (FEA) of free vibration and wave propagation in composite beams with structural discontinuities. A spectral finite element model was presented by Mahapatra and Gopalakrishnan [73] for analysis of wave propagation in composite tubular structure where its performance was compared with analytical solution based on the membrane shell model. Manconi and Mace [74] presented a wave finite element method for prediction of wave characteristics of cylindrical and curved panels by combining the conventional finite elements and the theory of wave propagation. Xiao et al. [75] investigated the dispersion characteristics of guided waves in a multilayered magneto-electro-elastic curved in

which the spectral finite element method was applied to obtain the dispersion equation of waves. In another study by Liang et al. [76], wave propagation in piezoelectric helical waveguides was studied using the spectral finite element method. Tsai and Palazotto [77] determined the non-linear vibration of cylindrical shells using the finite element analysis with high-order shear deformation theory. Ramesh and Ganesan [78] obtained vibration and damping characteristics of multi-layered cylindrical shells with a viscoelastic core using the finite element analysis. In another study, Chakravorty et al. [79] used the finite element method for free vibration analysis of point supported laminated composite cylindrical shells.

Although the dynamic behaviors of smart composites can be modeled and studied by FEA and the results of analysis can be used as a guidance for NDE applications and to possibly solve the wave propagation and frequency problems, but the accurate finite element modeling of composites and calculations are usually not efficient requiring significant calculation costs especially for vibration and wave propagation in infinite media (both computer power and calculation time). Hence, based on the limitations of FEM, analytical approaches are developed in this thesis to investigate wave dynamics and vibration behaviors of smart laminated composite cylindrical shells with the effects of various parameters.

1.2.1.3. Dynamics of Piezoelectric Structures

In the literature, piezoelectric materials were modeled and studied by considering the axial poling [80,81], circumferential polarization [81], and polarizing in the thickness direction (or radial polarization) [81–90]. Buckling behavior of pure piezoelectric shells and piezoelectric-coupled composite shells have been investigated in the literature. For example, Dai and Zheng [91] investigated the buckling behavior of a laminated cylindrical shell of functionally graded material (FGM) with the piezoelectric fiber-reinforced composite (PFRC) actuators with the radial

polarization in thermal environment without considering the transverse shear effects and rotary inertia in the mathematical modeling. In another study, Nasihatgozar et al. [92] investigated the buckling response of piezoelectric composite panels reinforced with carbon nanotubes with the axial poling using the classical laminated plate theory (CLPT) in which the transverse shear effects and rotary inertia were not included.

Analysis of wave propagation and vibration characteristics of piezoelectric materials and structures have also been performed previously in the literature. Hussein and Heyliger [93] analyzed free vibration behavior of laminated piezoelectric cylindrical shells using a semi-analytical layer model. They used piecewise-linear variation method to find approximate solutions for static and dynamic problems and finite element approximations for the transverse displacement. David and Touratier [85] presented a two-dimensional theory for analysis of a multilayered piezoelectric shell, where the theory is based on a hybrid approach in which continuity conditions at layer interfaces as well as the boundary conditions are satisfied. Jiangong et al. [81] used linear three-dimensional piezoelectricity to determine wave propagation characteristics in hollow cylinders composed of the functionally graded piezoelectric materials, where the displacements and electric potentials are expressed in a series of Legendre polynomials. Sheng and Wang [94] investigated the thermo-elastic vibration and buckling characteristics of the functionally graded piezoelectric cylindrical shell using the Hamilton's principle and Maxwell equation with a quadratic variation of the electric potential along the thickness direction. In their study, the effects of material composition, thermal loading, external voltage, and shell geometry parameters on the free vibration characteristics were also studied. Hasheminejad et al. [95,96] employed an exact three-dimensional piezoelectric model to investigate the free vibration of a smart piezocomposite hollow cylinder and a thick-walled liquid-coupled piezo-laminated

cylindrical vessel, where the piezoelectric cylinder is considered to be infinitely long, and short circuit electrical boundary condition is applied at the inner and outer surfaces of the shell. They utilized the transfer matrix approach along with the state space method to calculate the natural frequencies of an infinite cylinder.

Studying wave propagation in piezocomposites reinforced with nanoparticles is still a gap in the literature. It is very important to propose an appropriate wave propagation model to evaluate the effects of nano-sized reinforcements such as CNTs on dynamics and wave propagation characteristics of piezocomposites. This problem is very important to be solved and developing analytical models considering nanocomposite effects on wave dynamics helps us to clearly understand wave dispersion results of piezocomposites reinforced with nanofibers leading to optimize the nanocomposite designs for various engineering applications such as energy harvesting and structural health monitoring with NDE.

1.2.1.4. Dynamics of Smart Laminated Shell Structures

Wave propagation in smart cylindrical shells integrated with piezoelectric actuators has also been studied in the literature. For example, Wang [39,97] and Wang and Liew [98] studied analytically the wave propagation in piezoelectric coupled metallic cylindrical shells by the membrane, the Love bending, and the Cooper-Naghdi shell theories. Dong and Wang [99–101] investigated wave propagation characteristics in the piezoelectric coupled cylindrical shell with the effects of large deformation and rotary inertia, however, they did not consider the effects of the transverse shear, and only the in-plane stresses were considered in their study and transverse shear stresses and the resultant shear forces were assumed negligible. Hasheminejad and Alaei-Varnosfaderani [102] investigated the steady-state non-axisymmetric fluid-structure-coupled vibrations of thick hollow cylinder of finite length coupled with axially/circumferentially/radially

polarized functionally graded piezo-ceramic material using the linear three-dimensional elasticity theory in conjunction with the transfer matrix approach. In another study by Hasheminejad and Alaei-Varnosfaderani [103], they used the three-dimensional piezo-elasticity theory and the spatial state-space approach to study the steady-state non-axisymmetric sound radiation and scattering characteristics of an infinitely long, arbitrarily thick, orthotropic functionally graded hollow circular cylinder, coupled with a functionally graded piezo-ceramic material.

Based on the above literature review, the processes considering the nano-sized reinforcing fiber and its effects on the composite wave model, the exact piezoelectric effects with different poling directions on the wave behaviors of smart composites as well as the transverse shear effects of composite shells are still gaps in the related research field. By accurate modeling of piezoelectric effects with considering shear effects on wave dynamics, we can design an appropriate smart laminated composite shells for the applications of noise and vibration control, structural stability analysis, and structural health monitoring with NDE.

1.2.2. CNT Effects on Structural Dynamics

1.2.2.1. A Brief Introduction to Modeling CNTs in Composites

The material properties of a composite lamina are function of its constituent properties, geometric characteristics, such as fiber volume fraction and distribution. To estimate the effective material properties of CNT-reinforced composites, some micromechanics models such as the Mori-Tanaka [104] and the rule of mixture [105] models can be applied. One major advantage of the Mori-Tanaka model rather to other micromechanics models such as the rule of mixture is that it can be used in the case of composites reinforced with both aligned and randomly oriented, straight CNTs. While, the rule of mixture model does not differentiate between these two cases [106]. Moreover, the Mori-Tanaka model is capable to estimate the effective elastic properties for

the case that CNTs are agglomerated in a matrix. On the other hand, the rule of mixture model is simpler than the Mori-Tanaka model [106]. The Mori-Tanaka model has been led to a successful estimation of the resulting effective elastic properties of composites reinforced with both aligned and randomly oriented, straight CNTs [92,106–109]. This is because of its accuracy even at high volume fraction of inclusion [107]. Hence, the straight-forward Mori-Tanaka model [104] is employed in this thesis to calculate the resulting effective elastic properties of cylindrical composite shells reinforced with angled, randomly oriented, and agglomerated CNTs for the wave propagation and vibration studies.

There are other methods such nonlocal continuum mechanics theory and molecular dynamics simulations which can estimate the mechanical behaviors of nanoscale structures in which small effects are considered. In this study, we consider CNTs that are embedded in a composite shell which is in macro scale, therefore, the nanoscale effect of CNTs is usually simplified by the micromechanical modeling, similar to other studies in the literature [92,107,15,16]. Considering the small-scale effect is usually essential when the mechanical behavior of an individual CNT is studied.

1.2.2.2. Dynamics of CNT-Reinforced Composite Structures

Regarding dynamics of CNT-reinforced composite structures, there are many research works in the literature which studied buckling and free vibration behaviors of CNT-reinforced plates and shells. For example, Shen and Zhang [110] investigated the thermal buckling and post-buckling behaviors of functionally graded nanocomposite plates reinforced by SWCNTs subjected to in-plane temperature variation. Shen and Xiang [111] studied the post-buckling response for CNT-reinforced composite cylindrical panels resting on elastic foundations in thermal conditions. Keleshteri et al. [112] analyzed the post-buckling behavior of smart functionally graded CNT-

reinforced annular sector plates coupled with the piezoelectric layers using generalized differential quadrature method. Kiani [113] presented a research dealing with the post-buckling phenomenon in CNT-reinforced composite plates exposed to a temperature change. In another research by Keleshteri et al. [114], post-buckling characteristics were determined for CNT-reinforced composite rectangular plates coupled with piezoelectric layers subjected to in-plane compressive loads.

Heydarpour et al. [115] carried out free vibration analysis for functionally graded CNT-reinforced composite truncated conical shells based on the first-order shear deformation shell theory. Alibeigloo [116] investigated free vibration behavior of functionally graded CNT-reinforced cylindrical panels coupled with the piezoelectric layers with simply supported boundary conditions using three-dimensional theory of elasticity. Mirzaei and Kiani [117] studied free vibration behavior of functionally graded CNT-reinforced composite cylindrical panels using the first-order shear deformation shell theory and Donnell-type kinematic assumptions. Wang et al. [118] performed a vibration analysis of the functionally graded CNT-reinforced composite shallow shells with arbitrary boundary conditions using the first-order shear deformation shell theory. Free vibration analysis of functionally graded CNT-reinforced composite spherical shell panels was performed by Kiani [119] based on the first-order shear deformation shell theory and the Sanders kinematics. Torabi and Ansari [120] carried out a nonlinear free vibration analysis of thermally induced functionally graded CNT-reinforced annular plates. In another study by Kiani [121], free vibration behavior of functionally graded CNT-reinforced composite plates integrated with the piezoelectric layers at the bottom and top surfaces was analyzed. Mohammadzadeh-Keleshteri et al. [122] obtained the nonlinear free vibration responses of functionally graded CNT-reinforced composite annular sector plates coupled with the piezoelectric layers. Free vibration responses of

a functionally graded piezoelectric cylindrical nanoshell were obtained by Razavi et al. [123] based on consistent couple stress theory. Kamarian et al. [124] investigated the effect of CNT agglomeration on free vibration behaviors of CNT-reinforced composite conical shells. A free vibration analysis of laminated CNT-reinforced composite doubly-curved shells and panels considering the effect of CNT agglomeration was performed by Tornabene et al. [125]. Furthermore, Wang [126] studied wave propagation in CNTs with two nonlocal continuum mechanics models: elastic Euler-Bernoulli and Timoshenko beam models. The effect of shear deformation on wave propagation in fluid-filled MWCNTs embedded in an elastic matrix has also been investigated in Refs. [127,128]. Janghorban and Nami [129], investigated the wave propagation characteristics of functionally graded nanocomposite plates reinforced with carbon nanotubes using the second-order shear deformation theory.

Wave propagation study of smart CNT-reinforced composite shells with various nanoparticle distributions is still a void in the literature, where an efficient and appropriate analytical model is required to investigate their effects clearly. By developing analytical models considering nanoparticle effects with various distributions on wave dispersion results, we can clearly interpret and analyze the results and data of structural health monitoring of smart nanocomposites and or optimize the design of smart nanocomposites for the application of energy harvesting and structural enhancement in dynamic testing.

1.2.3. Wave Propagation and Vibration Characteristics of Smart Composite Shell Structures in Hygrothermal Environments

Constituents of composite materials are sensitive to the temperature/moisture change. As a result, composite materials may be exposed to hygrothermal loading as well as mechanical loading.

Therefore, the effects of hygrothermal environmental conditions should be considered accurately in wave propagation and vibration characteristics of smart composite structures.

Composite shells are commonly subjected to dynamic loading under different boundary conditions based on their applications, hence, determining vibration characteristics of composite shells has a great importance in their successful applications. It was reported that the elastic moduli and strength of composites decrease at high temperature and moisture [130–132]. Therefore, the environmental conditions may influence on the wave dynamics, vibrational behaviors, and natural frequencies of composite shell structures. Boundary conditions of shell structures lead to different vibration characteristics which should be investigated clearly.

Many methods, ranging from analytical methods to energy methods based on the Rayleigh-Ritz approach in which, respectively, iterative solution methods and closed form solutions of the governing equations were used [133,134,55,135,136], have been developed to determine vibration characteristics of thin shells. In the literature, methods commonly used to investigate vibration of cylindrical shells with various boundary conditions are based on the state-space approach [135,137–139] and a numerical approach by assuming an unknown axial modal function [140–142]. Using beam functions as the axial modal functions is a straight forward approach for treating cylindrical shells with various boundary conditions. This method is relatively less computationally intensive and leads to more accurate and reasonable natural frequencies. The new feature of this method is the use of beam functions as the axial modal functions to determine vibration characteristics of smart laminated CNT-reinforced composite cylindrical shells in general environment under different boundary conditions which has not been seen in the literature. The three-dimensional linear elasticity and an iterative approach were employed by Soldatos and Hadjigeoriou [141] to investigate the free vibration of cylindrical panels and shells. Lam and Loy

[143] investigated the free vibration behaviors of a multi-layered isotropic cylindrical shell under various boundary conditions using beam functions as the axial modal functions based on the Love bending shell theory. Lam and Loy [144] studied the vibrational behaviors of thin cylindrical panels with simply supported boundary condition based on the Flügge shell theory. In another study, Lam and Loy [136] obtained vibration characteristics of rotating cylindrical panels under simply supported boundary condition. Loy et al. [145] investigated vibrational behaviors of cylindrical shells with different boundary conditions using the generalized differential quadrature (GDQ) method. Zhang et al. [146] carried out vibration analysis for cylindrical panels using the wave propagation approach.

Numerous research works have been made on vibration and wave propagation analysis of laminated composite plates and shells. For example, Ng et al. [147] conducted the free vibrational analysis for a rotating thin truncated circular symmetrical cross-ply laminated composite conical shell with various boundary conditions by the GDQ method. Malekzadeh et al. [148] performed three-dimensional free vibration analysis of arbitrary laminated circular cylindrical shells using a mixed layer wise theory and differential quadrature method (LW-DQ). An exact solution method was developed by Jin et al. [149] to determine free vibrational behaviors of laminated composite cylindrical shells with different stacking sequences under general boundary conditions. Mechanics, dynamics, and vibration of pure CNTs have been studied in many research works [150–154]. On the other hand, vibration and dynamics of composite plates, panels, and shells reinforced with CNTs under different boundary conditions have been investigated in the literature [117,155–162]. Yas et al. [156] studied the vibrational behavior of functionally graded nanocomposite panels reinforced with SWCNTs with simply supported boundary condition based on the three-dimensional theory of elasticity for different distributions and volume fractions of

CNTs. Safaei et al. [162] studied the dynamics of nanocomposite sandwich plates with the effects of loading frequency for periodic thermo-mechanical loadings.

Many studies have also been conducted on vibration, bending, and buckling of laminated composite plates [15,163–165,16,166–171], and shells [172–181] in hygrothermal environments. For example, Shen [15] presented an investigation on the nonlinear bending of simply supported functionally graded nanocomposite plates reinforced with SWCNTs subjected to a transverse uniform or sinusoidal load in thermal environment, where the results showed that characteristics of nonlinear bending are influenced by the temperature rise. A free vibration analysis of functionally graded nanocomposite plates reinforced by SWCNTs was presented by Lei et al. [16] using the element-free kp-Ritz method in thermal environment, where the governing equations were obtained based on the first-order shear deformation plate theory and the two-dimensional displacement fields are approximated by mesh-free kernel particle functions. Atanasov et al. [169] studied the dynamic stability of a double microbeam system under thermal effect. Naidu and Sinha [172] used the finite element method to investigate the nonlinear free vibration characteristics of laminated composite shells in hygrothermal environmental conditions. Malekzadeh and Heydarpour [174] investigated the free vibration behavior of rotating functionally graded cylindrical shells subjected to the temperature change using the first-order shear deformation shell theory. The effects of hygrothermal environmental conditions on the linear and nonlinear free flexural vibration of anisotropic shear deformable laminated cylindrical shells were investigated by Shen and Yang [176], where the cylindrical shell is made up of fiber-reinforced composites with the reinforcement being distributed either uniformly or functionally graded of piece-wise type along the thickness of the shells and the motion equations were derived based on a higher order shear deformation shell theory with a von Kármán-type of kinematic nonlinearity, and the results

displayed that the temperature and moisture variations have a moderate effect on the natural frequencies. Biswal et al. [178] studied the effects of hygrothermal environmental conditions on free vibration of woven fiber glass/epoxy laminated composite cylindrical shallow shells both numerically and experimentally based on the FEA and the first-order shear deformation shell theory, where the results showed that the frequency of vibration decreases with the increase of temperature and moisture. An investigation on the nonlinear vibration behavior of graphene-reinforced composite laminated cylindrical shells in thermal environment has been done by Shen at al. [180] based on the Reddy's third-order shear deformation theory and the von Kármán-type kinematic nonlinearity, where the results of their study revealed that the nonlinear vibration characteristics of the shells are significantly influenced by the temperature variation, the shell geometric parameter, the shell end conditions, and the stacking sequence. However, investigating vibration and wave propagation characteristics of smart laminated composite plates and shells integrated with the piezoelectric materials in hygrothermal environmental conditions are limited in number. Wang et al. [182] investigated the hygrothermal effects on dynamic inter-laminar stresses in laminated plates with the piezoelectric actuator layers under free vibration. Dong and Wang [99,101] studied the influence of large deformation and rotary inertia on wave propagation in long piezoelectric cylindrically laminated shells in thermal environment. Aeroelastic performances of smart composite plates under aerodynamic loading in hygrothermal environments were investigated by Mahato and Maiti [183]. Nanda [184] studied non-linear free vibration and transient response of laminated composite cylindrical and spherical shells with piezoelectric layers in thermal environment. An analysis of delaminated fiber-reinforced composite plates with integrated active fibre composite actuators and sensor under hygrothermal environments has been

investigated by Shankar et al. [185], where the results of this study illustrated that there will be a reduction in the natural frequencies in the presence of delamination and hygrothermal loading.

Due to temperature- and moisture-dependent material properties of CNT-reinforced composites, it is very important to consider the effects of temperature/moisture variation on wave propagation and vibration characteristics of smart laminated CNT-reinforced composites with the influence of various boundary conditions using wave propagation approach. By developing an analytical model considering hygrothermal effects on wave dynamics and vibration characteristics using the wave propagation approach, we can design smart laminated composite shells according to unexpected environmental conditions and different mechanical boundary conditions required for various engineering applications such as energy harvesting and or interpret the results of structural health monitoring by NDE**.**

1.3. Problems Definition and Motivation

According to the literature review which has been done in the previous section, there are still some meaningful gaps in the research field related to wave dynamics and vibration characteristics of smart composite shell structures, where (i) wave propagation characteristics of smart laminated fiber-reinforced composite cylindrical shells with the coupling effects of piezoelectricity, transverse shear, and rotary inertia, (ii) wave dynamics of smart composite cylindrical shells reinforced with high stiffness nano-sized fibers such as CNTs with different distributions, (iii) hygrothermal effects on wave dynamics of smart laminated CNT-reinforced composite cylindrical shells, and (iv) vibration characteristics of smart laminated CNT-reinforced composite cylindrical shells using the wave propagation approach under various boundary conditions are still unsolved and should be studied. These problems are important due to the significant effects of transverse

shear, piezoelectricity, nanoparticles, hygrothermal environmental conditions, and boundary conditions on wave dynamics and vibration characteristics of smart composite cylindrical shells.

Since high wavenumbers (or frequencies) are required to determine dynamics and wave propagation characteristics of smart laminated composite shell structures, theories considering the transverse shear effects as well as in-plane stresses are desired to see the dispersion results in all wave modes. In smart structures made up of host stacked composite and piezoelectric layers, shear may occur between layers. Therefore, for smart laminated composite structures, transverse shear stresses should be considered in the mathematical modeling for wave propagation studies. By including the transverse shear effects, wave modes corresponding to the shear planes are obtained as well as axial, circumferential, and radial wave modes. Considering piezoelectricity and shear effects is very helpful in design of smart laminated composites used for noise and vibration control, structural stability analysis, and structural health monitoring with NDE. The transverse shear effects were not considered in the previous research studies in wave propagation modeling of smart laminated fiber-reinforced composite cylindrical shell structures, because of the complexity in mathematical modeling considering the resultant shear forces and challenge in numerical computations corresponding to higher shear wave modes for smart multi-layered composites with piezoelectric coupling effects. Hence, in this research, an analytical approach, including the transverse shear effects and rotary inertia, is proposed to investigate wave propagation in smart laminated fiber-reinforced composite cylindrical shell structures and the results are compared with those obtained without the effects of transverse shear and rotary inertia.

Effects of CNTs on buckling and vibration of CNT-reinforced composite plates and shells were studied in many research works. However, their effects on wave dispersion solutions have not been modeled and investigated by considering different CNT distributions and volume fractions in the

piezocomposite cylindrical shells as well as the shear effects. Wave propagation problem in CNT-reinforced composites has some challenges considering the nano-sized fiber reinforcement with different distributions and volume fractions. As discussed before, available methods to consider nano-fiber reinforcement effects are non-local mechanics, molecular dynamics, and micromechanics models. The micromechanics model is chosen as the feasible analytical method due to its advantages in directly obtaining the effective material properties for the resultant composite with various nanotube distributions, where a simple and efficient analytical model can be developed to analyze the wave propagation in smart CNT-reinforced composites. The accuracy of the micromechanical model was proven with experimental testing by validating the estimated effective mechanical properties for the resultant composite reinforced with nanoparticles for a specific orientation and volume fraction [186]. It is very important to model wave propagation in CNT-reinforced composites to understand their dynamics when a wave is excited on their surface for the structural health monitoring and energy harvesting applications. To perform this investigation, micromechanical modeling must be developed for the wave propagation problem which is not simple and has some difficulties in the mathematical modeling due to the CNT reinforcement, where in this research, appropriate wave propagation models for different types of CNT orientation and distribution are developed by incorporating the micromechanics model and shell theory. Analysis of wave propagation in composites reinforced with nanoparticles helps us to understand their wave behaviors at various axial and circumferential wavenumbers as well as wave modes. Understanding the effects of CNT distributions on wave dynamics helps us to optimize the design process of customized CNT-reinforced piezocomposites for various engineering applications such as energy harvesting and structural health monitoring by NDE.

Constituents of composite materials are temperature-and moisture-dependant, where their effects on dynamics of composite structures are important and significant. Material properties of CNTs are also temperature-dependant. For the design of advanced smart structures used in energy harvesting application and analysis of data of structural health monitoring by NDE, we hence need to study the wave dispersion results for smart laminated CNT-reinforced composite shells in the hygrothermal environments to characterize wave behaviors for the case of temperature and moisture variations in order to optimize the design. This study was not presented before due to the challenge of mechanical-temperature and -moisture coupling effects with applied hygrothermal strains and also obtaining the effective thermal and moisture coefficients. An analytical model considering temperature and moisture couplings is proposed and developed in this research to find the effects of hygrothermal environmental conditions on wave propagation and vibration characteristics of smart composites.

Vibration characteristics of smart laminated CNT-reinforced composite cylindrical shells with finite length under various boundary conditions lead to an accurate design of smart composites for various engineering applications such as energy harvesting and stability analysis. Developing an analytical model using the wave propagation approach leads to determine vibration characteristics of smart laminated composite cylindrical shells simpler and easier than other existing approaches. Hence, an approach based on the wave propagation method is developed in this thesis to find the natural frequencies of smart laminated CNT-reinforced composite cylindrical shells under various mechanical boundary conditions.

According to the above-mentioned voids in the research field, analytical models are developed by combining the existing theories/models to bridge the existing gapes in the wave dynamics and vibration problems of smart laminated composite cylindrical shells by considering the effects of

various parameters. Composite materials, especially CNT-reinforced composites, are totally different from other isotropic materials such as steel and aluminium with different constitutive equations, not like just replacing some numbers for the material properties. We need to first obtain and develop the corresponding constitutive equations and governing equations of motion for smart customized composite structures used in the wave propagation and vibration problems with the effects of transverse shear, piezoelectric coupling, CNT distribution, hygrothermal environmental conditions, and mechanical boundary conditions, and then model and solve the wave dynamics and vibration problems.

Removing the existing gaps by developing analytical models including the parameters neglected in previous studies contributes the research fields utilizing the wave propagation and vibration modeling such as structural health monitoring, energy harvesting, and structural stability analysis.

1.4. Research Objectives and Innovations/Novelties

Based on the gaps introduced in the previous section, the objectives of this research thesis are summarized as following:

- Developing a theoretical foundation/framework to study the wave propagation and vibration characteristics of smart laminated fiber-reinforced composite cylindrical shells.
- Modeling and solving the wave propagation problem in smart laminated fiber-reinforced composite cylindrical shells integrated by the piezoelectric layer and studying the effects of transverse shear and rotary inertia with the proposed analytical model, which provides detailed description and understanding of the wave parameters and physical phenomena.

- Modeling and studying the effects of nano-sized reinforcement on wave propagation characteristics of customized smart composite cylindrical shells with various types of nanoparticle distribution by presenting an analytical approach combining the Mori-Tanaka micromechanics model and the first-order shear deformation shell theory.
- Modeling and studying the effects of temperature and moisture variations on the structural dynamics of smart laminated CNT-reinforced composites by a developed analytical model considering the hygrothermal effects.
- Modeling free vibration problem in finite length smart laminated CNT-reinforced composite cylindrical shells using the wave propagation approach and determining vibration characteristics under various mechanical boundary conditions and hygrothermal environmental conditions.

1.5. Outline of the Thesis

Smart composite cylindrical shells reinforced with Carbon, E-Glass, and CNT fibers and integrated with the piezoelectric materials are the studied objects of this thesis and their dynamic behaviors are modeled and studied considering the effects of various parameters. The focus of this thesis is to propose and develop analytical models to investigate structural dynamic characteristics of smart laminated composite cylindrical shells and build a theoretical foundation and framework for composite NDE by combining the existing mathematical and micromechanical models. Accordingly, this thesis is organized into four Chapters.

The first Chapter introduces the background, scope, and motivation, and also indicates the necessity of the present study. Literature review is conducted in the related areas including dynamics of smart composites, CNT effects on structural dynamics, and hygrothermal effects on

structural dynamics of smart composite shell structures. Problems definition and research objectives and innovations are also explained in detail.

Chapter two of the thesis presents the derivation of constitutive equations for laminated fiber-reinforced composite cylindrical shells and piezoelectric cylindrical shells with different polarization directions based on the classical shell theory and the first-order shear deformation shell theory. Then wave propagation problem in laminated fiber-reinforced composite cylindrical shells coupled with the piezoelectric layer is modeled based on various shell theories with the coupling effects of transverse shear and piezoelectricity. Afterward, an analytical model combining mathematical and micromechanical models is developed to model wave dynamics of CNT-reinforced piezocomposite shells with different CNT distributions. The effective material properties for piezocomposite shells reinforced with CNTs are estimated using the Mori-Tanaka micromechanics model. Then, the constitutive equations are derived for various CNT arrangements (angled and randomly CNT distributions and agglomerated CNTs with different volume fractions) and the wave propagation problem is modeled and solved based on the first-order shear deformation shell theory. In the next step, a structural dynamic model in combination with the micromechanics model and the shell theory is developed to simulate the hygrothermal environmental conditions on wave dynamics of smart laminated CNT-reinforced composite cylindrical shells based on the first-order shear deformation shell theory. Finally, free vibration problem is modeled for finite length smart laminated CNT-reinforced composite cylindrical shells using the wave propagation approach to determine vibration characteristics under various mechanical boundary conditions.

Chapter three mainly presents the results obtained based on the structural dynamic modeling presented in Chapter two. The presented analytical approach, computer programming, and

numerical implementation are evaluated and validated against the available results in the literature. The effects of transverse shear and rotary inertia, piezoelectric coupling, composite stacking sequence, shell geometry, and material properties on wave dispersion solutions are examined. A comparison of dispersion solutions by different shell theories is also provided. Furthermore, the results present the influence of nanotube distribution and fraction on wave propagation characteristics of smart composite cylindrical shell structures. Effects of temperature and moisture variations on the wave propagation and vibration characteristics are also studied and investigated. Finally, the effects of shell boundary conditions, axial and circumferential modes, temperature and moisture variations, nanoparticles, and shell geometry parameters on vibration characteristics are investigated and discussed.

Finally, Chapter four summarizes key findings and implications of the results, as well as conclusions and recommendations for future works.

To summarize, a methodology, which is described schematically in Fig. 1.18, is adopted in the present thesis in order to develop appropriate correlations for predicting structural dynamics of smart composite shell structures with the coupling effects of various parameters including transverse shear, rotary inertia, piezoelectricity, nanoparticles, hygrothermal environmental conditions, shell geometry, and boundary conditions.

Presented methodology in this thesis and the obtained results were published in eight journal papers [187–194].

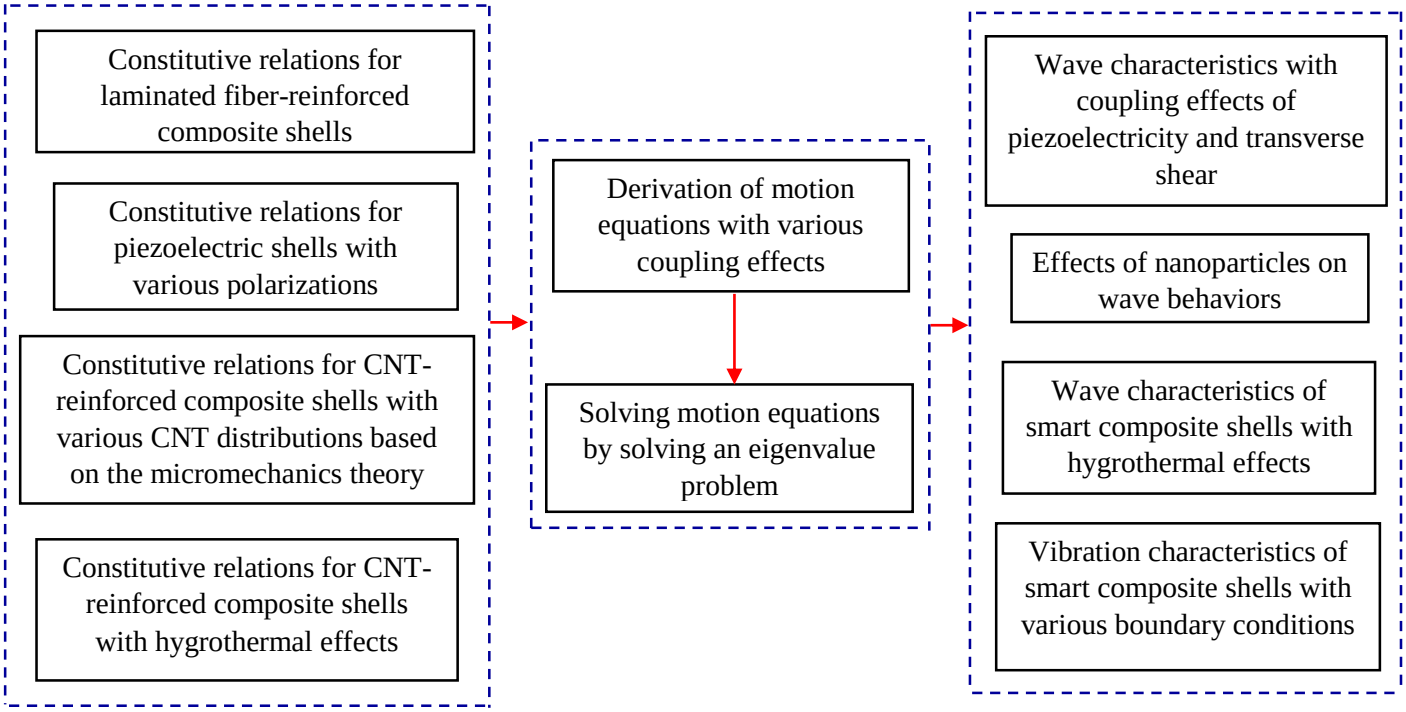

Figure 1.18. A schematic flow of the adopted methodology.

Chapter 2

Structural Dynamic Modeling of Smart Composite Cylindrical Shells

In this Chapter, structural dynamic modeling of smart composite cylindrical shells are proposed and presented and constitutive equations are derived and developed by considering the effects of transverse shear, piezoelectricity, nanoparticles, and hygrothermal environmental conditions by incorporating the composite lamination, wave propagation, and shell theories/models.

Firstly, the geometry of the problem is portrayed (section 2.1) and then constitutive relations for laminated fiber-reinforced composite cylindrical shells and piezoelectric cylindrical shells are derived based on shell theories and piezoelectricity polarizations (section 2.2). Afterward, wave propagation problems are modeled and solved with coupling effects of various parameters including transverse shear (section 2.3), nanoparticles (section 2.4), and temperature and moisture variations (section 2.5). Finally, the free vibration problem is modeled and solved using the wave propagation approach with the effects of various mechanical boundary conditions (section 2.6).

2.1. Geometry of a Smart Laminated Fiber-Reinforced Composite Cylindrical Shell

Configuration of a laminated fiber-reinforced composite cylinder, layout of a laminated fiber-reinforced composite cylindrical shell coupled with the piezoelectric layers at the top and bottom surfaces, and a single ply of fiber-reinforced unidirectional composite cylindrical shell with its material principle and cylindrical coordinate systems are shown in Fig. 2.1. A cross-sectional view of a laminated composite cylindrical shell coupled with the piezoelectric layers at the top and bottom surfaces with coordinate notation of individual plies are displayed in Fig. 2.2. Coordinate x represents the direction along the shell axial direction, θ for the circumferential direction, and z for the radial direction. Material principle axes along fiber and in transverse directions of fiber are presented by 1, 2, and 3, respectively. The angle β is measured positive counter clockwise from the x-axis to 1-axis. The $x-\theta$ plane is equidistant from the top and bottom surfaces of the shell and is called the reference plane or the midplane. R is the reference plane radius, h_p denotes the piezoelectric layer thickness, and h is the total thickness of the laminated composite cylindrical shell which is sum of the thickness of each lamina or ply (h_K) as,

$$h = \sum_{K=1}^{N} h_K \tag{2.1}$$

where N is is the total number of plies. Abovementioned notations are constant throughout the theoretical development. The force and moment resultants at an infinitesimal element of the shell are shown in Fig. 2.3.

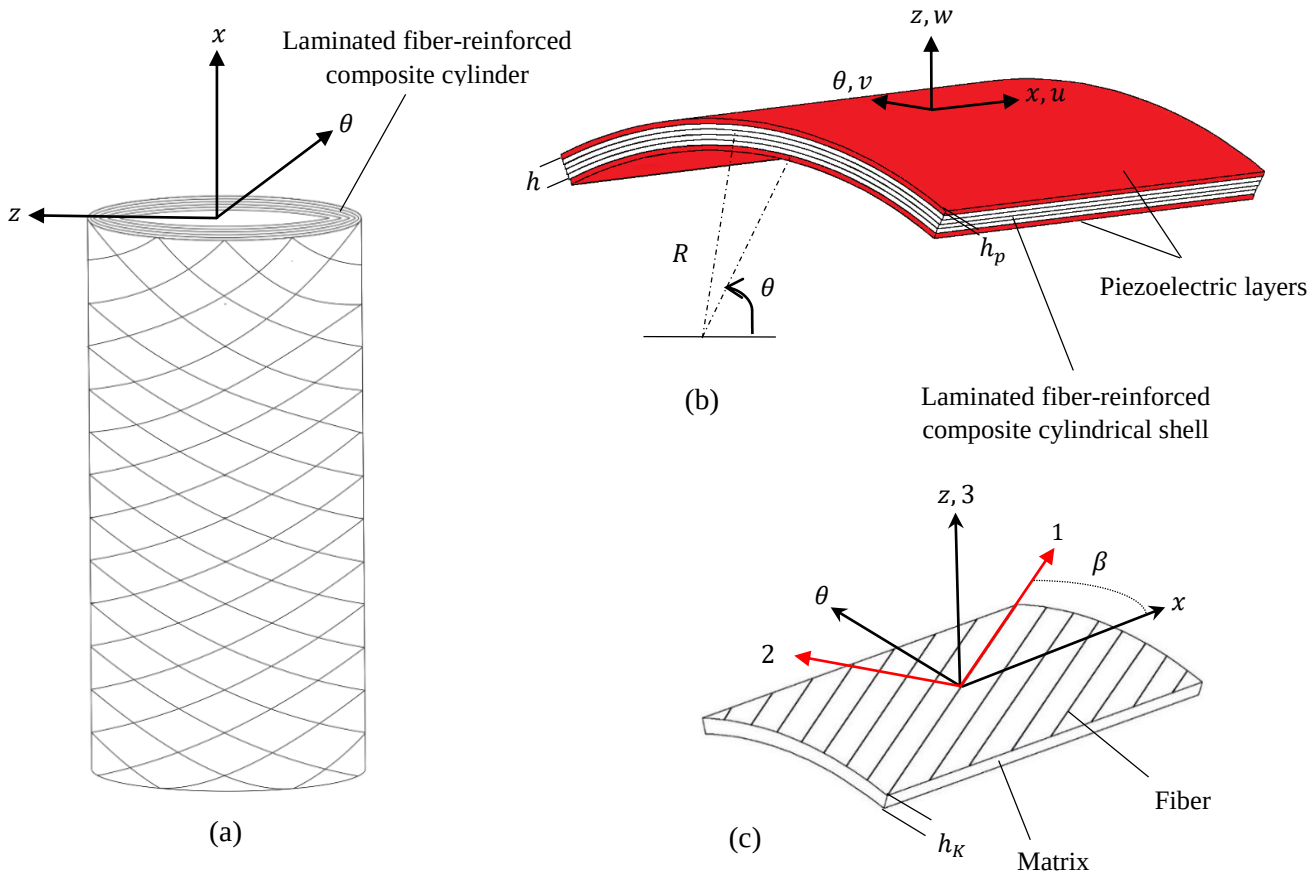

Figure 2.1. (a) Configuration of a laminated fiber-reinforced composite cylinder, (b) layout of a laminated fiber-reinforced composite cylindrical shell coated with the piezoelectric layers at the top and bottom surfaces, (c) a single ply of fiber-reinforced unidirectional composite cylindrical shell with its material principle and cylindrical coordinate systems.

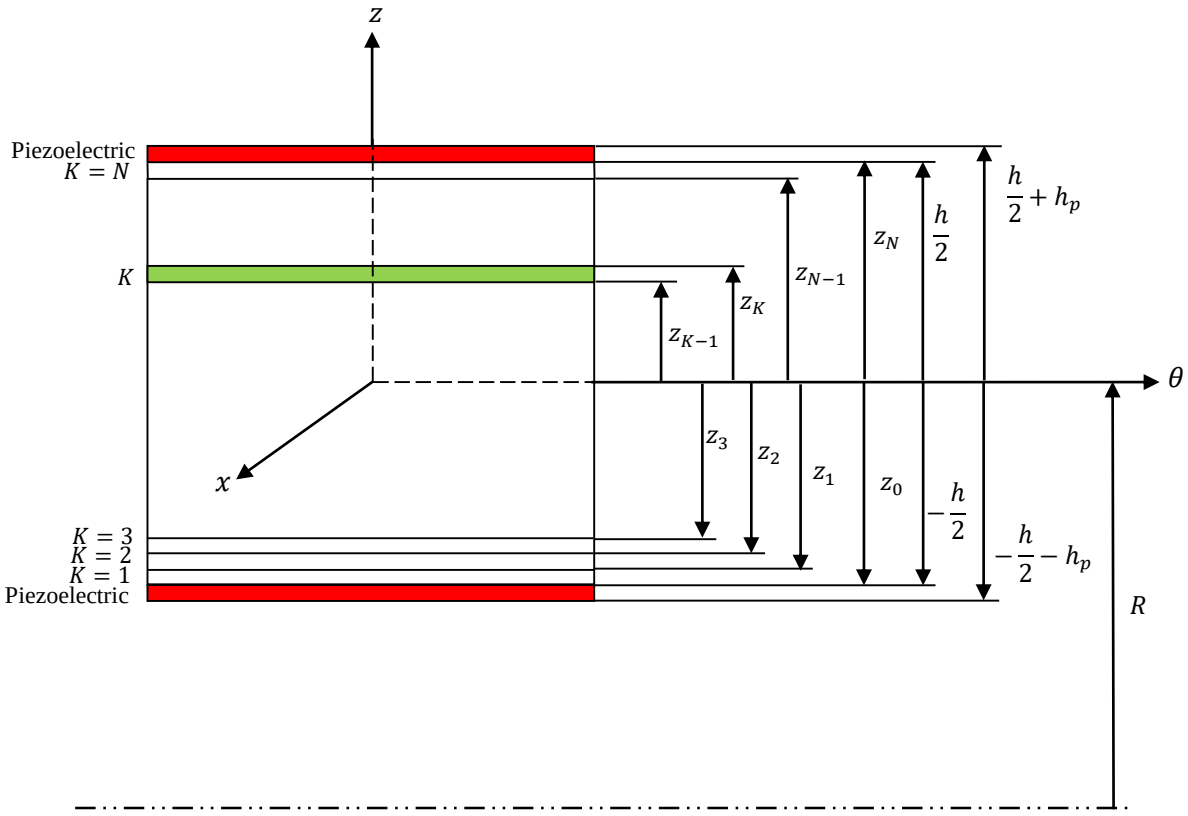

Figure 2.2. A cross-sectional view of a laminated composite cylindrical shell coupled with the piezoelectric layers at the top and bottom surfaces with coordinate notation of individual plies.

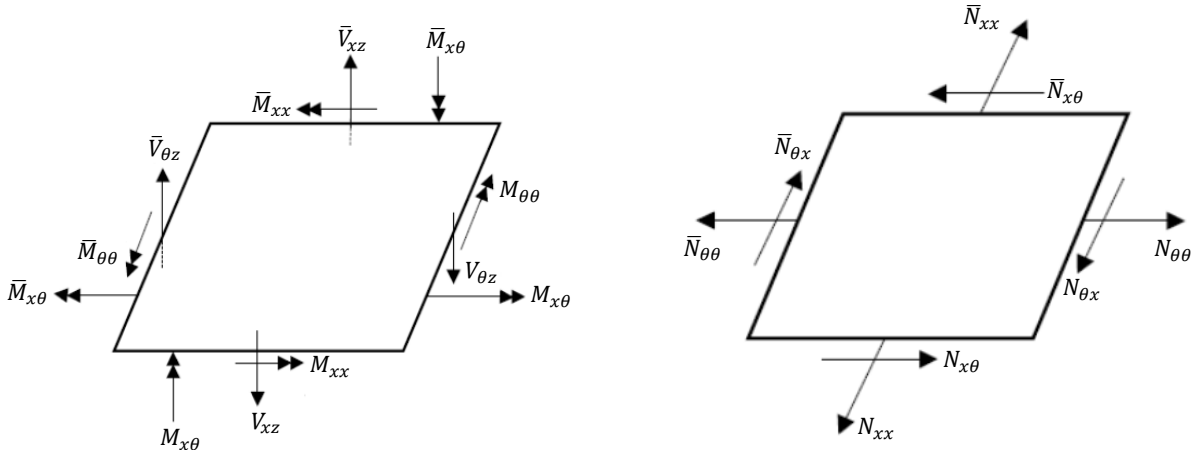

$$\bar{N}_{xx} = N_{xx} + \frac{\partial N_{xx}}{\partial x}dx\,,\ \bar{N}_{\theta\theta} = N_{\theta\theta} + \frac{\partial N_{\theta\theta}}{\partial \theta}d\theta\,,\ \bar{N}_{x\theta} = N_{x\theta} + \frac{\partial N_{x\theta}}{\partial x}dx\,,\ \bar{M}_{xx} = M_{xx} + \frac{\partial M_{xx}}{\partial x}dx\,,$$

$$\bar{M}_{\theta\theta} = M_{\theta\theta} + \frac{\partial M_{\theta\theta}}{\partial \theta}d\theta\,,\ \bar{M}_{x\theta} = M_{x\theta} + \frac{\partial M_{x\theta}}{\partial x}dx\,,\ \bar{V}_{xz} = V_{xz} + \frac{\partial V_{xz}}{\partial x}dx\,,\ \bar{V}_{\theta z} = V_{\theta z} + \frac{\partial V_{\theta z}}{\partial \theta}d\theta.$$

Figure 2.3. The force and moment resultants at an infinitesimal element of the shell.

2.2. Constitutive Equations for Laminated Fiber-Reinforced Composite Cylindrical Shells and Piezoelectric Cylindrical Shells

2.2.1. Strain-Displacement Relations in the Cylindrical Coordinate System

The general strain-displacement relations in the cylindrical coordinate system (x, θ, z) are given by Ref. [195] as,

$$\varepsilon_{xx} = \frac{\partial u}{\partial x} \qquad \varepsilon_{\theta\theta} = \frac{1}{R}\left(\frac{\partial v}{\partial \theta} + w\right) \qquad \varepsilon_{zz} = \frac{\partial w}{\partial z}$$

$$\gamma_{x\theta} = \frac{\partial v}{\partial x} + \frac{\partial u}{R\partial \theta} \qquad \gamma_{xz} = \frac{\partial w}{\partial x} + \frac{\partial u}{\partial z} \qquad \gamma_{\theta z} = \frac{1}{R}\frac{\partial w}{\partial \theta} + \frac{\partial v}{\partial z} - \frac{v}{R} \tag{2.2}$$

where u, v, and w represent the displacements of a generic point of cylinder in $x-$, $\theta-$, and $z-$ directions, respectively. Eq. (2.2) is used in the derivation of governing or field equations in this Chapter.

2.2.1.1. Strain-Displacement Relations using the Classical Shell Theory

In this section, the strain-displacement relations are derived for a cylindrical shell using the classical shell theory in which the transverse shear effects are neglected ($\gamma_{xz} = \gamma_{\theta z} = 0$)[6]. Fig. 2.4 shows a section of a laminate normal to the θ −axis before and after deformation without considering the transverse shear effects, where straight lines normal to the middle surface remain straight and normal to that surface after deformation [6,196]. First of all, the displacement fields are needed to derive the strain field equations based on the classical shell theory, where the displacement kinematics based on this theory are given by Ref. [196] as,

$$u(x,\theta,z,t) = u_0(x,\theta,t) - z\frac{\partial w_0(x,\theta,z,t)}{\partial x} \tag{2.3a}$$

$$v(x,\theta,z,t) = v_0(x,\theta,t) - \frac{z}{R}\frac{\partial w_0(x,\theta,z,t)}{\partial \theta} \tag{2.3b}$$

$$w(x,\theta,z,t) = w_0(x,\theta,t) \tag{2.3c}$$

where $u_0(x,\theta,t)$, $v_0(x,\theta,t)$, and $w_0(x,\theta,t)$ denote the reference plane displacements in x −, θ −, and z −directions, respectively, where they are not function of z for a thin shell structure, thus, their derivatives with respect to z will vanish in further calculations throughout the theoretical development.

In the classical shell theory, it is assumed that the transverse shear strains γ_{xz} and $\gamma_{\theta z}$ are negligibly small. Thus, by substituting Eq. (2.3) into Eq. (2.2), the in-plane strain-displacement relations are derived as,

$$\varepsilon_{xx} = \frac{\partial u_0}{\partial x} - z\frac{\partial^2 w_0}{\partial x^2} \qquad \varepsilon_{\theta\theta} = \frac{1}{R}\left(\frac{\partial v_0}{\partial \theta} + w_0\right) - \frac{z}{R^2}\frac{\partial^2 w_0}{\partial \theta^2} \qquad \gamma_{x\theta} = \left(\frac{\partial v_0}{\partial x} + \frac{\partial u_0}{R\partial \theta}\right) - \frac{2z}{R}\frac{\partial^2 w_0}{\partial x \partial \theta} \tag{2.4}$$

By defining the in-plane strain components on the reference plane $(x-\theta)$ of the shell as,

$$\varepsilon^0_{xx} = \frac{\partial u_0}{\partial x} \qquad \varepsilon^0_{\theta\theta} = \frac{1}{R}\left(\frac{\partial v_0}{\partial \theta} + w_0\right) \qquad \gamma^0_{x\theta} = \frac{\partial v_0}{\partial x} + \frac{\partial u_0}{R\partial \theta} \tag{2.5}$$

and the in-plane curvatures of the shell as,

$$\mathrm{K}_{xx} = -\frac{\partial^2 w_0}{\partial x^2} \qquad \mathrm{K}_{\theta\theta} = -\frac{\partial^2 w_0}{R^2 \partial \theta^2} \qquad \mathrm{K}_{x\theta} = -\frac{2}{R}\frac{\partial^2 w_0}{\partial x \partial \theta} \tag{2.6}$$

the in-plane strains at any point in the cylindrical shell can be related to the in-plane strains of the reference plane and the in-plane curvatures of the shell as follows,

$$\begin{Bmatrix} \varepsilon_{xx} \\ \varepsilon_{\theta\theta} \\ \gamma_{x\theta} \end{Bmatrix} = \begin{Bmatrix} \varepsilon_{xx}^0 \\ \varepsilon_{\theta\theta}^0 \\ \gamma_{x\theta}^0 \end{Bmatrix} + z \begin{Bmatrix} \mathrm{K}_{xx} \\ \mathrm{K}_{\theta\theta} \\ \mathrm{K}_{x\theta} \end{Bmatrix} \tag{2.7}$$

where z is the distance of any point from the reference plane.

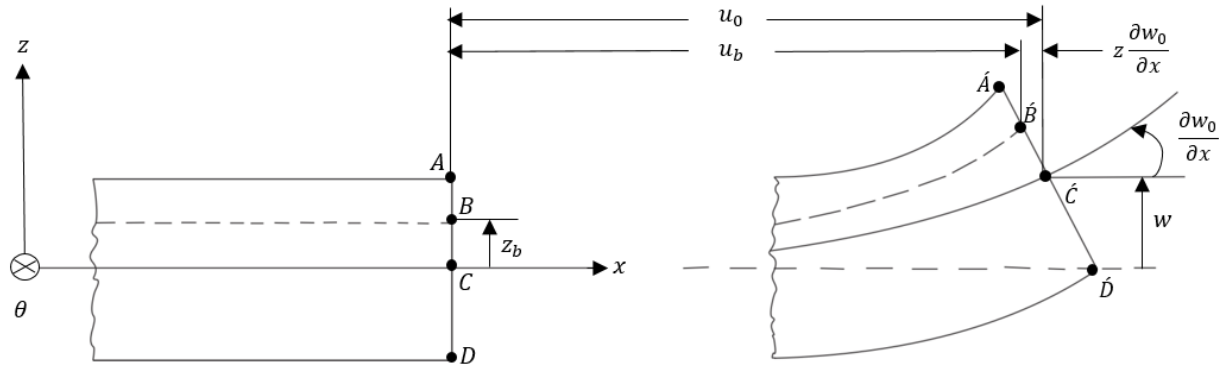

Figure 2.4. Shell section before (ABCD) and after (A′B′C′D′) deformation [6].

2.2.1.2. Strain-Displacement Relations using the First-Order Shear Deformation Shell Theory

Strain-displacement relations are derived in this section for a cylindrical shell based on the first-order shear deformation shell theory in which the transverse shear effects are included. Fig. 2.5 shows a section of a cylindrical shell normal to the θ-axis before and after deformation, including the effects of transverse shear, where straight lines normal to the middle surface remain straight but not normal to that surface after deformation. The result of this deformation is the rotation of the cross-section $ABCD$ by angle α_x to a location $\acute{A}\acute{B}\acute{C}\acute{D}$, which is normal to the deformed middle

surface [6,196]. The displacement kinematics required to derive the strain-displacement relations based on the first-order shear deformation shell theory are given by Ref. [196] as,

$$u(x,\theta,z,t) = u_0(x,\theta,t) + z\alpha_x(x,\theta,t) \tag{2.8a}$$

$$v(x,\theta,z,t) = v_0(x,\theta,t) + z\alpha_\theta(x,\theta,t) \tag{2.8b}$$

$$w(x,\theta,z,t) = w_0(x,\theta,t) \tag{2.8c}$$

where $\alpha_x(x,\theta,t)$ and $\alpha_\theta(x,\theta,t)$ are the rotation of the cross-section normal to x -axis and θ-axis, respectively, where they are not also function of z for a thin shell structure, thus, their derivatives with respect to z will vanish in subsequent computations throughout this thesis. By using the displacement kinematics introduced in Eq. (2.8), the transverse shear effects are included in the mathematical modeling. Substituting Eq. (2.8) into Eq. (2.2) yields the strain field equations based on the first-order shear deformation shell theory as follows,

$$\varepsilon_{xx} = \frac{\partial u_0}{\partial x} + z\frac{\partial \alpha_x}{\partial x} \qquad \varepsilon_{\theta\theta} = \frac{1}{R}\left(\frac{\partial v_0}{\partial \theta} + w_0\right) + \frac{z}{R}\frac{\partial \alpha_\theta}{\partial \theta} \qquad \varepsilon_{zz} = 0$$

$$\gamma_{x\theta} = \frac{\partial v_0}{\partial x} + \frac{\partial u_0}{R\partial \theta} + z\left(\frac{\partial \alpha_\theta}{\partial x} + \frac{\partial \alpha_x}{R\partial \theta}\right) \qquad \gamma_{xz} = \frac{\partial w_0}{\partial x} + \alpha_x \qquad \gamma_{\theta z} = \frac{\partial w_0}{R\partial \theta} - \frac{v_0}{R} + \alpha_\theta \tag{2.9}$$

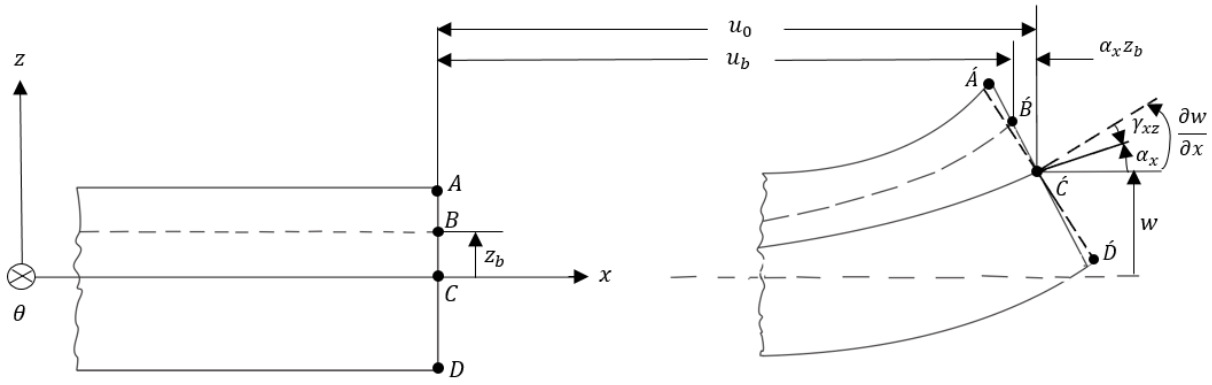

Figure 2.5. Shell section before (ABCD) and after (A′B′C′D′) deformation with noticeable effects of transverse shear [6].

From the above relations, it is observed that the transverse shear strains γ_{xz} and $\gamma_{\theta z}$ are equal to the rotations of the cross sections relative to the normal to the middle surface after deformation. Therefore, the in-plane strain components on the reference plane (ε^0_{xx}, $\varepsilon^0_{\theta\theta}$, and $\gamma^0_{x\theta}$) are the same as Eq. (2.5), but the in-plane curvatures are attained as,

$$\mathrm{K}_{xx} = \frac{\partial \alpha_x}{\partial x} \qquad \mathrm{K}_{\theta\theta} = \frac{\partial \alpha_\theta}{R\partial \theta} \qquad \mathrm{K}_{x\theta} = \frac{\partial \alpha_\theta}{\partial x} + \frac{\partial \alpha_x}{R\partial \theta} \tag{2.10}$$

So, for the first-order shear deformation shell theory, we use Eq. (2.9) or Eq. (2.7) with the in-plane curvatures introduced in Eq. (2.10), as the in-plane strain components of any point in a cylindrical shell with distance z from the reference plane.

2.2.2. Constitutive Relations for a Laminated Fiber-Reinforced Composite Cylindrical Shell

The in-plane strains at any point in a laminated composite cylindrical shell are given by Eq. (2.7). The in-plane stress-strain relations of lamina (layer) K within the laminate, which are decoupled from the transverse shear terms, are given by Ref. [6] as,

$$\begin{Bmatrix} \sigma^{(1)}_{xx} \\ \sigma^{(1)}_{\theta\theta} \\ \tau^{(1)}_{x\theta} \end{Bmatrix}_K = \begin{bmatrix} Q_{xx} & Q_{x\theta} & Q_{xs} \\ Q_{\theta x} & Q_{\theta\theta} & Q_{\theta s} \\ Q_{sx} & Q_{s\theta} & Q_{ss} \end{bmatrix}_K \begin{Bmatrix} \varepsilon_{xx} \\ \varepsilon_{\theta\theta} \\ \gamma_{x\theta} \end{Bmatrix}_K \tag{2.11}$$

where $\left[Q_{ij}\right]_K$ $(i,j = x,\theta,s)$ is the transformed reduced stiffness matrix for lamina K in the $x-\theta$ system of coordinates as a function of the principal stiffness matrix $\left[Q_{ij}\right]_K$ $(i,j = 1,2,6)$ of the lamina reinforced with fibers, where their components are given in Appendix A, superscript (1) represents variables corresponding to the host laminated composite cylindrical shell, and the subscript s in the above equations corresponds to shear stress and strain components referred to the $x-\theta$ system of coordinates. Substituting Eq. (2.7) into Eq. (2.11) yields,

$$\begin{Bmatrix} \sigma_{xx}^{(1)} \\ \sigma_{\theta\theta}^{(1)} \\ \tau_{x\theta}^{(1)} \end{Bmatrix}_K = \begin{bmatrix} Q_{xx} & Q_{x\theta} & Q_{xs} \\ Q_{\theta x} & Q_{\theta\theta} & Q_{\theta s} \\ Q_{sx} & Q_{s\theta} & Q_{ss} \end{bmatrix}_K \begin{Bmatrix} \varepsilon_{xx}^0 \\ \varepsilon_{\theta\theta}^0 \\ \gamma_{x\theta}^0 \end{Bmatrix} + z \begin{bmatrix} Q_{xx} & Q_{x\theta} & Q_{xs} \\ Q_{\theta x} & Q_{\theta\theta} & Q_{\theta s} \\ Q_{sx} & Q_{s\theta} & Q_{ss} \end{bmatrix}_K \begin{Bmatrix} \mathrm{K}_{xx} \\ \mathrm{K}_{\theta\theta} \\ \mathrm{K}_{x\theta} \end{Bmatrix} \tag{2.12}$$

as the in-plane stress-strain relations for an individual lamina K whose midplane is at a distance z from the laminate reference plane. The transverse shear stress-strain relations for an individual lamina K, which are decoupled from the in-plane stress and strain terms, are given by Ref. [6] as,

$$\begin{Bmatrix} \tau_{\theta z}^{(1)} \\ \tau_{xz}^{(1)} \end{Bmatrix}_K = \begin{bmatrix} C_{qq} & C_{qr} \\ C_{rq} & C_{rr} \end{bmatrix}_K \begin{Bmatrix} \gamma_{\theta z} \\ \gamma_{xz} \end{Bmatrix}_K \tag{2.13}$$

where C_{qq}, C_{qr}, C_{rq}, and C_{rr} are given in Appendix A, and $\gamma_{\theta z}$ and γ_{xz} are given in Eq. (2.9).

The in-plane force and moment resultants and the transverse shear (out-of-plane) force resultants for a laminated fiber-reinforced composite cylindrical shell are obtained by integrating the corresponding stresses across the shell thickness as,

$$\begin{Bmatrix} N_{xx}^{(1)} \\ N_{\theta\theta}^{(1)} \\ N_{x\theta}^{(1)} \end{Bmatrix} = \sum_{K=1}^{N} \int_{z_{K-1}}^{z_K} \begin{Bmatrix} \sigma_{xx}^{(1)} \\ \sigma_{\theta\theta}^{(1)} \\ \tau_{x\theta}^{(1)} \end{Bmatrix}_K dz \tag{2.14a}$$

$$\begin{Bmatrix} M_{xx}^{(1)} \\ M_{\theta\theta}^{(1)} \\ M_{x\theta}^{(1)} \end{Bmatrix} = \sum_{K=1}^{N} \int_{z_{K-1}}^{z_K} \begin{Bmatrix} \sigma_{xx}^{(1)} \\ \sigma_{\theta\theta}^{(1)} \\ \tau_{x\theta}^{(1)} \end{Bmatrix}_K z dz \tag{2.14b}$$

$$\begin{Bmatrix} V_{\theta z}^{(1)} \\ V_{xz}^{(1)} \end{Bmatrix} = K_s \sum_{K=1}^{N} \int_{z_{K-1}}^{z_K} \begin{Bmatrix} \tau_{\theta z}^{(1)} \\ \tau_{xz}^{(1)} \end{Bmatrix}_K dz \tag{2.14c}$$

where z_{K-1} and z_K stand for the $z-$coordinate of the lower and upper surfaces of lamina K, respectively, as shown in Fig. 2.2, and K_s is the so-called shear correction factor introduced to account for the uniform distribution of transverse shear stress through the thickness of the layer. Based on to the work by Mirsky [197], shear correction factor K_s is chosen 0.8333 throughout this thesis. According to Eq. (2.14), the force and moment resultants for a laminated fiber-

reinforced composite cylindrical shell made up of N layers can be obtained. Hence, substituting Eqs. (2.12) and (2.13) for the lamina (layer) in-plane and out-of-plane (transverse shear) stresses, respectively, into Eq. (2.14) and taking integration across the shell thickness yields to the in-plane force and moment resultants and the out-of-plane (transverse shear) force resultants for a laminated fiber-reinforced composite cylindrical shell as,

$$\begin{Bmatrix} N_{xx}^{(1)} \\ N_{\theta\theta}^{(1)} \\ N_{x\theta}^{(1)} \end{Bmatrix} = \begin{bmatrix} A_{xx} & A_{x\theta} & A_{xs} \\ A_{\theta x} & A_{\theta\theta} & A_{\theta s} \\ A_{sx} & A_{s\theta} & A_{ss} \end{bmatrix} \begin{Bmatrix} \varepsilon_{xx}^{0} \\ \varepsilon_{\theta\theta}^{0} \\ \gamma_{x\theta}^{0} \end{Bmatrix} + \begin{bmatrix} B_{xx} & B_{x\theta} & B_{xs} \\ B_{\theta x} & B_{\theta\theta} & B_{\theta s} \\ B_{sx} & B_{s\theta} & B_{ss} \end{bmatrix} \begin{Bmatrix} \mathrm{K}_{xx} \\ \mathrm{K}_{\theta\theta} \\ \mathrm{K}_{x\theta} \end{Bmatrix} \tag{2.15a}$$

$$\begin{Bmatrix} M_{xx}^{(1)} \\ M_{\theta\theta}^{(1)} \\ M_{x\theta}^{(1)} \end{Bmatrix} = \begin{bmatrix} B_{xx} & B_{x\theta} & B_{xs} \\ B_{\theta x} & B_{\theta\theta} & B_{\theta s} \\ B_{sx} & B_{s\theta} & B_{ss} \end{bmatrix} \begin{Bmatrix} \varepsilon_{xx}^{0} \\ \varepsilon_{\theta\theta}^{0} \\ \gamma_{x\theta}^{0} \end{Bmatrix} + \begin{bmatrix} D_{xx} & D_{x\theta} & D_{xs} \\ D_{\theta x} & D_{\theta\theta} & D_{\theta s} \\ D_{sx} & D_{s\theta} & D_{ss} \end{bmatrix} \begin{Bmatrix} \mathrm{K}_{xx} \\ \mathrm{K}_{\theta\theta} \\ \mathrm{K}_{x\theta} \end{Bmatrix} \tag{2.15b}$$

$$\begin{Bmatrix} V_{\theta z}^{(1)} \\ V_{xz}^{(1)} \end{Bmatrix} = K_s \begin{bmatrix} \acute{A}_{qq} & \acute{A}_{qr} \\ \acute{A}_{rq} & \acute{A}_{rr} \end{bmatrix} \begin{Bmatrix} \gamma_{\theta z} \\ \gamma_{xz} \end{Bmatrix} \tag{2.15c}$$

where

$$[A_{ij}] = \sum_{K=1}^{N} [Q_{ij}]_K (z_K - z_{K-1}) \tag{2.16a}$$

$$[B_{ij}] = \frac{1}{2} \sum_{K=1}^{N} [Q_{ij}]_K (z_K^2 - z_{K-1}^2) \tag{2.16b}$$

$$[D_{ij}] = \frac{1}{3} \sum_{K=1}^{N} [Q_{ij}]_K (z_K^3 - z_{K-1}^3) \tag{2.16c}$$

$$[\acute{A}_{ij}] = \sum_{K=1}^{N} [C_{ij}]_K (z_K - z_{K-1}) \tag{2.16d}$$

where $A_{ij} = A_{ji}$, $B_{ij} = B_{ji}$, $D_{ij} = D_{ji}$ $(i,j = x,\theta,s)$, and $\acute{A}_{ij} = \acute{A}_{ji}$ $(i,j = q,r)$. $[A_{ij}]$, $[B_{ij}]$, $[D_{ij}]$, and $[\acute{A}_{ij}]$ are laminate stiffness matrices, which are function of the geometry, material properties, and stacking sequence of the individual plies.

2.2.3. Constitutive Relations for a Piezoelectric Cylindrical Shell

The generalized constitutive equations for a piezoelectric shell in the cylindrical coordinate system (x, θ, z) are given by Ref. [81] as,

$$\begin{Bmatrix} \sigma_{\theta\theta}^{(2)} \\ \sigma_{xx}^{(2)} \\ \sigma_{zz}^{(2)} \\ \tau_{xz}^{(2)} \\ \tau_{\theta z}^{(2)} \\ \tau_{x\theta}^{(2)} \end{Bmatrix} = \begin{bmatrix} c_{11} & c_{12} & c_{13} & 0 & 0 & 0 \\ c_{12} & c_{22} & c_{23} & 0 & 0 & 0 \\ c_{13} & c_{23} & c_{33} & 0 & 0 & 0 \\ 0 & 0 & 0 & c_{44} & 0 & 0 \\ 0 & 0 & 0 & 0 & c_{55} & 0 \\ 0 & 0 & 0 & 0 & 0 & c_{66} \end{bmatrix} \begin{Bmatrix} \varepsilon_{\theta\theta} \\ \varepsilon_{xx} \\ \varepsilon_{zz} \\ \gamma_{xz} \\ \gamma_{\theta z} \\ \gamma_{x\theta} \end{Bmatrix} - \begin{bmatrix} e_{11} & e_{21} & e_{31} \\ e_{12} & e_{22} & e_{32} \\ e_{13} & e_{23} & e_{33} \\ e_{14} & e_{24} & e_{34} \\ e_{15} & e_{25} & e_{35} \\ e_{16} & e_{26} & e_{36} \end{bmatrix} \begin{Bmatrix} E_{\theta\theta} \\ E_{xx} \\ E_{zz} \end{Bmatrix} \tag{2.17a}$$

$$\begin{Bmatrix} D_{\theta\theta} \\ D_{xx} \\ D_{zz} \end{Bmatrix} = \begin{bmatrix} e_{11} & e_{12} & e_{13} & e_{14} & e_{15} & e_{16} \\ e_{21} & e_{22} & e_{23} & e_{24} & e_{25} & e_{26} \\ e_{31} & e_{32} & e_{33} & e_{34} & e_{35} & e_{36} \end{bmatrix} \begin{Bmatrix} \varepsilon_{\theta\theta} \\ \varepsilon_{xx} \\ \varepsilon_{zz} \\ \gamma_{xz} \\ \gamma_{\theta z} \\ \gamma_{x\theta} \end{Bmatrix} + \begin{bmatrix} \in_{11} & 0 & 0 \\ 0 & \in_{22} & 0 \\ 0 & 0 & \in_{33} \end{bmatrix} \begin{Bmatrix} E_{\theta\theta} \\ E_{xx} \\ E_{zz} \end{Bmatrix} \tag{2.17b}$$

where σ_{ij}, ε_{ij} $(i, j = x, \theta, z)$, and D_{ii}, E_{ii} $(i = x, \theta, z)$ represent the stresses, the strains, the electric displacements, and the electric field intensities, respectively; c_{ij} , e_{ij}, $\in_{ij}$ $(i, j = 1,2, \dots ,6)$ denote the elastic constants, the piezoelectric constants, and the dielectric constants, respectively; and superscript (2) stands for variables corresponding to the piezoelectric layer. It is noted that regardless of the direction of polarization, there should be only five nonzero piezoelectric constants. The electric field intensities E_{ii} $(i = x, \theta, z)$, which are function of the electric potential $\varphi(x, \theta, t)$, in the cylindrical coordinate system are given by Ref. [81] as,

$$E_{xx} = -\frac{\partial \varphi}{\partial x} \qquad E_{\theta\theta} = -\frac{\partial \varphi}{R\partial \theta} \qquad E_{zz} = -\frac{\partial \varphi}{\partial z} \tag{2.18}$$

In the following subsections, the constitutive equations are developed for a piezoelectric cylindrical shell by considering different polarization directions and without (based on the classical shell theory) and with the transverse shear effects (based on the first-order shear deformation shell theory).

2.2.3.1. Constitutive Equations for a Piezoelectric Cylindrical Shell with Axial Polarization

For the axial polarization of the piezoelectricity, there are only five piezoelectric constants e_{16}, e_{21}, e_{22}, e_{23}, e_{34}, and other piezoelectric constants are considered zero. Coefficients e_{21}, e_{22}, and e_{23} relate the normal stresses in the 1, 2, and 3 directions, respectively, to a field along the poling direction, E_{xx}. The coefficients e_{16} and e_{34}, respectively, relate the shear stress in the $\theta - x$ plane to the field $E_{\theta\theta}$, and shear stress in the $z - x$ plane to the field E_{zz}. Note that it is usually not possible to obtain shear in the $\theta - z$ plane purely by application of the electric field E_{xx} considering the transverse isotropic property of the perfect polled piezoelectric material studied here. Hence, the constitutive relations, Eq. (2.17), for a piezoelectric shell with the axial polarization in the cylindrical coordinate system (x, θ, z) are reduced to,

$$\begin{Bmatrix} \sigma_{\theta\theta}^{(2)} \\ \sigma_{xx}^{(2)} \\ \sigma_{zz}^{(2)} \\ \tau_{xz}^{(2)} \\ \tau_{\theta z}^{(2)} \\ \tau_{x\theta}^{(2)} \end{Bmatrix} = \begin{bmatrix} c_{11} & c_{12} & c_{13} & 0 & 0 & 0 \\ c_{12} & c_{22} & c_{23} & 0 & 0 & 0 \\ c_{13} & c_{23} & c_{33} & 0 & 0 & 0 \\ 0 & 0 & 0 & c_{44} & 0 & 0 \\ 0 & 0 & 0 & 0 & c_{55} & 0 \\ 0 & 0 & 0 & 0 & 0 & c_{66} \end{bmatrix} \begin{Bmatrix} \varepsilon_{\theta\theta} \\ \varepsilon_{xx} \\ \varepsilon_{zz} \\ \gamma_{xz} \\ \gamma_{\theta z} \\ \gamma_{x\theta} \end{Bmatrix} - \begin{bmatrix} 0 & e_{21} & 0 \\ 0 & e_{22} & 0 \\ 0 & e_{23} & 0 \\ 0 & 0 & e_{34} \\ 0 & 0 & 0 \\ e_{16} & 0 & 0 \end{bmatrix} \begin{Bmatrix} E_{\theta\theta} \\ E_{xx} \\ E_{zz} \end{Bmatrix} \tag{2.19a}$$

$$\begin{Bmatrix} D_{\theta\theta} \\ D_{xx} \\ D_{zz} \end{Bmatrix} = \begin{bmatrix} 0 & 0 & 0 & 0 & 0 & e_{16} \\ e_{21} & e_{22} & e_{23} & 0 & 0 & 0 \\ 0 & 0 & 0 & e_{34} & 0 & 0 \end{bmatrix} \begin{Bmatrix} \varepsilon_{\theta\theta} \\ \varepsilon_{xx} \\ \varepsilon_{zz} \\ \gamma_{xz} \\ \gamma_{\theta z} \\ \gamma_{x\theta} \end{Bmatrix} + \begin{bmatrix} \in_{11} & 0 & 0 \\ 0 & \in_{22} & 0 \\ 0 & 0 & \in_{33} \end{bmatrix} \begin{Bmatrix} E_{\theta\theta} \\ E_{xx} \\ E_{zz} \end{Bmatrix} \tag{2.19b}$$

2.2.3.1.1. Constitutive Equations for a Piezoelectric Cylindrical Shell with Axial Polarization Based on the Classical Shell Theory

Based on the classical shell theory, the normal stress in the shell thickness direction, σ_{zz}, the transverse shear stresses, τ_{xz} and $\tau_{\theta z}$, are assumed to be negligible. Therefore, based on this theory, from $\sigma_{zz}=0$, $\tau_{xz}=0$, and $\tau_{\theta z}=0$ in Eq. (2.19a), one obtains,

$$\varepsilon_{zz}=\frac{e_{23}}{c_{33}}E_{xx}-\frac{c_{13}}{c_{33}}\varepsilon_{\theta\theta}-\frac{c_{23}}{c_{33}}\varepsilon_{xx}\qquad \gamma_{xz}=\frac{e_{34}}{c_{44}}E_{zz}\qquad \gamma_{\theta z}=0 \tag{2.20}$$

Substituting Eq. (2.20) into Eq. (2.19) yields,

$$\begin{Bmatrix}\sigma_{\theta\theta}^{(2)}\\ \sigma_{xx}^{(2)}\\ \tau_{x\theta}^{(2)}\end{Bmatrix}=\begin{bmatrix}\bar{c}_{11} & \bar{c}_{12} & 0\\ \bar{c}_{12} & \bar{c}_{22} & 0\\ 0 & 0 & \bar{c}_{66}\end{bmatrix}\begin{Bmatrix}\varepsilon_{\theta\theta}\\ \varepsilon_{xx}\\ \gamma_{x\theta}\end{Bmatrix}-\begin{bmatrix}0 & \bar{e}_{21} & 0\\ 0 & \bar{e}_{22} & 0\\ \bar{e}_{16} & 0 & 0\end{bmatrix}\begin{Bmatrix}E_{\theta\theta}\\ E_{xx}\\ E_{zz}\end{Bmatrix} \tag{2.21a}$$

$$\begin{Bmatrix}D_{\theta\theta}\\ D_{xx}\\ D_{zz}\end{Bmatrix}=\begin{bmatrix}0 & 0 & \bar{e}_{16}\\ \bar{e}_{21} & \bar{e}_{22} & 0\\ 0 & 0 & 0\end{bmatrix}\begin{Bmatrix}\varepsilon_{\theta\theta}\\ \varepsilon_{xx}\\ \gamma_{x\theta}\end{Bmatrix}+\begin{bmatrix}\bar{\in}_{11} & 0 & 0\\ 0 & \bar{\in}_{22} & 0\\ 0 & 0 & \bar{\in}_{33}\end{bmatrix}\begin{Bmatrix}E_{\theta\theta}\\ E_{xx}\\ E_{zz}\end{Bmatrix} \tag{2.21b}$$

where $\bar{c}_{11}$, $\bar{c}_{12}$, $\bar{c}_{22}$, $\bar{c}_{66}$, $\bar{e}_{16}$, $\bar{e}_{21}$, $\bar{e}_{22}$, and $\bar{\in}_{11}$, $\bar{\in}_{22}$, $\bar{\in}_{33}$ are given in Appendix B.

2.2.3.1.2. Constitutive Equations for a Piezoelectric Cylindrical Shell with Axial Polarization Based on the First-Order Shear Deformation Shell Theory

According to the first-order shear deformation shell theory, the transverse shear stresses, τ_{xz} and $\tau_{\theta z}$, are not zero and only the normal stress in the piezoelectric shell thickness direction, σ_{zz}, is assumed to be infinitesimal. Thus, from Eq. (2.19a) by considering $\sigma_{zz}=0$, we obtain,

$$\varepsilon_{zz}=\frac{e_{23}}{c_{33}}E_{xx}-\frac{c_{13}}{c_{33}}\varepsilon_{\theta\theta}-\frac{c_{23}}{c_{33}}\varepsilon_{xx} \tag{2.22}$$

Substituting Eq. (2.22) into Eq. (2.19) leads to,

$$\begin{Bmatrix}\sigma_{\theta\theta}^{(2)}\\ \sigma_{xx}^{(2)}\\ \tau_{xz}^{(2)}\\ \tau_{\theta z}^{(2)}\\ \tau_{x\theta}^{(2)}\end{Bmatrix}=\begin{bmatrix}\bar{c}_{11} & \bar{c}_{12} & 0 & 0 & 0\\ \bar{c}_{12} & \bar{c}_{22} & 0 & 0 & 0\\ 0 & 0 & \bar{c}_{44} & 0 & 0\\ 0 & 0 & 0 & \bar{c}_{55} & 0\\ 0 & 0 & 0 & 0 & \bar{c}_{66}\end{bmatrix}\begin{Bmatrix}\varepsilon_{\theta\theta}\\ \varepsilon_{xx}\\ \gamma_{xz}\\ \gamma_{\theta z}\\ \gamma_{x\theta}\end{Bmatrix}-\begin{bmatrix}0 & \bar{e}_{21} & 0\\ 0 & \bar{e}_{22} & 0\\ 0 & 0 & \bar{e}_{34}\\ 0 & 0 & 0\\ \bar{e}_{16} & 0 & 0\end{bmatrix}\begin{Bmatrix}E_{\theta\theta}\\ E_{xx}\\ E_{zz}\end{Bmatrix} \tag{2.23a}$$

$$\begin{Bmatrix}D_{\theta\theta}\\ D_{xx}\\ D_{zz}\end{Bmatrix}=\begin{bmatrix}0 & 0 & 0 & \bar{e}_{16}\\ \bar{e}_{21} & \bar{e}_{22} & 0 & 0\\ 0 & 0 & \bar{e}_{34} & 0\end{bmatrix}\begin{Bmatrix}\varepsilon_{\theta\theta}\\ \varepsilon_{xx}\\ \gamma_{xz}\\ \gamma_{x\theta}\end{Bmatrix}+\begin{bmatrix}\bar{\in}_{11} & 0 & 0\\ 0 & \bar{\in}_{22} & 0\\ 0 & 0 & \bar{\in}_{33}\end{bmatrix}\begin{Bmatrix}E_{\theta\theta}\\ E_{xx}\\ E_{zz}\end{Bmatrix} \tag{2.23b}$$

where $\bar{c}_{11}$, $\bar{c}_{12}$, $\bar{c}_{22}$, $\bar{c}_{44}$, $\bar{c}_{55}$, $\bar{c}_{66}$, $\bar{e}_{16}$, $\bar{e}_{21}$, $\bar{e}_{22}$, $\bar{e}_{34}$, and $\bar{\in}_{11}$, $\bar{\in}_{22}$, $\bar{\in}_{33}$ are given in Appendix B.

2.2.3.2. Constitutive Equations for a Piezoelectric Cylindrical Shell with Circumferential Polarization

Five piezoelectric constants e_{11}, e_{12}, e_{13}, e_{26}, and e_{35} are considered for the circumferential polarization of the piezoelectricity. Coefficients e_{11}, e_{12}, and e_{13} relate the normal stresses in the 1, 2, and 3 directions, respectively, to a field along the poling direction, $E_{\theta\theta}$. The coefficients e_{26} and e_{35}, respectively, relate the shear stress in the $x-\theta$ plane to the field E_{xx}, and shear stress in the $z-\theta$ plane to the field E_{zz}. Note that it is not possible to obtain shear in the $x-z$ plane purely by application of the electric field $E_{\theta\theta}$. Hence, the constitutive relations, Eq. (2.17), for a piezoelectric cylindrical shell with the circumferential polarization are reduced to,

$$\begin{Bmatrix}\sigma_{\theta\theta}^{(2)}\\ \sigma_{xx}^{(2)}\\ \sigma_{zz}^{(2)}\\ \tau_{xz}^{(2)}\\ \tau_{\theta z}^{(2)}\\ \tau_{x\theta}^{(2)}\end{Bmatrix}=\begin{bmatrix}c_{11} & c_{12} & c_{13} & 0 & 0 & 0\\ c_{12} & c_{22} & c_{23} & 0 & 0 & 0\\ c_{13} & c_{23} & c_{33} & 0 & 0 & 0\\ 0 & 0 & 0 & c_{44} & 0 & 0\\ 0 & 0 & 0 & 0 & c_{55} & 0\\ 0 & 0 & 0 & 0 & 0 & c_{66}\end{bmatrix}\begin{Bmatrix}\varepsilon_{\theta\theta}\\ \varepsilon_{xx}\\ \varepsilon_{zz}\\ \gamma_{xz}\\ \gamma_{\theta z}\\ \gamma_{x\theta}\end{Bmatrix}-\begin{bmatrix}e_{11} & 0 & 0\\ e_{12} & 0 & 0\\ e_{13} & 0 & 0\\ 0 & 0 & 0\\ 0 & 0 & e_{35}\\ 0 & e_{26} & 0\end{bmatrix}\begin{Bmatrix}E_{\theta\theta}\\ E_{xx}\\ E_{zz}\end{Bmatrix} \tag{2.24a}$$

$$\begin{Bmatrix}D_{\theta\theta}\\ D_{xx}\\ D_{zz}\end{Bmatrix}=\begin{bmatrix}e_{11} & e_{12} & e_{13} & 0 & 0 & 0\\ 0 & 0 & 0 & 0 & 0 & e_{26}\\ 0 & 0 & 0 & 0 & e_{35} & 0\end{bmatrix}\begin{Bmatrix}\varepsilon_{\theta\theta}\\ \varepsilon_{xx}\\ \varepsilon_{zz}\\ \gamma_{xz}\\ \gamma_{\theta z}\\ \gamma_{x\theta}\end{Bmatrix}+\begin{bmatrix}\in_{11} & 0 & 0\\ 0 & \in_{22} & 0\\ 0 & 0 & \in_{33}\end{bmatrix}\begin{Bmatrix}E_{\theta\theta}\\ E_{xx}\\ E_{zz}\end{Bmatrix} \tag{2.24b}$$

2.2.3.2.1. Constitutive Equations for a Piezoelectric Cylindrical Shell with Circumferential Polarization Based on the Classical Shell Theory

Based on the classical shell theory, by assuming $\sigma_{zz} = 0$, $\tau_{xz} = 0$, and $\tau_{\theta z} = 0$ in Eq. (2.24a), one obtains,

$$\varepsilon_{zz} = \frac{e_{13}}{c_{33}} E_{\theta\theta} - \frac{c_{13}}{c_{33}} \varepsilon_{\theta\theta} - \frac{c_{23}}{c_{33}} \varepsilon_{xx} \tag{2.25}$$

Replacing Eq. (2.25) into Eq. (2.24) gives,

$$\begin{Bmatrix} \sigma_{\theta\theta}^{(2)} \\ \sigma_{xx}^{(2)} \\ \tau_{x\theta}^{(2)} \end{Bmatrix} = \begin{bmatrix} \bar{c}_{11} & \bar{c}_{12} & 0 \\ \bar{c}_{12} & \bar{c}_{22} & 0 \\ 0 & 0 & \bar{c}_{66} \end{bmatrix} \begin{Bmatrix} \varepsilon_{\theta\theta} \\ \varepsilon_{xx} \\ \gamma_{x\theta} \end{Bmatrix} - \begin{bmatrix} \bar{e}_{11} & 0 & 0 \\ \bar{e}_{12} & 0 & 0 \\ 0 & \bar{e}_{26} & 0 \end{bmatrix} \begin{Bmatrix} E_{\theta\theta} \\ E_{xx} \\ E_{zz} \end{Bmatrix} \tag{2.26a}$$

$$\begin{Bmatrix} D_{\theta\theta} \\ D_{xx} \\ D_{zz} \end{Bmatrix} = \begin{bmatrix} \bar{e}_{11} & \bar{e}_{12} & 0 \\ 0 & 0 & \bar{e}_{26} \\ 0 & 0 & 0 \end{bmatrix} \begin{Bmatrix} \varepsilon_{\theta\theta} \\ \varepsilon_{xx} \\ \gamma_{x\theta} \end{Bmatrix} + \begin{bmatrix} \bar{\in}_{11} & 0 & 0 \\ 0 & \bar{\in}_{22} & 0 \\ 0 & 0 & \bar{\in}_{33} \end{bmatrix} \begin{Bmatrix} E_{\theta\theta} \\ E_{xx} \\ E_{zz} \end{Bmatrix} \tag{2.26b}$$

where $\bar{c}_{11}$, $\bar{c}_{12}$, $\bar{c}_{22}$, $\bar{c}_{66}$, $\bar{e}_{11}$, $\bar{e}_{12}$, $\bar{e}_{26}$, and $\bar{\in}_{11}$, $\bar{\in}_{22}$, $\bar{\in}_{33}$ are given in Appendix C.

2.2.3.2.2. Constitutive Equations for a Piezoelectric Cylindrical Shell with Circumferential Polarization Based on the First-Order Shear Deformation Shell Theory

By considering the transverse shear effects via the first-order shear deformation shell theory, only the normal stress is considered zero ($\sigma_{zz} = 0$). Thus, assuming $\sigma_{zz} = 0$ in Eq. (2.24a) yields,

$$\varepsilon_{zz} = \frac{e_{13}}{c_{33}} E_{\theta\theta} - \frac{c_{13}}{c_{33}} \varepsilon_{\theta\theta} - \frac{c_{23}}{c_{33}} \varepsilon_{xx} \tag{2.27}$$

Substituting Eq. (2.27) into Eq. (2.24) leads to,

$$\begin{Bmatrix} \sigma_{\theta\theta}^{(2)} \\ \sigma_{xx}^{(2)} \\ \tau_{xz}^{(2)} \\ \tau_{\theta z}^{(2)} \\ \tau_{x\theta}^{(2)} \end{Bmatrix} = \begin{bmatrix} \bar{c}_{11} & \bar{c}_{12} & 0 & 0 & 0 \\ \bar{c}_{12} & \bar{c}_{22} & 0 & 0 & 0 \\ 0 & 0 & \bar{c}_{44} & 0 & 0 \\ 0 & 0 & 0 & \bar{c}_{55} & 0 \\ 0 & 0 & 0 & 0 & \bar{c}_{66} \end{bmatrix} \begin{Bmatrix} \varepsilon_{\theta\theta} \\ \varepsilon_{xx} \\ \gamma_{xz} \\ \gamma_{\theta z} \\ \gamma_{x\theta} \end{Bmatrix} - \begin{bmatrix} \bar{e}_{11} & 0 & 0 \\ \bar{e}_{12} & 0 & 0 \\ 0 & 0 & 0 \\ 0 & 0 & \bar{e}_{35} \\ 0 & \bar{e}_{26} & 0 \end{bmatrix} \begin{Bmatrix} E_{\theta\theta} \\ E_{xx} \\ E_{zz} \end{Bmatrix} \tag{2.28a}$$

$$\begin{Bmatrix} D_{\theta\theta} \\ D_{xx} \\ D_{zz} \end{Bmatrix} = \begin{bmatrix} \bar{e}_{11} & \bar{e}_{12} & 0 & 0 \\ 0 & 0 & 0 & \bar{e}_{26} \\ 0 & 0 & \bar{e}_{35} & 0 \end{bmatrix} \begin{Bmatrix} \varepsilon_{\theta\theta} \\ \varepsilon_{xx} \\ \gamma_{\theta z} \\ \gamma_{x\theta} \end{Bmatrix} + \begin{bmatrix} \bar{\in}_{11} & 0 & 0 \\ 0 & \bar{\in}_{22} & 0 \\ 0 & 0 & \bar{\in}_{33} \end{bmatrix} \begin{Bmatrix} E_{\theta\theta} \\ E_{xx} \\ E_{zz} \end{Bmatrix} \tag{2.28b}$$

where $\bar{c}_{11}$, $\bar{c}_{12}$, $\bar{c}_{22}$, $\bar{c}_{44}$, $\bar{c}_{55}$, $\bar{c}_{66}$, $\bar{e}_{11}$, $\bar{e}_{12}$, $\bar{e}_{26}$, $\bar{e}_{35}$, and $\bar{\in}_{11}$, $\bar{\in}_{22}$, $\bar{\in}_{33}$ are given in Appendix C.

2.2.3.3. Constitutive Equations for a Piezoelectric Cylindrical shell with Radial Polarization

The five piezoelectric constants for the radial polarization of the piezoelectricity are e_{15}, e_{24}, e_{31}, e_{32}, and e_{33}. Coefficients e_{31}, e_{32}, and e_{33} relate the normal stresses in the 1, 2, and 3 directions, respectively, to a field along the poling direction, E_{zz}. The coefficients e_{15} and e_{24}, respectively, relate the shear stress in the $\theta - z$ plane to the field $E_{\theta\theta}$, and shear stress in the $x - z$ plane to the field E_{xx}. Note that it is not possible to obtain shear in the $x - \theta$ plane purely by application of the electric field E_{zz}. So, Eq. (2.17) for the radial polarization is reduced to,

$$\begin{Bmatrix} \sigma_{\theta\theta}^{(2)} \\ \sigma_{xx}^{(2)} \\ \sigma_{zz}^{(2)} \\ \tau_{xz}^{(2)} \\ \tau_{\theta z}^{(2)} \\ \tau_{x\theta}^{(2)} \end{Bmatrix} = \begin{bmatrix} c_{11} & c_{12} & c_{13} & 0 & 0 & 0 \\ c_{12} & c_{22} & c_{23} & 0 & 0 & 0 \\ c_{13} & c_{23} & c_{33} & 0 & 0 & 0 \\ 0 & 0 & 0 & c_{44} & 0 & 0 \\ 0 & 0 & 0 & 0 & c_{55} & 0 \\ 0 & 0 & 0 & 0 & 0 & c_{66} \end{bmatrix} \begin{Bmatrix} \varepsilon_{\theta\theta} \\ \varepsilon_{xx} \\ \varepsilon_{zz} \\ \gamma_{xz} \\ \gamma_{\theta z} \\ \gamma_{x\theta} \end{Bmatrix} - \begin{bmatrix} 0 & 0 & e_{31} \\ 0 & 0 & e_{32} \\ 0 & 0 & e_{33} \\ 0 & e_{24} & 0 \\ e_{15} & 0 & 0 \\ 0 & 0 & 0 \end{bmatrix} \begin{Bmatrix} E_{\theta\theta} \\ E_{xx} \\ E_{zz} \end{Bmatrix} \tag{2.29a}$$

$$\begin{Bmatrix} D_{\theta\theta} \\ D_{xx} \\ D_{zz} \end{Bmatrix} = \begin{bmatrix} 0 & 0 & 0 & 0 & e_{15} & 0 \\ 0 & 0 & 0 & e_{24} & 0 & 0 \\ e_{31} & e_{32} & e_{33} & 0 & 0 & 0 \end{bmatrix} \begin{Bmatrix} \varepsilon_{\theta\theta} \\ \varepsilon_{xx} \\ \varepsilon_{zz} \\ \gamma_{xz} \\ \gamma_{\theta z} \\ \gamma_{x\theta} \end{Bmatrix} + \begin{bmatrix} \in_{11} & 0 & 0 \\ 0 & \in_{22} & 0 \\ 0 & 0 & \in_{33} \end{bmatrix} \begin{Bmatrix} E_{\theta\theta} \\ E_{xx} \\ E_{zz} \end{Bmatrix} \tag{2.29b}$$

2.2.3.3.1. Constitutive Equations for a Piezoelectric Cylindrical Shell with Radial Polarization Based on the Classical Shell Theory

Considering $\sigma_{zz} = 0$, $\tau_{xz} = 0$, and $\tau_{\theta z} = 0$ in Eq. (2.29a), based on the classical shell theory, we obtain,

$$\varepsilon_{zz} = \frac{e_{33}}{c_{33}} E_{zz} - \frac{c_{13}}{c_{33}} \varepsilon_{\theta\theta} - \frac{c_{23}}{c_{33}} \varepsilon_{xx} \tag{2.30}$$

By substituting Eq. (2.30) into Eq. (2.29), one obtains,

$$\begin{Bmatrix} \sigma_{\theta\theta}^{(2)} \\ \sigma_{xx}^{(2)} \\ \tau_{x\theta}^{(2)} \end{Bmatrix} = \begin{bmatrix} \bar{c}_{11} & \bar{c}_{12} & 0 \\ \bar{c}_{12} & \bar{c}_{22} & 0 \\ 0 & 0 & \bar{c}_{66} \end{bmatrix} \begin{Bmatrix} \varepsilon_{\theta\theta} \\ \varepsilon_{xx} \\ \gamma_{x\theta} \end{Bmatrix} - \begin{bmatrix} 0 & 0 & \bar{e}_{31} \\ 0 & 0 & \bar{e}_{32} \\ 0 & 0 & 0 \end{bmatrix} \begin{Bmatrix} E_{\theta\theta} \\ E_{xx} \\ E_{zz} \end{Bmatrix} \tag{2.31a}$$

$$\begin{Bmatrix} D_{\theta\theta} \\ D_{xx} \\ D_{zz} \end{Bmatrix} = \begin{bmatrix} 0 & 0 & 0 \\ 0 & 0 & 0 \\ \bar{e}_{31} & \bar{e}_{32} & 0 \end{bmatrix} \begin{Bmatrix} \varepsilon_{\theta\theta} \\ \varepsilon_{xx} \\ \gamma_{x\theta} \end{Bmatrix} + \begin{bmatrix} \bar{\epsilon}_{11} & 0 & 0 \\ 0 & \bar{\epsilon}_{22} & 0 \\ 0 & 0 & \bar{\epsilon}_{33} \end{bmatrix} \begin{Bmatrix} E_{\theta\theta} \\ E_{xx} \\ E_{zz} \end{Bmatrix} \tag{2.31b}$$

where $\bar{c}_{11}$, $\bar{c}_{12}$, $\bar{c}_{22}$, $\bar{c}_{66}$, $\bar{e}_{31}$, $\bar{e}_{32}$, and $\bar{\epsilon}_{11}$, $\bar{\epsilon}_{22}$, $\bar{\epsilon}_{33}$ are given in Appendix D.

2.2.3.3.2. Constitutive Equations for a Piezoelectric Cylindrical shell with Radial Polarization Based on the First-Order Shear Deformation Shell Theory

Including the transverse shear stresses (τ_{xz} and $\tau_{\theta z}$) and assuming negligible normal stress in the piezoelectric thickness direction ($\sigma_{zz} = 0$) in Eq. (2.29a) yields,

$$\varepsilon_{zz} = \frac{e_{33}}{c_{33}} E_{zz} - \frac{c_{13}}{c_{33}} \varepsilon_{\theta\theta} - \frac{c_{23}}{c_{33}} \varepsilon_{xx} \tag{2.32}$$

By substituting Eq. (2.32) into Eq. (2.29), we obtain,

$$\begin{Bmatrix} \sigma_{\theta\theta}^{(2)} \\ \sigma_{xx}^{(2)} \\ \tau_{xz}^{(2)} \\ \tau_{\theta z}^{(2)} \\ \tau_{x\theta}^{(2)} \end{Bmatrix} = \begin{bmatrix} \bar{c}_{11} & \bar{c}_{12} & 0 & 0 & 0 \\ \bar{c}_{12} & \bar{c}_{22} & 0 & 0 & 0 \\ 0 & 0 & \bar{c}_{44} & 0 & 0 \\ 0 & 0 & 0 & \bar{c}_{55} & 0 \\ 0 & 0 & 0 & 0 & \bar{c}_{66} \end{bmatrix} \begin{Bmatrix} \varepsilon_{\theta\theta} \\ \varepsilon_{xx} \\ \gamma_{xz} \\ \gamma_{\theta z} \\ \gamma_{x\theta} \end{Bmatrix} - \begin{bmatrix} 0 & 0 & \bar{e}_{31} \\ 0 & 0 & \bar{e}_{32} \\ 0 & \bar{e}_{24} & 0 \\ \bar{e}_{15} & 0 & 0 \\ 0 & 0 & 0 \end{bmatrix} \begin{Bmatrix} E_{\theta\theta} \\ E_{xx} \\ E_{zz} \end{Bmatrix} \tag{2.33a}$$

$$\begin{Bmatrix} D_{\theta\theta} \\ D_{xx} \\ D_{zz} \end{Bmatrix} = \begin{bmatrix} 0 & 0 & 0 & \bar{e}_{15} \\ 0 & 0 & \bar{e}_{24} & 0 \\ \bar{e}_{31} & \bar{e}_{32} & 0 & 0 \end{bmatrix} \begin{Bmatrix} \varepsilon_{\theta\theta} \\ \varepsilon_{xx} \\ \gamma_{xz} \\ \gamma_{\theta z} \end{Bmatrix} + \begin{bmatrix} \bar{\epsilon}_{11} & 0 & 0 \\ 0 & \bar{\epsilon}_{22} & 0 \\ 0 & 0 & \bar{\epsilon}_{33} \end{bmatrix} \begin{Bmatrix} E_{\theta\theta} \\ E_{xx} \\ E_{zz} \end{Bmatrix} \tag{2.33b}$$

where $\bar{c}_{11}$, $\bar{c}_{12}$, $\bar{c}_{22}$, $\bar{c}_{44}$, $\bar{c}_{55}$, $\bar{c}_{66}$, $\bar{e}_{15}$, $\bar{e}_{24}$, $\bar{e}_{31}$, $\bar{e}_{32}$, and $\bar{\epsilon}_{11}$, $\bar{\epsilon}_{22}$, $\bar{\epsilon}_{33}$ are given in Appendix D.

2.3. Wave Propagation Modeling in Piezoelectric Coupled Laminated Fiber-Reinforced Composite Cylindrical Shells

In this section, wave propagation problem in an infinitely long unbounded laminated fiber-reinforced composite cylindrical shell coupled with a piezoelectric layer at the top surface with the axial polarization is modeled and solved.

2.3.1. Force and Moment Resultants in a Piezoelectric Coupled Laminated Fiber-Reinforced Composite Cylindrical Shell

To consider the piezoelectric coupling effects, the force and moment resultants for a laminated composite cylindrical shell coupled with a piezoelectric layer at the top surface are obtained as sum of the force and moment resultants of the host laminated fiber-reinforced composite cylindrical shell and the piezoelectric layer ones.

The in-plane force resultants ($N_{xx}^{(1)}$, $N_{\theta\theta}^{(1)}$, and $N_{x\theta}^{(1)}$), bending and twisting moment resultants ($M_{xx}^{(1)}$, $M_{\theta\theta}^{(1)}$, and $M_{x\theta}^{(1)}$), and the transverse shear force resultants ($V_{xz}^{(1)}$ and $V_{\theta z}^{(1)}$) for a laminated fiber-reinforced composite cylindrical shell are given by Eq. (2.15).

The in-plane force and moment resultants and the transverse shear force resultants corresponding to a piezoelectric layer bonded to the top surface of a laminated composite cylindrical shell are also obtained by integrating the corresponding stresses across the thickness of the piezoelectric layer, i.e.

$$\begin{Bmatrix} N_{xx}^{(2)} \\ N_{\theta\theta}^{(2)} \\ N_{x\theta}^{(2)} \end{Bmatrix} = \int_{h/2}^{h/2+h_p} \begin{Bmatrix} \sigma_{xx}^{(2)} \\ \sigma_{\theta\theta}^{(2)} \\ \tau_{x\theta}^{(2)} \end{Bmatrix} dz \qquad (2.34a)$$

$$\begin{Bmatrix} M_{xx}^{(2)} \\ M_{\theta\theta}^{(2)} \\ M_{x\theta}^{(2)} \end{Bmatrix} = \int_{h/2}^{h/2+h_p} \begin{Bmatrix} \sigma_{xx}^{(2)} \\ \sigma_{\theta\theta}^{(2)} \\ \tau_{x\theta}^{(2)} \end{Bmatrix} z dz \tag{2.34b}$$

$$\begin{Bmatrix} V_{\theta z}^{(2)} \\ V_{xz}^{(2)} \end{Bmatrix} = K_s \int_{h/2}^{h/2+h_p} \begin{Bmatrix} \tau_{\theta z}^{(2)} \\ \tau_{xz}^{(2)} \end{Bmatrix} dz \tag{2.34c}$$

where $\sigma_{xx}^{(2)}$, $\sigma_{\theta\theta}^{(2)}$, $\tau_{x\theta}^{(2)}$, $\tau_{\theta z}^{(2)}$, and $\tau_{xz}^{(2)}$ are corresponding stresses of a piezoelectric cylindrical shell introduced in section 2.2.3 for the axial, circumferential, and radial polarization directions based on the classical shell theory and the first-order shear deformation shell theory.

Thus, the in-plane force resultants (N_{xx}, $N_{\theta\theta}$, and $N_{x\theta}$) are sum of Eq. (2.15a) and Eq. (2.34a), the bending and twisting moment resultants (M_{xx}, $M_{\theta\theta}$, and $M_{x\theta}$) are sum of Eq. (2.15b) and Eq. (2.34b), and the transverse shear force resultants (V_{xz}, and $V_{\theta z}$) are sum of Eq. (2.15c) and Eq. (2.34c) as,

$$\begin{aligned} &N_{xx} = N_{xx}^{(1)} + N_{xx}^{(2)} \qquad N_{\theta\theta} = N_{\theta\theta}^{(1)} + N_{\theta\theta}^{(2)} \qquad N_{x\theta} = N_{x\theta}^{(1)} + N_{x\theta}^{(2)} \\ &M_{xx} = M_{xx}^{(1)} + M_{xx}^{(2)} \qquad M_{\theta\theta} = M_{\theta\theta}^{(1)} + M_{\theta\theta}^{(2)} \qquad M_{x\theta} = M_{x\theta}^{(1)} + M_{x\theta}^{(2)} \\ &V_{xz} = V_{xz}^{(1)} + V_{xz}^{(2)} \qquad V_{\theta z} = V_{\theta z}^{(1)} + V_{\theta z}^{(2)} \end{aligned} \tag{2.35}$$

By some manipulations, the force and moment resultants for a laminated composite cylindrical shell integrated with a piezoelectric layer at the top surface with axial poling based on the first-order shear deformation shell theory are obtained as,

$$N_{xx} = A_1 \frac{\partial u_0}{\partial x} + \frac{A_2}{R}\left(w_0 + \frac{\partial v_0}{\partial \theta}\right) + A_3\left(\frac{\partial u_0}{R\partial\theta} + \frac{\partial v_0}{\partial x}\right) + A_4 \frac{\partial \alpha_x}{\partial x} + A_5 \frac{\partial \alpha_\theta}{R\partial\theta} + A_6\left(\frac{\partial \alpha_x}{R\partial\theta} + \frac{\partial \alpha_\theta}{\partial x}\right) + A_7 \frac{\partial \varphi}{\partial x} \tag{2.36a}$$

$$N_{\theta\theta} = B_1 \frac{\partial u_0}{\partial x} + \frac{B_2}{R}\left(w_0 + \frac{\partial v_0}{\partial \theta}\right) + B_3\left(\frac{\partial u_0}{R\partial\theta} + \frac{\partial v_0}{\partial x}\right) + B_4 \frac{\partial \alpha_x}{\partial x} + B_5 \frac{\partial \alpha_\theta}{R\partial\theta} + B_6\left(\frac{\partial \alpha_x}{R\partial\theta} + \frac{\partial \alpha_\theta}{\partial x}\right) + B_7 \frac{\partial \varphi}{\partial x} \tag{2.36b}$$

$$N_{x\theta} = C_1 \frac{\partial u_0}{\partial x} + \frac{C_2}{R}\left(w_0 + \frac{\partial v_0}{\partial \theta}\right) + C_3\left(\frac{\partial u_0}{R\partial\theta} + \frac{\partial v_0}{\partial x}\right) + C_4 \frac{\partial \alpha_x}{\partial x} + C_5 \frac{\partial \alpha_\theta}{R\partial\theta} + C_6\left(\frac{\partial \alpha_x}{R\partial\theta} + \frac{\partial \alpha_\theta}{\partial x}\right) + C_7 \frac{\partial \varphi}{R\partial\theta} \tag{2.36c}$$

$$M_{xx} = D_1 \frac{\partial u_0}{\partial x} + \frac{D_2}{R}\left(w_0 + \frac{\partial v_0}{\partial \theta}\right) + D_3\left(\frac{\partial u_0}{R\partial\theta} + \frac{\partial v_0}{\partial x}\right) + D_4 \frac{\partial \alpha_x}{\partial x} + D_5 \frac{\partial \alpha_\theta}{R\partial\theta} + D_6\left(\frac{\partial \alpha_x}{R\partial\theta} + \frac{\partial \alpha_\theta}{\partial x}\right) + D_7 \frac{\partial \varphi}{\partial x} \tag{2.36d}$$

$$M_{\theta\theta} = E_1\frac{\partial u_0}{\partial x} + \frac{E_2}{R}\left(w_0 + \frac{\partial v_0}{\partial \theta}\right) + E_3\left(\frac{\partial u_0}{R\partial\theta} + \frac{\partial v_0}{\partial x}\right) + E_4\frac{\partial \alpha_x}{\partial x} + E_5\frac{\partial \alpha_\theta}{R\partial\theta} + E_6(\frac{\partial \alpha_x}{R\partial\theta} + \frac{\partial \alpha_\theta}{\partial x}) + E_7\frac{\partial \varphi}{\partial x} \quad (2.36e)$$

$$M_{x\theta} = F_1\frac{\partial u_0}{\partial x} + \frac{F_2}{R}\left(w_0 + \frac{\partial v_0}{\partial \theta}\right) + F_3\left(\frac{\partial u_0}{R\partial\theta} + \frac{\partial v_0}{\partial x}\right) + F_4\frac{\partial \alpha_x}{\partial x} + F_5\frac{\partial \alpha_\theta}{R\partial\theta} + F_6(\frac{\partial \alpha_x}{R\partial\theta} + \frac{\partial \alpha_\theta}{\partial x}) + F_7\frac{\partial \varphi}{R\partial\theta} \quad (2.36f)$$

$$V_{xz} = G_1\left(\frac{\partial w_0}{R\partial\theta} - \frac{v_0}{R} + \alpha_\theta\right) + G_2\left(\frac{\partial w_0}{\partial x} + \alpha_x\right) \quad (2.36g)$$

$$V_{\theta z} = H_1\left(\frac{\partial w_0}{R\partial\theta} - \frac{v_0}{R} + \alpha_\theta\right) + H_2\left(\frac{\partial w_0}{\partial x} + \alpha_x\right) \quad (2.36h)$$

The force and moment resultants based on the classical shell theory are attained as,

$$N_{xx} = \acute{A}_1\frac{\partial u_0}{\partial x} + \frac{\acute{A}_2}{R}\left(w_0 + \frac{\partial v_0}{\partial \theta}\right) + \acute{A}_3\left(\frac{\partial u_0}{R\partial\theta} + \frac{\partial v_0}{\partial x}\right) + \acute{A}_4\frac{\partial^2 w_0}{\partial x^2} + \acute{A}_5\frac{\partial^2 w_0}{R^2\partial\theta^2} + \acute{A}_6\frac{\partial^2 w_0}{R\partial x\partial\theta} + \acute{A}_7\frac{\partial \varphi}{\partial x} \quad (2.37a)$$

$$N_{\theta\theta} = \acute{B}_1\frac{\partial u_0}{\partial x} + \frac{\acute{B}_2}{R}\left(w_0 + \frac{\partial v_0}{\partial \theta}\right) + \acute{B}_3\left(\frac{\partial u_0}{R\partial\theta} + \frac{\partial v_0}{\partial x}\right) + \acute{B}_4\frac{\partial^2 w_0}{\partial x^2} + \acute{B}_5\frac{\partial^2 w_0}{R^2\partial\theta^2} + \acute{B}_6\frac{\partial^2 w_0}{R\partial x\partial\theta} + \acute{B}_7\frac{\partial \varphi}{\partial x} \quad (2.37b)$$

$$N_{x\theta} = \acute{C}_1\frac{\partial u_0}{\partial x} + \frac{\acute{C}_2}{R}\left(w_0 + \frac{\partial v_0}{\partial \theta}\right) + \acute{C}_3\left(\frac{\partial u_0}{R\partial\theta} + \frac{\partial v_0}{\partial x}\right) + \acute{C}_4\frac{\partial^2 w_0}{\partial x^2} + \acute{C}_5\frac{\partial^2 w_0}{R^2\partial\theta^2} + \acute{C}_6\frac{\partial^2 w_0}{R\partial x\partial\theta} + \acute{C}_7\frac{\partial \varphi}{R\partial\theta} \quad (2.37c)$$

$$M_{xx} = \acute{D}_1\frac{\partial u_0}{\partial x} + \frac{\acute{D}_2}{R}\left(w_0 + \frac{\partial v_0}{\partial \theta}\right) + \acute{D}_3\left(\frac{\partial u_0}{R\partial\theta} + \frac{\partial v_0}{\partial x}\right) + \acute{D}_4\frac{\partial^2 w_0}{\partial x^2} + \acute{D}_5\frac{\partial^2 w_0}{R^2\partial\theta^2} + \acute{D}_6\frac{\partial^2 w_0}{R\partial x\partial\theta} + \acute{D}_7\frac{\partial \varphi}{\partial x} \quad (2.37d)$$

$$M_{\theta\theta} = \acute{E}_1\frac{\partial u_0}{\partial x} + \frac{\acute{E}_2}{R}\left(w_0 + \frac{\partial v_0}{\partial \theta}\right) + \acute{E}_3\left(\frac{\partial u_0}{R\partial\theta} + \frac{\partial v_0}{\partial x}\right) + \acute{E}_4\frac{\partial^2 w_0}{\partial x^2} + \acute{E}_5\frac{\partial^2 w_0}{R^2\partial\theta^2} + \acute{E}_6\frac{\partial^2 w_0}{R\partial x\partial\theta} + \acute{E}_7\frac{\partial \varphi}{\partial x} \quad (2.37e)$$

$$M_{x\theta} = \acute{F}_1\frac{\partial u_0}{\partial x} + \frac{\acute{F}_2}{R}\left(w_0 + \frac{\partial v_0}{\partial \theta}\right) + \acute{F}_3\left(\frac{\partial u_0}{R\partial\theta} + \frac{\partial v_0}{\partial x}\right) + \acute{F}_4\frac{\partial^2 w_0}{\partial x^2} + \acute{F}_5\frac{\partial^2 w_0}{R^2\partial\theta^2} + \acute{F}_6\frac{\partial^2 w_0}{R\partial x\partial\theta} + \acute{F}_7\frac{\partial \varphi}{R\partial\theta} \quad (2.37f)$$

The expression of coefficients, $A_i(i = 1, \dots, 7)$, $B_i(i = 1, \dots, 7)$, $C_i(i = 1, \dots, 7), D_i(i = 1, \dots, 7)$, $E_i(i = 1, \dots, 7)$, $F_i(i = 1, \dots, 7)$, $G_i(i = 1,2)$, $H_i(i = 1,2)$, $\acute{A}_i(i = 1, \dots, 7)$, $\acute{B}_i(i = 1, \dots, 7)$, $\acute{C}_i(i = 1, \dots, 7), \acute{D}_i(i = 1, \dots, 7)$, $\acute{E}_i(i = 1, \dots, 7)$, $\acute{F}_i(i = 1, \dots, 7)$ are given in Appendices E and F.

By substituting corresponding stresses of a piezoelectric cylindrical shell with circumferential and radial polarizations into Eq. (2.34) and performing mathematical procedure as explained in Eqs. (2.35) – (2.37), we can also obtain the force and moment resultants for piezoelectric coupled laminated fiber-reinforced composite cylindrical shells with circumferential and radial

polarizations which can be used for determining dispersion characteristics based on circumferential and radial polarizations of the piezoelectric material.

2.3.2. Equations of Motion

The equations of motion are illustrated in this section based on the first-order shear deformation shell theory, the Love bending shell theory, and the membrane shell theory. The kinematics of displacements, the strain and stress fields, and the force and moment resultants used in the membrane and Love bending shell theories are given by those obtained from the classical shell theory.

2.3.2.1. Equations of Motion for a Piezoelectric Coupled Laminated Composite Cylindrical Shell Based on the First-Order Shear Deformation Shell Theory

The equations of motion are derived in this section based on the first-order shear deformation shell theory. To derive the equations of motion for a laminated fiber-reinforced composite cylindrical shell coupled with a piezoelectric layer at the top surface, the Hamilton's principle extended to the shell structure is given by,

$$\int_0^T (\delta E_k - \delta E_s) dt = 0 \tag{2.38}$$

where E_k and E_s denote the kinetic energy and the strain energy, respectively, which are given by,

$$E_k = \frac{1}{2} \iint_A \left[\int_{-\frac{h}{2}}^{\frac{h}{2}+h_p} \rho(\dot{u}^2 + \dot{v}^2 + \dot{w}^2) R dz \right] dx d\theta \tag{2.39}$$

and

$$E_s = \frac{1}{2}\iint_A \left[\int_{-\frac{h}{2}}^{\frac{h}{2}} \left(\sigma_{xx}^{(1)}\varepsilon_{xx} + \sigma_{\theta\theta}^{(1)}\varepsilon_{\theta\theta} + \sigma_{zz}^{(1)}\varepsilon_{zz} + \tau_{x\theta}^{(1)}\gamma_{x\theta} + K_s\tau_{xz}^{(1)}\gamma_{xz} + K_s\tau_{\theta z}^{(1)}\gamma_{\theta z}\right) Rdz\right] dxd\theta$$

$$+ \frac{1}{2}\iint_A \left[\int_{\frac{h}{2}}^{\frac{h}{2}+h_p} \left(\sigma_{xx}^{(2)}\varepsilon_{xx} + \sigma_{\theta\theta}^{(2)}\varepsilon_{\theta\theta} + \sigma_{zz}^{(2)}\varepsilon_{zz} + \tau_{x\theta}^{(2)}\gamma_{x\theta} + K_s\tau_{xz}^{(2)}\gamma_{xz}\right.\right.$$

$$\left.\left. + K_s\tau_{\theta z}^{(2)}\gamma_{\theta z}\right) Rdz\right] dxd\theta \tag{2.40}$$

where ρ is the mass density. Considering the effect of transverse shear, in-surface and rotary inertias, and using Eqs. (2.8), (2.14), and (2.34) and substituting the expressions for E_k and E_s, Eqs. (2.39) and (2.40), in to Eq. (2.38) and then integrating the expressions by parts, the equations of motion for a laminated fiber-reinforced composite cylindrical shell coupled with a piezoelectric layer at the top surface are derived as,

$$\delta u_0: \quad \frac{\partial N_{xx}}{\partial x} + \frac{\partial N_{x\theta}}{R\partial\theta} = I_0\frac{\partial^2 u_0}{\partial t^2} + I_1\frac{\partial^2 \alpha_x}{\partial t^2} \tag{2.41a}$$

$$\delta v_0: \quad \frac{\partial N_{\theta\theta}}{R\partial\theta} + \frac{\partial N_{x\theta}}{\partial x} + \frac{V_{\theta z}}{R} = I_0\frac{\partial^2 v_0}{\partial t^2} + I_1\frac{\partial^2 \alpha_\theta}{\partial t^2} \tag{2.41b}$$

$$\delta w_0: \quad \frac{\partial V_{xz}}{\partial x} + \frac{\partial V_{\theta z}}{R\partial\theta} - \frac{N_{\theta\theta}}{R} = I_0\frac{\partial^2 w_0}{\partial t^2} \tag{2.41c}$$

$$\delta \alpha_x: \quad \frac{\partial M_{xx}}{\partial x} + \frac{\partial M_{x\theta}}{R\partial\theta} - V_{xz} = I_1\frac{\partial^2 u_0}{\partial t^2} + I_2\frac{\partial^2 \alpha_x}{\partial t^2} \tag{2.41d}$$

$$\delta \alpha_\theta: \quad \frac{\partial M_{x\theta}}{\partial x} + \frac{\partial M_{\theta\theta}}{R\partial\theta} - V_{\theta z} = I_1\frac{\partial^2 v_0}{\partial t^2} + I_2\frac{\partial^2 \alpha_\theta}{\partial t^2} \tag{2.41e}$$

where I_i $(i = 0,1,2)$ are the inertias which for a laminated fiber-reinforced composite cylindrical shell coupled with a piezoelectric layer at the top surface are obtained as,

$$I_0 = \sum_{K=1}^{N}\int_{z_{K-1}}^{z_K} \rho_K dz + \int_{\frac{h}{2}}^{\frac{h}{2}+h_p} \rho_p dz = \sum_{K=1}^{N} \rho_K(z_K - z_{K-1}) + \rho_p h_p \tag{2.42a}$$

$$I_1 = \sum_{K=1}^{N} \int_{z_{K-1}}^{z_K} \rho_K z dz + \int_{\frac{h}{2}}^{\frac{h}{2}+h_p} \rho_p z dz = \frac{1}{2} \sum_{K=1}^{N} \rho_K (z_K^2 - z_{K-1}^2) + \frac{\rho_p}{2}(h h_p + h_p^2) \quad (2.42b)$$

$$I_2 = \sum_{K=1}^{N} \int_{z_{K-1}}^{z_K} \rho_K z^2 dz + \int_{\frac{h}{2}}^{\frac{h}{2}+h_p} \rho_p z^2 dz = \frac{1}{3} \sum_{K=1}^{N} \rho_K (z_K^3 - z_{K-1}^3) + \rho_p \left(\frac{h_p h^2}{4} + \frac{h h_p^2}{2} + \frac{h_p^3}{3} \right) \quad (2.42c)$$

where ρ_K and ρ_p are the mass densities of each host composite layer and the piezoelectric layer, respectively.

2.3.2.2. Equations of Motion for a Piezoelectric Coupled Laminated Composite Cylindrical Shell Based on the Love Bending Shell Theory

Based on the Love bending shell theory, the rotary inertias, I_1 and I_2, are assumed negligible. In this theory, shell is with bending resistance based on the Love's shear-rigidity assumption. Thus, the equations of motion based on this theory are given by Ref. [97] as,

$$\frac{\partial N_{xx}}{\partial x} + \frac{\partial N_{\theta x}}{R \partial \theta} = I_0 \frac{\partial^2 u_0}{\partial t^2} \quad (2.43a)$$

$$\frac{\partial N_{\theta\theta}}{R \partial \theta} + \frac{\partial N_{x\theta}}{\partial x} - \frac{V_{\theta z}}{R} = I_0 \frac{\partial^2 v_0}{\partial t^2} \quad (2.43b)$$

$$\frac{\partial V_{xz}}{\partial x} + \frac{\partial V_{\theta z}}{R \partial \theta} - \frac{N_{\theta\theta}}{R} = I_0 \frac{\partial^2 w_0}{\partial t^2} \quad (2.43c)$$

$$\frac{\partial M_{xx}}{\partial x} + \frac{\partial M_{x\theta}}{R \partial \theta} - V_{xz} = 0 \quad (2.43d)$$

$$\frac{\partial M_{x\theta}}{\partial x} + \frac{\partial M_{\theta\theta}}{R \partial \theta} - V_{\theta z} = 0 \quad (2.43e)$$

From Eqs. (2.43d) and (2.43e), the transverse shear forces, V_{xz} and $V_{\theta z}$, are obtained as,

$$V_{xz} = \frac{\partial M_{xx}}{\partial x} + \frac{\partial M_{x\theta}}{R \partial \theta} \qquad V_{\theta z} = \frac{\partial M_{x\theta}}{\partial x} + \frac{\partial M_{\theta\theta}}{R \partial \theta} \quad (2.44)$$

By substituting Eq. (2.44) into Eqs. (2.43b) and (2.43c), the equations of motion based on the Love bending shell theory in the longitudinal (x), tangential (θ), and radial (z) directions, respectively, are reduced to,

$$\frac{\partial N_{xx}}{\partial x}+\frac{\partial N_{\theta x}}{R\partial\theta}=I_0\frac{\partial^2 u_0}{\partial t^2} \tag{2.45a}$$

$$\frac{\partial N_{\theta\theta}}{R\partial\theta}+\frac{\partial N_{x\theta}}{\partial x}-\frac{1}{R}\left(\frac{\partial M_{x\theta}}{\partial x}+\frac{\partial M_{\theta\theta}}{R\partial\theta}\right)=I_0\frac{\partial^2 v_0}{\partial t^2} \tag{2.45b}$$

$$\frac{\partial^2 M_{xx}}{\partial x^2}+\frac{2\partial^2 M_{x\theta}}{R\partial x\partial\theta}+\frac{\partial^2 M_{\theta\theta}}{R^2\partial\theta^2}-\frac{N_{\theta\theta}}{R}=I_0\frac{\partial^2 w_0}{\partial t^2} \tag{2.45c}$$

2.3.2.3. Equations of Motion for a Piezoelectric Coupled Laminated Composite Cylindrical Shell Based on the Membrane Shell Theory

According to the membrane shell theory, in addition to the rotary inertias (I_1 and I_2), the transverse shear forces (V_{xz} and $V_{\theta z}$) and the bending and twisting moments (M_{xx}, $M_{\theta\theta}$, and $M_{x\theta}$) are assumed negligible and only the in-plane normal and shear forces (N_{xx}, $N_{\theta\theta}$, and $N_{x\theta}$) applying on the mid-surface of the shell are considered. Thus, the equations of motion based on this theory in the longitudinal (x), tangential (θ), and radial (z) directions are, respectively, given by Ref. [198] as,

$$\frac{\partial N_{xx}}{\partial x}+\frac{\partial N_{\theta x}}{R\partial\theta}=I_0\frac{\partial^2 u_0}{\partial t^2} \tag{2.46a}$$

$$\frac{\partial N_{\theta\theta}}{R\partial\theta}+\frac{\partial N_{x\theta}}{\partial x}=I_0\frac{\partial^2 v_0}{\partial t^2} \tag{2.46b}$$

$$-\frac{N_{\theta\theta}}{R}=I_0\frac{\partial^2 w_0}{\partial t^2} \tag{2.46c}$$

2.3.3. Dispersion Characteristics for a Piezoelectric Coupled Laminated Fiber-Reinforced Composite Cylindrical Shell

In this section, dispersion characteristics are derived for a laminated fiber-reinforced composite cylindrical shell coupled with a piezoelectric layer at the top surface based on the first-order shear deformation shell theory, the Love bending shell theory, and the membrane shell theory in the following subsections.

2.3.3.1. Dispersion Characteristics Based on the First-Order Shear Deformation Shell Theory

Substituting the derived force and moment resultants with the effects of transvers shear according to the first-order shear deformation shell theory, Eq. (2.36), into the equilibrium equations of motion based on the first-order shear deformation shell theory, Eq. (2.41), yields the following equations in terms of u_0, v_0, w_0, α_x, α_θ, and φ,

$$A_1\frac{\partial^2 u_0}{\partial x^2}+\frac{A_2}{R}\left(\frac{\partial w_0}{\partial x}+\frac{\partial^2 v_0}{\partial x\partial\theta}\right)+A_3\left(\frac{\partial^2 u_0}{R\partial x\partial\theta}+\frac{\partial^2 v_0}{\partial x^2}\right)+A_4\frac{\partial^2\alpha_x}{\partial x^2}+A_5\frac{\partial^2\alpha_\theta}{R\partial x\partial\theta}+A_6\left(\frac{\partial^2\alpha_\theta}{\partial x^2}+\frac{\partial^2\alpha_x}{R\partial x\partial\theta}\right)+A_7\frac{\partial^2\varphi}{\partial x^2}+$$
$$C_1\frac{\partial^2 u_0}{R\partial x\partial\theta}+\frac{C_2}{R^2}\left(\frac{\partial w_0}{\partial\theta}+\frac{\partial^2 v_0}{\partial\theta^2}\right)+\frac{C_3}{R}\left(\frac{\partial^2 u_0}{R\partial\theta^2}+\frac{\partial^2 v_0}{\partial x\partial\theta}\right)+C_4\frac{\partial^2\alpha_x}{R\partial x\partial\theta}+C_5\frac{\partial^2\alpha_\theta}{R^2\partial\theta^2}+\frac{C_6}{R}\left(\frac{\partial^2\alpha_\theta}{\partial x\partial\theta}+\frac{\partial^2\alpha_x}{R\partial\theta^2}\right)+C_7\frac{\partial^2\varphi}{R^2\partial\theta^2}=$$
$$I_0\frac{\partial^2 u_0}{\partial t^2}+I_1\frac{\partial^2\alpha_x}{\partial t^2} \tag{2.47a}$$

$$B_1\frac{\partial^2 u_0}{R\partial x\partial\theta}+\frac{B_2}{R^2}\left(\frac{\partial w_0}{\partial\theta}+\frac{\partial^2 v_0}{\partial\theta^2}\right)+\frac{B_3}{R}\left(\frac{\partial^2 u_0}{R\partial\theta^2}+\frac{\partial^2 v_0}{\partial x\partial\theta}\right)+B_4\frac{\partial^2\alpha_x}{R\partial x\partial\theta}+B_5\frac{\partial^2\alpha_\theta}{R^2\partial\theta^2}+\frac{B_6}{R}\left(\frac{\partial^2\alpha_\theta}{\partial x\partial\theta}+\frac{\partial^2\alpha_x}{R\partial\theta^2}\right)+B_7\frac{\partial^2\varphi}{R\partial x\partial\theta}+$$
$$C_1\frac{\partial^2 u_0}{\partial x^2}+\frac{C_2}{R}\left(\frac{\partial w_0}{\partial x}+\frac{\partial^2 v_0}{\partial x\partial\theta}\right)+C_3\left(\frac{\partial^2 u_0}{R\partial x\partial\theta}+\frac{\partial^2 v_0}{\partial x^2}\right)+C_4\frac{\partial^2\alpha_x}{\partial x^2}+C_5\frac{\partial^2\alpha_\theta}{R\partial x\partial\theta}+C_6\left(\frac{\partial^2\alpha_\theta}{\partial x^2}+\frac{\partial^2\alpha_x}{R\partial x\partial\theta}\right)+C_7\frac{\partial^2\varphi}{R\partial x\partial\theta}+$$
$$\frac{H_1}{R}\left(\frac{\partial w_0}{R\partial\theta}-\frac{v_0}{R}+\alpha_\theta\right)+\frac{H_2}{R}\left(\frac{\partial w_0}{\partial x}+\alpha_x\right)=I_0\frac{\partial^2 v_0}{\partial t^2}+I_1\frac{\partial^2\alpha_\theta}{\partial t^2} \tag{2.47b}$$

$$G_1\left(\frac{\partial^2 w_0}{R\partial x\partial\theta}-\frac{\partial v_0}{R\partial x}+\frac{\partial\alpha_\theta}{\partial x}\right)+G_2\left(\frac{\partial^2 w_0}{\partial x^2}+\frac{\partial\alpha_x}{\partial x}\right)+\frac{H_1}{R}\left(\frac{\partial^2 w_0}{R\partial\theta^2}-\frac{\partial v_0}{R\partial\theta}+\frac{\partial\alpha_\theta}{\partial\theta}\right)+\frac{H_2}{R}\left(\frac{\partial^2 w_0}{\partial x\partial\theta}+\frac{\partial\alpha_x}{\partial\theta}\right)$$
$$-B_1\frac{\partial u_0}{R\partial x}-\frac{B_2}{R^2}\left(w_0+\frac{\partial v_0}{\partial\theta}\right)-\frac{B_3}{R}\left(\frac{\partial v_0}{\partial x}+\frac{\partial u_0}{R\partial\theta}\right)-\frac{B_4}{R}\frac{\partial\alpha_x}{\partial x}-\frac{B_5}{R^2}\frac{\partial\alpha_\theta}{\partial\theta}-\frac{B_6}{R}\left(\frac{\partial\alpha_\theta}{\partial x}+\frac{\partial\alpha_x}{R\partial\theta}\right)$$
$$-\frac{B_7}{R}\frac{\partial\varphi}{\partial x}=I_0\frac{\partial^2 w_0}{\partial t^2} \tag{2.47c}$$

$$D_1\frac{\partial^2 u_0}{\partial x^2}+\frac{D_2}{R}\left(\frac{\partial w_0}{\partial x}+\frac{\partial^2 v_0}{\partial x\partial\theta}\right)+D_3\left(\frac{\partial^2 u_0}{R\partial x\partial\theta}+\frac{\partial^2 v_0}{\partial x^2}\right)+D_4\frac{\partial^2\alpha_x}{\partial x^2}+D_5\frac{\partial^2\alpha_\theta}{R\partial x\partial\theta}+D_6\left(\frac{\partial^2\alpha_\theta}{\partial x^2}+\frac{\partial^2\alpha_x}{R\partial x\partial\theta}\right)+D_7\frac{\partial^2\varphi}{\partial x^2}+$$
$$F_1\frac{\partial^2 u_0}{R\partial x\partial\theta}+\frac{F_2}{R^2}\left(\frac{\partial w_0}{\partial\theta}+\frac{\partial^2 v_0}{\partial\theta^2}\right)+\frac{F_3}{R}\left(\frac{\partial^2 u_0}{R\partial\theta^2}+\frac{\partial^2 v_0}{\partial x\partial\theta}\right)+F_4\frac{\partial^2\alpha_x}{R\partial x\partial\theta}+F_5\frac{\partial^2\alpha_\theta}{R^2\partial\theta^2}+\frac{F_6}{R}\left(\frac{\partial^2\alpha_\theta}{\partial x\partial\theta}+\frac{\partial^2\alpha_x}{R\partial\theta^2}\right)+F_7\frac{\partial^2\varphi}{R^2\partial\theta^2}-$$
$$G_1\left(\frac{\partial w_0}{R\partial\theta}-\frac{v_0}{R}+\alpha_\theta\right)-G_2\left(\frac{\partial w_0}{\partial x}+\alpha_x\right)=I_1\frac{\partial^2 u_0}{\partial t^2}+I_2\frac{\partial^2\alpha_x}{\partial t^2} \tag{2.47d}$$

$$F_1\frac{\partial^2 u_0}{\partial x^2}+\frac{F_2}{R}\left(\frac{\partial w_0}{\partial x}+\frac{\partial^2 v_0}{\partial x\partial\theta}\right)+F_3\left(\frac{\partial^2 u_0}{R\partial x\partial\theta}+\frac{\partial^2 v_0}{\partial x^2}\right)+F_4\frac{\partial^2\alpha_x}{\partial x^2}+F_5\frac{\partial^2\alpha_\theta}{R\partial x\partial\theta}+F_6\left(\frac{\partial^2\alpha_\theta}{\partial x^2}+\frac{\partial^2\alpha_x}{R\partial x\partial\theta}\right)$$
$$+F_7\frac{\partial^2\varphi}{R\partial x\partial\theta}+E_1\frac{\partial^2 u_0}{R\partial x\partial\theta}+\frac{E_2}{R^2}\left(\frac{\partial w_0}{\partial\theta}+\frac{\partial^2 v_0}{\partial\theta^2}\right)+\frac{E_3}{R}\left(\frac{\partial^2 u_0}{R\partial\theta^2}+\frac{\partial^2 v_0}{\partial x\partial\theta}\right)+E_4\frac{\partial^2\alpha_x}{R\partial x\partial\theta}$$
$$+E_5\frac{\partial^2\alpha_\theta}{R^2\partial\theta^2}+\frac{E_6}{R}\left(\frac{\partial^2\alpha_\theta}{\partial x\partial\theta}+\frac{\partial^2\alpha_x}{R\partial\theta^2}\right)+E_7\frac{\partial^2\varphi}{R\partial x\partial\theta}-H_1\left(\frac{\partial w_0}{R\partial\theta}-\frac{v_0}{R}+\alpha_\theta\right)$$
$$-H_2\left(\frac{\partial w_0}{\partial x}+\alpha_x\right)=I_1\frac{\partial^2 v_0}{\partial t^2}+I_2\frac{\partial^2\alpha_\theta}{\partial t^2} \tag{2.47e}$$

The electric variables should satisfy the Maxwell's static electricity equation in which the divergence of the electric displacement vanishes at any point within the piezoelectric media. To fulfill this condition, it is enforced that the integration of the divergence of the electric displacement across the thickness of the piezoelectric layer vanishes.

By substituting the strain-displacement relations based on the first-order shear deformation shell theory, Eq. (2.9), into the electric displacements of the piezoelectric layer with the axial polarization based on this theory, Eq. (2.23b), we obtain,

$$D_{\theta\theta}=\bar{e}_{16}\left(\frac{\partial v_0}{\partial x}+\frac{\partial u_0}{R\partial\theta}\right)+\bar{e}_{16}z\left(\frac{\partial\alpha_\theta}{\partial x}+\frac{\partial\alpha_x}{R\partial\theta}\right)-\bar{\epsilon}_{11}\frac{\partial\varphi}{R\partial\theta} \tag{2.48a}$$

$$D_{xx}=\frac{\bar{e}_{21}}{R}\left(w_0+\frac{\partial v_0}{\partial\theta}\right)+\bar{e}_{21}z\frac{\partial\alpha_\theta}{R\partial\theta}+\bar{e}_{22}\left(\frac{\partial u_0}{\partial x}+z\frac{\partial\alpha_x}{\partial x}\right)-\bar{\epsilon}_{22}\frac{\partial\varphi}{\partial x} \tag{2.48b}$$

$$D_{zz}=\bar{e}_{34}\left(\frac{\partial w_0}{\partial x}+\alpha_x\right) \tag{2.48c}$$

Satisfying the Maxwell equation $\int_{\frac{h}{2}}^{\frac{h}{2}+h_p}\nabla D dz=0$ for the piezoelectric layer, in view of Eq. (2.48), yields,

$$\bar{e}_{22}\frac{\partial^2 u_0}{\partial x^2}+\frac{\bar{e}_{22}}{2}(h+h_p)\frac{\partial^2\alpha_x}{\partial x^2}+\frac{\bar{e}_{21}}{R}\left(\frac{\partial w_0}{\partial x}+\frac{\partial^2 v_0}{\partial x\partial\theta}\right)+\frac{\bar{e}_{21}}{2}(h+h_p)\frac{\partial^2\alpha_\theta}{R\partial x\partial\theta}+\bar{e}_{16}\left(\frac{\partial^2 u_0}{R^2\partial\theta^2}+\frac{\partial^2 v_0}{R\partial x\partial\theta}\right)$$
$$+\frac{\bar{e}_{16}}{2}(h+h_p)\left(\frac{\partial^2\alpha_\theta}{R\partial x\partial\theta}+\frac{\partial^2\alpha_x}{R^2\partial\theta^2}\right)-\bar{\epsilon}_{22}\frac{\partial^2\varphi}{\partial x^2}-\bar{\epsilon}_{11}\frac{\partial^2\varphi}{R^2\partial\theta^2}=0 \tag{2.49}$$

Eqs. (2.47) and (2.49) show the equations of motion in term of the shell displacements ($u_0, v_0,$ and w_0), the rotations of shell cross-section normal to x –axis and θ-axis or shear effects (α_x and α_θ), and the electric potential (φ) for a laminated fiber-reinforced composite cylindrical shell coupled with a piezoelectric layer at the top surface based on first-order shear deformation shell theory.

2.3.3.2. Dispersion Characteristics Based on the Love Bending Shell Theory

By substituting the derived force and moment resultants based on the classical shell theory, Eq. (2.37), into the equations of motion based on the Love bending shell theory, Eq. (2.45), one obtains the following equations in terms of u_0, v_0, w_0, and φ,

$$\begin{aligned}
&\acute{A}_1\frac{\partial^2 u_0}{\partial x^2}+\frac{\acute{A}_2}{R}\left(\frac{\partial w_0}{\partial x}+\frac{\partial^2 v_0}{\partial x\partial\theta}\right)+\acute{A}_3\left(\frac{\partial^2 u_0}{R\partial x\partial\theta}+\frac{\partial^2 v_0}{\partial x^2}\right)+\acute{A}_4\frac{\partial^3 w_0}{\partial x^3}+\acute{A}_5\frac{\partial^3 w_0}{R^2\partial x\partial\theta^2}+\acute{A}_6\frac{\partial^3 w_0}{R\partial x^2\partial\theta}\\
&\quad+\acute{A}_7\frac{\partial^2\varphi}{\partial x^2}+\acute{C}_1\frac{\partial^2 u_0}{R\partial x\partial\theta}+\frac{\acute{C}_2}{R^2}\left(\frac{\partial w_0}{\partial\theta}+\frac{\partial^2 v_0}{\partial\theta^2}\right)+\frac{\acute{C}_3}{R}\left(\frac{\partial^2 u_0}{R\partial\theta^2}+\frac{\partial^2 v_0}{\partial x\partial\theta}\right)+\acute{C}_4\frac{\partial^3 w_0}{R\partial x^2\partial\theta}\\
&\quad+\acute{C}_5\frac{\partial^3 w_0}{R^3\partial\theta^3}+\acute{C}_6\frac{\partial^3 w_0}{R^2\partial x\partial\theta^2}+\acute{C}_7\frac{\partial^2\varphi}{R^2\partial\theta^2}=I_0\frac{\partial^2 u_0}{\partial t^2} \qquad (2.50a)\\
&\frac{\acute{B}_1}{R}\frac{\partial^2 u_0}{\partial x\partial\theta}+\frac{\acute{B}_2}{R^2}\left(\frac{\partial w_0}{\partial\theta}+\frac{\partial^2 v_0}{\partial\theta^2}\right)+\frac{\acute{B}_3}{R}\left(\frac{\partial^2 u_0}{R\partial\theta^2}+\frac{\partial^2 v_0}{\partial x\partial\theta}\right)+\acute{B}_4\frac{\partial^3 w_0}{R\partial x^2\partial\theta}+\acute{B}_5\frac{\partial^3 w_0}{R^3\partial\theta^3}+\acute{B}_6\frac{\partial^3 w_0}{R^2\partial x\partial\theta^2}\\
&\quad+\frac{\acute{B}_7}{R}\frac{\partial^2\varphi}{\partial x\partial\theta}+\acute{C}_1\frac{\partial^2 u_0}{\partial x^2}+\frac{\acute{C}_2}{R}\left(\frac{\partial w_0}{\partial x}+\frac{\partial^2 v_0}{\partial x\partial\theta}\right)+\acute{C}_3\left(\frac{\partial^2 u_0}{R\partial x\partial\theta}+\frac{\partial^2 v_0}{\partial x^2}\right)+\acute{C}_4\frac{\partial^3 w_0}{\partial x^3}\\
&\quad+\acute{C}_5\frac{\partial^3 w_0}{R^2\partial x\partial\theta^2}+\acute{C}_6\frac{\partial^3 w_0}{R\partial x^2\partial\theta}+\acute{C}_7\frac{\partial^2\varphi}{R\partial x\partial\theta}-\frac{\acute{F}_1}{R}\frac{\partial^2 u_0}{\partial x^2}-\frac{\acute{F}_2}{R^2}\left(\frac{\partial w_0}{\partial x}+\frac{\partial^2 v_0}{\partial x\partial\theta}\right)\\
&\quad-\frac{\acute{F}_3}{R}\left(\frac{\partial^2 u_0}{R\partial x\partial\theta}+\frac{\partial^2 v_0}{\partial x^2}\right)-\frac{\acute{F}_4}{R}\frac{\partial^3 w_0}{\partial x^3}-\acute{F}_5\frac{\partial^3 w_0}{R^3\partial x\partial\theta^2}-\acute{F}_6\frac{\partial^3 w_0}{R^2\partial x^2\partial\theta}-\acute{F}_7\frac{\partial^2\varphi}{R^2\partial x\partial\theta}\\
&\quad-\acute{E}_1\frac{\partial^2 u_0}{R^2\partial x\partial\theta}-\frac{\acute{E}_2}{R^3}\left(\frac{\partial w_0}{\partial\theta}+\frac{\partial^2 v_0}{\partial\theta^2}\right)-\frac{\acute{E}_3}{R^2}\left(\frac{\partial^2 u_0}{R\partial\theta^2}+\frac{\partial^2 v_0}{\partial x\partial\theta}\right)-\acute{E}_4\frac{\partial^3 w_0}{R^2\partial x^2\partial\theta}-\frac{\acute{E}_5}{R^4}\frac{\partial^3 w_0}{\partial\theta^3}\\
&\quad-\acute{E}_6\frac{\partial^3 w_0}{R^3\partial x\partial\theta^2}-\acute{E}_7\frac{\partial^2\varphi}{R^2\partial x\partial\theta}=I_0\frac{\partial^2 v_0}{\partial t^2} \qquad (2.50b)
\end{aligned}$$

$$\acute{D}_1\frac{\partial^3 u_0}{\partial x^3}+\frac{\acute{D}_2}{R}\left(\frac{\partial^2 w_0}{\partial x^2}+\frac{\partial^3 v_0}{\partial x^2\partial\theta}\right)+\acute{D}_3\left(\frac{\partial^3 u_0}{R\partial x^2\partial\theta}+\frac{\partial^3 v_0}{\partial x^3}\right)+\acute{D}_4\frac{\partial^4 w_0}{\partial x^4}+\acute{D}_5\frac{\partial^4 w_0}{R^2\partial x^2\partial\theta^2}+\acute{D}_6\frac{\partial^4 w_0}{R\partial x^3\partial\theta}+\acute{D}_7\frac{\partial^3\varphi}{\partial x^3}+$$

$$\frac{2\acute{F}_1}{R}\frac{\partial^3 u_0}{\partial x^2\partial\theta}+\frac{2\acute{F}_2}{R^2}\left(\frac{\partial^2 w_0}{\partial x\partial\theta}+\frac{\partial^3 v_0}{\partial x\partial\theta^2}\right)+\frac{2\acute{F}_3}{R}\left(\frac{\partial^3 u_0}{R\partial x\partial\theta^2}+\frac{\partial^3 v_0}{\partial x^2\partial\theta}\right)+2\acute{F}_4\frac{\partial^4 w_0}{R\partial x^3\partial\theta}+2\acute{F}_5\frac{\partial^4 w_0}{R^3\partial x\partial\theta^3}+2\acute{F}_6\frac{\partial^4 w_0}{R^2\partial x^2\partial\theta^2}+$$

$$2\acute{F}_7\frac{\partial^3\varphi}{R^2\partial x\partial\theta^2}+\acute{E}_1\frac{\partial^3 u_0}{R^2\partial x\partial\theta^2}+\frac{\acute{E}_2}{R^3}\left(\frac{\partial^2 w_0}{\partial\theta^2}+\frac{\partial^3 v_0}{\partial\theta^3}\right)+\frac{\acute{E}_3}{R^2}\left(\frac{\partial^3 u_0}{R\partial\theta^3}+\frac{\partial^3 v_0}{\partial x\partial\theta^2}\right)+\acute{E}_4\frac{\partial^4 w_0}{R^2\partial x^2\partial\theta^2}+\acute{E}_5\frac{\partial^4 w_0}{R^4\partial\theta^4}+$$

$$\acute{E}_6\frac{\partial^4 w_0}{R^3\partial x\partial\theta^3}+\acute{E}_7\frac{\partial^3\varphi}{R^2\partial x\partial\theta^2}-\frac{\acute{B}_1}{R}\frac{\partial u_0}{\partial x}-\frac{\acute{B}_2}{R^2}\left(w_0+\frac{\partial v_0}{\partial\theta}\right)-\frac{\acute{B}_3}{R}\left(\frac{\partial u_0}{R\partial\theta}+\frac{\partial v_0}{\partial x}\right)-\frac{\acute{B}_4}{R}\frac{\partial^2 w_0}{\partial x^2}-\acute{B}_5\frac{\partial^2 w_0}{R^3\partial\theta^2}-\acute{B}_6\frac{\partial^2 w_0}{R^2\partial x\partial\theta}-$$

$$\frac{\acute{B}_7}{R}\frac{\partial\varphi}{\partial x}=I_0\frac{\partial^2 w_0}{\partial t^2} \tag{2.50c}$$

Replacing the strain-displacement relations based on the classical shell theory, Eq. (2.4), into the electric displacements in the piezoelectric layer with the axial polarization based on this theory, Eq. (2.21b), yields,

$$D_{\theta\theta}=\bar{e}_{16}\left(\frac{\partial v_0}{\partial x}+\frac{\partial u_0}{R\partial\theta}\right)-\bar{e}_{16}2z\frac{\partial^2 w_0}{R\partial x\partial\theta}-\bar{\in}_{11}\frac{\partial\varphi}{R\partial\theta} \tag{2.51a}$$

$$D_{xx}=\frac{\bar{e}_{21}}{R}\left(w_0+\frac{\partial v_0}{\partial\theta}\right)-\bar{e}_{21}z\frac{\partial^2 w_0}{R^2\partial\theta^2}+\bar{e}_{22}\left(\frac{\partial u_0}{\partial x}-z\frac{\partial^2 w_0}{\partial x^2}\right)-\bar{\in}_{22}\frac{\partial\varphi}{\partial x} \tag{2.51b}$$

$$D_{zz}=0 \tag{2.51c}$$

Satisfying the Maxwell equation $\int_{\frac{h}{2}}^{\frac{h}{2}+h_p}\nabla D dz=0$, in view of Eq. (2.51), leads to,

$$\bar{e}_{22}\frac{\partial^2 u_0}{\partial x^2}-\frac{\bar{e}_{22}}{2}(h+h_p)\frac{\partial^3 w_0}{\partial x^3}+\frac{\bar{e}_{21}}{R}\left(\frac{\partial w_0}{\partial x}+\frac{\partial^2 v_0}{\partial x\partial\theta}\right)-\bar{e}_{21}(h+h_p)\frac{\partial^3 w_0}{R^2\partial x\partial\theta^2}+\frac{\bar{e}_{16}}{R}\left(\frac{\partial^2 u_0}{R\partial\theta^2}+\frac{\partial^2 v_0}{\partial x\partial\theta}\right)$$

$$-\bar{e}_{16}(h+h_p)\frac{\partial^3 w_0}{R^2\partial x\partial\theta^2}-\bar{\in}_{22}\frac{\partial^2\varphi}{\partial x^2}-\bar{\in}_{11}\frac{\partial^2\varphi}{R^2\partial\theta^2}=0 \tag{2.52}$$

Eqs. (2.50) and (2.52) represent the equations of motion in term of the shell displacements (u_0, v_0, and w_0) and the electric potential (φ) for a laminated fiber-reinforced composite cylindrical shell integrated with a piezoelectric layer at the top surface according to the Love bending shell theory.

2.3.3.3. Dispersion Characteristics Based on the Membrane Shell Theory

By substituting the in-plane force resultants (N_{xx}, $N_{\theta\theta}$, and $N_{x\theta}$) according to the classical shell theory, Eqs. (2.37a) - (2.37c), into the equations of motion based on the membrane shell theory, Eq. (2.46), the following equations in terms of u_0, v_0, w_0, and φ are obtained,

$$\acute{A}_1\frac{\partial^2 u_0}{\partial x^2}+\frac{\acute{A}_2}{R}\left(\frac{\partial w_0}{\partial x}+\frac{\partial^2 v_0}{\partial x\partial\theta}\right)+\acute{A}_3\left(\frac{\partial^2 u_0}{R\partial x\partial\theta}+\frac{\partial^2 v_0}{\partial x^2}\right)+\acute{A}_4\frac{\partial^3 w_0}{\partial x^3}+\acute{A}_5\frac{\partial^3 w_0}{R^2\partial x\partial\theta^2}+\acute{A}_6\frac{\partial^3 w_0}{R\partial x^2\partial\theta}$$
$$+\acute{A}_7\frac{\partial^2\varphi}{\partial x^2}+\acute{C}_1\frac{\partial^2 u_0}{R\partial x\partial\theta}+\frac{\acute{C}_2}{R^2}\left(\frac{\partial w_0}{\partial\theta}+\frac{\partial^2 v_0}{\partial\theta^2}\right)+\acute{C}_3\left(\frac{\partial^2 u_0}{R^2\partial\theta^2}+\frac{\partial^2 v_0}{R\partial x\partial\theta}\right)+\acute{C}_4\frac{\partial^3 w_0}{R\partial x^2\partial\theta}$$
$$+\acute{C}_5\frac{\partial^3 w_0}{R^3\partial\theta^3}+\acute{C}_6\frac{\partial^3 w_0}{R^2\partial x\partial\theta^2}+\acute{C}_7\frac{\partial^2\varphi}{R^2\partial\theta^2}=I_0\frac{\partial^2 u_0}{\partial t^2} \tag{2.53a}$$

$$\frac{\acute{B}_1}{R}\frac{\partial^2 u_0}{\partial x\partial\theta}+\frac{\acute{B}_2}{R^2}\left(\frac{\partial w_0}{\partial\theta}+\frac{\partial^2 v_0}{\partial\theta^2}\right)+\acute{B}_3\left(\frac{\partial^2 u_0}{R^2\partial\theta^2}+\frac{\partial^2 v_0}{R\partial x\partial\theta}\right)+\frac{\acute{B}_4}{R}\frac{\partial^3 w_0}{\partial x^2\partial\theta}+\acute{B}_5\frac{\partial^3 w_0}{R^3\partial\theta^3}+\acute{B}_6\frac{\partial^3 w_0}{R^2\partial x\partial\theta^2}$$
$$+\frac{\acute{B}_7}{R}\frac{\partial^2\varphi}{\partial x\partial\theta}+\acute{C}_1\frac{\partial^2 u_0}{\partial x^2}+\frac{\acute{C}_2}{R}\left(\frac{\partial w_0}{\partial x}+\frac{\partial^2 v_0}{\partial x\partial\theta}\right)+\acute{C}_3\left(\frac{\partial^2 u_0}{R\partial x\partial\theta}+\frac{\partial^2 v_0}{\partial x^2}\right)+\acute{C}_4\frac{\partial^3 w_0}{\partial x^3}$$
$$+\acute{C}_5\frac{\partial^3 w_0}{R^2\partial x\partial\theta^2}+\acute{C}_6\frac{\partial^3 w_0}{R\partial x^2\partial\theta}+\acute{C}_7\frac{\partial^2\varphi}{R\partial x\partial\theta}=I_0\frac{\partial^2 v_0}{\partial t^2} \tag{2.53b}$$

$$-\frac{\acute{B}_1}{R}\frac{\partial u_0}{\partial x}-\frac{\acute{B}_2}{R^2}\left(w_0+\frac{\partial v_0}{\partial\theta}\right)-\frac{\acute{B}_3}{R}\left(\frac{\partial u_0}{R\partial\theta}+\frac{\partial v_0}{\partial x}\right)-\frac{\acute{B}_4}{R}\frac{\partial^2 w_0}{\partial x^2}-\acute{B}_5\frac{\partial^2 w_0}{R^3\partial\theta^2}-\acute{B}_6\frac{\partial^2 w_0}{R^2\partial x\partial\theta}-\frac{\acute{B}_7}{R}\frac{\partial\varphi}{\partial x}$$
$$=I_0\frac{\partial^2 w_0}{\partial t^2} \tag{2.53c}$$

The electric displacements and the equations of motion for a piezoelectric layer based on the membrane shell theory are the same as those for the Love bending shell theory, Eqs. (2.51) and (2.52). Thus, Eqs. (2.53) and (2.52) express the equations of motion in term of the shell displacements ($u_0, v_0,$ and w_0) and the electric potential (φ) for a laminated fiber-reinforced composite cylindrical shell coupled with a piezoelectric layer at the top surface based on the membrane shell theory.

2.3.4. Solution Procedure

The shell displacements (u_0, v_0, and w_0), the rotations of shell cross-section normal to x -axis and θ-axis or shear effects (α_x and α_θ), and the electric potential (φ) for wave propagation are assumed to be in the following forms,

$$u_0(x,\theta,t) = Ue^{in\theta}e^{i\gamma(x-ct)} \tag{2.54a}$$

$$v_0(x,\theta,t) = Ve^{in\theta}e^{i\gamma(x-ct)} \tag{2.54b}$$

$$w_0(x,\theta,t) = We^{in\theta}e^{i\gamma(x-ct)} \tag{2.54c}$$

$$\alpha_x(x,\theta,t) = A_x e^{in\theta}e^{i\gamma(x-ct)} \tag{2.54d}$$

$$\alpha_\theta(x,\theta,t) = A_\theta e^{in\theta}e^{i\gamma(x-ct)} \tag{2.54e}$$

$$\varphi(x,\theta,t) = \Phi e^{in\theta}e^{i\gamma(x-ct)} \tag{2.54f}$$

where γ, n, and c are axial wavenumber, circumferential wavenumber, and wave phase velocity, respectively; U, V, W, A_x, A_θ and Φ are the wave amplitudes; and $\omega = c\gamma$ is the corresponding frequency.

Substituting Eq. (2.54) into the equations of motion according to the first-order shear deformation shell theory, Eqs. (2.47) and (2.49), yields a set of homogenous equations as,

$$\begin{bmatrix} L_{11} & L_{12} & L_{13} & L_{14} & L_{15} & L_{16} \\ L_{21} & L_{22} & L_{23} & L_{24} & L_{25} & L_{26} \\ L_{31} & L_{32} & L_{33} & L_{34} & L_{35} & L_{36} \\ L_{41} & L_{42} & L_{43} & L_{44} & L_{45} & L_{46} \\ L_{51} & L_{52} & L_{53} & L_{54} & L_{55} & L_{56} \\ L_{61} & L_{62} & L_{63} & L_{64} & L_{65} & L_{66} \end{bmatrix} \begin{Bmatrix} U \\ V \\ W \\ A_x \\ A_\theta \\ \Phi \end{Bmatrix} = \{0\} \tag{2.55}$$

Substituting the displacements and electric potential for wave propagation from Eq. (2.54) into the equations of motion based on the Love bending shell theory, Eqs. (2.50) and (2.52), leads to a set of homogenous equations as,

$$\begin{bmatrix} S_{11} & S_{12} & S_{13} & S_{14} \\ S_{21} & S_{22} & S_{23} & S_{24} \\ S_{31} & S_{32} & S_{33} & S_{34} \\ S_{41} & S_{42} & S_{43} & S_{44} \end{bmatrix} \begin{Bmatrix} U \\ V \\ W \\ \Phi \end{Bmatrix} = \{0\} \tag{2.56}$$

By substituting the displacements and electric potential for wave propagation from Eq. (2.54) into the equations of motion according to the membrane shell theory, Eqs. (2.53) and (2.52), one obtains a set of homogenous equations as,

$$\begin{bmatrix} T_{11} & T_{12} & T_{13} & T_{14} \\ T_{21} & T_{22} & T_{23} & T_{24} \\ T_{31} & T_{32} & T_{33} & T_{34} \\ T_{41} & T_{42} & T_{43} & T_{44} \end{bmatrix} \begin{Bmatrix} U \\ V \\ W \\ \Phi \end{Bmatrix} = \{0\} \tag{2.57}$$

where the components of matrices $[L_{ij}]_{6\times6}$, $[S_{ij}]_{4\times4}$, and $[T_{ij}]_{4\times4}$ are given in Appendices G, H, and I, respectively. Due to the eigenvalue problem, the above matrix equations has a nontrivial solution for U, V, W, A_x, A_θ, and Φ only if, the determinant of matrices $[L_{ij}]$, $[S_{ij}]$, and $[T_{ij}]$ is equal to zero. By solving Eq. (2.55), five positive roots are obtained for any specific axial wavenumber γ and circumferential wavenumber n which are the wave phase velocities c for the laminated composite cylindrical shell motions corresponding to the axial (x), circumferential (θ), and radial (z) displacements, and the rotations of the shell cross-section normal to x -axis ($z-\theta$ plane) and θ-axis ($x-z$ plane), respectively. These five roots are called the wave phase velocities corresponding to the first five wave modes denoted, respectively, by $M1$, $M2$, $M3$, $M4$ and $M5$ in this thesis. While one obtains three positive roots by solving Eqs. (2.56) and (2.57) as the wave phase velocities c corresponding to the first three wave modes $M1$, $M2$, and $M3$. The lowest of the five roots ($M1$) represents the flexural (forward) motion of the shell particles and other roots ($M2$ - $M5$) are in-plane and out-of-plane motions of the shell particles.

To solve the eigenvalue problem addressing the real roots of Eqs. (2.55) - (2.57), a Matlab code is provided based on the Bisection method where it is an iterative discretization root-finding method solving the equation $f(x)=0$ for real variable x with continuous function f. If the continuous function f is defined on an interval $[a,b]$ and where $f(a)$ and $f(b)$ have opposite

signs ($f(a) \times f(b) < 0$), a and b bracket a root, and the continuous function f must have at least one root in the interval $[a, b]$.

Firstly, a relatively small interval ($< 5\%$ of the whole variable range $[a, b]$) is defined to scan the whole variable range during the Bisection root search. At each iterative step at the interval $[a, b]$ with $f(a) \times f(b) < 0$, the method divides the interval in two by computing the midpoint $c = (a + b) / 2$ of the interval and the value of the function $f(c)$ at that point. Unless c is itself a root of $f(x) = 0$ (this is very unlikely but could be possible), there are two possibilities: either $f(a)$ and $f(c)$ have opposite signs and bracket a root, or $f(c)$ and $f(b)$ have opposite signs and bracket a root. We then select the subinterval that is guaranteed to bracket the root as the new interval to be used in the next iteration. In this way, the size of an interval that contains $f(x) = 0$ is reduced by half at each iteration step. The process is continued until the interval is sufficiently small ($< 0.1\%$ of whole variable range) with c very close to the analytical root of $f(x) = 0$ [199].

Therefore, by using the above method, the dispersion or frequency curves for different wave modes can be obtained by finding the wave phase velocity c or the frequency ω at any specific axial wavenumber γ and circumferential wavenumber n.

Carbon/epoxy and E-glass/epoxy unidirectional composites are considered for the host laminated composite cylindrical shell where their material properties are given in Table 2.1, and for the piezoelectric actuator, PZT-4 is chosen where its material properties are listed in Table 2.2.

To investigate wave propagation in a laminated fiber-reinforced composite cylindrical shell coupled with a piezoelectric layer, the non-dimensional wave phase velocity is employed in the numerical analysis. The axial wavenumber is defined by,

$$\gamma = \frac{2\pi}{\lambda} \tag{2.58}$$

where γ is the axial wavenumber with unit $\frac{rad}{m}$ and λ is the wavelength with unit meter (m). By multiplying the axial wavenumber γ with $\frac{H}{2\pi}(^{m}/_{rad})$, we obtain the non-dimensional axial wavenumber as,

$$\xi = \frac{\gamma H}{2\pi} = \frac{H}{\lambda} \tag{2.59}$$

where $H = h + h_p$ is the total thickness of a laminated composite cylindrical shell coupled with a piezoelectric layer at the top surface. For any specific non-dimensional axial wavenumber ξ, its corresponding axial wavenumber γ or wavelength λ is obtained from Eq. (2.59), and then by substituting the calculated corresponding axial wavenumber γ or wavelength λ and a specific value of circumferential wavenumber n ($n = 0,1,2, ...$) into Eqs. (2.55) - (2.57), the corresponding wave phase velocities c are calculated, respectively, based on the first-order deformation shell theory, the Love bending shell theory, and the membrane shell theory for different wave modes. The non-dimensional wave phase velocity is defined as,

$$\mathrm{v} = \frac{c}{c_t} \tag{2.60}$$

where c is the wave phase velocity computed from Eqs. (2.55) - (2.57), and c_t is the torsional wave phase velocity which for the first-order shear deformation shell theory and the Love bending shell theory is employed as [97,98],

$$c_t = \sqrt{\frac{G_{12}h + \bar{c}_{66}h_p\left(1 - ((h + h_p)/R)\right)}{\rho_K h + \rho_p h_p}} \tag{2.61}$$

and for the membrane shell theory is employed as [39],

$$c_t = \sqrt{\frac{G_{12}h + \bar{c}_{66}h_p}{\rho_K h + \rho_p h_p}} \tag{2.62}$$

in the numerical simulations, because all simulations here are compared with those of the Refs. [39,97,98] and G_{12} is the in-plane shear modulus of a fiber-reinforced unidirectional composite given in Table 2.1 and $\bar{c}_{66}$ is the effective in-plane shear modulus for the piezoelectric layer. In the case of no piezoelectric layer ($h_p = 0$), Eqs. (2.61) and (2.62) are reduced to,

$$c_t = \sqrt{\frac{G_{12}}{\rho_K}} \tag{2.63}$$

The ratio of piezoelectric layer thickness (h_p) to the host laminated composite shell thickness (h) is defined as $r = \frac{h_p}{h}$.

Table 2.1. Material properties for fiber-reinforced unidirectional composites [6].

Property	Carbon/Epoxy (AS4/3501-6)	E-Glass/Epoxy
Fiber volume fraction, f_r	0.63	0.55
Mass density, ρ, (kg/m^3)	1600	1970
Longitudinal modulus, E_{11}, (GPa)	149	41
Transverse modulus, E_{22}, (GPa)	10.3	10.4
In-plane shear modulus, G_{12}, (GPa)	7	4.3
Major Poisson's ratio, v_{12}	0.27	0.28
Longitudinal coefficient of thermal expansion, Γ_{11}, (10^{-6}/K)	-0.9	7
Transverse coefficient of thermal expansion, Γ_{22}, (10^{-6}/K)	27	26
Longitudinal coefficient of moisture expansion, Υ_{11}	0.01	0
Transverse coefficient of moisture expansion, Υ_{22}	0.2	0.2

Table 2.2. Material properties for the PZT-4 [92,103].

$\rho = 7500\ (\mathrm{kg/m^3}),\quad E = 78\ (GPa),\quad v = 0.31$				
Elastic constants, c_{ij} (GPa)				
$c_{11} = 139\ ,\ c_{12} = 78\ ,\ c_{13} = 74\ ,\ c_{22} = 139\ ,\ c_{23} = 74\ ,\ c_{33} = 115\ ,\ c_{44} = 25.6\ ,\ c_{55} = 25.6\ ,\ c_{66} = 30.5$				
		Dielectric constants, $\in_{ij}\ (\times 10^{-11} F/m^2)$		
Polarization	Piezoelectric constants, $e_{ij}\ (C/m^2)$	$\in_{11}$	$\in_{22}$	$\in_{33}$
Axial	$e_{16} = -12.7\ ,\ e_{21} = -15.1\ ,\ e_{22} = 5.2\ ,\ e_{23} = 5.2\ ,\ e_{34} = -12.7$	650	560	650
Circumferential	$e_{11} = -15.1\ ,\ e_{12} = 5.2\ ,\ e_{13} = 5.2\ ,\ e_{26} = -12.7\ ,\ e_{35} = -12.7$	560	650	650
Radial	$e_{15} = 12.7\ ,\ e_{24} = 12.7\ ,\ e_{31} = -5.2\ ,\ e_{32} = -5.2\ ,\ e_{33} = 15.1$	650	650	560

2.4. Wave Propagation Modeling in Piezocomposite Cylindrical Shells Reinforced with Carbon Nanotubes

As particles in nano sizes, CNTs can be dispersed in a matrix in different manners. They can be angled dispersed with a specific orientation to the global coordinate system, randomly oriented particles, and or agglomerated partially and completely in the matrix. Various dispersions of CNTs in the matrix lead to different dynamic properties of composites. Modeling CNTs embedded in composites has always been a challenge and been studied through different methodologies such as the Mori-Tanaka model [104] and the rule of mixture model [105]. Wave propagation behaviors for piezocomposite cylindrical shells reinforced with CNTs with different orientations and distributions have not been investigated in the literature. Hence, in this section, wave propagation in CNT-reinforced piezocomposites is modeled.

2.4.1. Constitutive Relations for Piezoelectric Composite Cylindrical Shells Reinforced with CNTs

The poling direction of the piezoelectric cylindrical shell is assumed to be in the axial x-direction of the shell, which also means the x-direction is the axis of symmetry of the piezoelectric shell. In view of Eq. (2.19), the generalized constitutive relations for a piezoelectric cylindrical shell with the axial polarization in the cylindrical coordinate system (x, θ, z) can be developed to [81],

$$\begin{Bmatrix}\sigma_{\theta\theta}\\ \sigma_{xx}\\ \sigma_{zz}\\ \tau_{xz}\\ \tau_{\theta z}\\ \tau_{x\theta}\end{Bmatrix}=\begin{bmatrix}C_{\theta\theta} & C_{\theta x} & C_{\theta z} & 0 & 0 & C_{\theta s}\\ C_{\theta x} & C_{xx} & C_{xz} & 0 & 0 & C_{xs}\\ C_{\theta z} & C_{xz} & C_{zz} & 0 & 0 & C_{zs}\\ 0 & 0 & 0 & C_{rr} & C_{rq} & 0\\ 0 & 0 & 0 & C_{rq} & C_{qq} & 0\\ C_{\theta s} & C_{xs} & C_{zs} & 0 & 0 & C_{ss}\end{bmatrix}\begin{Bmatrix}\varepsilon_{\theta\theta}\\ \varepsilon_{xx}\\ \varepsilon_{zz}\\ \gamma_{xz}\\ \gamma_{\theta z}\\ \gamma_{x\theta}\end{Bmatrix}-\begin{bmatrix}0 & e_{21} & 0\\ 0 & e_{22} & 0\\ 0 & e_{23} & 0\\ 0 & 0 & e_{34}\\ 0 & 0 & 0\\ e_{16} & 0 & 0\end{bmatrix}\begin{Bmatrix}E_{\theta\theta}\\ E_{xx}\\ E_{zz}\end{Bmatrix} \tag{2.64a}$$

$$\begin{Bmatrix}D_{\theta\theta}\\ D_{xx}\\ D_{zz}\end{Bmatrix}=\begin{bmatrix}0 & 0 & 0 & 0 & 0 & e_{16}\\ e_{21} & e_{22} & e_{23} & 0 & 0 & 0\\ 0 & 0 & 0 & e_{34} & 0 & 0\end{bmatrix}\begin{Bmatrix}\varepsilon_{\theta\theta}\\ \varepsilon_{xx}\\ \varepsilon_{zz}\\ \gamma_{xz}\\ \gamma_{\theta z}\\ \gamma_{x\theta}\end{Bmatrix}+\begin{bmatrix}\in_{11} & 0 & 0\\ 0 & \in_{22} & 0\\ 0 & 0 & \in_{33}\end{bmatrix}\begin{Bmatrix}E_{\theta\theta}\\ E_{xx}\\ E_{zz}\end{Bmatrix} \tag{2.64b}$$

In view of Eq. (2.34), the in-plane force and moment resultants and the transverse shear force resultants for a piezocomposite cylindrical shell reinforced by CNTs are obtained by integrating the corresponding stresses across the piezoelectric thickness as,

$$\begin{Bmatrix}N_{xx}\\ N_{\theta\theta}\\ N_{x\theta}\end{Bmatrix}=\int_{-\frac{h}{2}}^{\frac{h}{2}}\begin{Bmatrix}\sigma_{xx}\\ \sigma_{\theta\theta}\\ \tau_{x\theta}\end{Bmatrix}dz \tag{2.65a}$$

$$\begin{Bmatrix}M_{xx}\\ M_{\theta\theta}\\ M_{x\theta}\end{Bmatrix}=\int_{-\frac{h}{2}}^{\frac{h}{2}}\begin{Bmatrix}\sigma_{xx}\\ \sigma_{\theta\theta}\\ \tau_{x\theta}\end{Bmatrix}zdz \tag{2.65b}$$

$$\begin{Bmatrix}V_{\theta z}\\ V_{xz}\end{Bmatrix}=K_s\int_{-\frac{h}{2}}^{\frac{h}{2}}\begin{Bmatrix}\tau_{\theta z}\\ \tau_{xz}\end{Bmatrix}dz \tag{2.65c}$$

In this section, h represents the thickness of the piezoelectric cylindrical shell. In the following subsections, constitutive equations are derived and developed by considering various CNT distributions in piezocomposite cylindrical shells. The proposed model leads to derive the stiffness matrix and material properties and then develop a composite wave propagation approach for any kind of customized composites with various distributions of CNTs.

2.4.2. Constitutive Relations for a Piezoelectric Composite Cylindrical Shell Reinforced with Angled, Straight CNTs

In this section, constitutive equations are derived and developed for a linear elastic piezoelectric composite reinforced by a large number of dispersed CNTs which are angled and straight. Configuration of an infinitely long unbounded piezoelectric composite cylindrical shells reinforced with angled, straight CNTs is shown in Fig. 2.6 with corresponding material principle $(1, 2, 3)$ and cylindrical coordinate $(x,\ \theta,\ z)$ systems.

Due to the advantages of the Mori-Tanaka [104] micromechanics model rather to the rule of mixture [105] micromechanics model, as explained in section 1.2.2.1, the Mori-Tanaka model is employed to estimate the resulting effective elastic properties of a piezoelectric composite cylindrical shell reinforced with aligned, straight CNTs.

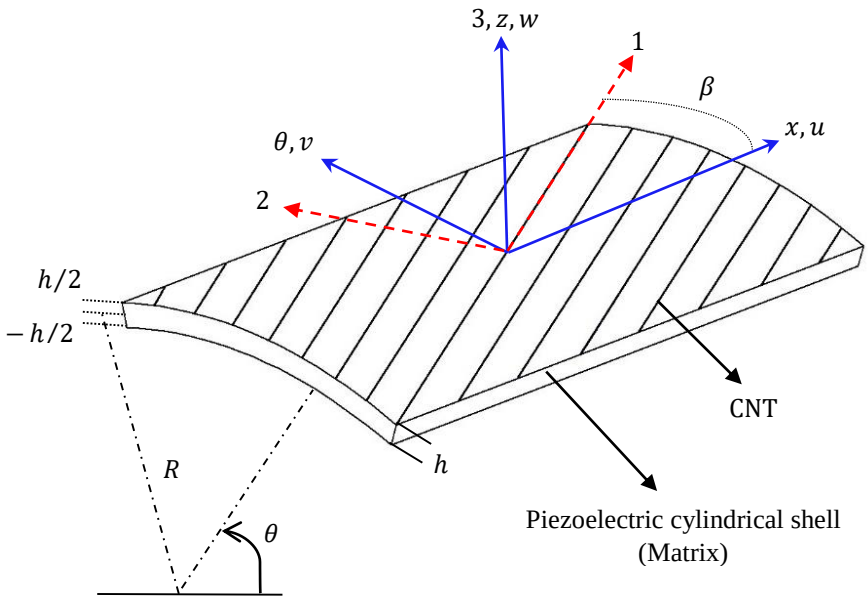

Figure 2.6. Configuration of a piezoelectric composite cylindrical shell reinforced with angled, straight CNTs.

We consider a piezoelectric composite cylindrical shell reinforced with straight CNTs which have angle β with the x-axis (see Fig. 2.6). The matrix is considered to be elastic and isotropic with Young's modulus E_m and Poisson's ratio v_m. Each straight CNT is modeled as a long fiber with transversely isotropic elastic properties. The resulting composite shell is also transversely isotropic with $2-3$ plane of isotropy and its constitutive relations in the principle coordinate system (1,2,3), $\boldsymbol{\sigma} = \boldsymbol{C}:\boldsymbol{\varepsilon}$, based on the Mori-Tanaka micromechanics model are given by Ref. [107] as,

$$\begin{Bmatrix}\sigma_{11}\\ \sigma_{22}\\ \sigma_{33}\\ \tau_{23}\\ \tau_{13}\\ \tau_{12}\end{Bmatrix} = \begin{bmatrix} n & l & l & 0 & 0 & 0\\ l & k+m & k-m & 0 & 0 & 0\\ l & k-m & k+m & 0 & 0 & 0\\ 0 & 0 & 0 & m & 0 & 0\\ 0 & 0 & 0 & 0 & p & 0\\ 0 & 0 & 0 & 0 & 0 & p \end{bmatrix} \begin{Bmatrix}\varepsilon_{11}\\ \varepsilon_{22}\\ \varepsilon_{33}\\ \gamma_{23}\\ \gamma_{13}\\ \gamma_{12}\end{Bmatrix} \tag{2.66}$$

where k, l, m, n, and p are the Hill's elastic moduli [200]; k is the plane strain bulk modulus normal to the fiber direction, n is the uniaxial tension modulus in the fiber direction, l is the

associated cross modulus, m and p are the shear moduli in planes normal and parallel to the fiber direction, respectively. The Hill's elastic moduli are defined as [200],

$$k = \frac{E_m\{E_m f_m + 2k_r(1+v_m)[1+f_r(1-2v_m)]\}}{2(1+v_m)[E_m(1+f_r-2v_m)+2f_m k_r(1-v_m-2v_m^2)]} \tag{2.67a}$$

$$l = \frac{E_m\{f_m v_m[E_m+2k_r(1+v_m)]+2f_r l_r(1-v_m^2)\}}{(1+v_m)[E_m(1+f_r-2v_m)+2f_m k_r(1-v_m-2v_m^2)]} \tag{2.67b}$$

$$n = \frac{E_m^2 f_m(1+f_r-f_m v_m)+2f_m f_r(k_r n_r - l_r^2)(1+v_m)^2(1-2v_m)}{(1+v_m)[E_m(1+f_r-2v_m)+2f_m k_r(1-v_m-2v_m^2)]} + \frac{E_m[2f_m^2 k_r(1-v_m)+f_r n_r(1+f_r-2v_m)-4f_m l_r v_m]}{E_m(1+f_r-2v_m)+2f_m k_r(1-v_m-2v_m^2)} \tag{2.67c}$$

$$p = \frac{E_m[E_m f_m + 2p_r(1+v_m)(1+f_r)]}{2(1+v_m)[E_m(1+f_r)+2f_m p_r(1+v_m)]} \tag{2.67d}$$

$$m = \frac{E_m[E_m f_m + 2m_r(1+v_m)(3+f_r-4v_m)]}{2(1+v_m)\{E_m[f_m+4f_r(1-v_m)]+2f_m m_r(3-v_m-4v_m^2)\}} \tag{2.67e}$$

where f_m and f_r stand for the volume fraction for the matrix and the reinforcement phases, respectively; k_r, l_r, m_r, n_r, and p_r are the Hill's elastic moduli for the reinforcement phase (SWCNTs) obtained from the analytical solutions [201], in which the elastic moduli of CNTs are computed. Subscripts m and r stand for the quantities corresponding to the matrix and the reinforcement phase, respectively. For CNT-reinforced composites, the SWCNT (10, 10) is used as the reinforcement phase where its properties are listed in Table 2.3.

Table 2.3. Material properties for the SWCNT (10, 10) [202,16].

Temperature (K)	E_{11}(TPa)	E_{22}(TPa)	G_{12}(TPa)	$\Gamma_{11}(10^{-6}/\mathrm{K})$	$\Gamma_{22}\ (10^{-6}/\mathrm{K})$
300	5.6466	7.0800	1.9445	3.4584	5.1682
500	5.5308	6.9348	1.9643	4.5361	5.0189
700	5.4744	6.8641	1.9644	4.6677	4.8943
Mass density ($\mathrm{kg/m^3}$), $\rho = 1400$; Poisson's ratio, $v_{12} = 0.175$					
Hill elastic moduli (GPa): $k_r = 271$, $l_r = 88$, $m_r = 17$, $n_r = 1089$, $p_r = 442$					

Therefore, the components of stiffness matrix in the principle coordinate system $(1,2,3)$, C_{ij} $(i,j = 1,2,\dots,6)$, for a piezoelectric composite cylindrical shell reinforced with angled, straight CNTs are obtained from Eq. (2.66) as,

$$C_{11} = n \quad C_{22} = C_{33} = k + m, \quad C_{12} = C_{13} = l, \quad C_{23} = k - m, \quad C_{44} = m, \qquad C_{55} = C_{66} = p \tag{2.68}$$

where $C_{ij} = C_{ji}$. The stiffness matrix in the cylindrical coordinate system (x,θ,z) for a composite reinforced with angled CNTs is obtained as,

$$[C]_{(x,\theta,z)} = \left[T_{ij}^{-1}\right][C]_{(1,2,3)}[T_{ij}] \tag{2.69}$$

where the transformation matrix $[T_{ij}]$ and its inverse $[T_{ij}^{-1}]$, and components of the stiffness matrix $[C]_{(x,\theta,z)}$ are given in Appendix J.

According to the first-order shear deformation shell theory, the transverse shear effects are included $(\tau_{xz} \neq \tau_{\theta z} \neq 0)$, and only the normal stress in the shell thickness direction (σ_{zz}) is assumed to be negligibly small. Thus, from Eq. (2.64a) by assuming $\sigma_{zz} = 0$, one obtains,

$$\varepsilon_{zz} = \frac{e_{23}}{C_{zz}} E_{xx} - \frac{C_{\theta z}}{C_{zz}} \varepsilon_{\theta\theta} - \frac{C_{xz}}{C_{zz}} \varepsilon_{xx} - \frac{C_{zs}}{C_{zz}} \gamma_{x\theta} \tag{2.70}$$

Substituting Eq. (2.70) into the stress-strain relations, Eq. (2.64a), and the electric displacement relation, Eq. (2.64b), yields,

$$\begin{Bmatrix} \sigma_{\theta\theta} \\ \sigma_{xx} \\ \tau_{xz} \\ \tau_{\theta z} \\ \tau_{x\theta} \end{Bmatrix} = \begin{bmatrix} \bar{C}_{\theta\theta} & \bar{C}_{\theta x} & 0 & 0 & \bar{C}_{\theta s} \\ \bar{C}_{\theta x} & \bar{C}_{xx} & 0 & 0 & \bar{C}_{xs} \\ 0 & 0 & \bar{C}_{rr} & \bar{C}_{rq} & 0 \\ 0 & 0 & \bar{C}_{rq} & \bar{C}_{qq} & 0 \\ \bar{C}_{\theta s} & \bar{C}_{xs} & 0 & 0 & \bar{C}_{ss} \end{bmatrix} \begin{Bmatrix} \varepsilon_{\theta\theta} \\ \varepsilon_{xx} \\ \gamma_{xz} \\ \gamma_{\theta z} \\ \gamma_{x\theta} \end{Bmatrix} - \begin{bmatrix} 0 & \bar{e}_{21} & 0 \\ 0 & \bar{e}_{22} & 0 \\ 0 & 0 & \bar{e}_{34} \\ 0 & 0 & 0 \\ \bar{e}_{16} & \bar{e}_{23} & 0 \end{bmatrix} \begin{Bmatrix} E_{\theta\theta} \\ E_{xx} \\ E_{zz} \end{Bmatrix} \tag{2.71a}$$

$$\begin{Bmatrix} D_{\theta\theta} \\ D_{xx} \\ D_{zz} \end{Bmatrix} = \begin{bmatrix} 0 & 0 & 0 & \bar{e}_{16} \\ \bar{e}_{21} & \bar{e}_{22} & 0 & \bar{e}_{23} \\ 0 & 0 & \bar{e}_{34} & 0 \end{bmatrix} \begin{Bmatrix} \varepsilon_{\theta\theta} \\ \varepsilon_{xx} \\ \gamma_{xz} \\ \gamma_{x\theta} \end{Bmatrix} + \begin{bmatrix} \bar{\in}_{11} & 0 & 0 \\ 0 & \bar{\in}_{22} & 0 \\ 0 & 0 & \bar{\in}_{33} \end{bmatrix} \begin{Bmatrix} E_{\theta\theta} \\ E_{xx} \\ E_{zz} \end{Bmatrix} \tag{2.71b}$$

where $\bar{C}_{\theta\theta}$, $\bar{C}_{\theta x}$, $\bar{C}_{\theta s}$, $\bar{C}_{xx}$, $\bar{C}_{xs}$, $\bar{C}_{rr}$, $\bar{C}_{rq}$, $\bar{C}_{qq}$, $\bar{C}_{ss}$, $\bar{e}_{16}$, $\bar{e}_{21}$, $\bar{e}_{22}$, $\bar{e}_{23}$, $\bar{e}_{34}$, and $\bar{\in}_{11}$, $\bar{\in}_{22}$, $\bar{\in}_{33}$ for a piezoelectric cylindrical composite shell reinforced with angled, straight CNTs are given in

Appendix K. Therefore, Eq. (2.71) leads to derivation of constitutive equations for piezocomposite cylindrical shells reinforced with angled, straight CNTs considering the effects of transverse shear.

2.4.3. Constitutive Equations for a Piezoelectric Composite Cylindrical Shell Reinforced with Randomly Oriented, Straight CNTs

Constitutive equations are derived in this section for a linear elastic piezocomposite reinforced by a large number of dispersed CNTs which are randomly oriented and straight. Layout of an infinitely long unbounded piezoelectric composite cylindrical shell reinforced with randomly oriented, straight CNTs is shown in Fig. 2.7. The orientation of a straight CNT is determined by two Euler angles α and β, as shown in Fig. 2.7.

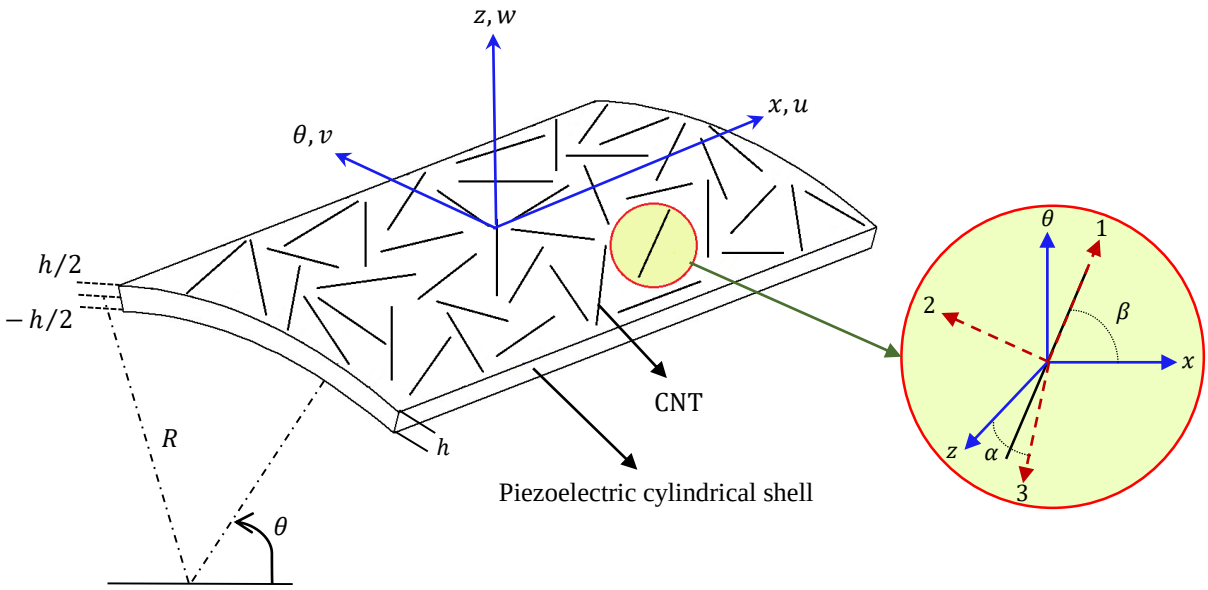

Figure 2.7. Configuration of a piezoelectric composite cylindrical shell reinforced with randomly oriented, straight CNTs.

When CNTs are completely randomly oriented in the matrix, the composite is then isotropic and its bulk modulus K and shear modulus G are derived as [107],

$$K = K_m + \frac{f_r(\delta_r - 3K_m\alpha_r)}{3(f_m + f_r\alpha_r)} \tag{2.72a}$$

$$G = G_m + \frac{f_r(\eta_r - 2G_m\beta_r)}{2(f_m + f_r\beta_r)} \tag{2.72b}$$

where

$$K_m = \frac{E_m}{3(1 - 2v_m)} \tag{2.73a}$$

$$G_m = \frac{E_m}{2(1 + v_m)} \tag{2.73b}$$

$$\alpha_r = \frac{3(K_m + G_m) + k_r - l_r}{3(G_m + k_r)} \tag{2.73c}$$

$$\beta_r = \frac{1}{5}\left\{\frac{4G_m + 2k_r + l_r}{3(G_m + k_r)} + \frac{4G_m}{G_m + p_r} + \frac{2[G_m(3K_m + G_m) + G_m(3K_m + 7G_m)]}{G_m(3K_m + G_m) + m_r(3K_m + 7G_m)}\right\} \tag{2.73d}$$

$$\delta_r = \frac{1}{3}\left[n_r + 2l_r + \frac{(2k_r + l_r)(3K_m + 2G_m - l_r)}{G_m + k_r}\right] \tag{2.73e}$$

$$\eta_r = \frac{1}{5}\left[\frac{2}{3}(n_r - l_r) + \frac{8G_m p_r}{G_m + p_r} + \frac{8m_r G_m(3K_m + 4G_m)}{3K_m(m_r + G_m) + G_m(7m_r + G_m)} + \frac{2(k_r - l_r)(2G_m + l_r)}{3(G_m + k_r)}\right] \tag{2.73f}$$

where E_m, K_m, G_m, and v_m are Young's modulus, bulk modulus, shear modulus, and Poisson's ratio of the isotropic matrix, respectively. The effective Young's modulus E, Poisson's ratio v, and shear modulus G of the resulting composite are given by,

$$E = \frac{9KG}{3K + G} \tag{2.74a}$$

$$v = \frac{3K - 2G}{6K + 2G} \tag{2.74b}$$

$$G = \frac{E}{2(1 + v)} \tag{2.74c}$$

Therefore, the stress-strain relations in the cylindrical coordinate system (x, θ, z) for the resulting isotropic composite cylindrical shell, which is only function of the effective Young's modulus E and Poisson's ratio v, will be,

$$\begin{Bmatrix} \sigma_{\theta\theta} \\ \sigma_{xx} \\ \sigma_{zz} \\ \tau_{xz} \\ \tau_{\theta z} \\ \tau_{x\theta} \end{Bmatrix} = \begin{bmatrix} C_{\theta\theta} & C_{\theta x} & C_{\theta z} & 0 & 0 & 0 \\ C_{\theta x} & C_{xx} & C_{xz} & 0 & 0 & 0 \\ C_{\theta z} & C_{xz} & C_{zz} & 0 & 0 & 0 \\ 0 & 0 & 0 & C_{rr} & 0 & 0 \\ 0 & 0 & 0 & 0 & C_{qq} & 0 \\ 0 & 0 & 0 & 0 & 0 & C_{ss} \end{bmatrix} \begin{Bmatrix} \varepsilon_{\theta\theta} \\ \varepsilon_{xx} \\ \varepsilon_{zz} \\ \gamma_{xz} \\ \gamma_{\theta z} \\ \gamma_{x\theta} \end{Bmatrix} \tag{2.75}$$

where the components of stiffness matrix in the cylindrical coordinate system (x, θ, z) for a composite reinforced with randomly oriented CNTs are obtained as,

$$C_{\theta\theta} = C_{xx} = C_{zz} = \frac{E(1-v)}{(1-2v)(1+v)} \tag{2.76a}$$

$$C_{\theta x} = C_{\theta z} = C_{xz} = \frac{Ev}{(1-2v)(1+v)} \tag{2.76b}$$

$$C_{rr} = C_{qq} = C_{ss} = G = \frac{E}{2(1+v)} \tag{2.76c}$$

Thus, the general stress-strain relations for a piezoelectric composite cylindrical shell reinforced with completely randomly oriented, straight CNTs with the axial polarization in the cylindrical coordinate system (x, θ, z) are given by,

$$\begin{Bmatrix} \sigma_{\theta\theta} \\ \sigma_{xx} \\ \sigma_{zz} \\ \tau_{xz} \\ \tau_{\theta z} \\ \tau_{x\theta} \end{Bmatrix} = \begin{bmatrix} C_{\theta\theta} & C_{\theta x} & C_{\theta z} & 0 & 0 & 0 \\ C_{\theta x} & C_{xx} & C_{xz} & 0 & 0 & 0 \\ C_{\theta z} & C_{xz} & C_{zz} & 0 & 0 & 0 \\ 0 & 0 & 0 & C_{rr} & 0 & 0 \\ 0 & 0 & 0 & 0 & C_{qq} & 0 \\ 0 & 0 & 0 & 0 & 0 & C_{ss} \end{bmatrix} \begin{Bmatrix} \varepsilon_{\theta\theta} \\ \varepsilon_{xx} \\ \varepsilon_{zz} \\ \gamma_{xz} \\ \gamma_{\theta z} \\ \gamma_{x\theta} \end{Bmatrix} - \begin{bmatrix} 0 & e_{21} & 0 \\ 0 & e_{22} & 0 \\ 0 & e_{23} & 0 \\ 0 & 0 & e_{34} \\ 0 & 0 & 0 \\ e_{16} & 0 & 0 \end{bmatrix} \begin{Bmatrix} E_{\theta\theta} \\ E_{xx} \\ E_{zz} \end{Bmatrix} \tag{2.77}$$

where $C_{ij}(i, j = x, \theta, z, r, q, s)$ are given by Eq. (2.76), which are only function of Young's modulus E and Poisson's ratio v of the resulting isotropic composite given by Eq. (2.74).

Based on the first-order shear deformation shell theory, considering the transverse shear stresses (τ_{xz} and $\tau_{\theta z}$) and assuming negligible normal stress in the shell thickness direction ($\sigma_{zz} = 0$) in Eq. (2.77) yields,

$$\varepsilon_{zz} = \frac{e_{23}}{C_{zz}} E_{xx} - \frac{C_{\theta z}}{C_{zz}} \varepsilon_{\theta\theta} - \frac{C_{xz}}{C_{zz}} \varepsilon_{xx} \tag{2.78}$$

Substituting Eq. (2.78), into the stress-strain relations, Eq. (2.77), and the electric displacement relations, Eq. (2.64b), yields,

$$\begin{Bmatrix} \sigma_{\theta\theta} \\ \sigma_{xx} \\ \tau_{xz} \\ \tau_{\theta z} \\ \tau_{x\theta} \end{Bmatrix} = \begin{bmatrix} \bar{C}_{\theta\theta} & \bar{C}_{\theta x} & 0 & 0 & 0 \\ \bar{C}_{\theta x} & \bar{C}_{xx} & 0 & 0 & 0 \\ 0 & 0 & \bar{C}_{rr} & 0 & 0 \\ 0 & 0 & 0 & \bar{C}_{qq} & 0 \\ 0 & 0 & 0 & 0 & \bar{C}_{ss} \end{bmatrix} \begin{Bmatrix} \varepsilon_{\theta\theta} \\ \varepsilon_{xx} \\ \gamma_{xz} \\ \gamma_{\theta z} \\ \gamma_{x\theta} \end{Bmatrix} - \begin{bmatrix} 0 & \bar{e}_{21} & 0 \\ 0 & \bar{e}_{22} & 0 \\ 0 & 0 & \bar{e}_{34} \\ 0 & 0 & 0 \\ \bar{e}_{16} & 0 & 0 \end{bmatrix} \begin{Bmatrix} E_{\theta\theta} \\ E_{xx} \\ E_{zz} \end{Bmatrix} \tag{2.79a}$$

$$\begin{Bmatrix} D_{\theta\theta} \\ D_{xx} \\ D_{zz} \end{Bmatrix} = \begin{bmatrix} 0 & 0 & 0 & \bar{e}_{16} \\ \bar{e}_{21} & \bar{e}_{22} & 0 & 0 \\ 0 & 0 & \bar{e}_{34} & 0 \end{bmatrix} \begin{Bmatrix} \varepsilon_{\theta\theta} \\ \varepsilon_{xx} \\ \gamma_{xz} \\ \gamma_{x\theta} \end{Bmatrix} + \begin{bmatrix} \bar{\in}_{11} & 0 & 0 \\ 0 & \bar{\in}_{22} & 0 \\ 0 & 0 & \bar{\in}_{33} \end{bmatrix} \begin{Bmatrix} E_{\theta\theta} \\ E_{xx} \\ E_{zz} \end{Bmatrix} \tag{2.79b}$$

where $\bar{C}_{\theta\theta}$, $\bar{C}_{\theta x}$, $\bar{C}_{xx}$, $\bar{C}_{rr}$, $\bar{C}_{qq}$, $\bar{C}_{ss}$, $\bar{e}_{16}$, $\bar{e}_{21}$, $\bar{e}_{22}$, $\bar{e}_{34}$, and $\bar{\in}_{11}$, $\bar{\in}_{22}$, $\bar{\in}_{33}$ for a piezoelectric cylindrical composite shell reinforced with randomly oriented, straight CNTs are given in Appendix K. Eq. (2.79) provides a derivation of constitutive equations for piezocomposite cylindrical shells reinforced with randomly oriented CNTs in which the transverse shear is included as well.

2.4.4. Constitutive Equations for a Piezoelectric Composite Cylindrical Shell Reinforced with Agglomerated CNTs

In this section the constitutive equations in the cylindrical coordinate system (x, θ, z) are derived for a piezocomposite cylindrical shell reinforced with agglomerated CNTs. To obtain the desired properties for a CNT-reinforced composite, CNTs must be dispersed uniformly in the matrix [107]. However, relative low bending stiffness of CNTs (because of their small diameter and low elastic modulus in the radial direction) and their high aspect ratio lead to their agglomeration in a polymer matrix [203,204]. Therefore, CNT agglomeration prevents to achieve the desired properties for a CNT-reinforced composite where its effect on dynamic responses of

composite materials reinforced with CNTs should be considered and studied if the agglomeration happens at certain location of composite structures.

The influence of a CNT agglomeration on the mechanical properties of CNT-reinforced composites is explained herein based on a two-parameter micromechanics model developed in Ref. [107]. The spatial distribution of CNTs in the matrix is non-uniform leading to higher concentration of CNTs at some local regions than the average volume fraction in the material. It is assumed that the regions with concentrated CNTs have spherical shapes and are considered as "inclusions" with different elastic properties from the surrounding material. The total volume V_r of CNTs in the Representative Volume Element (RVE) is given by,

$$V_r = V_r^{in} + V_r^m \tag{2.80}$$

where V_r^{in} and V_r^m represent the volumes of CNTs dispersed in the inclusions (concentrated regions) and in the matrix, respectively.

Agglomeration is described by two parameters μ and η as [107],

$$\mu = \frac{V_{in}}{V} \qquad \eta = \frac{V_r^{in}}{V_r} \tag{2.81}$$

where V_{in} is the volume of sphere inclusions in the RVE, V stands for the total volume of the RVE, parameter μ denotes the volume fraction of inclusions with respect to the volume V of the RVE, and parameter η represents the volume ratio of nanotubes that are dispersed in the inclusions and the total volume of nanotubes in the RVE. According to Eq. (2.81), when $\mu = 1$, CNTs are uniformly dispersed in the matrix and decrease in μ leads to the increase of agglomeration degree. The case $\eta = 1$ indicates that all CNTs are dispersed in the inclusions. When $\mu = \eta$, all CNTs are dispersed uniformly in the matrix and the volume fractions of CNTs inside and outside the inclusions are exactly the same. Therefore, as shown in Fig. 2.8, based on the spatial distribution of CNTs, three cases occur as following: (a) uniformly dispersion of CNTs in the matrix with $\mu =$

η, (b) partial agglomeration of CNTs in the matrix with $\mu \leq \eta$, and (c) complete CNT agglomeration with $\eta = 1$ and $\mu \leq \eta$.

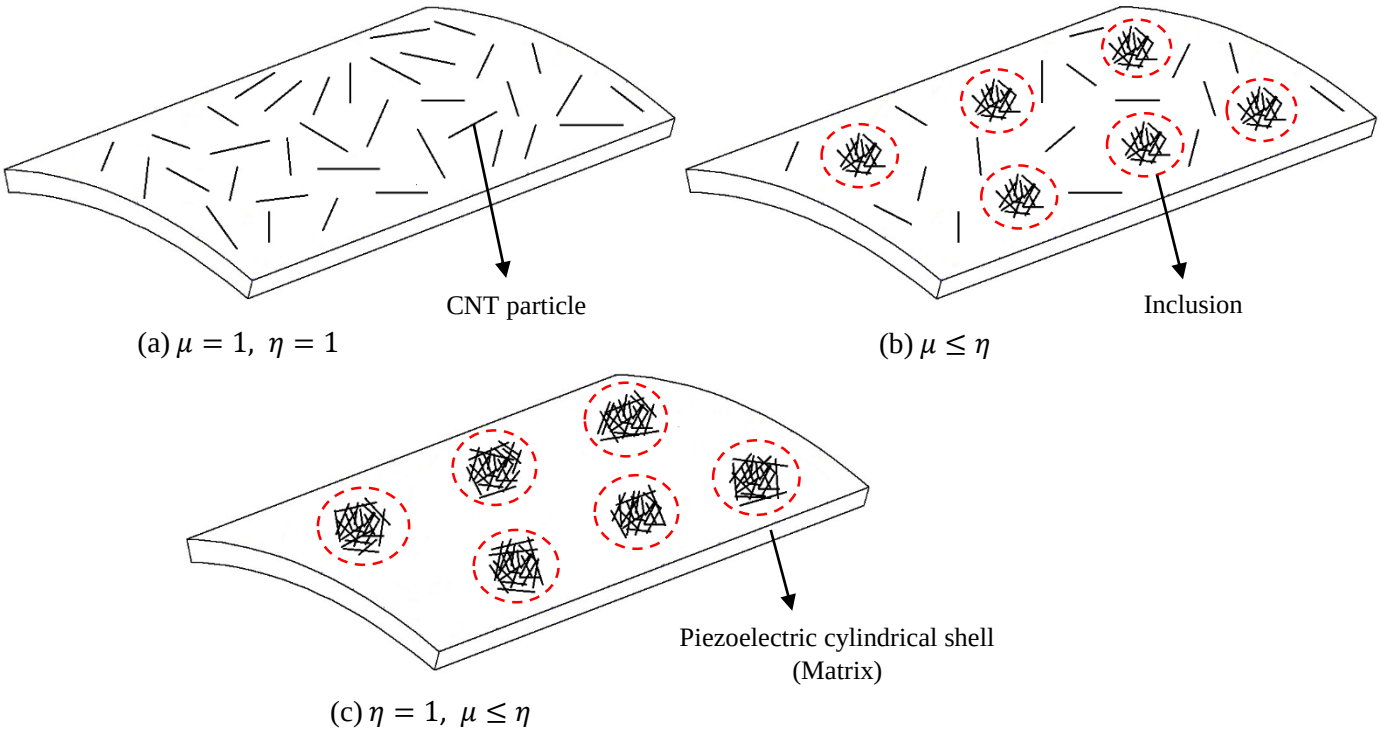

Figure 2.8. Explanation of CNT agglomeration: (a) uniformly dispersion of CNTs in a piezo-shell element with $\mu = \eta = 1$; (b) example of partial agglomeration of CNTs with $\mu \leq \eta$; and (c) example of complete CNT agglomeration with $\eta = 1$ and $\mu \leq \eta$.

The effective bulk modulus K_{in} and shear modulus G_{in} of the inclusion, and the effective bulk modulus K_{out} and shear modulus G_{out} of the equivalent matrix outside the inclusion are given by [107],

$$K_{in} = K_m + \frac{f_r \eta (\delta_r - 3K_m \alpha_r)}{3(\mu - f_r \eta + f_r \eta \alpha_r)} \tag{2.82a}$$

$$K_{out} = K_m + \frac{f_r (1-\eta)(\delta_r - 3K_m \alpha_r)}{3[1 - \mu - f_r (1-\eta) + f_r (1-\eta)\alpha_r]} \tag{2.82b}$$

$$G_{in} = G_m + \frac{f_r \eta (\eta_r - 2G_m \beta_r)}{2(\mu - f_r \eta + f_r \eta \beta_r)} \tag{2.82c}$$

$$G_{out} = G_m + \frac{f_r(1-\eta)(\eta_r - 2G_m\beta_r)}{2[1-\mu-f_r(1-\eta)+f_r(1-\eta)\beta_r]} \tag{2.82d}$$

The effective bulk modulus K and the effective shear modulus G of the resulting composite are derived from the Mori-Tanaka micromechanics model as [107],

$$K = K_{out}\left[1 + \frac{\mu\left(\frac{K_{in}}{K_{out}} - 1\right)}{1 + \alpha_c(1-\mu)\left(\frac{K_{in}}{K_{out}} - 1\right)}\right] \tag{2.83a}$$

$$G = G_{out}\left[1 + \frac{\mu\left(\frac{G_{in}}{G_{out}} - 1\right)}{1 + \beta_c(1-\mu)\left(\frac{G_{in}}{G_{out}} - 1\right)}\right] \tag{2.83b}$$

where

$$\alpha_c = \frac{1+v_{out}}{3(1-v_{out})} \tag{2.84a}$$

$$\beta_c = \frac{8-10v_{out}}{15(1-v_{out})} \tag{2.84b}$$

where v_{out} is given by,

$$v_{out} = \frac{3K_{out}-2G_{out}}{2(3K_{out}+G_{out})} \tag{2.85}$$

Finally, the effective Young's modulus E and Poisson's ratio v of the resulting composite with the effects of CNT agglomeration are defined by substituting Eq. (2.83) in to Eq. (2.74). Other procedures to derive the constitutive equations for a CNT-reinforced piezocomposite cylindrical shell affected by CNT agglomeration are the same as those for a piezocomposite cylindrical shell reinforced with randomly oriented CNTs as shown in Eqs. (2.75) – (2.79).

2.4.5. Force and Moment Resultants for Piezoelectric Composite Cylindrical Shells Reinforced with Angled and Randomly Oriented (or Agglomerated) CNTs

The in-plane force resultants ($N_{xx}, N_{\theta\theta}, N_{x\theta}$), the bending and twisting moment resultants ($M_{xx}, M_{\theta\theta}, M_{x\theta}$), and the transverse shear force resultants ($V_{xz}, V_{\theta z}$) for a piezoelectric composite cylindrical shell reinforced with angled, straight CNTs are obtained by substituting the corresponding stresses, Eq. (2.71a), into Eq. (2.65) and integrating across the thickness of the piezoelectric composite shell as follows,

$$N_{xx} = A_1\frac{\partial u_0}{\partial x} + A_2\left(\frac{\partial u_0}{R\partial\theta} + \frac{\partial v_0}{\partial x}\right) + \frac{A_3}{R}\left(w_0 + \frac{\partial v_0}{\partial\theta}\right) + A_4\frac{\partial\varphi}{\partial x} \tag{2.86a}$$

$$N_{\theta\theta} = B_1\frac{\partial u_0}{\partial x} + B_2\left(\frac{\partial u_0}{R\partial\theta} + \frac{\partial v_0}{\partial x}\right) + \frac{B_3}{R}\left(w_0 + \frac{\partial v_0}{\partial\theta}\right) + B_4\frac{\partial\varphi}{\partial x} \tag{2.86b}$$

$$N_{x\theta} = C_1\frac{\partial u_0}{\partial x} + C_2\left(\frac{\partial u_0}{R\partial\theta} + \frac{\partial v_0}{\partial x}\right) + \frac{C_3}{R}\left(w_0 + \frac{\partial v_0}{\partial\theta}\right) + C_4\frac{\partial\varphi}{\partial x} + C_5\frac{\partial\varphi}{R\partial\theta} \tag{2.86c}$$

$$M_{xx} = D_1\frac{\partial\alpha_x}{\partial x} + D_2\frac{\partial\alpha_\theta}{R\partial\theta} + D_3\left(\frac{\partial\alpha_\theta}{\partial x} + \frac{\partial\alpha_x}{R\partial\theta}\right) \tag{2.86d}$$

$$M_{\theta\theta} = E_1\frac{\partial\alpha_x}{\partial x} + E_2\frac{\partial\alpha_\theta}{R\partial\theta} + E_3\left(\frac{\partial\alpha_\theta}{\partial x} + \frac{\partial\alpha_x}{R\partial\theta}\right) \tag{2.86e}$$

$$M_{x\theta} = F_1\frac{\partial\alpha_x}{\partial x} + F_2\frac{\partial\alpha_\theta}{R\partial\theta} + F_3\left(\frac{\partial\alpha_\theta}{\partial x} + \frac{\partial\alpha_x}{R\partial\theta}\right) \tag{2.86f}$$

$$V_{xz} = G_1\left(\frac{\partial w_0}{\partial x} + \alpha_x\right) + G_2\left(\frac{\partial w_0}{R\partial\theta} - \frac{v_0}{R} + \alpha_\theta\right) \tag{2.86g}$$

$$V_{\theta z} = H_1\left(\frac{\partial w_0}{\partial x} + \alpha_x\right) + H_2\left(\frac{\partial w_0}{R\partial\theta} - \frac{v_0}{R} + \alpha_\theta\right) \tag{2.86h}$$

where expression of coefficients A_i $(i = 1,\dots,4)$, B_i $(i = 1,\dots,4)$, C_i $(i = 1,\dots,5)$, D_i $(i = 1,2,3)$, E_i $(i = 1,2,3)$, F_i $(i = 1,2,3)$, G_i $(i = 1,2)$, and H_i $(i = 1,2)$ are given in Appendix L.

The force and moment resultants for a piezoelectric composite cylindrical shell reinforced with randomly oriented (or agglomerated) straight CNTs are obtained by substituting the corresponding

stresses, Eq. (2.79a), into Eq. (2.65) and integrating across the thickness of the piezoelectric composite shell as follows,

$$N_{xx} = \acute{A}_1 \frac{\partial u_0}{\partial x} + \frac{\acute{A}_2}{R}\left(w_0 + \frac{\partial v_0}{\partial \theta}\right) + \acute{A}_3 \frac{\partial \varphi}{\partial x} \tag{2.87a}$$

$$N_{\theta\theta} = \acute{B}_1 \frac{\partial u_0}{\partial x} + \frac{\acute{B}_2}{R}\left(w_0 + \frac{\partial v_0}{\partial \theta}\right) + \acute{B}_3 \frac{\partial \varphi}{\partial x} \tag{2.87b}$$

$$N_{x\theta} = \acute{C}_1 \left(\frac{\partial u_0}{R\partial \theta} + \frac{\partial v_0}{\partial x}\right) + \acute{C}_2 \frac{\partial \varphi}{R\partial \theta} \tag{2.87c}$$

$$M_{xx} = \acute{D}_1 \frac{\partial \alpha_x}{\partial x} + \acute{D}_2 \frac{\partial \alpha_\theta}{R\partial \theta} \tag{2.87d}$$

$$M_{\theta\theta} = \acute{E}_1 \frac{\partial \alpha_x}{\partial x} + \acute{E}_2 \frac{\partial \alpha_\theta}{R\partial \theta} \tag{2.87e}$$

$$M_{x\theta} = \acute{F}_1 \left(\frac{\partial \alpha_\theta}{\partial x} + \frac{\partial \alpha_x}{R\partial \theta}\right) \tag{2.87f}$$

$$V_{xz} = \acute{G}_1 \left(\frac{\partial w_0}{\partial x} + \alpha_x\right) \tag{2.87g}$$

$$V_{\theta z} = \acute{H}_1 \left(\frac{\partial w_0}{R\partial \theta} - \frac{v_0}{R} + \alpha_\theta\right) \tag{2.87h}$$

where expression of coefficients $\acute{A}_i$ $(i = 1,2,3)$, $\acute{B}_i$ $(i = 1,2,3)$, $\acute{C}_i (i = 1,2)$, $\acute{D}_i (i = 1,2)$, $\acute{E}_i (i = 1,2)$, $\acute{F}_i$ $(i = 1)$, $\acute{G}_i$ $(i = 1)$, and $\acute{H}_i (i = 1)$ are given in Appendix L.

2.4.6. Equations of Motion for Piezoelectric Composite Cylindrical Shells Reinforced with Angled and Randomly Oriented (or Agglomerated) CNTs

The derivation of equations of motion based on the first-order shear deformation shell theory has been explained in details in section 2.3.2.1 and are given by Eq. (2.41). The mass inertias I_i $(i = 0,1,2)$ required for the motion equations for a piezoelectric cylindrical shell with thickness h are given by,

$$I_i = \int_{-\frac{h}{2}}^{\frac{h}{2}} \rho z^i \, dz \qquad (i = 0,1,2) \tag{2.88}$$

where ρ is the mass density of a piezoelectric composite cylindrical shell reinforced with CNTs, which is given by,

$$\rho = \rho_m f_m + \rho_r f_r \tag{2.89}$$

where ρ_m and ρ_r are the mass densities of the matrix phase, PZT-4, and the reinforcement phase, CNT, respectively.

Substituting the force and moment resultants for a piezoelectric composite cylindrical shell reinforced with angled and randomly oriented (or agglomerated) straight CNTs, Eqs. (2.86) and (2.87), into Eq. (2.41) yields the equations of motion, respectively, for angled and randomly (or agglomerated) distributions of CNTs in a piezoelectric composite cylindrical shell in terms of u_0, v_0, w_0, α_x, α_θ, and φ.

Replacing the strain-displacement relations based on the first-order shear deformation shell theory, Eq. (2.9), and the electric field intensities, Eq. (2.18), into the electric displacements for a piezoelectric composite cylindrical shell reinforced with angled and randomly oriented (or agglomerated) CNTs, Eqs. (2.71b) and Eq. (2.79b), and satisfying the Maxwell equation $\int_{-\frac{h}{2}}^{\frac{h}{2}} \nabla D dz = 0$, yields the following governing equations, respectively, for angled and randomly (or agglomerated) distributions of CNTs in a piezoelectric cylindrical shell,

$$\bar{e}_{22}\frac{\partial^2 u_0}{\partial x^2} + \bar{e}_{16}\left(\frac{\partial^2 u_0}{R^2\partial\theta^2} + \frac{\partial^2 v_0}{R\partial x\partial\theta}\right) + \bar{e}_{23}\left(\frac{\partial^2 u_0}{R\partial x\partial\theta} + \frac{\partial^2 v_0}{\partial x^2}\right) + \frac{\bar{e}_{21}}{R}\left(\frac{\partial w_0}{\partial x} + \frac{\partial^2 v_0}{\partial x\partial\theta}\right) - \bar{\epsilon}_{22}\frac{\partial^2\varphi}{\partial x^2}$$

$$- \bar{\epsilon}_{11}\frac{\partial^2\varphi}{R^2\partial\theta^2} = 0 \tag{2.90}$$

$$\bar{e}_{22}\frac{\partial^2 u_0}{\partial x^2} + \bar{e}_{16}\left(\frac{\partial^2 u_0}{R^2\partial\theta^2} + \frac{\partial^2 v_0}{R\partial x\partial\theta}\right) + \frac{\bar{e}_{21}}{R}\left(\frac{\partial w_0}{\partial x} + \frac{\partial^2 v_0}{\partial x\partial\theta}\right) - \bar{\epsilon}_{22}\frac{\partial^2\varphi}{\partial x^2} - \bar{\epsilon}_{11}\frac{\partial^2\varphi}{R^2\partial\theta^2} = 0 \tag{2.91}$$

Eq. (2.41), in view of Eq. (2.86), and Eq. (2.90), represent the equations of motion when angled CNTs are dispersed in a piezoelectric cylindrical shell, and Eq. (2.41), in view of Eq. (2.87), and Eq. (2.91) express the equations of motion in the case of randomly (or agglomerated) distribution of CNTs in a piezoelectric cylindrical shell.

2.4.7. Solution Method

The shell displacements (u_0, v_0, and w_0), the rotations of shell cross-section normal to x -axis and θ-axis or shear effects (α_x and α_θ), and the electric potential (φ) for wave propagation are given by Eq. (2.54). Substituting Eq. (2.54) into the equations of motion, obtained using the first-order shear deformation shell theory in the previous section for piezoelectric composite cylindrical shells reinforced with angled and randomly oriented (or agglomerated) CNTs, leads to a set of homogenous equations as obtained in Eq. (2.55). The components of characteristics matrix $\left[L_{ij}\right]_{6\times6}(i,j=1,\ldots,6)$ for piezoelectric composite cylindrical shells reinforced with angled and randomly oriented (agglomerated), straight CNTs are given in Appendix M. The wave phase velocities c for different wave modes are calculated based on the Bisection method presented in section 2.3.4.

The PZT-4 and the SWCNT (10, 10) are chosen as the matrix and the reinforcement phases, respectively, where their material properties are listed in Tables 2.2 and 2.3, respectively. The non-dimensional wave phase velocity ($\mathrm{v}=\frac{c}{c_t}$) is used for analysis of wave propagation characteristics as illustrated in section 2.3.4, where the piezoelectric shell thickness is only considered in Eq. (2.59), and the torsional wave phase velocity c_t is employed as,

$$c_t=\sqrt{\frac{G_m}{\rho_m}} \tag{2.92}$$

2.5. Wave Propagation Modeling in Smart Laminated CNT-Reinforced Composite Cylindrical Shells in Hygrothermal Environments

In this section, an analytical model is developed for wave propagation in smart laminated CNT-reinforced composite cylindrical shells considering the effects of hygrothermal environmental conditions. For this purpose, an infinitely long unbounded laminated CNT-reinforced composite cylindrical shell coated with the piezoelectric layers at the top and bottom surfaces is considered. Axial polarization is also assumed for the piezoelectric layers. First of all, we need to derive the hygrothermal strains when a temperature/moisture change occurs in the structure.

2.5.1. Coefficients of Thermal and Moisture Expansion of a Unidirectional Lamina

The hygrothermal behavior of a unidirectional lamina is fully determined in terms of two principal coefficients of thermal expansion (CTEs), Γ_{11} and Γ_{22}, and two principal coefficients of moisture expansion (CMEs), Υ_{11} and Υ_{22}. These coefficients can be related to the geometric and material properties of the constituents.

The expressions for the principle longitudinal coefficient of thermal expansion (CTE), Γ_{11}, and the principle transverse coefficient of thermal expansion (CTE), Γ_{22}, for a fiber-reinforced unidirectional composite with orthotropic reinforcement phase (fiber) and isotropic matrix phase are given by [6],

$$\Gamma_{11} = \frac{E_{11r}\Gamma_{11r}f_r + E_m\Gamma_m f_m}{E_{11}} \tag{2.93}$$

$$\Gamma_{22} = \Gamma_{22r}f_r\left[1 + v_{12r}\frac{\Gamma_{11r}}{\Gamma_{22r}}\right] + (1 + v_m)\Gamma_m f_m - v_{12}\Gamma_{11} \tag{2.94}$$

where

$$E_{11} = E_{11r} f_r + E_m f_m \tag{2.95}$$

$$v_{12} = v_{12r} f_r + v_m f_m \tag{2.96}$$

and f_r and f_m stand for the volume fraction for the reinforcement and the matrix phases, respectively, E_{11r} is the longitudinal modulus of the reinforcing phase (fiber), E_m is the elastic modulus of the matrix phase, E_{11} is the longitudinal composite modulus as obtained by the rule of mixture, v_{12r} and v_m are Poisson's ratio of the reinforcement and the matrix phases, respectively, v_{12} is the major Poisson's ratio of composite lamina as obtained by the rule of mixture, Γ_{11r} and Γ_{22r} are the longitudinal and the transverse CTE of the reinforcement phase, and Γ_m is the CTE of the matrix phase. The longitudinal modulus E_{11} and the major Poisson's ratio v_{12} for a polymer composite reinforced with CNTs based on the Mori-Tanaka micromechanics model are given in Eq. (2.111).

Micromechanical relations for the coefficient of moisture expansion are entirely analogous. However, based on the fact that in most cases the reinforcing fiber does not absorb moisture, its principle CMEs are zero ($\Upsilon_{11r} = \Upsilon_{22r} = 0$). The expressions for the principle longitudinal coefficient of moisture expansion (CME), Υ_{11}, and the principle transverse coefficient of moisture expansion (CME), Υ_{22}, for a fiber-reinforced unidirectional composite with orthotropic reinforcement phase (fiber) and isotropic matrix phase are given by [6],

$$\Upsilon_{11} = \Upsilon_m \frac{E_m f_m}{E_{11}} \tag{2.97}$$

$$\Upsilon_{22} = \Upsilon_m \frac{f_m}{E_{11}} [E_{11} + f_r (v_m E_{11r} - v_{12r} E_m)] \tag{2.98}$$

where Υ_m is the CME of the matrix phase.

Once the principal CTEs, $\Gamma_{11}$and Γ_{22}, and the principal CMEs, $\Upsilon_{11}$and Υ_{22} are known ($\Gamma_{12} = \Upsilon_{12} = 0$), the coefficients referred to any system of coordinates (x, θ) can be obtained by the following transformation relations as,

$$\begin{Bmatrix}\Gamma_{xx}\\ \Gamma_{\theta\theta}\\ \Gamma_{x\theta}\end{Bmatrix} = \begin{bmatrix} \acute{m}^2 & \acute{n}^2 & -2\acute{m}\acute{n} \\ \acute{n}^2 & \acute{m}^2 & 2\acute{m}\acute{n} \\ 2\acute{m}\acute{n} & -2\acute{m}\acute{n} & 2(\acute{m}^2 - \acute{n}^2)\end{bmatrix}\begin{Bmatrix}\Gamma_{11}\\ \Gamma_{22}\\ 0\end{Bmatrix} \tag{2.99}$$

$$\begin{Bmatrix}\Upsilon_{xx}\\ \Upsilon_{\theta\theta}\\ \Upsilon_{x\theta}\end{Bmatrix} = \begin{bmatrix} \acute{m}^2 & \acute{n}^2 & -2\acute{m}\acute{n} \\ \acute{n}^2 & \acute{m}^2 & 2\acute{m}\acute{n} \\ 2\acute{m}\acute{n} & -2\acute{m}\acute{n} & 2(\acute{m}^2 - \acute{n}^2)\end{bmatrix}\begin{Bmatrix}\Upsilon_{11}\\ \Upsilon_{22}\\ 0\end{Bmatrix} \tag{2.100}$$

where

$$\acute{m} = cos\beta, \qquad \acute{n} = sin\beta \tag{2.101}$$

and Γ_{xx}, $\Gamma_{\theta\theta}$, and $\Gamma_{x\theta}$ are the transformed lamina CTEs , and Υ_{xx}, $\Upsilon_{\theta\theta}$, and $\Upsilon_{x\theta}$ are the transformed lamina CMEs in the cylindrical coordinate system (x, θ).

2.5.2. Hygrothermal Strains in a Unidirectional Lamina

When a lamina is subjected to a uniform change in temperature, Θ, and change in moisture concentration, Λ, from its reference hygrothermal state, it undergoes a hygrothermal deformation. The hygrothermal strains referred to the principle material axes of the lamina (1,2) are given by [6],

$$e_{11}^{(1)} = \Gamma_{11}\Theta + \Upsilon_{11}\Lambda \tag{2.102a}$$

$$e_{22}^{(1)} = \Gamma_{22}\Theta + \Upsilon_{22}\Lambda \tag{2.102b}$$

$$e_{12}^{(1)} = 0 \tag{2.102c}$$

The transformed hygrothermal strains referred to the $x - \theta$ coordinate system are obtained as,

$$\begin{Bmatrix}e_{xx}^{(1)}\\ e_{\theta\theta}^{(1)}\\ e_{x\theta}^{(1)}\end{Bmatrix} = \begin{bmatrix} \acute{m}^2 & \acute{n}^2 & -2\acute{m}\acute{n} \\ \acute{n}^2 & \acute{m}^2 & 2\acute{m}\acute{n} \\ 2\acute{m}\acute{n} & -2\acute{m}\acute{n} & 2(\acute{m}^2 - \acute{n}^2)\end{bmatrix}\begin{Bmatrix}e_{11}^{(1)}\\ e_{22}^{(1)}\\ 0\end{Bmatrix} \tag{2.103}$$

Substituting $e_{11}^{(1)}$ and $e_{22}^{(1)}$ from Eq. (2.102) into Eq. (2.103) and in view of relations in Eqs. (2.99) and (2.100), we obtain,

$$\begin{Bmatrix} e_{xx}^{(1)} \\ e_{\theta\theta}^{(1)} \\ e_{x\theta}^{(1)} \end{Bmatrix} = \begin{Bmatrix} \Gamma_{xx} \\ \Gamma_{\theta\theta} \\ \Gamma_{x\theta} \end{Bmatrix} \Theta + \begin{Bmatrix} \Upsilon_{xx} \\ \Upsilon_{\theta\theta} \\ \Upsilon_{x\theta} \end{Bmatrix} \Lambda \tag{2.104}$$

2.5.3. Hygrothermoelastic Load-Deformation Relations

The hygrothermal effects are considered as the resultant forces due to the temperature/moisture change and by substituting these forces in the dynamic governing equations. When a multidirectional laminate is subjected to mechanical and hygrothermal loadings, a lamina (layer) K within the laminate is under a state of stress $[\sigma]_{x,\theta}^{K}$ and strain $[\varepsilon]_{x,\theta}^{K}$. The in-plane stress relations of lamina K within the laminate are given by [6],

$$\begin{Bmatrix} \sigma_{xx}^{(1)} \\ \sigma_{\theta\theta}^{(1)} \\ \tau_{x\theta}^{(1)} \end{Bmatrix}_K = \begin{bmatrix} Q_{xx} & Q_{x\theta} & Q_{xs} \\ Q_{\theta x} & Q_{\theta\theta} & Q_{\theta s} \\ Q_{sx} & Q_{s\theta} & Q_{ss} \end{bmatrix}_K \left[\begin{Bmatrix} \varepsilon_{xx}^{(1)} \\ \varepsilon_{\theta\theta}^{(1)} \\ \gamma_{x\theta}^{(1)} \end{Bmatrix} - \begin{Bmatrix} e_{xx}^{(1)} \\ e_{\theta\theta}^{(1)} \\ e_{x\theta}^{(1)} \end{Bmatrix} \right]_K \tag{2.105}$$

where $\left[Q_{ij}\right]_K$ $(i,j = x,\theta,s)$ is the transformed reduced stiffness matrix for each lamina (layer) in $x-\theta$ direction as a function of the principal stiffness matrix $\left[Q_{ij}\right]_K$ $(i,j = 1,2,6)$ of the lamina reinforced with fibers, where their components are given in Appendix A. As explained before, in the contracted notation used here, the subscript s in the above equations corresponds to shear stress and strain components referred to the $x-\theta$ system of coordinates. Substituting the mechanical strains, Eq. (2.7), and hygrothermal strains, Eq. (2.104) into Eq. (2.105) yields,

$$\begin{Bmatrix} \sigma_{xx}^{(1)} \\ \sigma_{\theta\theta}^{(1)} \\ \tau_{x\theta}^{(1)} \end{Bmatrix}_K = \begin{bmatrix} Q_{xx} & Q_{x\theta} & Q_{xs} \\ Q_{\theta x} & Q_{\theta\theta} & Q_{\theta s} \\ Q_{sx} & Q_{s\theta} & Q_{ss} \end{bmatrix}_K \left[\begin{Bmatrix} \varepsilon_{xx}^{0} \\ \varepsilon_{\theta\theta}^{0} \\ \gamma_{x\theta}^{0} \end{Bmatrix} + z \begin{Bmatrix} \mathrm{K}_{xx} \\ \mathrm{K}_{\theta\theta} \\ \mathrm{K}_{x\theta} \end{Bmatrix} - \begin{Bmatrix} \Gamma_{xx} \\ \Gamma_{\theta\theta} \\ \Gamma_{x\theta} \end{Bmatrix} \Theta - \begin{Bmatrix} \Upsilon_{xx} \\ \Upsilon_{\theta\theta} \\ \Upsilon_{x\theta} \end{Bmatrix} \Lambda \right]_K \tag{2.106}$$

or, in brief,

$$\left[\sigma^{(1)}\right]_{x,\theta}^{K} = [Q]_{x,\theta}^{K}[\varepsilon^{0}]_{x,\theta} + [Q]_{x,\theta}^{K}[\mathrm{K}]_{x,\theta} z - [Q]_{x,\theta}^{K}[\Gamma]_{x,\theta}^{K}\Theta - [Q]_{x,\theta}^{K}[\Upsilon]_{x,\theta}^{K}\Lambda \tag{2.107}$$

Eq. (2.106) is the in-plane stress-strain relations due to the mechanical and hygrothermal loadings for an individual lamina (layer) K whose midplane is at a distance z from the reference plane. The transverse shear stress-strain relations for an individual lamina K, which are decoupled from the in-plane stress and strain terms are given by [6],

$$\begin{Bmatrix}\tau_{\theta z}^{(1)}\\ \tau_{xz}^{(1)}\end{Bmatrix}_{K} = \begin{bmatrix}C_{qq} & C_{qr}\\ C_{rq} & C_{rr}\end{bmatrix}_{K}\begin{Bmatrix}\gamma_{\theta z}^{(1)}\\ \gamma_{xz}^{(1)}\end{Bmatrix}_{K} \tag{2.108}$$

where C_{qq}, C_{qr}, C_{rq}, and C_{rr} are given in Appendix A, and $\gamma_{\theta z}^{(1)}$ and $\gamma_{xz}^{(1)}$ are given by Eq. (2.9).

The in-plane force and moment resultants and the transverse shear (out-of-plane) force resultants of a laminated fiber-reinforced composite cylindrical shell are obtained by integrating the corresponding stresses across the shell thickness as shown in Eq. (2.14).

Substituting Eqs. (2.106) and (2.108) for the layer in-plane and out-of-plane (transverse shear) stresses, respectively, into Eq. (2.14) and taking integration across the shell thickness yields the in-plane force and moment resultants and the transverse shear (out-of-plane) force resultants as,

$$\begin{Bmatrix}N_{xx}^{(1)}\\ N_{\theta\theta}^{(1)}\\ N_{x\theta}^{(1)}\end{Bmatrix} = \begin{bmatrix}A_{xx} & A_{x\theta} & A_{xs}\\ A_{\theta x} & A_{\theta\theta} & A_{\theta s}\\ A_{sx} & A_{s\theta} & A_{ss}\end{bmatrix}\begin{Bmatrix}\varepsilon_{xx}^{0}\\ \varepsilon_{\theta\theta}^{0}\\ \gamma_{x\theta}^{0}\end{Bmatrix} + \begin{bmatrix}B_{xx} & B_{x\theta} & B_{xs}\\ B_{\theta x} & B_{\theta\theta} & B_{\theta s}\\ B_{sx} & B_{s\theta} & B_{ss}\end{bmatrix}\begin{Bmatrix}\mathrm{K}_{xx}\\ \mathrm{K}_{\theta\theta}\\ \mathrm{K}_{x\theta}\end{Bmatrix} - \begin{Bmatrix}E_{xx}\\ E_{\theta\theta}\\ E_{x\theta}\end{Bmatrix}\Theta - \begin{Bmatrix}F_{xx}\\ F_{\theta\theta}\\ F_{x\theta}\end{Bmatrix}\Lambda \tag{2.109a}$$

$$\begin{Bmatrix}M_{xx}^{(1)}\\ M_{\theta\theta}^{(1)}\\ M_{x\theta}^{(1)}\end{Bmatrix} = \begin{bmatrix}B_{xx} & B_{x\theta} & B_{xs}\\ B_{\theta x} & B_{\theta\theta} & B_{\theta s}\\ B_{sx} & B_{s\theta} & B_{ss}\end{bmatrix}\begin{Bmatrix}\varepsilon_{xx}^{0}\\ \varepsilon_{\theta\theta}^{0}\\ \gamma_{x\theta}^{0}\end{Bmatrix} + \begin{bmatrix}D_{xx} & D_{x\theta} & D_{xs}\\ D_{\theta x} & D_{\theta\theta} & D_{\theta s}\\ D_{sx} & D_{s\theta} & D_{ss}\end{bmatrix}\begin{Bmatrix}\mathrm{K}_{xx}\\ \mathrm{K}_{\theta\theta}\\ \mathrm{K}_{x\theta}\end{Bmatrix} - \begin{Bmatrix}G_{xx}\\ G_{\theta\theta}\\ G_{x\theta}\end{Bmatrix}\Theta - \begin{Bmatrix}H_{xx}\\ H_{\theta\theta}\\ H_{x\theta}\end{Bmatrix}\Lambda \tag{2.109b}$$

$$\begin{Bmatrix}V_{\theta z}^{(1)}\\ V_{xz}^{(1)}\end{Bmatrix} = K_s\begin{bmatrix}\acute{A}_{qq} & \acute{A}_{qr}\\ \acute{A}_{rq} & \acute{A}_{rr}\end{bmatrix}\begin{Bmatrix}\gamma_{\theta z}^{(1)}\\ \gamma_{xz}^{(1)}\end{Bmatrix} \tag{2.109c}$$

where $[A_{ij}]$, $[B_{ij}]$, $[D_{ij}]$, and $[\acute{A}_{ij}]$ are given by Eq. (2.16) and $\{E_{ij}\}$, $\{F_{ij}\}$, $\{G_{ij}\}$, and $\{H_{ij}\}$ are given by,

$$\{E_{ij}\} = \sum_{K=1}^{N} \left[Q_{ij}\right]_K \{\Gamma_{ij}\}_K (z_K - z_{K-1}) \tag{2.110a}$$

$$\{F_{ij}\} = \sum_{K=1}^{N} \left[Q_{ij}\right]_K \{\Upsilon_{ij}\}_K (z_K - z_{K-1}) \tag{2.110b}$$

$$\{G_{ij}\} = \frac{1}{2}\sum_{K=1}^{N} \left[Q_{ij}\right]_K \{\Gamma_{ij}\}_K (z_K^2 - z_{K-1}^2) \tag{2.110c}$$

$$\{H_{ij}\} = \frac{1}{2}\sum_{K=1}^{N} \left[Q_{ij}\right]_K \{\Upsilon_{ij}\}_K (z_K^2 - z_{K-1}^2) \tag{2.110d}$$

Eq. (2.109) is the stress-strain relations when there is hygrothermal loading as well as mechanical loading in a laminated composite cylindrical shell.

2.5.4. Constitutive Equations for a CNT-Reinforced Unidirectional Composite

In section 2.4.2, the estimation of effective material properties based on the Mori-Tanaka model has been explained for a linear elastic polymer matrix reinforced with angled, straight CNTs. Therefore, the components of stiffness matrix in the principle coordinate system (1,2,3), C_{ij} $(i,j = 1,2,\ldots,6)$ for a composite cylindrical shell reinforced with angled, straight CNTs, which are required in the calculation of components of principal stiffness matrix $\left[Q_{ij}\right]_k$ $(i,j = 1,2,6)$ (see Appendix A), are given by Eq. (2.68).

The effective elastic moduli E_{11} and E_{22}, respectively, parallel and normal to the CNT orientation, the effective Poisson's ratio v_{12}, and the effective shear moduli for a polymer composite reinforced by straight CNTs are given by [106,107],

$$E_{11} = n - \frac{l^2}{k}, \qquad E_{22} = \frac{4m(kn - l^2)}{kn - l^2 + mn}, \qquad v_{12} = \frac{1}{2k}, \qquad G_{12} = G_{13} = p, \qquad G_{23} = m \tag{2.111}$$

2.5.5. Constitutive Equations for Piezoelectric Layers Bonded to the Top and Bottom Surfaces of the Host Composite Shell

The poling direction of the piezoelectric layers is assumed to be in the axial x- direction of the shell. The constitutive relations for a piezoelectric layer with the axial polarization in the cylindrical coordinate system (x, θ, z) based on the first-order shear deformation shell theory are given by Eq. (2.23).

The in-plane force and moment resultants and the transverse shear force resultants corresponding to the piezoelectric layers bonded to the top and bottom surfaces of a laminated composite cylindrical shell are obtained by integrating the corresponding stresses, Eq. (2.23a), across the thickness of the piezoelectric layers, i.e.

$$\begin{Bmatrix} N_{xx}^{(2)} \\ N_{\theta\theta}^{(2)} \\ N_{x\theta}^{(2)} \end{Bmatrix} = \int_{-\frac{h}{2}-h_p}^{-\frac{h}{2}} \begin{Bmatrix} \sigma_{xx}^{(2)} \\ \sigma_{\theta\theta}^{(2)} \\ \tau_{x\theta}^{(2)} \end{Bmatrix} dz + \int_{\frac{h}{2}}^{\frac{h}{2}+h_p} \begin{Bmatrix} \sigma_{xx}^{(2)} \\ \sigma_{\theta\theta}^{(2)} \\ \tau_{x\theta}^{(2)} \end{Bmatrix} dz \tag{2.112a}$$

$$\begin{Bmatrix} M_{xx}^{(2)} \\ M_{\theta\theta}^{(2)} \\ M_{x\theta}^{(2)} \end{Bmatrix} = \int_{-\frac{h}{2}-h_p}^{-\frac{h}{2}} \begin{Bmatrix} \sigma_{xx}^{(2)} \\ \sigma_{\theta\theta}^{(2)} \\ \tau_{x\theta}^{(2)} \end{Bmatrix} z\, dz + \int_{\frac{h}{2}}^{\frac{h}{2}+h_p} \begin{Bmatrix} \sigma_{xx}^{(2)} \\ \sigma_{\theta\theta}^{(2)} \\ \tau_{x\theta}^{(2)} \end{Bmatrix} z dz \tag{2.112b}$$

$$\begin{Bmatrix} V_{\theta z}^{(2)} \\ V_{xz}^{(2)} \end{Bmatrix} = K_s \int_{-\frac{h}{2}-h_p}^{-\frac{h}{2}} \begin{Bmatrix} \tau_{\theta z}^{(2)} \\ \tau_{xz}^{(2)} \end{Bmatrix} dz + K_s \int_{\frac{h}{2}}^{\frac{h}{2}+h_p} \begin{Bmatrix} \tau_{\theta z}^{(2)} \\ \tau_{xz}^{(2)} \end{Bmatrix} dz \tag{2.112c}$$

2.5.6. Force and Moment Resultants for a Piezoelectric Coupled Laminated CNT-Reinforced Composite Cylindrical Shell Considering the Hygrothermal Effects

The force and moment resultants in a laminated CNT-reinforced composite cylindrical shell coupled with the piezoelectric layers at the top and bottom surfaces are attained as sum of the force and moment resultants of the host substrate laminated CNT-reinforced composite shell and the

piezoelectric layers ones. Thus, the in-plane force resultants (N_{xx}, $N_{\theta\theta}$, $N_{x\theta}$) are sum of Eq. (2.109a) and Eq. (2.112a), the bending and twisting moment resultants (M_{xx}, $M_{\theta\theta}$, $M_{x\theta}$) are sum of Eq. (2.109b) and Eq. (2.112b), and the transverse shear force resultants (V_{xz}, $V_{\theta z}$) are sum of Eq. (2.109c) and Eq. (2.112c) as,

$$N_{xx} = A_1\frac{\partial u_0}{\partial x} + \frac{A_2}{R}\left(w_0 + \frac{\partial v_0}{\partial \theta}\right) + A_3\left(\frac{\partial u_0}{R\partial \theta} + \frac{\partial v_0}{\partial x}\right) + A_4\frac{\partial \alpha_x}{\partial x} + A_5\frac{\partial \alpha_\theta}{R\partial \theta} + A_6\left(\frac{\partial \alpha_x}{R\partial \theta} + \frac{\partial \alpha_\theta}{\partial x}\right) + A_7\frac{\partial \varphi}{\partial x} + A_8\Theta + A_9\Lambda \quad (2.113a)$$

$$N_{\theta\theta} = B_1\frac{\partial u_0}{\partial x} + \frac{B_2}{R}\left(w_0 + \frac{\partial v_0}{\partial \theta}\right) + B_3\left(\frac{\partial u_0}{R\partial \theta} + \frac{\partial v_0}{\partial x}\right) + B_4\frac{\partial \alpha_x}{\partial x} + B_5\frac{\partial \alpha_\theta}{R\partial \theta} + B_6\left(\frac{\partial \alpha_x}{R\partial \theta} + \frac{\partial \alpha_\theta}{\partial x}\right) + B_7\frac{\partial \varphi}{\partial x} + B_8\Theta + B_9\Lambda \quad (2.113b)$$

$$N_{x\theta} = C_1\frac{\partial u_0}{\partial x} + \frac{C_2}{R}\left(w_0 + \frac{\partial v_0}{\partial \theta}\right) + C_3\left(\frac{\partial u_0}{R\partial \theta} + \frac{\partial v_0}{\partial x}\right) + C_4\frac{\partial \alpha_x}{\partial x} + C_5\frac{\partial \alpha_\theta}{R\partial \theta} + C_6\left(\frac{\partial \alpha_x}{R\partial \theta} + \frac{\partial \alpha_\theta}{\partial x}\right) + C_7\frac{\partial \varphi}{R\partial \theta} + C_8\Theta + C_9\Lambda \quad (2.113c)$$

$$M_{xx} = D_1\frac{\partial u_0}{\partial x} + \frac{D_2}{R}\left(w_0 + \frac{\partial v_0}{\partial \theta}\right) + D_3\left(\frac{\partial u_0}{R\partial \theta} + \frac{\partial v_0}{\partial x}\right) + D_4\frac{\partial \alpha_x}{\partial x} + D_5\frac{\partial \alpha_\theta}{R\partial \theta} + D_6\left(\frac{\partial \alpha_x}{R\partial \theta} + \frac{\partial \alpha_\theta}{\partial x}\right) + D_7\Theta + D_8\Lambda \quad (2.113d)$$

$$M_{\theta\theta} = E_1\frac{\partial u_0}{\partial x} + \frac{E_2}{R}\left(w_0 + \frac{\partial v_0}{\partial \theta}\right) + E_3\left(\frac{\partial u_0}{R\partial \theta} + \frac{\partial v_0}{\partial x}\right) + E_4\frac{\partial \alpha_x}{\partial x} + E_5\frac{\partial \alpha_\theta}{R\partial \theta} + E_6\left(\frac{\partial \alpha_x}{R\partial \theta} + \frac{\partial \alpha_\theta}{\partial x}\right) + E_7\Theta + E_8\Lambda \quad (2.113e)$$

$$M_{x\theta} = F_1\frac{\partial u_0}{\partial x} + \frac{F_2}{R}\left(w_0 + \frac{\partial v_0}{\partial \theta}\right) + F_3\left(\frac{\partial u_0}{R\partial \theta} + \frac{\partial v_0}{\partial x}\right) + F_4\frac{\partial \alpha_x}{\partial x} + F_5\frac{\partial \alpha_\theta}{R\partial \theta} + F_6\left(\frac{\partial \alpha_x}{R\partial \theta} + \frac{\partial \alpha_\theta}{\partial x}\right) + F_7\Theta + F_8\Lambda \quad (2.113f)$$

$$V_{xz} = G_1\left(\frac{\partial w_0}{R\partial \theta} - \frac{v_0}{R} + \alpha_\theta\right) + G_2\left(\frac{\partial w_0}{\partial x} + \alpha_x\right) \quad (2.113g)$$

$$V_{\theta z} = H_1\left(\frac{\partial w_0}{R\partial \theta} - \frac{v_0}{R} + \alpha_\theta\right) + H_2\left(\frac{\partial w_0}{\partial x} + \alpha_x\right) \quad (2..113h)$$

where expression of coefficients, $A_i(i = 1, \dots, 9)$, $B_i(i = 1, \dots, 9)$, $C_i(i = 1, \dots, 9)$, $D_i(i = 1, \dots, 8)$, $E_i(i = 1, \dots, 8)$, $F_i(i = 1, \dots, 8)$, $G_i(i = 1,2)$, and $H_i(i = 1,2)$ are given in Appendix N.

2.5.7. Equations of Motion for a Piezoelectric Coupled Laminated CNT-Reinforced Composite Cylindrical Shell Considering the Hygrothermal Effects

The equations of motion based on the first-order shear deformation shell theory are given by Eq. (2.41). The mass inertias I_i $(i = 0,1,2)$ required for the equations of motion for a laminated CNT-reinforced composite cylindrical shell coated with the piezoelectric layers at the top and bottom surfaces are defined by,

$$I_0 = \sum_{K=1}^{N} \int_{z_{K-1}}^{z_K} \rho_K dz + \int_{-\frac{h}{2}-h_p}^{-\frac{h}{2}} \rho_p dz + \int_{\frac{h}{2}}^{\frac{h}{2}+h_p} \rho_p dz = \sum_{K=1}^{N} \rho_K (z_K - z_{K-1}) + 2\rho_p h_p \tag{2.114a}$$

$$I_1 = \sum_{K=1}^{N} \int_{z_{K-1}}^{z_K} \rho_K z dz + \int_{-\frac{h}{2}-h_p}^{-\frac{h}{2}} \rho_p z dz + \int_{\frac{h}{2}}^{\frac{h}{2}+h_p} \rho_p z dz = \frac{1}{2} \sum_{K=1}^{N} \rho_K (z_K^2 - z_{K-1}^2) \tag{2.114b}$$

$$I_2 = \sum_{K=1}^{N} \int_{z_{K-1}}^{z_K} \rho_K z^2 dz + \int_{-\frac{h}{2}-h_p}^{-\frac{h}{2}} \rho_p z^2 dz + \int_{\frac{h}{2}}^{\frac{h}{2}+h_p} \rho_p z^2 dz$$

$$= \frac{1}{3} \sum_{K=1}^{N} \rho_K (z_K^3 - z_{K-1}^3) + \rho_p \left(\frac{h_p h^2}{2} + h h_p^2 + \frac{2h_p^3}{3} \right) \tag{2.114c}$$

where ρ_p is the mass density of the piezoelectric layer, and ρ_K is the mass density of the lamina (layer) K reinforced with CNTs which is given by,

$$\rho_K = \rho_r f_r + \rho_m f_m \tag{2.115}$$

where ρ_r and ρ_m are the mass densities of the reinforcement phase (CNT), and the polymer matrix phase, respectively.

Substituting the force and moment resultants, Eq. (2.113), into Eq. (2.41), leads to the equations of motion for a laminated CNT-reinforced composite cylindrical shell coupled with the

piezoelectric layers at the top and bottom surfaces based on the first-order shear deformation shell theory in terms of u_0, v_0, w_0, α_x, α_θ, φ, Θ, and Λ.

The electric displacements of the piezoelectric layer with the axial polarization based on the first-order shear deformation shell theory are given by Eq. (2.48).

Satisfying the Maxwell's static electricity equation, $\int_{-\frac{h}{2}-h_p}^{-\frac{h}{2}} \nabla D dz + \int_{\frac{h}{2}}^{\frac{h}{2}+h_p} \nabla D dz = 0$, for the piezoelectric layers, in view of Eq. (2.48), yields,

$$\bar{e}_{22}\frac{\partial^2 u_0}{\partial x^2} + \frac{\bar{e}_{21}}{R}\left(\frac{\partial w_0}{\partial x} + \frac{\partial^2 v_0}{\partial x \partial \theta}\right) + \bar{e}_{16}\left(\frac{\partial^2 u_0}{R^2 \partial \theta^2} + \frac{\partial^2 v_0}{R \partial x \partial \theta}\right) - \bar{\epsilon}_{22}\frac{\partial^2 \varphi}{\partial x^2} - \bar{\epsilon}_{11}\frac{\partial^2 \varphi}{R^2 \partial \theta^2} = 0 \tag{2.116}$$

Concerning hygrothermal modeling, the heat conduction and the moisture diffusion equations should be considered. The moisture diffusion equation is analogous to the heat conduction equation [205]. By assuming constant thermal conductivity coefficients and constant moisture diffusivity coefficients in longitudinal, circumferential, and radial directions, the steady-state Fourier heat conduction equation without internal heat source, and the Fickian moisture diffusion equation in cylindrical coordinate system are, respectively, reduced to,

$$\frac{\partial^2 \Theta}{\partial x^2} + \frac{\partial^2 \Theta}{R^2 \partial \theta^2} = 0 \tag{2.117}$$

$$\frac{\partial^2 \Lambda}{\partial x^2} + \frac{\partial^2 \Lambda}{R^2 \partial \theta^2} = 0 \tag{2.118}$$

Eq. (2.41), in view of Eq. (2.113), and Eqs. (2.116) - (2.118) express the equations of motion in term of the shell displacements (u_0, v_0, and w_0), the rotations of shell cross-section normal to x -axis and θ-axis or shear effects (α_x and α_θ), the electric potential (φ), the temperature change (Θ), and the moisture concentration change (Λ) for a laminated CNT-reinforced composite cylindrical shell coupled with the piezoelectric layers at the top and bottom surfaces. The analytical

model presented in the above is capable to capture the effects of temperature/moisture change as well as the effects of transverse shear, nanoparticles, and piezoelectric coupling.

2.5.8. Solution Methodology

To solve the wave propagation problem, the shell displacements (u_0, v_0, and w_0), the rotations of shell cross-section normal to x -axis and θ-axis or shear effects (α_x and α_θ), the electric potential (φ), the temperature change (Θ), and the moisture concentration change (Λ) are considered in the following forms,

$$u_0(x,\theta,t) = Ue^{in\theta}e^{i\gamma(x-ct)} \tag{2.119a}$$

$$v_0(x,\theta,t) = Ve^{in\theta}e^{i\gamma(x-ct)} \tag{2.119b}$$

$$w_0(x,\theta,t) = We^{in\theta}e^{i\gamma(x-ct)} \tag{2.119c}$$

$$\alpha_x(x,\theta,t) = A_xe^{in\theta}e^{i\gamma(x-ct)} \tag{2.119d}$$

$$\alpha_\theta(x,\theta,t) = A_\theta e^{in\theta}e^{i\gamma(x-ct)} \tag{2.119e}$$

$$\varphi(x,\theta,t) = \Phi e^{in\theta}e^{i\gamma(x-ct)} \tag{2.119f}$$

$$\Theta(x,\theta,t) = Te^{in\theta}e^{i\gamma(x-ct)} \tag{2.119g}$$

$$\Lambda(x,\theta,t) = Ce^{in\theta}e^{i\gamma(x-ct)} \tag{2.119h}$$

Substituting Eq. (2.119) into the equations of motion yields a set of homogenous equations as,

$$\begin{bmatrix} L_{11} & L_{12} & L_{13} & L_{14} & L_{15} & L_{16} & L_{17} & L_{18} \\ L_{21} & L_{22} & L_{23} & L_{24} & L_{25} & L_{26} & L_{27} & L_{28} \\ L_{31} & L_{32} & L_{33} & L_{34} & L_{35} & L_{36} & L_{37} & L_{38} \\ L_{41} & L_{42} & L_{43} & L_{44} & L_{45} & L_{46} & L_{47} & L_{48} \\ L_{51} & L_{52} & L_{53} & L_{54} & L_{55} & L_{56} & L_{57} & L_{58} \\ L_{61} & L_{62} & L_{63} & L_{64} & L_{65} & L_{66} & L_{67} & L_{68} \\ L_{71} & L_{72} & L_{73} & L_{74} & L_{75} & L_{76} & L_{77} & L_{78} \\ L_{81} & L_{82} & L_{83} & L_{84} & L_{85} & L_{86} & L_{87} & L_{88} \end{bmatrix} \begin{Bmatrix} U \\ V \\ W \\ A_x \\ A_\theta \\ \Phi \\ T \\ C \end{Bmatrix} = \{0\} \tag{2.120}$$

where the components of characteristics matrix $[L_{ij}]$ $(i,j = 1,\dots,8)$ are given in Appendix O. From the above matrix equation, a nontrivial solution for U, V, W, A_x, A_θ, Φ, T, and C is obtained only if, the determinant of matrix $[L_{ij}]$ is equal to zero, i.e.

$$\begin{vmatrix} L_{11} & L_{12} & L_{13} & L_{14} & L_{15} & L_{16} & L_{17} & L_{18} \\ L_{21} & L_{22} & L_{23} & L_{24} & L_{25} & L_{26} & L_{27} & L_{28} \\ L_{31} & L_{32} & L_{33} & L_{34} & L_{35} & L_{36} & L_{37} & L_{38} \\ L_{41} & L_{42} & L_{43} & L_{44} & L_{45} & L_{46} & L_{47} & L_{48} \\ L_{51} & L_{52} & L_{53} & L_{54} & L_{55} & L_{56} & L_{57} & L_{58} \\ L_{61} & L_{62} & L_{63} & L_{64} & L_{65} & L_{66} & L_{67} & L_{68} \\ L_{71} & L_{72} & L_{73} & L_{74} & L_{75} & L_{76} & L_{77} & L_{78} \\ L_{81} & L_{82} & L_{83} & L_{84} & L_{85} & L_{86} & L_{87} & L_{88} \end{vmatrix} = 0 \tag{2.121}$$

where $|\dots|$ denotes the determinant of a matrix. By solving Eq. (2.121) based on the method illustrated in section 2.3.4, five positive roots are obtained for any specific axial wavenumber γ and circumferential wavenumber n which are the wave phase velocities c corresponding to the first five wave modes $M1$, $M2$, $M3$, $M4$, and $M5$.

Numerical results are obtained for laminated CNT-reinforced composite cylindrical shells integrated with the piezoelectric layers at the top and bottom surfaces in hygrothermal environmental conditions. The SWCNT (10, 10) is chosen as the reinforcement phase where its properties at different temperatures are listed in Table 2.3. The material properties of polymer used as the matrix phase are assumed to be $\rho_m = 1200\ \mathrm{kg/m^3}$, $v_m = 0.34$, $\Upsilon_m = 2.68 \times 10^{-3}/\mathrm{wt}$ percent H_2O, $\Gamma_m = 45 \times (1 + 0.001\Delta T) \times 10^{-6}/K$ and $\mathrm{E}_m = (3.51 - 0.003T - 0.142C)\mathrm{GPa}$, in which $T = T_0 + \Delta T$ and $T_0 = 300K$ (room temperature), and $C = C_0 + \Delta C$ and $C_0 = 0$ wt percent $\mathrm{H_2O}$ [176]. The PZT-4 with the axial polarization is chosen for the piezoelectric layers where its material properties are given in Table 2.2.

The non-dimensional wave phase velocity ($\mathrm{v} = \frac{c}{c_t}$) is employed to analysis wave propagation characteristics as illustrated in section 2.3.4, where $H = h + 2h_p$ is considered in Eq. (2.59) as the

total thickness of a laminated CNT-reinforced composite cylindrical shell coupled with the piezoelectric layers at the top and bottom surfaces, and the torsional wave phase velocity c_t is employed as,

$$c_t = \sqrt{\frac{G_{12}h + \bar{c}_{66}(2h_p)\left(1 - ((h + 2h_p)/R)\right)}{\rho_K h + \rho_p(2h_p)}} \tag{2.122}$$

2.6. Vibration Characteristics of Smart Laminated CNT-Reinforced Composite Cylindrical Shells under Various Boundary Conditions in Hygrothermal Environments

In this section, an analytical model is presented to characterize vibration behaviors of finite length smart laminated CNT-reinforced composite cylindrical shells coupled with the piezoelectric layers at the top and bottom surfaces under various mechanical boundary conditions in hygrothermal environments using the wave propagation approach.

Constitutive relations and equations of motion are the same as those presented in section 2.5. In the following subsections, an analytical model based on the wave propagation approach with beam mode shape functions used as the axial modal functions is presented to solve the free vibration problem in smart laminated CNT-reinforced composite cylindrical shells under various mechanical boundary conditions.

2.6.1. Wave Propagation Approach

For any continuous system, its natural modes of vibration are obtained from superposition of equal but opposite-going propagating waves [146]. Understanding the physics of this phenomenon can help us to develop simple formulae to calculate the frequencies corresponding to free modes

of vibration. In the present study, the natural modes of vibration for a laminated CNT-reinforced composite cylindrical shell are treated as a mix of standing waves in the axial and circumferential directions. The axial standing wave is denoted by the axial modal parameter m, and the circumferential standing wave is described by the circumferential modal parameter n. The relationship of the natural frequency with the axial and circumferential modal parameters m and n is obtained. The axial and circumferential wavenumbers of standing waves are approximated from the wavenumber of the equivalent beam that has similar boundary conditions as the shell such as simply supported, clamped, sliding, free, etc. The abovementioned method is relatively simple so that the wavenumbers for different boundary conditions are determined quickly. This method, is less complicated than other methods and leads to more reasonable and accurate natural frequencies [146].

The expressions for the shell displacements (u_0, v_0, and w_0), the rotations of shell cross-section normal to x -axis and θ-axis or shear effects (α_x and α_θ), the electric potential (φ), the temperature change (Θ), and the moisture change (Λ) of the shell can be approximated in the form of wave propagation related to axial wavenumber γ_m and circumferential mode number n, as,

$$u_0(x,\theta,t) = U_{mn}e^{i(\gamma_m x+n\theta-\omega t)} \quad (2.123a)$$

$$v_0(x,\theta,t) = V_{mn}e^{i(\gamma_m x+n\theta-\omega t)} \quad (2.123b)$$

$$w_0(x,\theta,t) = W_{mn}e^{i(\gamma_m x+n\theta-\omega t)} \quad (2.123c)$$

$$\alpha_x(x,\theta,t) = A_{x_{mn}}e^{i(\gamma_m x+n\theta-\omega t)} \quad (2.123d)$$

$$\alpha_\theta(x,\theta,t) = A_{\theta_{mn}}e^{i(\gamma_m x+n\theta-\omega t)} \quad (2.123e)$$

$$\varphi(x,\theta,t) = \Phi_{mn}e^{i(\gamma_m x+n\theta-\omega t)} \quad (2.123f)$$

$$\Theta(x,\theta,t) = T_{mn}e^{i(\gamma_m x+n\theta-\omega t)} \quad (2.123g)$$

$$\Lambda(x,\theta,t) = C_{mn}e^{i(\gamma_m x+n\theta-\omega t)} \quad (2.123h)$$

where γ_m, m, n, and ω are the axial wavenumber, the axial mode number, the circumferential mode number, and the angular (circular) frequency of natural vibration mode (m,n), respectively, for free vibration of the cylindrical shell, and U_{mn}, V_{mn}, W_{mn}, $A_{x_{mn}}$, $A_{\theta_{mn}}$, Φ_{mn}, T_{mn}, and C_{mn} are the wave amplitudes. For vibration analysis of a finite length cylindrical shell, axial wavenumber γ_m is dependent on the axial mode number m according to the considered boundary condition (which will be explained in detail in section 2.6.2). While, for vibration of a complete cylindrical shell, circumferential wavenumber γ_n and circumferential modal number n are the same ($\gamma_n = n$), and they will be different if we consider a cylindrical panel with various boundary conditions which is not the topic of this research study.

By replacing Eq. (2.123) into the equations of motion, Eq. (2.41), in view of Eq. (2.113), and Eqs. (2.116) - (2.118), one obtains a set of homogenous equations as,

$$\begin{bmatrix} L_{11} & L_{12} & L_{13} & L_{14} & L_{15} & L_{16} & L_{17} & L_{18} \\ L_{21} & L_{22} & L_{23} & L_{24} & L_{25} & L_{26} & L_{27} & L_{28} \\ L_{31} & L_{32} & L_{33} & L_{34} & L_{35} & L_{36} & L_{37} & L_{38} \\ L_{41} & L_{42} & L_{43} & L_{44} & L_{45} & L_{46} & L_{47} & L_{48} \\ L_{51} & L_{52} & L_{53} & L_{54} & L_{55} & L_{56} & L_{57} & L_{58} \\ L_{61} & L_{62} & L_{63} & L_{64} & L_{65} & L_{66} & L_{67} & L_{68} \\ L_{71} & L_{72} & L_{73} & L_{74} & L_{75} & L_{76} & L_{77} & L_{78} \\ L_{81} & L_{82} & L_{83} & L_{84} & L_{85} & L_{86} & L_{87} & L_{88} \end{bmatrix} \begin{Bmatrix} U_{mn} \\ V_{mn} \\ W_{mn} \\ A_{x_{mn}} \\ A_{\theta_{mn}} \\ \Phi_{mn} \\ T_{mn} \\ C_{mn} \end{Bmatrix} = \{0\} \tag{2.124}$$

where components of characteristics matrix $[L_{ij}]$ $(i,j = 1,\dots,8)$ are given in Appendix P. The above matrix equation, due to the eigenvalue problem, has a nontrivial solution for U_{mn}, V_{mn}, W_{mn}, $A_{x_{mn}}$, $A_{\theta_{mn}}$, Φ_{mn}, T_{mn}, and C_{mn} only if, the determinant of matrix $[L_{ij}]$ is equal to zero. Eq. (2.124) is the system characteristics equation that can be used to determine the natural frequencies of a smart laminated composite cylindrical shell as well as wave propagation characteristics.

By solving Eq. (2.124) based on the Bisection method illustrated in section 2.3.4, one can obtain five positive roots for any axial and circumferential modes (m,n). The first three roots are the

angular frequencies corresponding to the cylindrical shell motion in the axial (x), circumferential (θ), and radial (z) directions, respectively, and the fourth and fifth roots are, respectively, the angular frequencies corresponding to the rotations of shell cross-section normal to x -axis ($z-\theta$ plane) and θ-axis ($x-z$ plane), respectively [146,206–209]. These five roots are corresponding to the angular frequencies of the first five wave modes of the laminated composite cylindrical shell denoted by $M1$, $M2$, $M3$, $M4$, and $M5$, respectively, in this study. The lowest of the five roots ($M1$) represents the flexural (forward) vibration and other roots ($M2$ - $M5$) are corresponding to in-plane and out-of-plane vibrations [146,206–209]. In the other words, the lowest frequency is called the frequency of the fundamental mode or the fundamental natural frequency and all other frequencies are called the frequencies of higher harmonics, or overtones [210]. The fundamental frequency provides the sound with its strongest audible pitch reference - it is the predominant frequency in any complex waveform. The fundamental frequency is the frequency we actually hear the sound at. Therefore, overtones are frequencies of a waveform that are higher than, but not directly related to, the fundamental frequency. From a graphical numerical method based on the Bisection method (as explained in section 2.3.4), one can obtain the frequency curves and the natural frequencies at any specific axial and circumferential modes (m, n) corresponding to the first five roots of Eq. (2.124) ($M1$, $M2$, $M3$, $M4$, and $M5$).

2.6.2. Wavenumbers

An accurate axial wavenumber γ_m must be calculated to satisfy the applied boundary conditions at the both ends of a cylindrical shell in order to compute the frequency of the shell from Eq. (2.124). The wave propagation in the axial direction of the shell is approximately obtained by studying the wave propagation in a similar beam. Wave propagation characteristics in a beam at any frequency are determined by the wavenumber $\gamma[= 2\pi/\lambda\ (wavelength)]$. This represents the

phase difference between two points in a continuous system. In the other words, when a wave propagates, its phase changes by γ per unit length. When wave propagates from the left-hand end to the right-hand end of the beam over the distance L, the total phase change is γL. An identical but opposite-going wave is reflected from the right-hand end which is back toward the left-hand end. Thus, the phase of the wave varies by another γL. A phase difference is defined between the incoming and reflected waves at each of the reflecting boundaries. In the case of a simply supported-simply supported (SS-SS) beam, the phase difference at the ends is zero. Thus, the total phase change as the "wave travels one complete circuit around the beam" is $2\gamma L$. When the total phase change is an integral number of $2\pi's$, natural vibration modes of the beam happen [146].

For the simply supported-simply supported (SS-SS) boundary condition, the characteristics equation for the beam is $Sin(2\gamma L) = 0$, so that wavenumber equation for SS-SS boundary condition can be written as $\gamma L = m\pi$. Thus, for a shell with SS-SS boundary condition, $\gamma_m = \frac{m\pi}{L}$ and n can be considered in Eq. (2.124) to find the natural frequencies of the cylindrical shell for axial and circumferential mode numbers (m, n).

For other types of boundary conditions, the characteristic equations are not as simple as that for the SS-SS boundary condition. However, approximate wavenumbers were proposed for other boundary conditions in Ref. [146]. In this study, we calculate the natural frequencies for clamped-clamped (C-C), clamped-simply supported (C-SS), simply supported-simply supported (SS-SS), clamped-sliding (C-SL), and clamped-free (C-F) boundary conditions, where axial wavenumber for these boundary conditions are listed in Table 2.4. The clamped end means it is completely prevented from any displacement and rotation. Simply supported boundary condition means that all translations (3 in three-dimensional) are fixed but rotations are unconstrained. A sliding

boundary condition is used to force a point to remain on a given surface and in the direction of force, displacement is zero, and other two displacements and all rotations are unconstrained.

Figs. 2.9 and 2.10 illustrate, respectively, the axial modal parameter m and the circumferential modal parameter n by presenting axial and circumferential modal patterns. The patterns shown in Figs. 2.9 and 2.10 describe the mode shapes along the axial and the circumferential directions of the shell, respectively. However, an exact particle motion of the shell can be along axial, circumferential, and radial directions or a combination of the axial and circumferential modes. From Figs. 2.9 and 2.10, the typical mode shapes can be explained as: i) when $n = 0$, the circumferential modal type is a circle illustrating an extensional mode corresponding to a breathing type mode, ii) when $m = 0$, the mode is a pure radial mode so that a constant cross-sectional shape along the length of cylinder is obtained, iii) when m and n are both equal to one, a circumferential mode is obtained. The mode is an axial bending mode when $n = 1$ and $m \neq 1$, and for $m = 1$ and $n \neq 1$, the mode is radial motion with shearing mode [211].

Table 2.4. Axial wavenumber for different boundary conditions [146].

Boundary condition	Axial wavenumber
Clamped-Clamped (C-C)	$\gamma_m = (2m + 1)\,\pi/2L$
Clamped-Simply Supported (C-SS)	$\gamma_m = (4m + 1)\,\pi/4L$
Simply Supported-Simply Supported (SS-SS)	$\gamma_m = m\pi/L$
Clamped-Sliding (C-SL)	$\gamma_m = (4m - 1)\,\pi/4L$
Clamped-Free (C-F)	$\gamma_m = (2m - 1)\,\pi/2\,L$

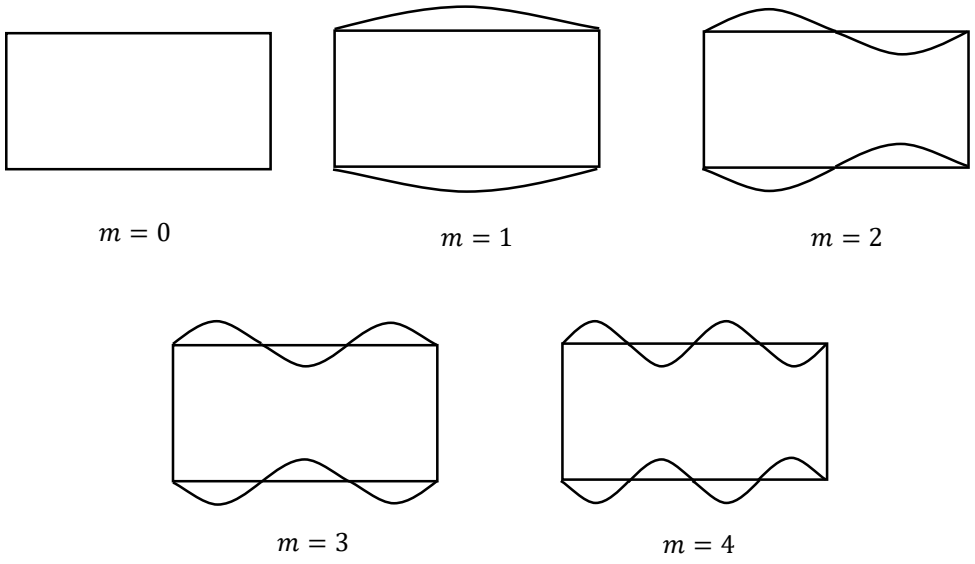

Figure 2.9. Axial modal parameter m identifying axial mode shapes for a cylinder [3].

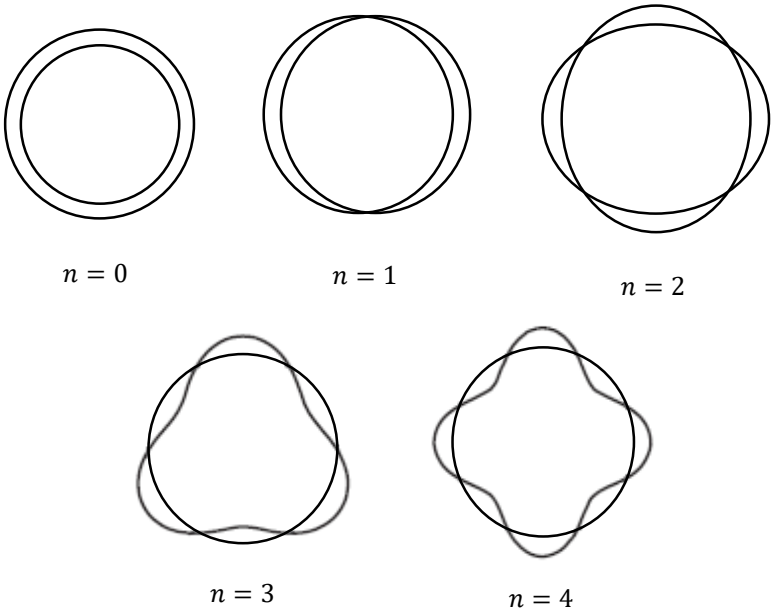

Figure 2.10. Circumferential modal parameter n identifying circumferential mode shapes for a cylinder [3].

2.6.3. Numerical Implementation

In numerical solution to find the free vibration characteristics of finite length smart laminated CNT-reinforced composite cylindrical shells with the effects of hygrothermal environmental conditions and different mechanical boundary conditions, the SWCNT (10, 10) is chosen for the reinforcement phase, where its properties are given in Table 2.3, and for the matrix phase, a polymer is considered with the material properties $\rho_m = 1200\ \mathrm{kg/m^3}$, $v_m = 0.34$, $\Upsilon_m = 2.68 \times 10^{-3}/\mathrm{wt\ percent}\ H_2O$, $\Gamma_m = 45 \times (1 + 0.001\Delta T) \times 10^{-6}/K$ and $\mathrm{E}_m = (3.51 - 0.003T - 0.142C)\mathrm{GPa}$, in which $T = T_0 + \Delta T$ and $T_0 = 300K$ (room temperature), and $C = C_0 + \Delta C$ and $C_0 = 0$ wt percent $\mathrm{H_2O}$ [176]. For the piezoelectric layers, the PZT-4 with axial polarization is considered where its mechanical and electrical properties are listed in Table 2.2.

To determine vibration characteristics of a piezoelectric coupled laminated composite cylindrical shell reinforced with CNTs, a non-dimensional frequency parameter is employed as,

$$\Omega = \frac{\omega H}{\pi c_t} \tag{2.125}$$

where $H = h + 2h_p$ expresses the total thickness of the piezoelectric coupled laminated composite cylindrical shell, ω is the frequency computed from Eq. (2.124) for axial and circumferential modes (m, n), and c_t is the torsional wave phase velocity that for a CNT-reinforced composite cylindrical shell integrated with the piezoelectric layers at the top and bottom surfaces is given by,

$$c_t = \sqrt{\frac{G_{12}h + \bar{c}_{66}(2h_p)}{\rho_K h + \rho_p(2h_p)}} \tag{2.126}$$

Chapter 3

Results and Discussions

Validations of the developed analytical models and the corresponding codes generating the numerical results in this study are first reported in this Chapter. Furthermore, wave propagation and vibration characteristics of smart composite cylindrical shell structures are obtained and discussed with the effects of transverse shear, piezoelectricity, nanoparticles, hygrothermal environmental conditions, and boundary conditions based on the analytical models and solution methods developed and presented in Chapter 2.

3.1. Validation of the Present Methodology and Solution Method

3.1.1. Verification of Numerical Implementation in Micromechanical Modeling

Numerical implementation in the micromechanical modeling is required to be verified in estimating the effective elastic properties of CNT-reinforced composites. Hence, in this section, the results of the Mori-Tanaka micromechanics model used in this research are compared with the existing results in the study by Li Shi et al. [107]. To this purpose, we use the following representative values of the elastic constants for SWCNTs: $n_r = 450$ GPa, $k_r = 30$ GPa, $m_r = p_r = 1$ GPa, and $l_r = 10$ GPa [201]; and for the matrix material, the polystyrene with Young's modulus $E_m = 1.9$ GPa and Poisson's ratio $v_m = 0.3$ is considered [107].

At the first step, the micromechanical modeling presented for the estimation of the elastic constants of a composite reinforced with angled CNTs is validated. For this case, longitudinal and transverse elastic moduli (E_{11} and E_{22}) of a polystyrene composite reinforced with 0° CNTs (aligned CNTs) for various CNT volume fractions (f_r) are calculated and then compared with the results of the study of Li Shi et al. [107]. As shown in Fig. 3.1, a good agreement is observed and we can conclude that the presented model and numerical implementation are valid in estimating the effective elastic properties of composites reinforced with angled CNTs.

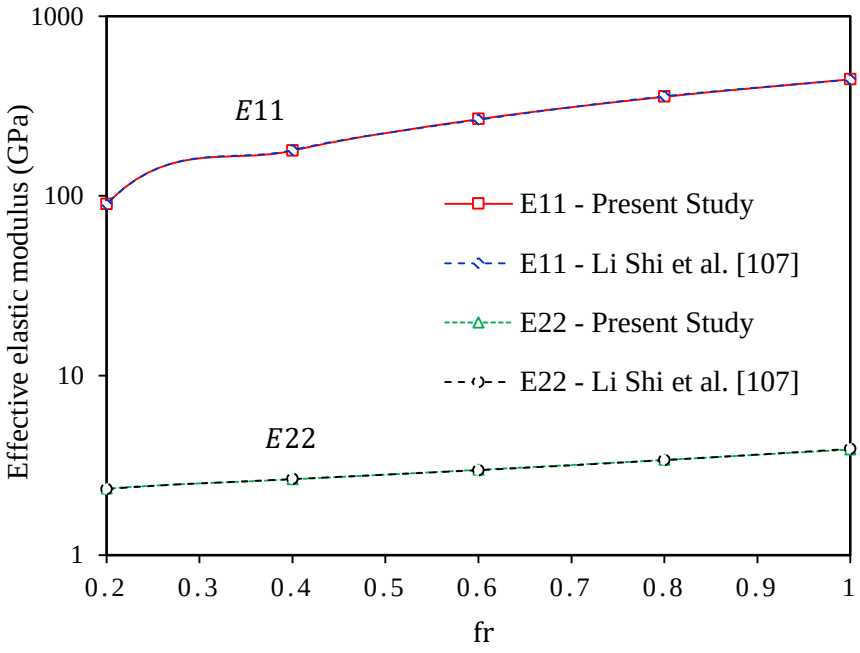

Figure 3.1. Comparison of the presented micromechanics model in estimating the longitudinal and transverse elastic moduli (E_{11} and E_{22}) of a polystyrene composite reinforced with 0° CNTs (aligned CNTs) for various CNT volume fractions (f_r).

In Chapter 2, a micromechanics model for calculating the effective elastic constants of composites reinforced with randomly oriented CNTs was also presented. To assure that the modeling is correct, a comparison is presented in Fig. 3.2 in estimating the effective Young's modulus (E) of a polystyrene composite reinforced with randomly oriented CNTs for various

CNT volume fractions (f_r) by the presented model in this study with the results obtained from the study of Li Shi et al. [107]. It can be seen that there is a good agreement between the results of the present study and those of the Ref. [107]. So, it can be inferred that the presented model is also capable to compute the effective elastic properties for composites reinforced with randomly oriented CNTs.

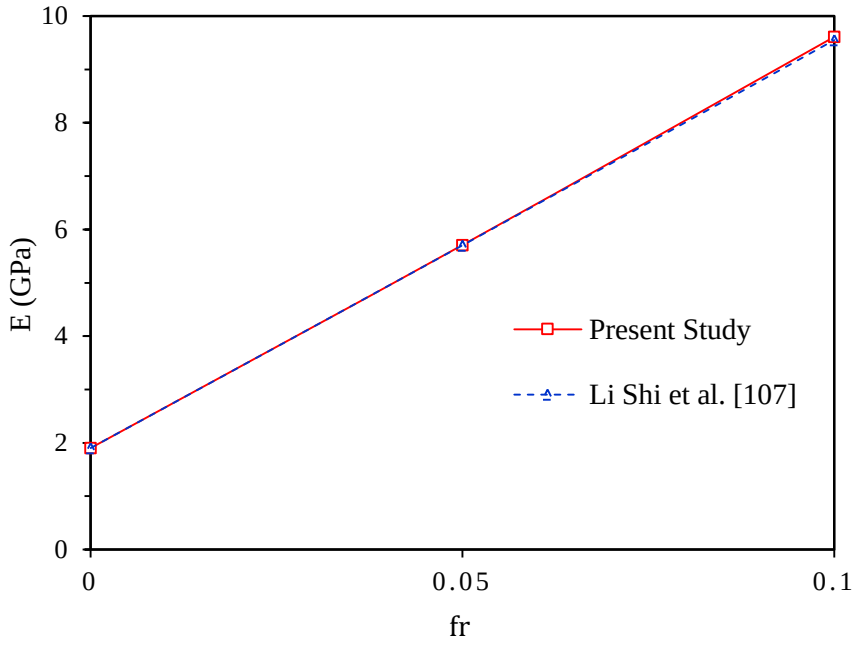

Figure 3.2. Comparison of the presented micromechanics model in estimating the effective Young's modulus (E) of a polystyrene composite reinforced with randomly oriented CNTs for various CNT volume fractions (f_r).

Finally, the results obtained from the micromechanics model presented for computing the effective elastic properties of agglomerated CNT-reinforced composites are verified and compared with the results of the study of Li Shi et al. [107] in estimating the effective Young's modulus (E) of a polystyrene composite reinforced with agglomerated CNTs. For this case, both complete agglomeration (when $\eta = 1$) and partial agglomeration (when $\mu = 0.5$) are considered. Table 3.1 presents a comparison study in estimating the effective Young's modulus (E) for a polystyrene

composite reinforced with agglomerated CNTs within various agglomeration parameters μ when $\eta = 1$ at different CNT volume fractions (f_r). Furthermore, Table 3.2 compares the effective Young's modulus (E) computed by the present micromechanics model and that obtained from the Ref. [107] for various agglomeration parameters η when $\mu = 0.5$ at different CNT volume fractions (f_r). The provided comparison study indicates that the presented micromechanics model has enough accuracy in estimating the elastic properties for composites reinforced with agglomerated CNTs.

Table 3.1. A comparison study in estimating the effective Young's modulus (E) for a polystyrene composite reinforced with agglomerated CNTs within various agglomeration parameters μ when $\eta = 1$ at different CNT volume fractions (f_r).

CNT volume fraction (f_r)	Agglomeration parameter (μ)						
	0.4	0.5	0.6	0.7	0.8	0.9	1
$f_r = 0.05$ (Present Study)	3.4467	3.8281	4.2076	4.5852	4.9609	5.3348	5.707
$f_r = 0.05$ (Li Shi et al. [107])	3.60953	3.90919	4.20648	4.50377	4.97824	5.27434	5.75238
$f_r = 0.1$ (Present Study)	3.8461	4.4913	5.227	6.074	7.0596	8.221	9.61
$f_r = 0.1$ (Li Shi et al. [107])	3.96627	4.62268	5.27672	6.10913	7.11872	8.13069	9.49702
$f_r = 0.2$ (Present Study)	4.1346	5.0298	6.1712	7.6771	9.7558	12.8113	17.7442
$f_r = 0.2$ (Li Shi et al. [107])	4.32421	5.1578	6.34577	7.71567	9.61713	12.4105	17.1671
$f_r = 0.4$ (Present Study)	4.3136	5.3929	6.8779	9.0513	12.5373	19.0411	35.4761
$f_r = 0.4$ (Li Shi et al. [107])	4.50258	5.69173	7.05926	9.14028	12.4699	18.8319	34.2921

Table 3.2. A comparison study in estimating the effective Young's modulus (E) for a polystyrene composite reinforced with agglomerated CNTs within various agglomeration parameters η when $\mu = 0.5$ at different CNT volume fractions (f_r).

CNT volume fraction (f_r)	Agglomeration parameter (η)					
	0.5	0.6	0.7	0.8	0.9	1
$f_r = 0.05$ (Present Study)	5.707	5.6536	5.4763	5.1438	4.6137	3.8281
$f_r = 0.05$ (Li Shi et al. [107])	5.48837	5.4697	5.26499	5.05931	4.57649	3.8146
$f_r = 0.1$ (Present Study)	9.61	9.4771	9.0248	8.1504	6.7096	4.4913
$f_r = 0.1$ (Li Shi et al. [107])	9.2093	9.00459	8.61382	7.85065	6.52998	4.46544
$f_r = 0.2$ (Present Study)	17.7442	17.4346	16.3563	14.2237	10.6392	5.0298
$f_r = 0.2$ (Li Shi et al. [107])	16.9302	16.6325	15.5906	13.7118	10.2506	5.02358

3.1.2. Verification of Solution Method and Numerical Implementation in Determining Wave Propagation Characteristics

As a part of validation, the dispersion results of the presented models are compared with those of the Ref. [98] for piezoelectric coupled metallic cylindrical shells. For this purpose, the dispersion curves are obtained for a piezoelectric coupled aluminium cylindrical shell with the piezoelectric thickness ratio $r = h_p/h = 0.05$ and $h/R = 1/30$ for wave modes 1 and 3 ($M1$ and $M3$) at circumferential wavenumber $n = 0$. Material properties of aluminium is listed in Table 3.3. From Fig. 3.3, it is observed that there is a good agreement between the results of the present model based on the membrane shell theory, the Love bending shell theory, and the first-order shear deformation shell theory and those of the Ref. [98].

Table 3.3. Material properties for the aluminium [39].

Property	Aluminium
Mass density, ρ, (kg/m^3)	2800
Young's modulus, E, (GPa)	70
Shear modulus, G, (GPa)	26.6
Poisson's ratio, v	0.33

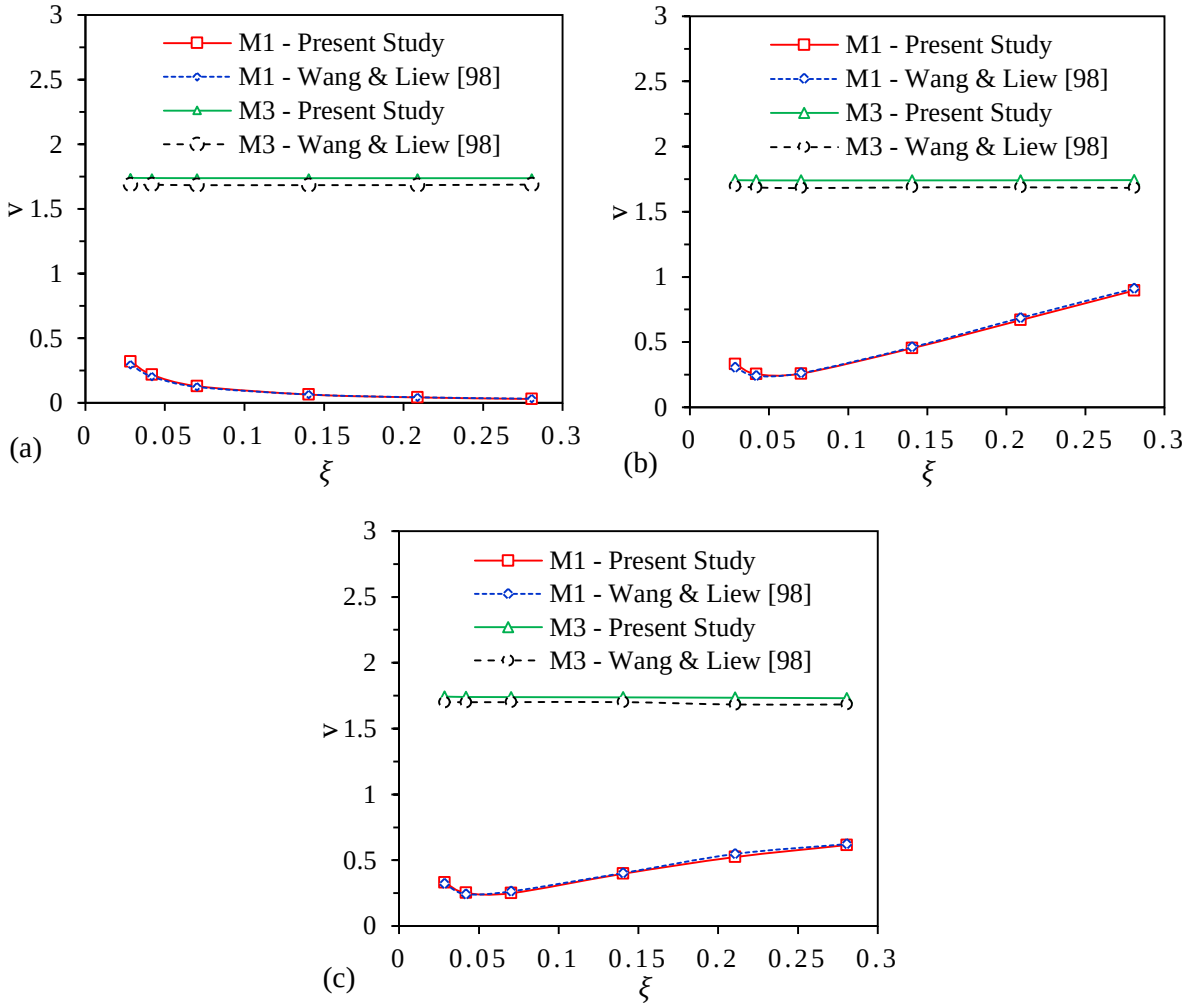

Figure 3.3. Comparison of dispersion curves of the present model and those of the Wang and Liew's study [98] for a piezoelectric coupled aluminium cylindrical shell with $r = 0.05$ and $h/R = 1/30$ for wave modes 1 and 3 ($M1$ and $M3$) at $n = 0$ based on (a) the membrane shell theory, (b) the Love bending shell theory, and (c) the first-order shear deformation shell theory.

3.1.3. Verification of the Present Model in Estimating Vibration Characteristics

To validate the presented methodology and solution method in characterizing vibration behaviors of smart laminated composite cylindrical shells using the beam modal functions based on the wave propagation approach, the natural frequencies corresponding to the first root of Eq. (2.124) ($M1$) are calculated for three examples and compared with the existing results in the literature.

In the first example, the non-dimensional frequencies $\Omega = \omega R\sqrt{\rho/E_{22}}$ for a $[0^\circ/90^\circ/0^\circ]$ cross-ply laminated composite cylindrical shell with SS-SS boundary condition are calculated and compared in Table 3.4 with the results of Zhang [206] and Lam and Loy [212] based on the Love bending shell theory for the first axial mode (i.e. $m = 1$) and the lowest six circumferential modes (i.e. $n = 1, 2, 3, 4, 5, 6$). In Table 3.4, comparisons are presented for the shell thickness to radius ratio $h/R = 0.002$ and the shell length to radius ratios $L/R = 1$, 5, 10, and 20.

As the second example, a $[0^\circ/90^\circ/0^\circ]$ cross-ply laminated composite cylindrical shell with C-C boundary condition is considered and the non-dimensional frequencies $\Omega = \omega R\sqrt{\rho/E_{22}}$ are computed and compared in Table 3.5 with the results of Jin et al. [149] based on the Love bending shell theory for axial mode $m = 1$ and circumferential modes $n = 1, 2, 3, 4, 5, 6$. For the second example, compressions are given for $h/R = 0.002$ and $L/R = 1$, 5, and 20. In both first and second examples, the material properties are given as: $E_{22} = 7.6GPa$, $E_{11}/E_{22} = 2.5$, $G_{12} = 4.1\ GPa$, $v_{12} = 0.26$, $\rho = 1643\ \mathrm{kg/m^3}$.

As the last example, the non-dimensional frequencies $\Omega = \omega(L^2/100h)\sqrt{\rho/E_{22}}$ for$[0^\circ/90^\circ]$ and $[0^\circ/90^\circ/0^\circ]$ cross-ply laminated composite cylindrical shells with various boundary

conditions are calculated and compared in Table 3.6 with the results of Malekzadeh et al. [148] based on the layer wise-differential quadrature (LW-DQ) method, the results of Khdeir et al. [138] based on the state-space technique, the results of Shen and Yang [176] using the higher-order shear deformation shell theory, and the results of Lam et al. [213] using the Ritz method. For the third example, the results are compared for $(m,n) = (1,1)$, $h/R = 0.2$, and $L/R = 1$, and 2, and the material properties are given as: $E_{11} = 40GPa$, $E_{22} = E_{33} = 1GPa$, $G_{12} = G_{13} = 0.6\,GPa$, $G_{23} = 0.5\,GPa$, $v_{12} = v_{13} = v_{23} = 0.25$, $\rho = 1\,\mathrm{kg/m^3}$.

Based on these comparison studies, a good agreement has been observed between the results of the present model and solution method and the available results of cross-ply laminated cylindrical shells in the literature. It should be noted that small deviations between the results could be related to different solution methods and computer powers used in the considered studies for the comparison. It should be noted that the material properties for the above examples are considered independent of temperature and moisture.

Table 3.4. Comparison of the non-dimensional frequency parameter $\Omega = \omega R\sqrt{\rho/E_{22}}$ for a $[0^{\circ}/90^{\circ}/0^{\circ}]$ cross-ply laminated composite cylindrical shell with SS-SS boundary condition ($E_{22} = 7.6GPa$, $E_{11}/E_{22} = 2.5$, $G_{12} = 4.1\ GPa$, $v_{12} = 0.26$, $\rho = 1643\,\mathrm{kg/m^3}$, $h/R = 0.002$, $m = 1$).

L/R	Source	$n=1$	$n=2$	$n=3$	$n=4$	$n=5$	$n=6$
1	Present Study	1.0613	0.8041	0.5984	0.4502	0.3453	0.2708
	Zhang [206]	1.061283	0.804052	0.598328	0.45014	0.345248	0.270747
	Lam & Loy [212]	1.061284	0.804054	0.598331	0.450144	0.345253	0.270754
5	Present Study	0.2486	0.1072	0.0551	0.0339	0.0259	0.0261
	Zhang [206]	0.248634	0.107202	0.055085	0.033788	0.02579	0.025873
	Lam & Loy [212]	0.248635	0.107203	0.055087	0.03379	0.025794	0.025873
10	Present Study	0.0839	0.03	0.0153	0.0124	0.0155	0.0215
	Zhang [206]	0.083908	0.030008	0.015191	0.012174	0.01523	0.021178
	Lam & Loy [212]	0.083908	0.030009	0.015193	0.012176	0.015231	0.021179
20	Present Study	0.0236	0.008	0.0061	0.0093	0.0145	0.0211
	Zhang [206]	0.023589	0.007903	0.005868	0.009019	0.014235	0.0208
	Lam & Loy [212]	0.02359	0.007904	0.005869	0.00902	0.014236	0.020801

Table 3.5. Comparison of the non-dimensional frequency parameter $\Omega = \omega R\sqrt{\rho/E_{22}}$ for a $[0^{\circ}/90^{\circ}/0^{\circ}]$ cross-ply laminated composite cylindrical shell with C-C boundary condition ($E_{22} = 7.6GPa$, $E_{11}/E_{22} = 2.5$, $G_{12} = 4.1\ GPa$, $v_{12} = 0.26$, $\rho = 1643\,\mathrm{kg/m^3}$, $h/R = 0.002$, $m = 1$).

L/R	Source	$n=1$	$n=2$	$n=3$	$n=4$	$n=5$	$n=6$
1	Present Study	1.1546	0.9939	0.8228	0.6741	0.5534	0.4579
	Jin et al. [149]	1.062242	0.813717	0.629498	0.500846	0.409156	0.341724
5	Present Study	0.4189	0.2081	0.1142	0.0705	0.049	0.0396
	Jin et al. [149]	0.303609	0.167527	0.099667	0.064699	0.046345	0.038222
20	Present Study	0.0503	0.0173	0.0095	0.0102	0.0148	0.0212
	Jin et al. [149]	0.04651	0.016933	0.009371	0.009975	0.014506	0.020895

Table 3.6. Comparison of the non-dimensional frequency parameter $\Omega = \omega(L^2/100h)\sqrt{\rho/E_{22}}$ for cross-ply laminated composite cylindrical shells with various boundary conditions ($E_{11} = 40GPa$, $E_{22} = E_{33} = 1GPa$, $G_{12} = G_{13} = 0.6\,GPa$, $G_{23} = 0.5\,GPa$, $v_{12} = v_{13} = v_{23} = 0.25$, $\rho = 1\,\mathrm{kg/m^3}$, $h/R = 0.2$, $m = n = 1$).

Lay-Up	Source	SS-SS		C-SS		C-C		C-F	
		$L/R = 1$	$L/R = 2$	$L/R = 1$	$L/R = 2$	$L/R = 1$	$L/R = 2$	$L/R = 1$	$L/R = 2$
$[0^\circ/90^\circ]$	Present Study	0.0912	0.1692	0.1177	0.2155	0.1452	0.2636	0.0423	0.0809
	Malekzadeh et al. [148]	0.1012	0.1908	0.1067	0.2016	0.1191	0.2142	0.0518	0.0983
	Khdeir et al. [138]	0.0791	0.1552	0.0893	0.1697	0.1002	0.1876	0.0435	0.0914
	Shen & Yang [176]	0.0896	0.1816	---	---	---	---	---	---
$[0^\circ/90^\circ/0^\circ]$	Present Study	0.1072	0.1958	0.1365	0.2529	0.1657	0.3111	0.049	0.0892
	Malekzadeh et al. [148]	0.1226	0.2242	0.1162	0.2334	0.1312	0.2511	0.0603	0.1122
	Khdeir et al. [138]	0.1004	0.1779	0.1036	0.1945	0.1093	0.2129	0.0495	0.0988
	Shen & Yang [176]	0.1085	0.1973	---	---	---	---	---	---
	Lam et al. [213]	0.1014	0.1885	---	---	---	---	---	---

3.2. Parametric Studies on Wave Propagation Characteristics of Smart Composite Cylindrical Shells

3.2.1. Variation of Dispersion Curves for Different Wave Modes

The dispersion curves for the first five wave modes ($M1, M2$, $M3$, $M4$, and $M5$) at the circumferential wavenumbers $n = 0, 1$, and 2, when $h/R = 1/30$ are displayed in Fig. 3.4 for a $[0^\circ/45^\circ/90^\circ]_s$ laminated carbon/epoxy composite cylindrical shell coupled with the piezoelectric layer at the top surface with the thickness ratio $r = 0.1$ by considering the transverse shear effects and rotary inertia via the first-order shear deformation shell theory. As shown in Fig. 3.4, within a very small range of axial wavenumbers, the non-dimensional wave phase velocity decreases dramatically at first, and then it changes smoothly with higher axial wavenumbers. However, the

non-dimensional wave phase velocity at $n = 2$ is a bit higher than that at $n = 1$ and $n = 0$, respectively.

Without considering the shear effects, no higher wave mode (> 3) solutions can be obtained. Only by using the proposed analytical model, we can attain the dispersion solutions in necessary shear wave modes for a smart laminated composite cylindrical shell. However, the trend of dispersion curves for a smart laminated fiber-reinforced composite cylindrical shell is different with the trend of dispersion curves for a smart isotropic cylindrical shell [98], especially at higher wave modes.

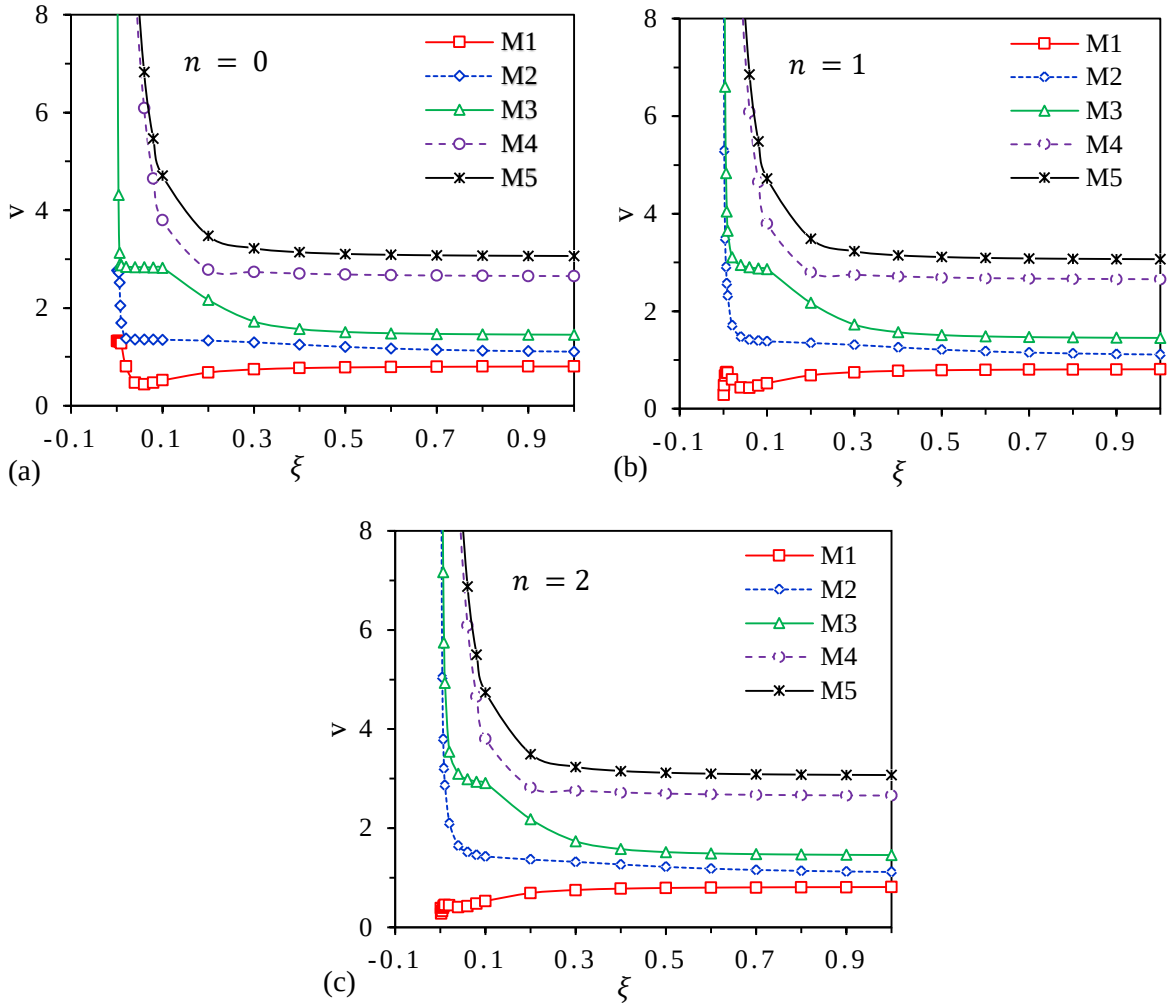

Figure 3.4. Dispersion curves for a $[0^{\circ}/45^{\circ}/90^{\circ}]_s$ laminated carbon/epoxy composite cylindrical shell coupled with a piezoelectric layer with $r = 0.1$ and $h/R = 1/30$ for the first five wave modes ($M1, M2, M3, M4$, and $M5$) at (a) $n = 0$, (b) $n = 1$, and (c) $n = 2$ using the first-order shear deformation shell theory.

3.2.2. Effect of Piezoelectric Coupling on Wave Dispersion Solutions

Fig. 3.5 illustrates the piezoelectric coupling effect on the dispersion curves of a $[0^{\circ}/45^{\circ}/90^{\circ}]_s$ laminated carbon/epoxy composite cylindrical shell for the first five wave modes ($M1, M2$, $M3$, $M4$, and $M5$) at $n = 1$ and $h/R = 1/30$ based on the first-order shear deformation shell theory. For this purpose, dispersion curves for a pure $[0^{\circ}/45^{\circ}/90^{\circ}]_s$ laminated carbon/epoxy composite cylindrical shell ($r = 0$) and piezoelectric coupled ones with thickness ratios $r = \frac{h_p}{h} = 0.1, 0.2,$ and 0.3 are plotted in Fig. 3.5. In this case study, axial poling for the piezoelectric layer is considered. For the first wave mode ($M1$), at very low axial wavenumbers ($\xi \leq 0.04$), there is no significant difference between the four dispersion curves with different piezoelectric layer thicknesses; while at the portion of medium axial wavenumbers ($0.04 < \xi < 0.3$), difference between four dispersion curves is more apparent and the non-dimensional wave phase velocity is higher with lower piezoelectric thickness ratio (r); and at higher axial wavenumbers there is not significant difference between four dispersion curves (see Fig. 3.5a). For the next four wave modes ($M2$, $M3$, $M4$, and $M5$), it is evident that, the non-dimensional wave phase velocity decreases dramatically within very small range of axial wavenumbers ($\xi < 0.02$ for $M2$ and $M3$; $\xi < 0.06$ for $M4$ and $M5$) and there is not obvious difference between four dispersion curves with different piezoelectric layer thicknesses, while at higher axial wavenumbers the velocity varies slightly and difference between four dispersion curves with different piezoelectric layer thicknesses is more apparent; thus, at higher axial wavenumbers in wave modes 2, 3, 4, and 5, by increasing the piezoelectric layer thickness, the non-dimensional wave phase velocity decreases (see Fig. 3.5b-e). For wave mode 2 ($M2$), the piezoelectricity also changes the dispersion curve trend at higher axial wavenumbers leading to the decrease of wave phase velocity with the increase of axial wavenumbers, while at other wave modes, it does not change the trend of dispersion curves.

Similar trend is also observed for other circumferential wavenumbers (n) where for brevity, the results are not shown here for other n. Since the stiffness of the piezoelectric layer is smaller than that of the host laminated CNT-reinforced composite, it is natural to see from Fig. 3.5 that wave phase velocity decreases as the thickness of the piezoelectric layer increases. It is interesting to see that this effect is much significant at higher non-dimensional axial wavenumbers ($\xi > 0.1$) for wave modes 2, 4, and 5, but more obvious for lower axial wavenumbers ($\xi < 0.5$) for wave mode 3. This decreasing effect is also observed in some isotropic materials such as steel and aluminium which are stiffer than the piezoelectric material, while for some other isotropic materials such as gold with lower stiffness than the piezoelectric material, the integration of piezoelectric material to the host shell with increasing piezo-layer thickness leads to the increase of the wave phase velocities. In addition, it is interesting to see that for higher wave modes ($M4$ and $M5$), the piezoelectric effect on the host composites is more significant compared with the piezo-coupled isotropic cases which can be due to the more significant shear effects in the piezo-composites [39,97,98]. In summary, it is concluded that the wave phase velocity at a pure laminated composite cylindrical shell is higher than that of piezoelectric coupled ones, and usually integrating piezoelectric material to the surfaces of host laminated composite shells and increasing its thickness leads to the reduction of the wave phase velocity due to the effect of electric fields, so by adjusting an applied electric field strength, we can control the wave phase velocity in smart laminated composite cylindrical shells coupled with the piezoelectric layers. However, the decreasing effect of the piezoelectric layer on the wave phase velocity depends on the wavenumbers and wave modes, where for some wavenumbers and wave modes ($M1$ and $M3$), this effect is almost negligible. These observations are not common sense and without this study we could not find them.

Therefore, the proposed mathematical model is capable to describe the piezoelectric coupling effects including shear, thickness, and polarization directions on wave propagation behaviors of smart laminated composite shells at various axial and circumferential wavenumbers and wave modes. The findings of piezoelectricity effects on wave dynamics of smart composites are helpful and applicable for the design of smart composite structures for vibration, noise, and instability control, and structural health monitoring by NDE.

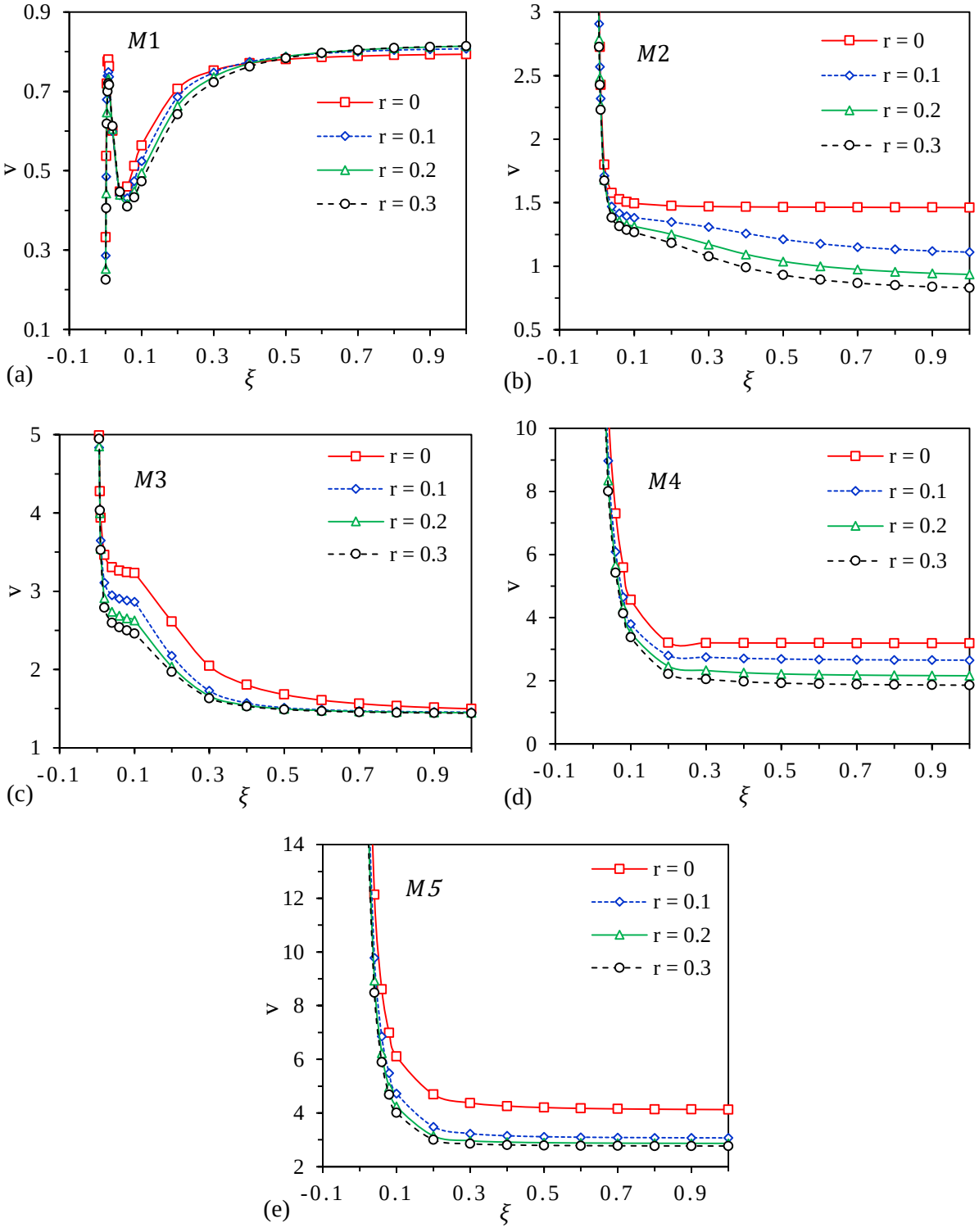

Figure 3.5. Dispersion curves for a $[0^{\circ}/45^{\circ}/90^{\circ}]_s$ laminated carbon/epoxy composite cylindrical shell coupled with a piezoelectric layer with different thickness ratios (r) and $h/R = 1/30$ for the first five wave modes ($M1, M2$, $M3$, $M4$, and $M5$) at $n = 1$ using the first-order shear deformation shell theory.

The variation of the non-dimensional wave phase velocity (v) with the changes of the piezoelectric layer thickness with the axial, circumferential, and radial polarizations for a $[0^{\circ}/45^{\circ}/90^{\circ}]_s$ laminated carbon/epoxy composite cylindrical shell with $h/R = 1/30$ is shown in Fig. 3.6 for the first five wave modes ($M1, M2$, $M3$, $M4$, and $M5$) at $\xi = 0.01$ and $n = 1$. As it is clearly shown, for the first three wave modes ($M1$, $M2$, and $M3$), for all three poling directions, the non-dimensional wave phase velocity decreases with the increase of the piezoelectric electric layer thickness ratio (r); while at wave modes 4 and 5 ($M4$ and $M5$), the non-dimensional wave phase velocity for all three poling directions decreases first for $r \leq 0.05$, and then it increases with the increase of the piezoelectric electric layer thickness ratio (r). For the first wave mode ($M1$), the circumferential and radial polarizations lead to the highest and lowest values of the non-dimensional wave phase velocities with the increase of the piezoelectric layer thickness ratio (r), respectively (see Fig. 3.6 a). For wave mode 2 ($M2$), the reduction of the non-dimensional wave phase velocity with the increment of r for the axial poling is the slowest, and the radial poling leads to the fastest reduction of the non-dimensional wave phase velocity and the lowest wave phase velocity values as well (see Fig. 3.6 b). For wave mode 3 ($M3$), the radial polarization also leads to faster decrease of the non-dimensional wave phase velocity with the increase of r, while the axial and circumferential polarizations have the same decrease trend of the non-dimensional wave phase velocity with the increase of r (see Fig. 3.6 c). For wave modes 4 and 5 ($M4$, and $M5$), for $r \leq 0.05$, all three polarizations lead to similar results, and at higher r, the results of the axial and circumferential polarizations coincide completely and the radial polarization provides slower increase of the wave phase velocity with the increment of the piezoelectric electric layer thickness ratio (r) (see Fig. 3.6 d and e). Thus, it can be concluded that for wave modes 1, 2, and 3 (M1-M3), the radial polarization leads to faster decrement of the wave phase velocity, and for wave

modes 4 and 5 ($M4$ and $M5$), it causes to slower increment of the wave phase velocity as the piezoelectric layer thickness increases. Furthermore, depending on the wave mode, various trends for wave phase velocity versus piezoelectric layer thickness are obtained. In summary, the effect of the piezoelectric layer thickness on wave behavior for radial polarization is lower than its effect for other two polarization directions.

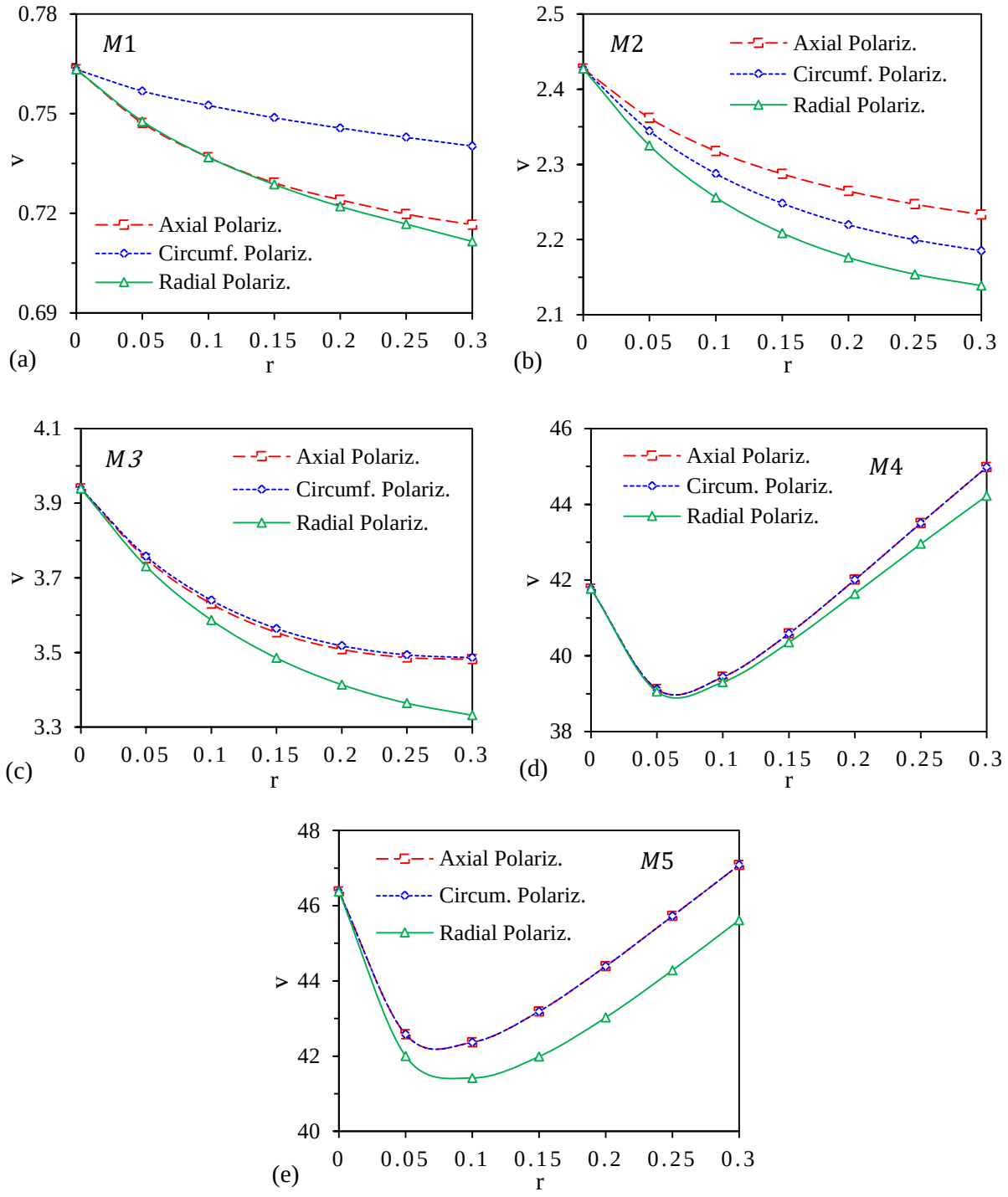

Figure 3.6. Variation of the non-dimensional wave phase velocity (v) with the piezoelectric thickness ratio (r) for a $[0^{\circ}/45^{\circ}/90^{\circ}]_s$ laminated carbon/epoxy composite cylindrical shell coupled with the piezoelectric layer with axial, circumferential, and radial polarizations when $h/R = 1/30$ at $\xi = 0.01$ and $n = 1$ for the first five wave modes ($M1, M2$, $M3$, $M4$, and $M5$).

3.2.3. Effect of Stacking Sequence on Wave Dispersion Solutions

The effects of stacking sequence on wave dispersion behaviors of a piezoelectric coupled laminated carbon/epoxy composite shell with $r = 0.1$ and $h/R = 1/30$ are illustrated in Fig. 3.7 for the first five wave modes ($M1, M2, M3, M4,$ and $M5$) at $n = 1$ using the first-order shear deformation shell theory. For this purpose, $[45^{\circ}/-45^{\circ}]_s$, $[0^{\circ}/90^{\circ}]_s$, and $[0^{\circ}/45^{\circ}/90^{\circ}]_s$ stacking sequences are considered for the host composite shell. There is a noticeable difference between the dispersion curves of these three stacking sequences. For the first wave mode ($M1$), angle-ply stacking sequence, $[45^{\circ}/-45^{\circ}]_s$, has lower wave phase velocities than $[0^{\circ}/90^{\circ}]_s$ and $[0^{\circ}/45^{\circ}/90^{\circ}]_s$ sequences, particularly at lower axial wavenumbers ($\xi < 0.7$); and at higher axial wavenumbers (specially $\xi \geq 0.7$), there is no significant difference between the dispersion curves of these three stacking sequences; however, within different axial wavenumbers, the wave phase velocities of $[0^{\circ}/90^{\circ}]_s$, and $[0^{\circ}/45^{\circ}/90^{\circ}]_s$ stacking sequences are very close to each other (see Fig. 3.7a). For the second wave mode ($M2$), the dispersion curve trend is different, where the $[45^{\circ}/-45^{\circ}]_s$ stacking sequence has the highest wave phase velocities and the cross-ply lamination $[0^{\circ}/90^{\circ}]_s$ has the lowest ones (see Fig. 3.7b). For wave mode 2 of $[45^{\circ}/-45^{\circ}]_s$ composite stacking sequence, sharp wave phase velocity increment is observed at non-dimensional axial wavenumber around 0.02, while this phenomenon is not noticed for the composites with $[0^{\circ}/90^{\circ}]_s$, and $[0^{\circ}/45^{\circ}/90^{\circ}]_s$ stacking sequences. At lower axial wavenumbers of the third wave mode ($M3$) ($\xi < 0.2$), wave phase velocities for the angle-ply lamination $[45^{\circ}/-45^{\circ}]_s$ are lower than those of the other two stacking sequences, while at higher axial wavenumbers, the cross-ply lamination $[0^{\circ}/90^{\circ}]_s$ leads to the lowest non-dimensional wave phase velocities and the $[45^{\circ}/-45^{\circ}]_s$ stacking sequence is with the highest ones (see Fig. 3.7c). In wave mode 3 ($M3$), there is a crossing point in the curves (at $\xi = 0.2$) showing the different wave phase velocity

variation trends after the certain wavenumber for different composite designs, which could not be seen without considering the shear effects. Dispersion curves for the fourth and fifth wave modes ($M4$ and $M5$) have similar trends and as shown in Fig. 3.7d and e, the cross-ply lamination $[0^\circ/90^\circ]_s$ has the highest non-dimensional wave phase velocities and the angle-ply stacking sequence $[45^\circ/-45^\circ]_s$ has the lowest ones. Thus, in all five wave modes, the non-dimensional wave phase velocities of the $[0^\circ/45^\circ/90^\circ]_s$ stacking sequence within different axial wavenumbers are between those of the $[45^\circ/-45^\circ]_s$ and $[0^\circ/90^\circ]_s$ sequences. Therefore, the present analytical model can determine the effects of stacking sequence on wave dynamics of smart laminated composite cylindrical shells. It can be concluded that various stacking sequences have clear effects on wave dispersion behaviors of smart laminated composite cylindrical shells due to their effects on the resultant constitutive equations, and depending on the wavenumber and wave mode, various trends for dispersion curves are attained for different stacking sequences. These results are important showing the composite effects on wave motion with different composite designs which means why the wave propagation in smart composite shells is studied in this thesis.

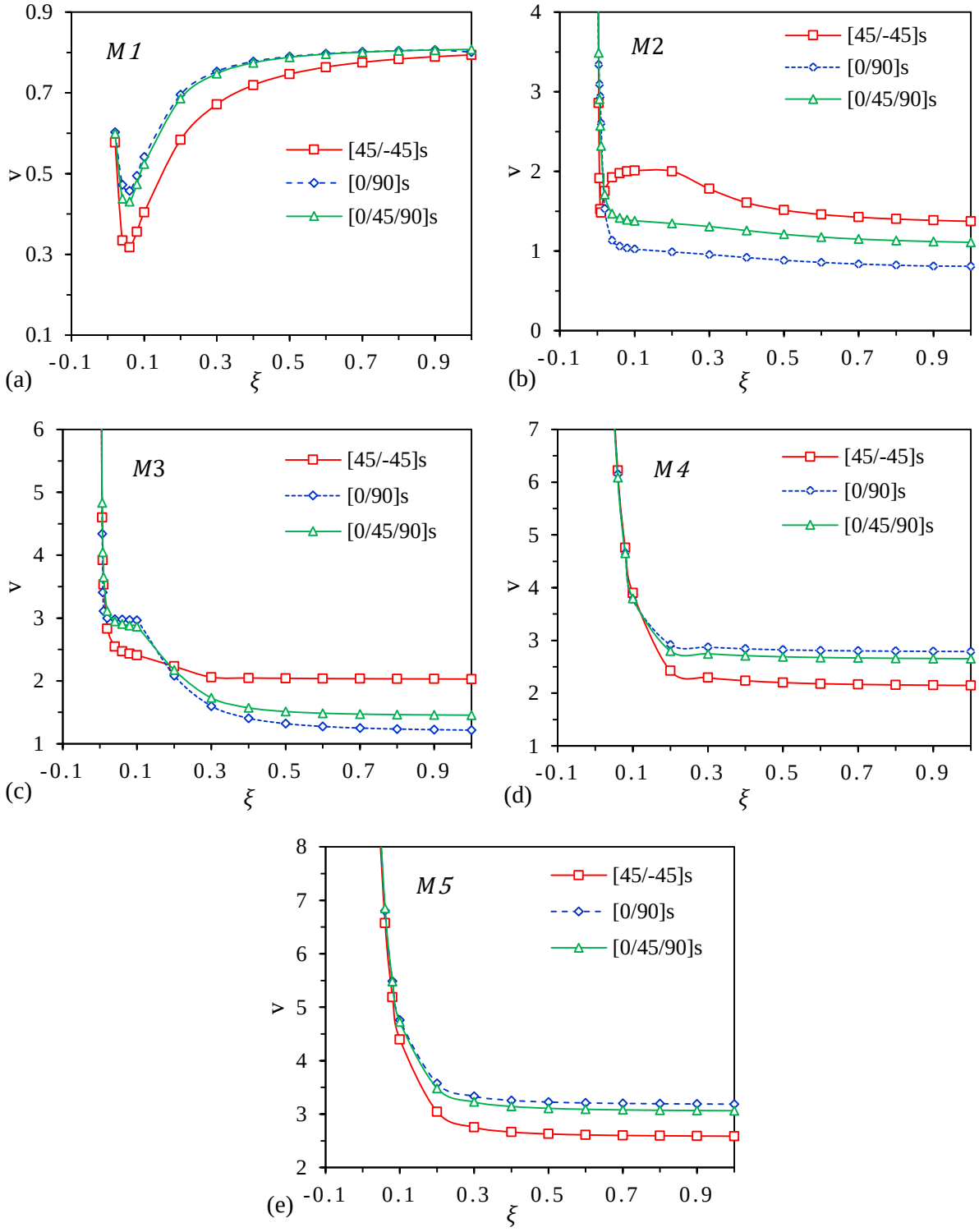

Figure 3.7. Dispersion curves for $[45^{\circ}/-45^{\circ}]_s$, $[0^{\circ}/90^{\circ}]_s$, and $[0^{\circ}/45^{\circ}/90^{\circ}]_s$ laminated carbon/epoxy composite cylindrical shells coupled with a piezoelectric layer with $r = 0.1$ and $h/R = 1/30$ for the first five wave modes ($M1, M2$, $M3$, $M4$, and $M5$) at $n = 1$ using the first-order shear deformation shell theory.

3.2.4. Comparison of Different Shell Theories on Wave Dispersion Solutions

The dispersion characteristics for a $[0^{\circ}/45^{\circ}/90^{\circ}]_s$ laminated carbon/epoxy composite cylindrical shell coated with a piezoelectric layer at the top surface with $r = 0.1$ by different shell theories are compared in Fig. 3.8 for the first three wave modes ($M1, M2,$ and $M3$) at $n = 1$ when $h/R = 1/30$. Dispersion solutions are provided using the membrane shell theory, the Love bending shell theory, and the first-order shear deformation shell theory (FSDT). As shown clearly in Fig. 3.8, the three shell theories lead to similar wave phase velocities at lower axial wavenumbers ($\xi \leq 0.04$ for $M1$, $\xi \leq 0.2$ for $M2$, and $\xi \leq 0.1$ for $M3$). However, at higher axial wavenumbers, the wave phase velocities obtained by the three shell models contrast each other completely. For the first wave mode ($M1$) at higher axial wavenumbers, the wave phase velocities computed by the membrane shell model are lower than those of other shell models, the wave phase velocities provided by the Love bending shell model have the highest values, and the results by the FSDT presents a compromise for the non-dimensional wave phase velocity (see Fig. 3.8a). However, for wave modes 2 and 3 ($M2$ and $M3$) at higher axial wavenumbers, the FSDT provides the lowest estimate of the non-dimensional wave phase velocity, while the Love bending shell theory provides the highest estimate of the non-dimensional wave phase velocity (see Fig. 3.8b and c). Therefore, it can be concluded that the Love bending shell theory leads to upper limit of the wave phase velocity and the transverses shear and rotary inertia have decreasing effect on the wave phase velocity at higher wave modes ($M2$ and $M3$).

The finding for isotropic host materials such as aluminum shell is different. For example, in wave mode 3 ($M3$), three shell theories lead to similar results at $\xi \leq 0.3$ for a piezoelectric coupled aluminum shell [98]. This indicates that the shear effects on dynamics of composite shells are more important and significant, where for composites at lower axial wavenumbers ($\xi > 0.04$ for $M1$,

$\xi > 0.2$ for $M2$, and $\xi > 0.1$ for $M3$) this discrepancy on wave behaviors occurs, while for isotropic materials, difference between various shell theories was observed at higher axial wavenumbers especially for higher wave modes (for example $\xi > 0.3$ for $M3$) [98].

The effects of transverse shear and rotary inertia are important for the applications that higher wavenumbers (frequencies) are required such as structural health monitoring by NDE and design of smart composites for energy harvesting, where we need to consider their effects in modeling accurately.

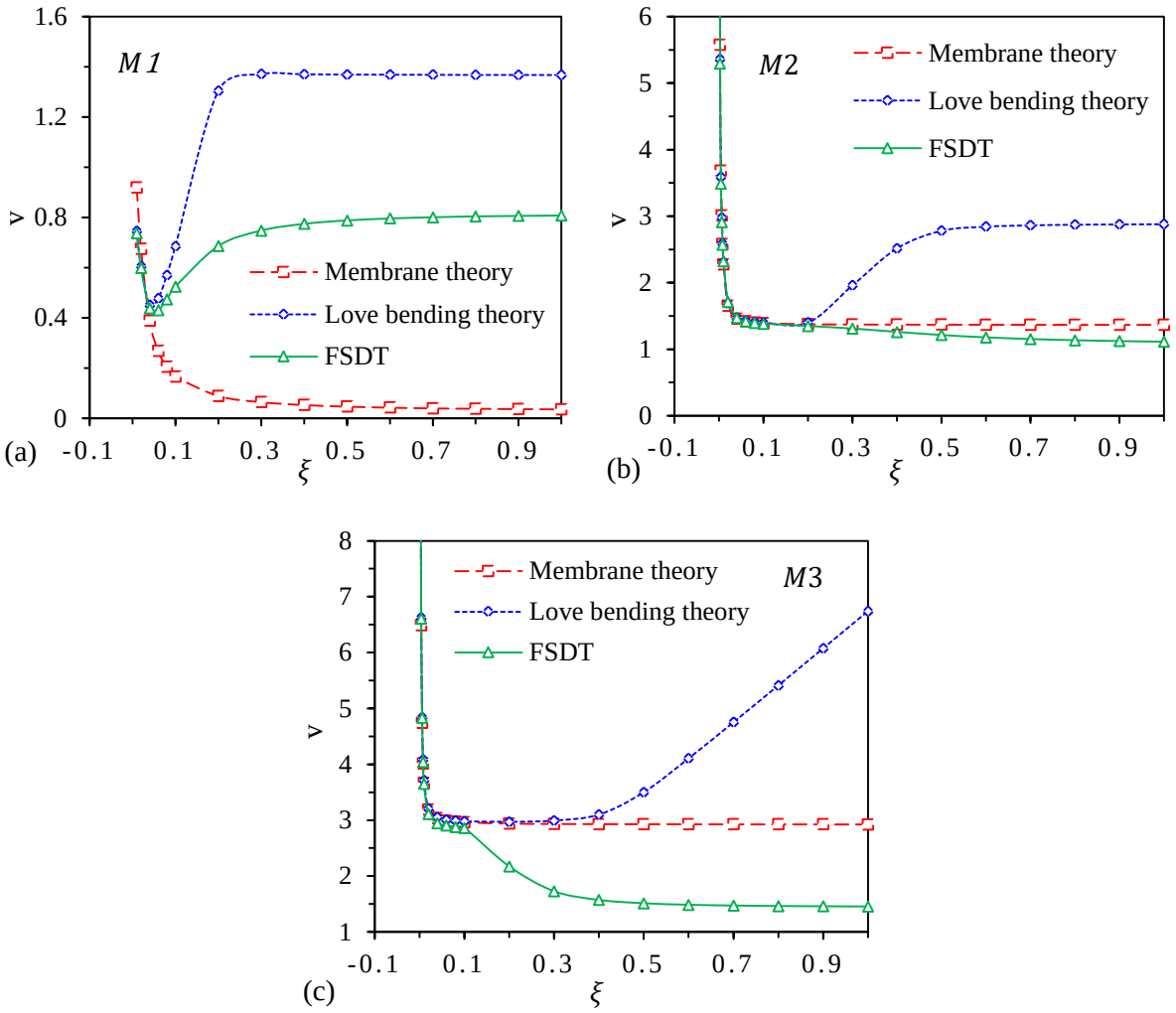

Figure 3.8. Comparison of dispersion curves of a $[0^{\circ}/45^{\circ}/90^{\circ}]_s$ laminated carbon/epoxy composite cylindrical shell coupled with a piezoelectric layer with $r = 0.1$ and $h/R = 1/30$ for the first three wave modes ($M1, M2$, and $M3$) at $n = 1$ by different shell theories.

The variations of the non-dimensional wave phase velocity (v) as a function of the circumferential wavenumber (n) are plotted in Fig. 3.9 for a $[0^{\circ}/45^{\circ}/90^{\circ}]_s$ laminated carbon/epoxy composite cylindrical shell integrated with a piezoelectric layer at the top surface with $r = 0.1$, and $h/R = 1/30$, at $\xi = 0.1$ and 1, by different shell theories for the first three wave modes ($M1, M2$, and $M3$). At low axial wavenumber $\xi = 0.1$; for wave mode 1 ($M1$), based on the Love bending shell theory and the FSDT, the non-dimensional wave phase velocity

increases slightly as n increases (from 0.6548 to 0.8099 for the Love bending shell model, and from 0.522 to 0.6115 for the FSDT within $0 \leq n \leq 10$), while for the membrane shell theory, the non-dimensional wave phase velocity changes smoothly with the increase of n (from 0.1685 to 0.1265 within $0 \leq n \leq 10$) (see Fig. 3.9a); for wave modes 2 and 3 ($M2$ and $M3$), the three shell models lead to similar trends of the wave phase velocity curve and the velocity increases sharply with the increase of n (from 1.3521 to 2.0086 for $M2$, and from 2.8231 to 3.5145 for $M3$ within $0 \leq n \leq 10$) (see Fig. 3.9c and e). However, at high axial wavenumber $\xi = 1$; the three shell models provide a smooth variation of the dispersion curve with the variation of circumferential wavenumber (n) for all three wave modes (see Fig. 3.9b, d and f). It is clearly shown that for the first three wave modes, the Love bending shell theory exhibits upper limit of the non-dimensional wave phase velocity at both low and high axial wavenumbers ($\xi = 0.1$ and 1). However, for wave mode 1 ($M1$), the membrane shell model leads to the lowest wave phase velocities among the other shell models at both low and high axial wavenumbers ($\xi = 0.1$ and 1); for wave mode 2 ($M2$), at $\xi = 0.1$, the three shell models lead to similar wave phase velocities, and at $\xi = 1$, the FSDT provides the lowest non-dimensional wave phase velocities; and finally for the third wave mode ($M3$), the results of the membrane shell theory and the FSDT coincide completely when $\xi = 0.1$, and at $\xi = 1$, again the FSDT leads to the lowest estimate of the non-dimensional wave phase velocity. It is interesting that we observe the same discrepancy between wave phase velocities obtained by different shell models within various circumferential wavenumbers (n) as that attained within various axial wavenumbers in Fig. 3.8. Therefore, we can infer that at higher axial wavenumbers, based on different shell theories, the variation of non-dimensional wave phase velocity with n is negligible, and wave motion is independent of the circumferential direction and

circumferential wavenumber (n), which indicates axisymmetric wave motion can be considered at higher axial wavenumbers.

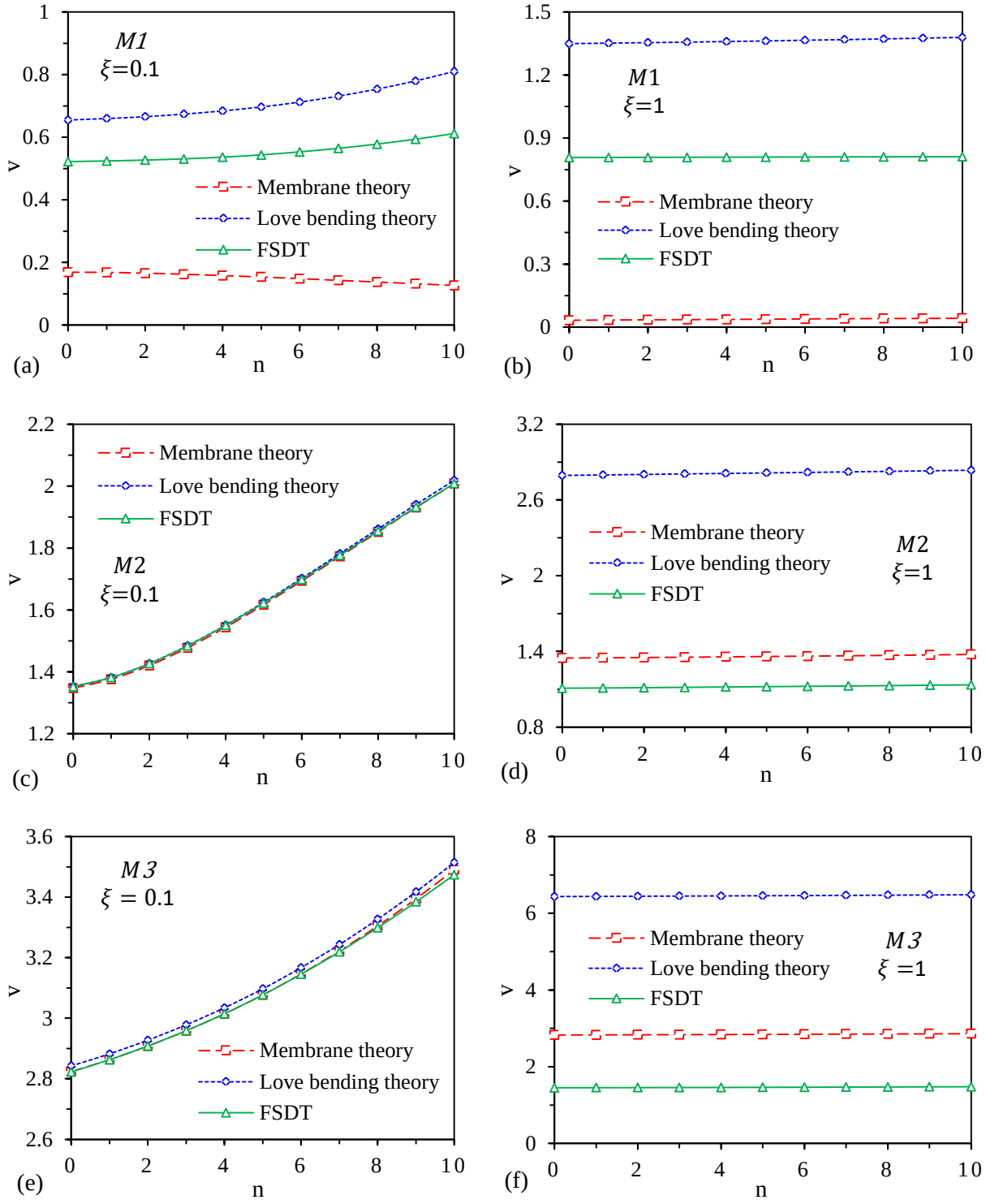

Figure 3.9. Effect of the circumferential wavenumber (n) on the non-dimensional wave phase velocity (v) for the first three wave modes ($M1, M2$, and $M3$) of a $[0^{\circ}/45^{\circ}/90^{\circ}]_s$ laminated carbon/epoxy composite cylindrical shell coupled with a piezoelectric layer with $r = 0.1$ and $h/R = 1/30$ at $\xi = 0.1$ and 1 by different shell theories.

The variations of the non-dimensional wave phase velocity (v) with the changes of the piezoelectric layer thickness based on the three shell theories for a $[0^{\circ}/45^{\circ}/90^{\circ}]_s$ laminated carbon/epoxy composite cylindrical shell with $h/R = 1/30$ are shown in Fig. 3.10 for the first three wave modes ($M1, M2,$ and $M3$) at $\xi = 0.1$ and 1. For the first wave mode ($M1$), based on the membrane shell model, the effect of the piezoelectric layer thickness on the dispersion curve is not significant at both $\xi = 0.1$ and 1; while the Love bending shell theory leads to the decrease of non-dimensional wave phase velocity as the thickness of the piezoelectric layer increases at both $\xi = 0.1$ and 1; and the FSDT provides a slight reduction in the non-dimensional wave phase velocity (from 0.5639 to 0.4729) with the thickness increment at $\xi = 0.1$, and a smooth variation at $\xi = 1$. Furthermore, in wave mode 1 ($M1$), the membrane shell model provides the lowest wave phase velocities and the Love bending shell model leads to the highest ones (see Fig. 3.10a and b). In wave mode 2 ($M2$), the increase of the piezoelectric layer thickness leads to the non-dimensional wave phase velocity reduction for the three shell models at both $\xi = 0.1$ and 1, while at $\xi = 0.1$, the results of the three shell models are similar, but at $\xi = 1$, the FSDT and the Love bending shell theory lead to the lowest and highest estimates of the non-dimensional wave phase velocity, respectively (see Fig. 3.10c and d). Finally, for the third wave mode ($M3$), the non-dimensional wave phase velocity decreases with the increase of the piezoelectric layer thickness for the three shell models at $\xi = 0.1$, while at $\xi = 1$, the FSDT leads to a smooth variation of the non-dimensional wave phase velocity, the membrane shell model provides a slight decrease of the non-dimensional wave phase velocity (from 3.1915 to 2.4693) with the increase of thickness, and the Love bending shell theory shows a clear non-dimensional wave phase velocity decrease (from 7.4145 to 5.762) as the piezoelectric layer thickness increases. In addition, as shown in Fig. 3.10e and f, for wave mode 3 ($M3$), the Love bending shell theory presents a higher estimate of the non-

dimensional wave phase velocity and the FSDT provides a lower estimate one at both $\xi = 0.1$ and 1. However, for all three wave modes, the Love bending shell theory exhibits upper limit of the non-dimensional wave phase velocity with the variation of the piezoelectric layer thickness at both low and high axial wavenumbers ($\xi = 0.1$ and 1).

Therefore, based on the above results, we can conclude that the developed analytical model is able to clearly portray the effects of transverse shear and rotary inertia which are very important to be included in the modeling of wave propagation in multi-layered shells stacked with the piezoelectric layers as a moderate thick shell. At lower axial wavenumbers, the effect of transverse shear is not important, while at higher axial wavenumbers, its effect is much significant and the obtained dispersion results are completely different from those of models ignoring the shear effects. It is recommended that the shear effects and rotary inertia are necessary to be included in the mathematical modeling when higher axial wavenumbers (frequencies) are desired. By including shear effects, necessary shear wave modes can be attained as well as axial, circumferential, and radial wave modes.

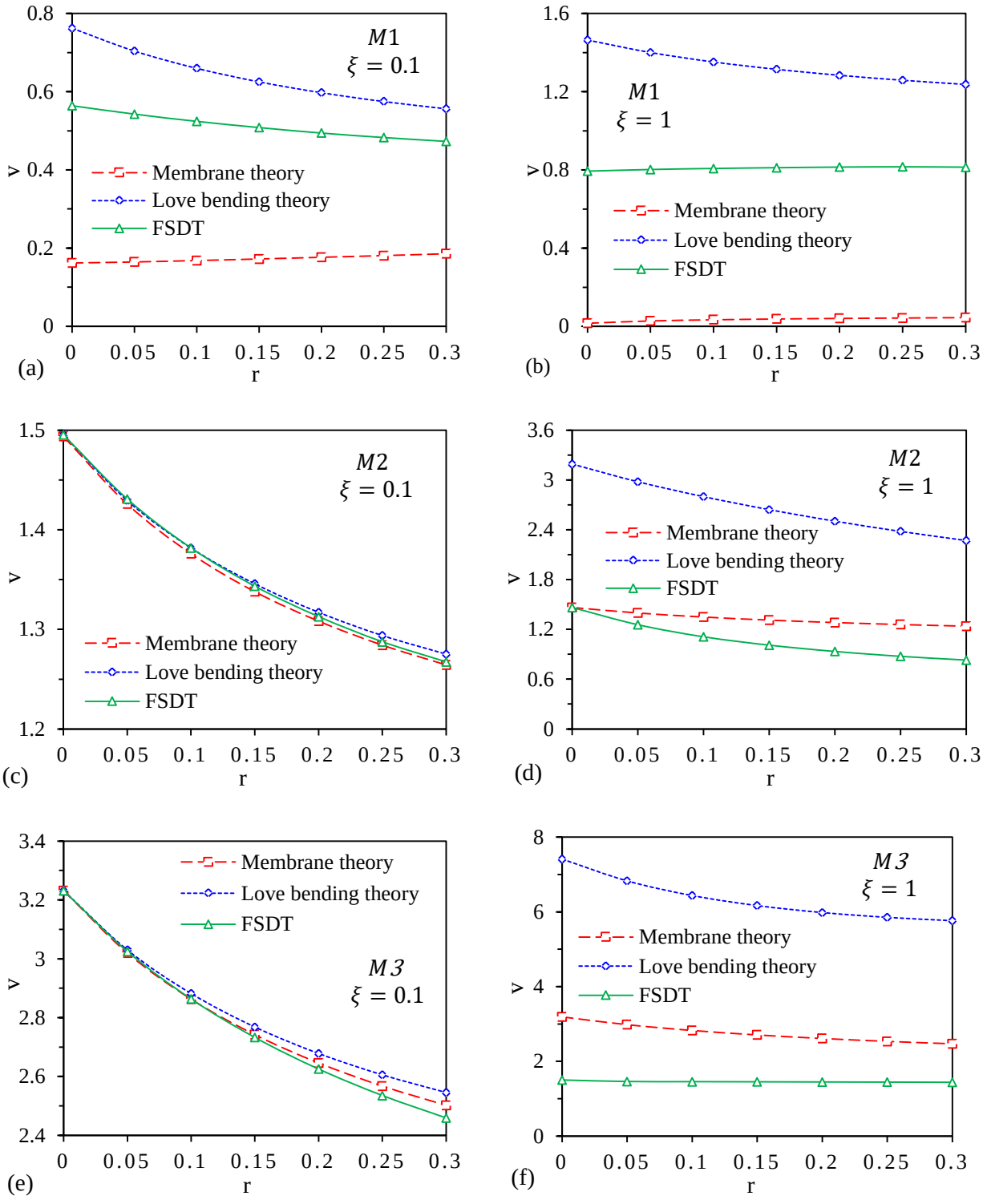

Figure 3.10. Variation of the non-dimensional wave phase velocity (v) with the piezoelectric thickness ratio (r) for a $[0^{\circ}/45^{\circ}/90^{\circ}]_s$ laminated carbon/epoxy composite cylindrical shell coupled with a piezoelectric layer with $h/R = 1/30$ for the first three wave modes ($M1, M2$, and $M3$) at $n = 1$ and $\xi = 0.1$ and 1 by different shell theories.

3.2.5. Effects of CNT Volume Fraction and Distribution on Wave Dispersion Solutions

Fig. 3.11 illustrates the effects of CNT volume fraction (f_r) and distribution on the dispersion curves of CNT-reinforced piezoelectric composite cylindrical shells with $h/R = 1/30$ within different non-dimensional axial wavenumbers (ξ) for the first wave mode ($M1$) at $n = 1$. In this example, CNTs with 0°, 45°, 90°, and random orientations are considered. As shown in Fig. 3.11, the non-dimensional wave phase velocity increases with the increase of CNT volume fraction for all four CNT distributions and this increase is higher at higher axial wavenumbers because of increasing effect of axial wavenumber on the wave phase velocity. The effect of CNT volume fraction on the variation of wave phase velocity with axial wavenumber is more noticeable for 0° orientation of CNTs, while this effect for 90° orientation is lower than that of 45°, randomly, and 0° oriented CNTs, respectively. For example, at $\xi = 1$, for 0° oriented CNTs, the non-dimensional wave phase velocity increases from 0.8324 to 1.5703 (88.64%) with the increase of CNT volume fraction from $f_r = 0$ to $f_r = 0.4$ (see Fig. 3.11a); while for 90° orientation, the increase of CNT volume fraction from 0 to 0.4 leads to the increase of the non-dimensional wave phase velocity from 0.8636 to 0.9454 (9.47%) (see Fig. 3.11c). The CNT reinforcing effect increases the wave phase velocity significantly, when the non-dimensional axial wavenumber (ξ) is larger than 0.1 for CNT orientations of 0°, 45° and random. However, this effect is not much significant for the 90° CNT orientation case. It means that the 90° CNT orientation will enhance the mechanical properties of the shell structure (such as elastic moduli) without changing the axial direction distributed wave behavior much at least for the lowest wave mode ($M1$). This phenomenon can be explained that when only axial wavenumber is increasing and the circumferential wavenumber is fixed, the wave phase velocity (the rate at which the phase of the wave propagates in space)

increases and this increase can be magnified by reinforcing the shell with CNTs along the axial wave direction because of an increase in the shell stiffness in the axial direction (x). This finding is useful for structural enhancement and health monitoring which can enhance the structure but still use similar condition monitoring process and equipment. Therefore, it is concluded that for CNTs along the direction of axial wavenumber (0° oriented CNTs), the rate of wave phase velocity increase with the increment of CNT volume fraction is higher than that for other orientations.

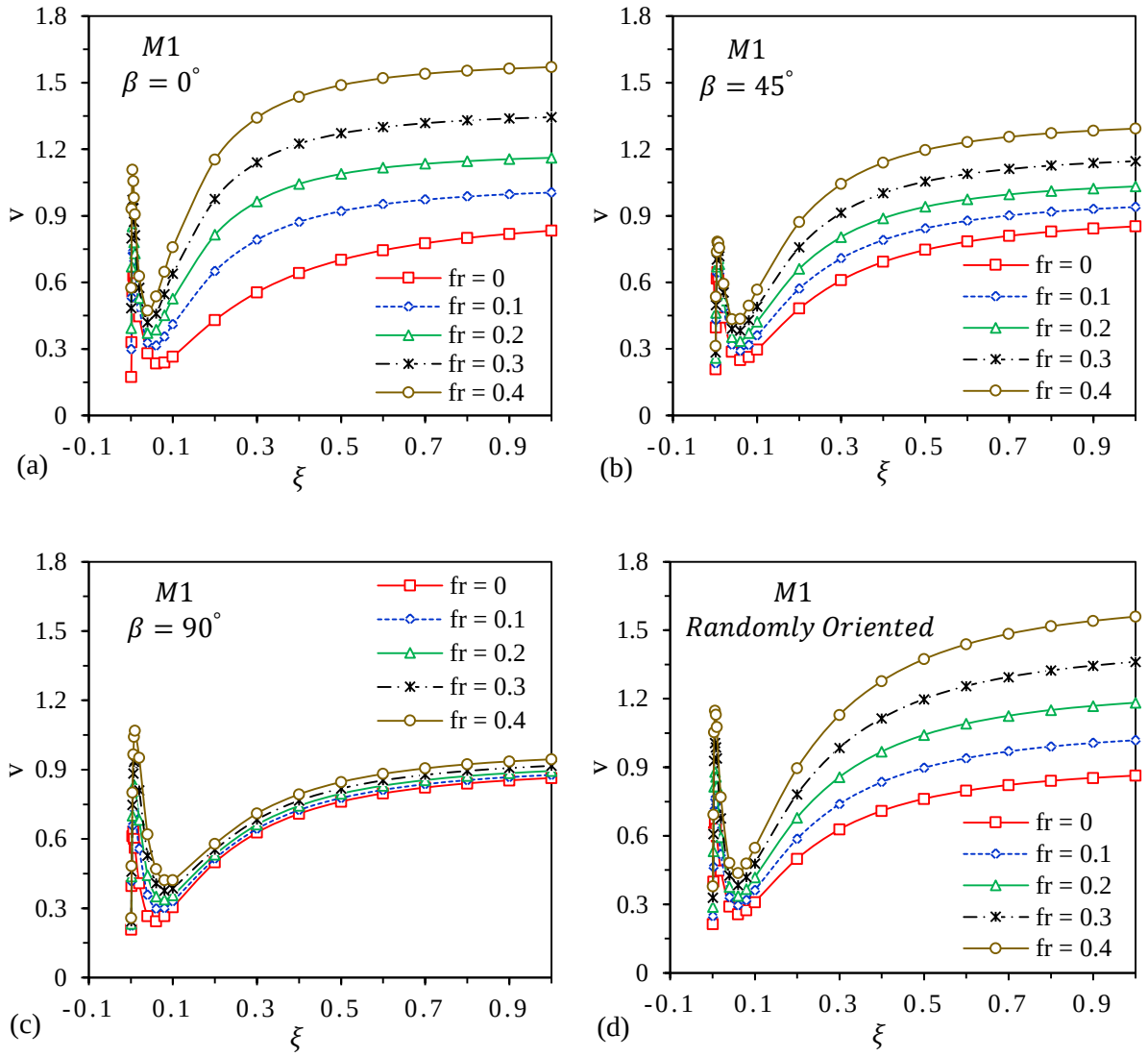

Figure 3.11. Effects of CNT volume fraction (f_r) and distribution on the variation of the non-dimensional wave phase velocity (v) with the non-dimensional axial wavenumber (ξ) for CNT-reinforced piezoelectric composite cylindrical shells with $h/R = 1/30$ for the first wave mode ($M1$) at $n = 1$.

The effect of CNT volume fraction (f_r) on the variation of the non-dimensional wave phase velocity (v) with the circumferential wavenumber (n) is depicted in Fig. 3.12 for piezoelectric composite cylindrical shells reinforced with 0°, 45°, 90°, and randomly oriented CNTs (when $h/R = 1/30$) for the wave mode 3 ($M3$) at $\xi = 0.01$. It can be seen that the wave phase velocity increases sharply with the increase of circumferential wavenumber (n), because when

circumferential wavenumber (n) increases, the wave phase velocity (representing the rate at which the phase of the wave propagates in space) and the corresponding frequency increases. As shown in Fig. 3.12, the non-dimensional wave phase velocity increases with the increase of CNT volume fraction for all four CNT distributions and this increase is higher at higher circumferential wavenumbers (n) because of increasing effect of circumferential wavenumber on the wave phase velocity. In this example, in which the axial wavenumber (ξ) is a fixed value and the circumferential wavenumber (n) is changing, the increase of CNT volume fraction influences more on the non-dimensional wave velocity when CNTs are oriented in 90° in comparison to other CNT orientations. As seen in Fig. 3.12, the rate of wave phase velocity increase for 0° oriented CNTs is lower than that for randomly, 45°, and 90° oriented CNTs, respectively. For instance, at $n = 20$, for the 0° orientation of CNTs, by increasing the CNT volume fraction from 0 to 0.4, the non-dimensional wave phase velocity increases from 18.57 to 23.62 (27.19%) (see Fig. 3.12a); while for the same situation, the non-dimensional wave phase velocity increases from 16.07 to 50.07 (211.57%) when CNTs are oriented in 90° (see Fig. 3.12c). Therefore, it can be concluded that when circumferential wavenumber (n) is changing with a fixed value of axial wavenumber, the influence of CNT enhancement on the wave phase velocity will be more significant at higher circumferential wavenumbers (n) especially for composites reinforced with 90° oriented CNTs (along the direction of the circumferential wave). This phenomenon indicates that CNTs oriented in the same direction of the circumferential wave (90°) have more significant reinforcing effect on the wave phase velocity with increasing the circumferential wavenumber (n). This phenomenon can be explained that when only circumferential wavenumber (n) is increasing and the axial wavenumber is fixed, the wave phase velocity increases and this increase can be magnified by

reinforcing the shell with CNTs along the circumferential wave direction because of an increase in the shell stiffness in the circumferential direction (θ).

Therefore, CNT volume fraction has significant effects on the wave dispersion solutions, where the effects of CNT volume fraction on the wave phase velocity for CNTs along the wave direction are relatively higher than those for other CNT orientations. On the other hand, the CNT reinforcement effect increasing the wave phase velocity is not much obvious with CNTs arranged perpendicular to the wave direction, while the composite mechanical properties (elastic moduli) are still enhanced by the CNTs. Therefore, it can be concluded that the effects of CNT volume fraction on the dispersion results are dependent on the CNT orientation and distribution.

The findings of Figs. 3.11 and 3.12 are important in design of nanocomposites used for energy harvesting application to increase the wave velocity and frequency to harvest more energies by considering the CNT orientation in the same direction of wave motion. The results of this study also helps us to design nanocomposite structures with high stiffness and lower wave phase velocity (frequency) increase without acoustic wave calibration.

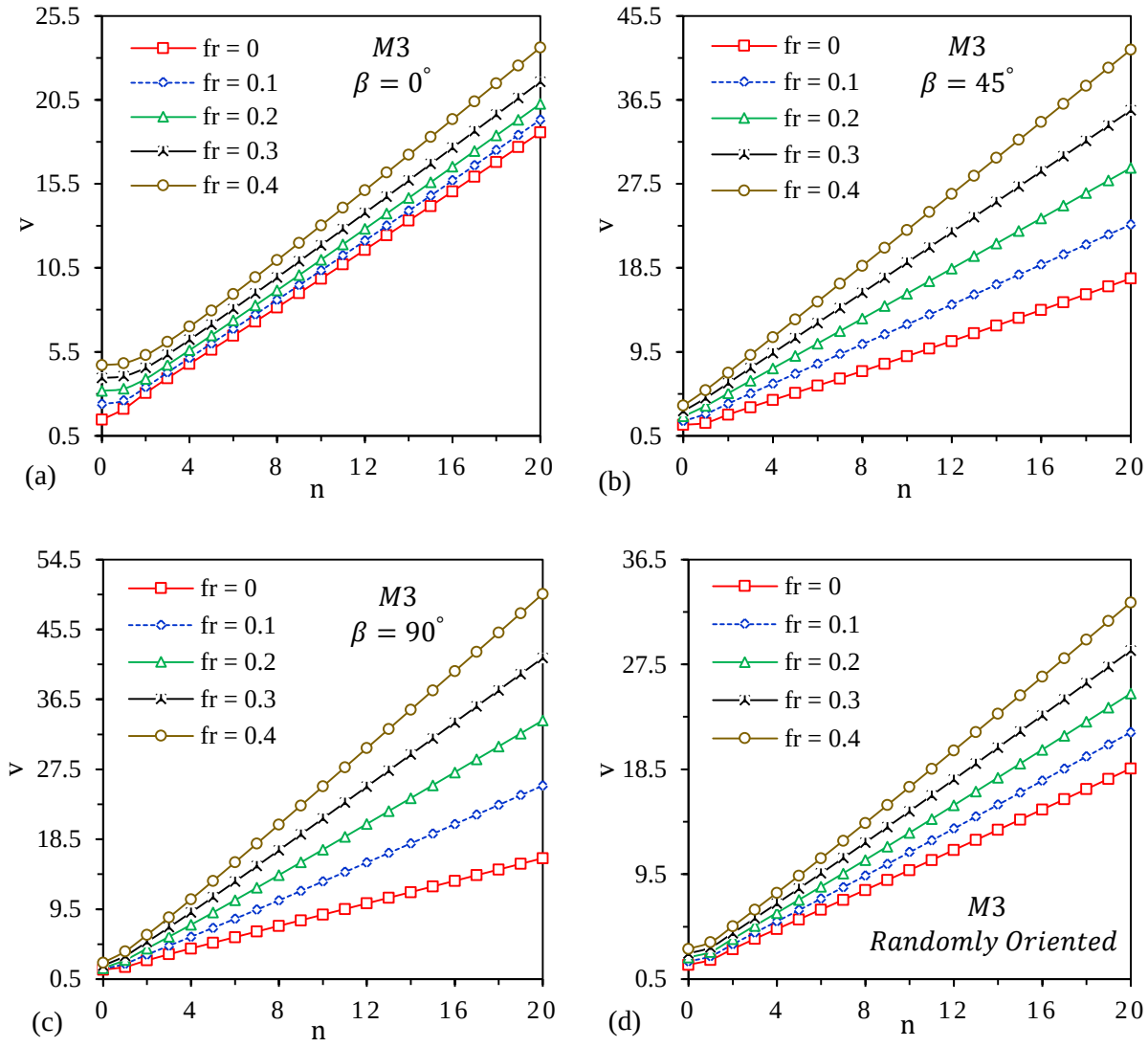

Figure 3.12. Effects of CNT volume fraction (f_r) and distribution on the variation of the non-dimensional wave phase velocity (v) with the circumferential wavenumber (n) for CNT-reinforced piezoelectric composite cylindrical shells with $h/R = 1/30$ for wave modes 3 ($M3$) at $\xi = 0.01$.

3.2.6. Effect of CNT Agglomeration on Wave Dispersion Solutions

In this section, the effect of CNT agglomeration on wave propagation behaviors of a CNT-reinforced piezocomposite cylindrical shell (with $h/R = 1/30$) are investigated by changing agglomeration parameters μ and η. As explained before in Chapter 2, agglomeration parameter μ stands for the volume fraction of inclusions in the composite and parameter η represents the volume fraction of CNTs which are concentrated in the inclusions.

Consider complete agglomeration of CNTs, i.e., $\eta = 1$ and $\mu \leq \eta$, where all CNTs are concentrated in spherical inclusions. In this case, we have only one agglomeration parameter μ (the volume fraction of inclusions). The non-dimensional wave phase velocities (v) for the first five wave modes ($M1$, $M2$, $M3$, $M4$, and $M5$) at $\xi = 0.1$ and $n = 1$ are plotted in Fig. 3.13 versus to the agglomeration parameter μ for different CNT volume fractions f_r. With the increase of parameter μ (increasing the volume fraction of inclusions), the velocity also increases where for uniformly dispersion of CNTs in the piezocomposite, i.e., $\mu = 1$, the velocity has the maximum value. This phenomenon can be explained that in the presence of a complete CNT agglomeration ($\eta = 1$), an increase of the volume fraction of inclusions (μ) leads to the increase of CNT uniformity in the composite and consequently enhances the effective elastic properties and increases the wave phase velocities. By decreasing the agglomeration parameter μ from unity, the wave phase velocity decreases very rapidly. The effect of agglomeration parameter μ on the wave phase velocity is more noticeable at higher CNT volume fraction (f_r), because at higher f_r, the parameter μ influences more on the rate of uniformity of CNTs in the matrix and the effective elastic properties. With lower CNT volume fraction ($f_r = 0.1$), the effect of inclusion volume fraction (μ) variation on the wave phase velocity change is not much significant.

To describe generally the agglomeration of CNTs, both parameters μ and η are needed. In the case $\mu \leq \eta$ and $\eta \neq 1$, we have partial CNT agglomeration in the piezocomposite. Under different CNT volume fractions (f_r), the non-dimensional wave phase velocities (v) for the first five wave modes ($M1$, $M2$, $M3$, $M4$, and $M5$) at $\xi = 0.1$ and $n = 1$ versus the agglomeration parameter η when $\mu = 0.5$ are displayed in Fig. 3.14. It is observed that an increase in the agglomeration parameter η (increasing the amount of CNTs concentrated in the inclusions) leads to the rapid decrease of the wave phase velocity of CNT-reinforced piezocomposite shells. In the case $\mu = \eta = 0.5$, where CNTs are dispersed uniformly in the piezocomposite, maximum value of the velocity is obtained. It is seen that the decrease of the wave phase velocity with the increase of parameter η is more observable at higher CNT volume fraction. This phenomenon is explained that the increase of agglomeration parameter η leads to an increase of nanotube agglomeration by the increase of amount of CNTs in the inclusions and consequently leading to the decrease of effective elastic properties and corresponding wave phase velocities. It is concluded from Figs. 3.13 and 3.14 that the CNT agglomeration reduces the wave phase velocities of CNT-reinforced piezocomposites because of its weakening influence on the effective elastic properties.

A comparison on the non-dimensional wave velocities (v) obtained based on different distributions of CNTs in a piezocomposite cylindrical shell within various non-dimensional axial wavenumbers (ξ) and circumferential wavenumbers (n), respectively, is shown in Tables 3.7 and 3.8. The results indicate that with $\mu = \eta$ (uniformly dispersed CNTs), the wave phase velocities are obtained the same as those calculated for randomly oriented CNTs, while by increasing the rate of agglomeration, the wave phase velocities decrease where the lowest velocities are attained for the complete agglomeration of CNTs within all considered non-dimensional axial wavenumbers (ξ) and circumferential wavenumbers (n).

Therefore, it can be concluded that agglomeration of CNTs in the nanocomposites leads to the decrease of the wave phase velocities because of a decrease in the effective elastic properties. Therefore, it is very important to have minimum agglomeration of CNTs in composites to reduce its effect on structural dynamics.

The developed analytical modeling can be useful to estimate the rate of agglomeration of CNTs in the composites after fabrication process by comparing the results of NDE and the results of analytical approach presented in this study. Due to the possibility of CNT agglomeration (because of low bending stiffness of CNTs) in the matrix during manufacturing process, we need to approximate the rate of agglomeration and understand its effect on the structural dynamics clearly.

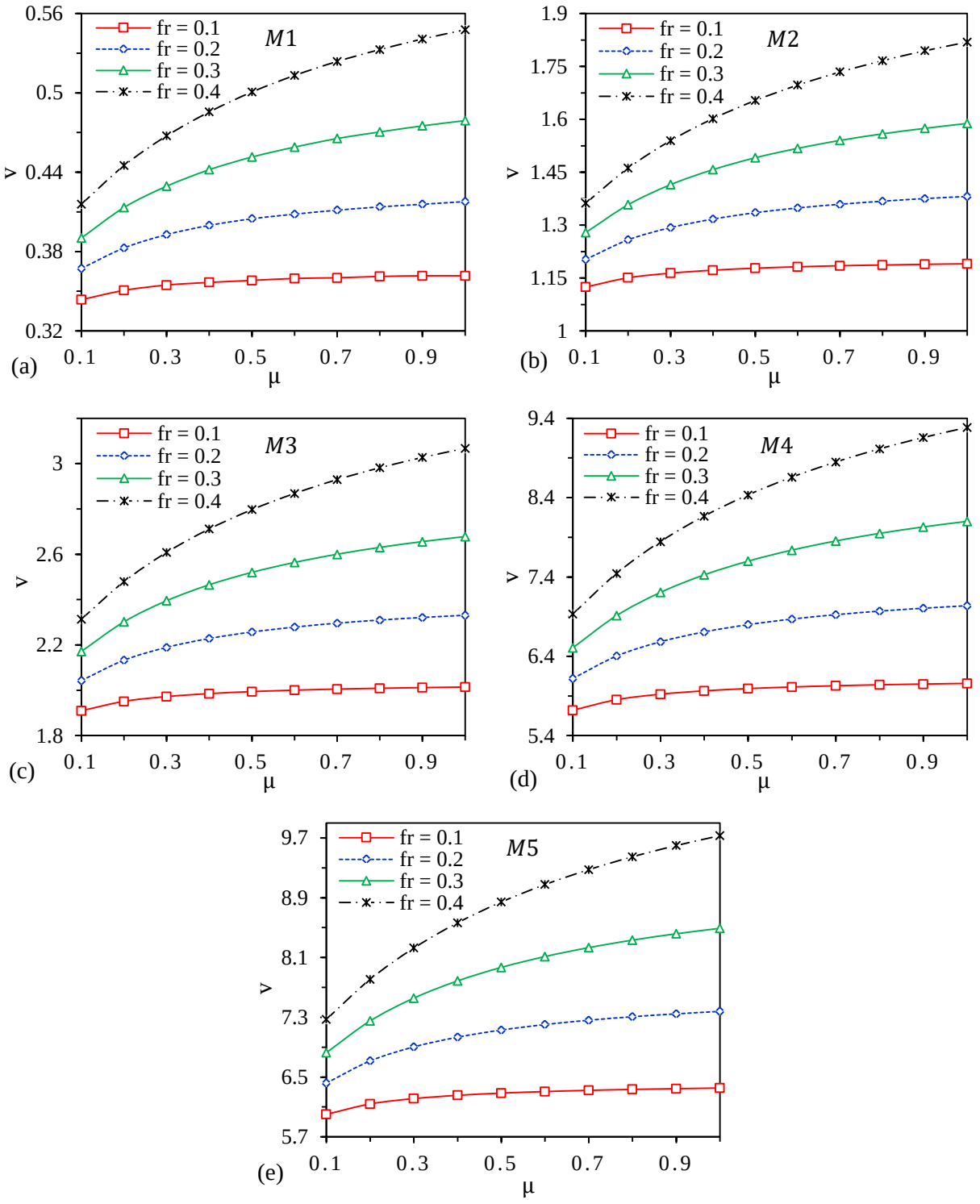

Figure 3.13. Variation of the non-dimensional wave phase velocity (v) with the agglomeration parameter μ (when $\eta = 1$) for a piezocomposite cylindrical shell with $h/R = 1/30$ for the first five wave modes ($M1$, $M2$, $M3$, $M4$, and $M5$) at $\xi = 0.1$ and $n = 1$ for various CNT volume fractions (f_r).

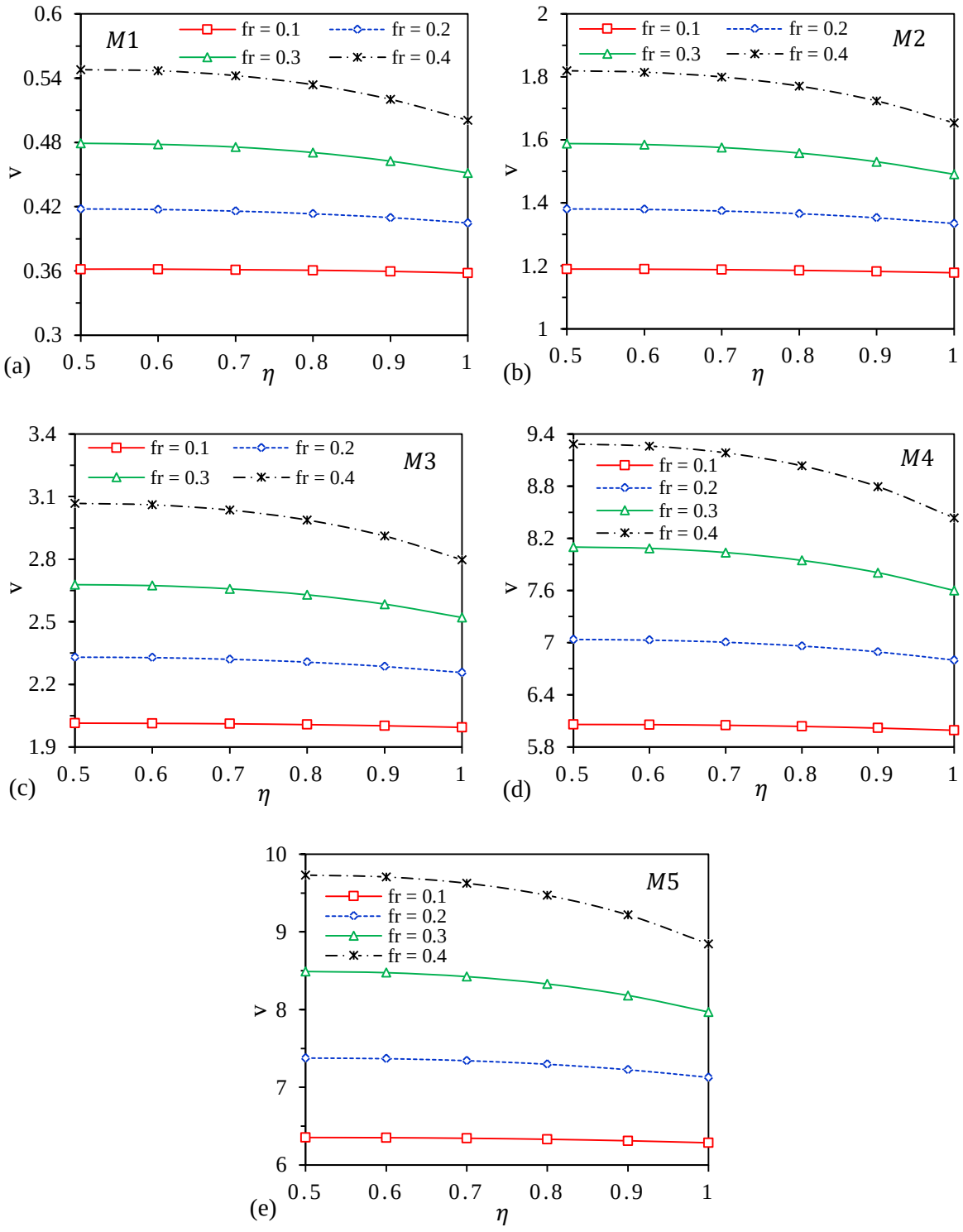

Figure 3.14. Variation of the non-dimensional wave phase velocity (v) with the agglomeration parameter η (when $\mu = 0.5$) for a piezocomposite cylindrical shell with $h/R = 1/30$ for the first five wave modes ($M1$, $M2$, $M3$, $M4$, and $M5$) at $\xi = 0.1$ and $n = 1$ for various CNT volume fractions (f_r).

Table 3.7. Comparison of non-dimensional wave phase velocities (v) for various distributions of CNTs in a piezocomposite cylindrical shell within different non-dimensional axial wavenumbers (ξ) for the first five wave modes ($M1$, $M2$, $M3$, $M4$, and $M5$) at $n = 1$ when $f_r = 0.4$ and $h/R = 1/30$.

Wave mode	CNT distribution	Non-dimensional axial wavenumber (ξ)				
		0.2	0.4	0.6	0.8	1
M1	Randomly oriented	0.8962	1.2771	1.4388	1.5176	1.5602
	Uniformly dispersed ($\mu = \eta = 1$)	0.8962	1.2771	1.4388	1.5176	1.5602
	Partially agglomerated ($\mu = 0.5, \eta = 0.75$)	0.8806	1.2545	1.4137	1.4904	1.5326
	Completely agglomerated ($\mu = 0.5, \eta = 1$)	0.8159	1.1617	1.3083	1.3795	1.4182
M2	Randomly oriented	1.8117	1.8097	1.8097	1.8092	1.8092
	Uniformly dispersed ($\mu = \eta = 1$)	1.8117	1.8097	1.8097	1.8092	1.8092
	Partially agglomerated ($\mu = 0.5, \eta = 0.75$)	1.7796	1.7775	1.777	1.777	1.777
	Completely agglomerated ($\mu = 0.5, \eta = 1$)	1.646	1.644	1.644	1.6435	1.6435
M3	Randomly oriented	3.0655	2.9079	2.3613	2.1374	2.0255
	Uniformly dispersed ($\mu = \eta = 1$)	3.0655	2.9079	2.3613	2.1374	2.0255
	Partially agglomerated ($\mu = 0.5, \eta = 0.75$)	3.0128	2.8562	2.3196	2.0993	1.9894
	Completely agglomerated ($\mu = 0.5, \eta = 1$)	2.7954	2.6414	2.1455	1.9417	1.8398
M4	Randomly oriented	4.8995	3.065	3.065	3.0645	3.0645
	Uniformly dispersed ($\mu = \eta = 1$)	4.8995	3.065	3.065	3.0645	3.0645
	Partially agglomerated ($\mu = 0.5, \eta = 0.75$)	4.8122	3.0118	3.0118	3.0118	3.0118
	Completely agglomerated ($\mu = 0.5, \eta = 1$)	4.4508	2.7944	2.7944	2.7944	2.7944
M5	Randomly oriented	5.6554	3.9494	3.5036	3.322	3.2306
	Uniformly dispersed ($\mu = \eta = 1$)	5.6554	3.9494	3.5036	3.322	3.2306
	Partially agglomerated ($\mu = 0.5, \eta = 0.75$)	5.555	3.8796	3.4424	3.2637	3.1744
	Completely agglomerated ($\mu = 0.5, \eta = 1$)	5.1414	3.5935	3.1894	3.0253	2.9425

Table 3.8. Comparison of non-dimensional wave phase velocities (v) for various distributions of CNTs in a piezocomposite cylindrical shell within different circumferential wavenumbers (n) for the first five wave modes ($M1$, $M2$, $M3$, $M4$, and $M5$) at $\xi = 0.1$ when $f_r = 0.4$ and $h/R = 1/30$.

Wave mode	CNT distribution	Circumferential wavenumber (n)					
		0	2	4	6	8	10
M1	Randomly oriented	0.5473	0.5509	0.5629	0.5845	0.6176	0.6623
	Uniformly dispersed ($\mu = \eta = 1$)	0.5473	0.5509	0.5629	0.5845	0.6176	0.6623
	Partially agglomerated ($\mu = 0.5, \eta = 0.75$)	0.5378	0.5413	0.5529	0.5744	0.6071	0.6507
	Completely agglomerated ($\mu = 0.5, \eta = 1$)	0.4997	0.5027	0.5132	0.5328	0.5629	0.6031
M2	Randomly oriented	1.8092	1.8478	1.9492	2.0817	2.2112	2.3201
	Uniformly dispersed ($\mu = \eta = 1$)	1.8092	1.8478	1.9492	2.0817	2.2112	2.3201
	Partially agglomerated ($\mu = 0.5, \eta = 0.75$)	1.777	1.8157	1.9181	2.0506	2.1796	2.287
	Completely agglomerated ($\mu = 0.5, \eta = 1$)	1.6435	1.6837	1.7891	1.9236	2.0506	2.151
M3	Randomly oriented	3.065	3.078	3.1217	3.2055	3.34	3.5267
	Uniformly dispersed ($\mu = \eta = 1$)	3.065	3.078	3.1217	3.2055	3.34	3.5267
	Partially agglomerated ($\mu = 0.5, \eta = 0.75$)	3.0123	3.0248	3.0675	3.1498	3.2828	3.4685
	Completely agglomerated ($\mu = 0.5, \eta = 1$)	2.7944	2.806	2.8446	2.9214	3.0489	3.2301
M4	Randomly oriented	9.2838	9.2858	9.2918	9.3013	9.3154	9.3329
	Uniformly dispersed ($\mu = \eta = 1$)	9.2838	9.2858	9.2918	9.3013	9.3154	9.3329
	Partially agglomerated ($\mu = 0.5, \eta = 0.75$)	9.1181	9.1201	9.1261	9.1357	9.1492	9.1668
	Completely agglomerated ($\mu = 0.5, \eta = 1$)	8.4335	8.4355	8.4405	8.4496	8.4621	8.4782
M5	Randomly oriented	9.7305	9.737	9.7571	9.7902	9.8364	9.8951
	Uniformly dispersed ($\mu = \eta = 1$)	9.7305	9.737	9.7571	9.7902	9.8364	9.8951
	Partially agglomerated ($\mu = 0.5, \eta = 0.75$)	9.5573	9.5638	9.5834	9.616	9.6617	9.7194
	Completely agglomerated ($\mu = 0.5, \eta = 1$)	8.8421	8.8481	8.8662	8.8963	8.9384	8.9921

3.2.7. Effect of CNT Orientation on Wave Dispersion Solutions

To illustrate the effect of CNT orientation on the wave phase velocity variation more clearly, the non-dimensional wave phase velocities (v) for the third and the fifth wave modes ($M3$ and $M5$) are displayed in Fig. 3.15 for a single layer of CNT-reinforced composite cylindrical shell coupled with the piezoelectric layers at the top and bottom surfaces with different CNT orientations β (in degree) for fixed values of $f_r = 0.6$, $r = 0.1$, and $h/R = 1/30$, at $\xi = 0.01, 0.1, 1$ and $n = 0,\ 1,\ 2,\ 3,\ 4,\ 5$. The material properties of polymer used as the matrix phase are assumed to be $\rho_m = 1200\ \text{kg/m}^3$, $v_m = 0.34$, and $\text{E}_m = 2.61$ and the material properties of PZT-4 are given in Table 2.2. It is obvious that at $n = 0$, for both wave modes $M3$ and $M5$ at $\xi = 0.01, 0.1, 1$, the wave phase velocity for $[\beta^\circ]$ orientation is the same as that for $[-\beta^\circ]$ orientation, indicating the non-dimensional wave phase velocity curves are symmetric with respect to 0° orientation. While, at $n = 1, 2, 3, 4$ and 5, the non-dimensional wave phase velocity curves are no longer symmetric in respect to 0° orientation, especially at $\xi = 0.01$, and 0.1, where the wave phase velocity for $[\beta^\circ]$ orientation of CNTs differs from that for $[-\beta^\circ]$ orientation, but for $[-90^\circ]$ and $[90^\circ]$ orientations, the wave phase velocities are the same. This non symmetry is more noticeable at $\xi = 0.01$, and 0.1, and the difference between the wave phase velocities for $[\beta^\circ]$ orientation and $[-\beta^\circ]$ orientation at higher n is more significant than this difference at lower n (see Fig. 3.15a-d). It can be seen that at $\xi = 1$, this non-symmetry is negligible, and also there is no significant difference between the non-dimensional wave phase velocities with different circumferential wavenumbers (n) (see Fig. 3.15e and f). Therefore, it can be concluded that at lower axial wavenumbers, circumferential wavenumber with $n > 0$ breaks the symmetry of the wave phase velocities corresponding to the negative and the positive CNT orientations. While at higher axial wavenumbers disregarding to the circumferential wavenumber, $[-\beta^\circ]$ and $[\beta^\circ]$ orientations give

approximately the same wave phase velocities. This phenomenon can be explained that when there is an axisymmetric wave propagation in the shell independent of the circumferential direction θ (when $n = 0$), we have only axial wave motion in the shell leading to symmetric wave responses for symmetric fiber angles with respect to 0°. Considering circumferential wave propagation as well as axial wave motion for lower axial wavenumbers provides an unbalance motion of the shell particles leading to asymmetry wave responses for $[\beta^{\circ}]$ and $[-\beta^{\circ}]$ fiber angles where at lower axial wavenumbers (long wavelengths) and higher circumferential wavenumbers (n), this asymmetry can become more significant. Higher axial wavenumbers may neutralize the effect of circumferential wave motion where even for higher circumferential wavenumbers, the wave responses are still symmetric with respect to 0°. This observation is in agreement with this fact that for $n > 0$, asymmetric wave response is obtained [3].

This result illustrates the importance of taking into consideration the CNT orientation in order to understand and/or optimize the dynamic response of smart laminated CNT-reinforced composite cylindrical shells for different applications. Hence, for applications that higher axial wavenumbers (or frequencies) are required or excited such as energy harvesting and structural health monitoring by NDE, $[\beta^{\circ}]$ or $[-\beta^{\circ}]$ orientation can be considered in design of smart composite shells leading to similar wave behaviors disregarding to the circumferential wavenumber (n), otherwise, for the applications with lower wavenumbers (long wavelength) such as vibration analysis, the fiber orientation should be carefully chosen.

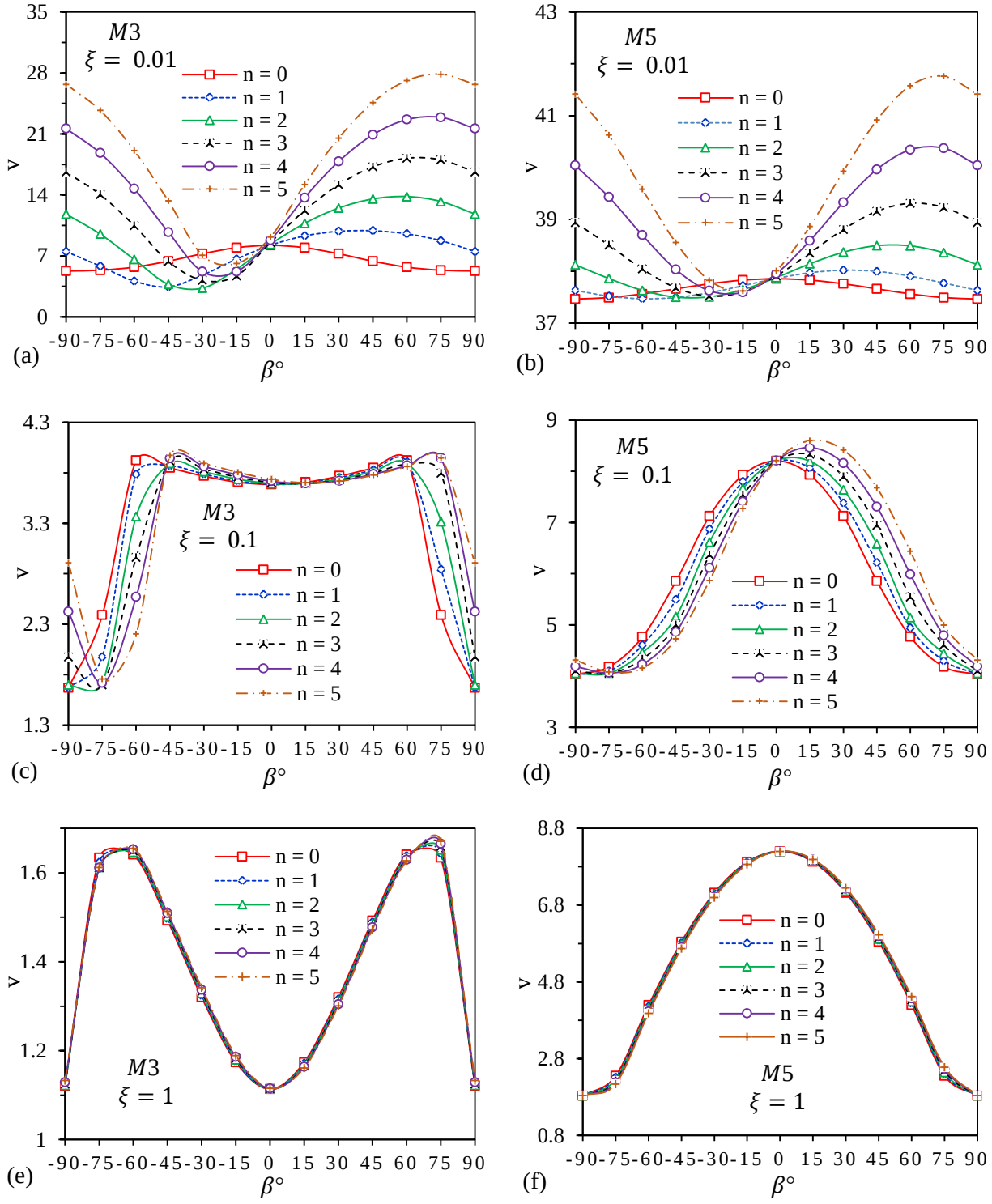

Figure 3.15. Effect of CNT orientation (β°) on the non-dimensional wave phase velocity (v) for the third and the fifth wave modes ($M3$ and $M5$) of a single layer of CNT-reinforced composite cylindrical shell coupled with the piezoelectric layers at the top and bottom surfaces with $r = 0.1$, $f_r = 0.6$, and $h/R = 1/30$ at $\xi = 0.01, 0.1, 1$, and $n = 0,\ 1,\ 2,\ 3,\ 4,\ 5$.

3.2.8. Effect of Composite Material Properties on Wave Dispersion Solutions

Fig. 3.16 shows the effect of material properties of the host substrate laminated composite cylindrical shell on the dispersion curves. We consider a piezoelectric coupled laminated composite cylindrical shell with $[0^{\circ}/45^{\circ}/90^{\circ}]_s$ stacking sequence with CNT/epoxy, carbon/epoxy, and E-glass/epoxy as the core material of the host substrate laminated composite shell for fixed values of $r = 0.1$ and $h/R = 1/30$. The material properties of epoxy (3501-6) matrix are assumed to be $\rho_m = 1200\,\mathrm{kg}/m^3$, $v_m = 0.35$, and $E_m = 4.3GPa$ [6]. CNT volume fraction in the polymer matrix is considered $f_r = 0.6$, while for carbon/epoxy and E-glass/epoxy unidirectional composites, volume fractions of carbon and E-glass fibers are considered 0.63 and 0.55, respectively [6]. Material properties of carbon/epoxy and E-glass/epoxy unidirectional composites are given in Table 2.1 and the material properties of PZT-4 are given in Table 2.2. The non-dimensional wave phase velocity (v) curves versus the non-dimensional axial wavenumbers (ξ) are obtained for the first five wave modes ($M1, M2$, $M3$, $M4$, and $M5$) at $n = 1$. As shown in Fig. 3.16, for all wave modes, CNT and E-glass fibers lead to the highest and the lowest wave phase velocities, respectively. This discrepancy in wave propagation results can be explained by different material properties of CNT, carbon, and E-glass reinforcing fibers dispersed in the epoxy matrix, where a CNT/epoxy, due to higher effective elastic moduli and strength than the carbon/epoxy and the E-glass/epoxy, leads to higher wave phase velocities. This is kind of common sense that stiffer materials lead to higher wave phase velocities, but the phenomenon is not noticed for all cases, for example, for $M1$ at higher axial wavenumbers, and for $M3$ at specific axial wavenumber 0.2. It is noted that for $M3$, the carbon and E-glass fibers lead to roughly the same wave phase velocities with axial wavenumber higher than 0.2, while the CNT fiber also leads to very close wave phase velocity at axial wavenumber 0.2. In addition, for wave mode 2, the CNT

fiber reinforced composite shows more significant wave phase velocity drop at the axial wavenumber changing from 0.2 to 0.4.

In summary, considering CNTs as the reinforcement phase leads to higher wave phase velocities than the carbon and E-glass fibers, which is related to higher specific stiffness and strength of CNTs, but researchers and designers should be careful with exceptions at some specific wave modes and wavenumbers.

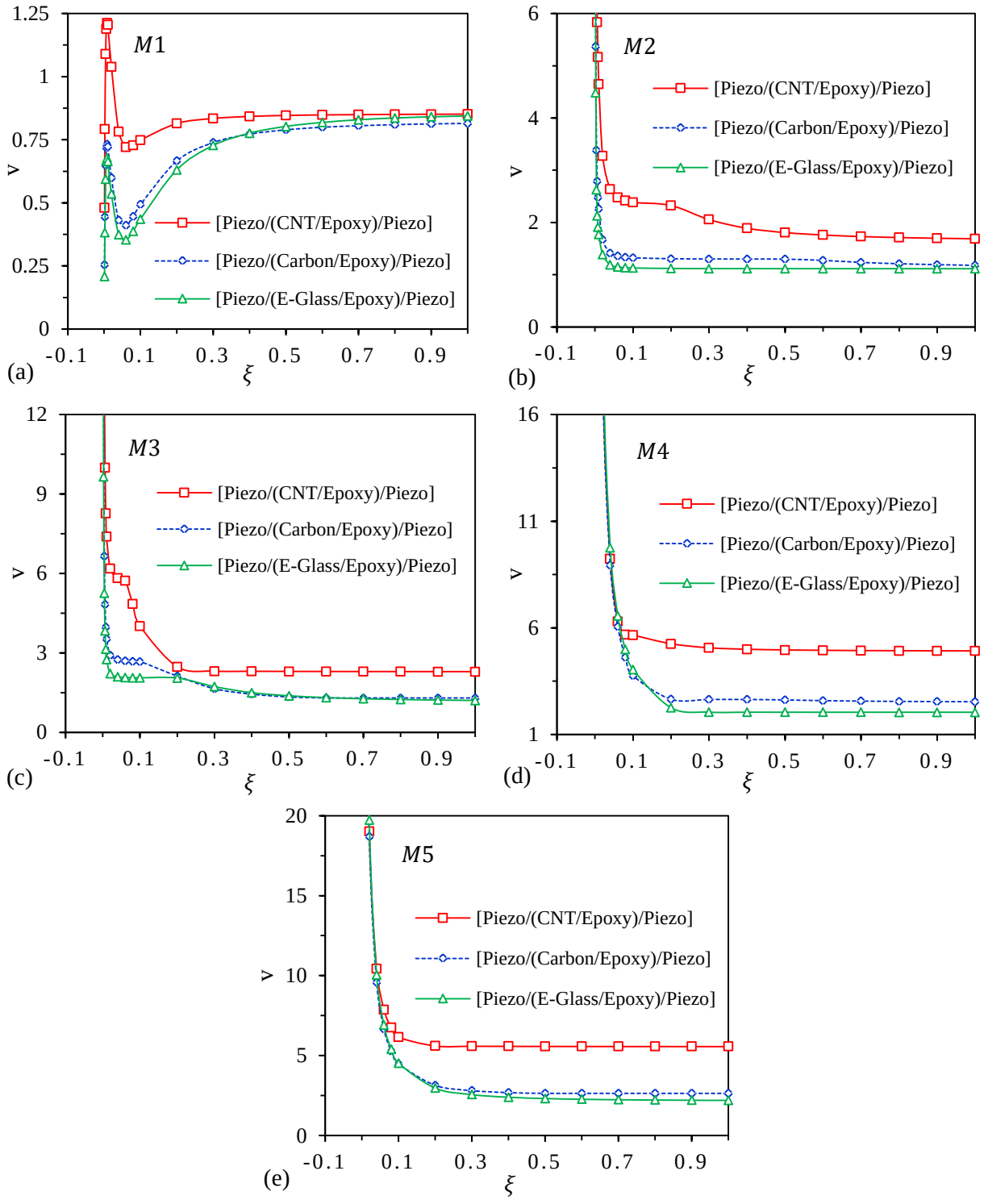

Figure 3.16. Effect of material properties of the host substrate laminated shell on the dispersion curves of a $[0^{\circ}/45^{\circ}/90^{\circ}]_s$ laminated composite cylindrical shell coupled with the piezoelectric layers at the top and bottom surfaces with $r = 0.1$, $f_r = 0.6$, and $h/R = 1/30$ for the first five modes ($M1$, $M2$, $M3$, $M4$, and $M5$) at $n = 1$.

3.2.9. Effects of Hygrothermal Environmental Conditions on Wave Dispersion Solutions

The effects of hygrothermal environmental conditions on the variation of the non-dimensional wave phase velocity (v) with the non-dimensional axial wavenumber (ξ) and the circumferential wavenumber (n) are illustrated, respectively, in Tables 3.9 and 3.10 for the first five wave modes ($M1, M2, M3, M4,$ and $M5$). For these examples, a $[0^\circ/45^\circ/90^\circ]_s$ laminated CNT-reinforced composite cylindrical shell coupled with the piezoelectric layers at the top and bottom surfaces with $f_r = 0.6$, $r = 0.1$, and $h/R = 1/30$ is considered. Seven sets of hygrothermal environmental conditions, i.e. $(\Delta T(K),\ \Delta C(\%)) = (0,0)$, $(0,2), (0,4), (200,0), (200,2), (400,0)$, and $(400,4)$, are considered. It is observed that the non-dimensional wave phase velocity decreases with the increase of temperature and/or moisture for various non-dimensional axial wavenumbers (ξ) and circumferential wavenumbers (n). This phenomenon can be explained by the temperature- and moisture-dependant material properties of the CNT reinforcing fiber and the polymer matrix. The increase of temperature/moisture reduces the elastic moduli and degrades the strength of the composites. It can also be seen that the effect of temperature change on the wave phase velocity is much more significant than the effect of moisture change. The results show that hygrothermal environmental conditions have more effect on the reduction of the wave phase velocity based on the variation of the axial wavenumber (ξ) than the variation of the circumferential wavenumber (n).

Table 3.11 describes the effects of stacking sequence of the host laminated CNT-reinforced composite cylindrical shell and hygrothermal environmental conditions on the non-dimensional wave phase velocity (v) for various non-dimensional axial wavenumbers (ξ) for wave modes 3 and 5 ($M3$ and $M5$) at $n = 1$. Three sets of stacking sequences, i.e. $[45^\circ/-45^\circ]_s$, $[0^\circ/90^\circ]_s$, and

$[0^\circ/45^\circ/90^\circ]_s$ are considered for the host laminated CNT-reinforced composite cylindrical shell coupled with the piezoelectric layers at the top and bottom surfaces with $f_r = 0.6$, $r = 0.1$, and $h/R = 1/30$. The hygrothermal environmental conditions are taken to be $(\Delta T(K),\ \Delta C(\%)) = (0, 0), (200, 2)$, and $(400, 4)$. It can be seen that for all three stacking sequences, the increase of temperature and moisture leads to the decrease of the non-dimensional wave phase velocities for different non-dimensional axial wavenumbers. For all three sets of hygrothermal environmental conditions, for wave mode 3 ($M3$), the cross-ply stacking sequence $[0^\circ/90^\circ]_s$ and the angle-ply stacking sequence $[45^\circ/-45^\circ]_s$ lead to the lowest and the highest non-dimensional wave phase velocities, respectively, while for the fifth wave mode ($M5$), the $[45^\circ/-45^\circ]_s$ and $[0^\circ/90^\circ]_s$ stacking sequences provide the lowest and the highest non-dimensional wave phase velocities, respectively. However, for both wave modes 3 and 5, the non-dimensional wave phase velocities of the $[0^\circ/45^\circ/90^\circ]_s$ stacking sequence are between those of the $[45^\circ/-45^\circ]_s$ and $[0^\circ/90^\circ]_s$ stacking sequences. So, the effect of stacking sequence on wave propagation characteristics of smart laminated composite shells is noticeable.

Therefore, the analytical model developed in section 2.5 is capable of capturing the effects of hygrothermal environmental conditions, where it indicates that increasing the temperature or the moisture leads to the decrease of the wave phase velocity, due to the degrading in the material stiffness and strength. The developed analytical model, considering the effects of hygrothermal environmental conditions, can be useful in design of smart laminated nanocomposites for energy harvesting application exposed to unexpected environmental conditions, and also for structural health monitoring application to compare the trends of wave dispersion curves for temperature/moisture variation with the dispersion curve trends obtained by the analytical model to detect any damage in the structure.

Table 3.9. Effects of temperature/moisture changes on the variation of the non-dimensional wave phase velocity (v) with the non-dimensional axial wavenumber (ξ) for a $[0^{\circ}/45^{\circ}/90^{\circ}]_s$ laminated CNT-reinforced composite cylindrical shell coupled with the piezoelectric layers at the top and bottom surfaces ($n = 1$, $f_r = 0.6$, $r = 0.1$, $h/R = 1/30$).

Wave mode	$\Delta T(K), \Delta C(\%)$	Non-dimensional axial wavenumber (ξ)				
		0.2	0.4	0.6	0.8	1
M1	(0,0)	0.8142	0.8422	0.8481	0.8502	0.8513
	(0,2)	0.8136	0.8416	0.8476	0.8497	0.8508
	(0,4)	0.8136	0.8416	0.8476	0.8497	0.8508
	(200,0)	0.7829	0.8061	0.8109	0.8125	0.8136
	(200,2)	0.7829	0.8061	0.8109	0.8125	0.8136
	(400,0)	0.7495	0.7673	0.7711	0.7727	0.7732
	(400,4)	0.7490	0.7668	0.7705	0.7721	0.7727
M2	(0,0)	2.3256	1.8904	1.7611	1.7126	1.6895
	(0,2)	2.3256	1.8904	1.7606	1.7126	1.6895
	(0,4)	2.3250	1.8898	1.7606	1.7126	1.6895
	(200,0)	2.3089	1.8629	1.7428	1.6981	1.6771
	(200,2)	2.3089	1.8629	1.7428	1.6981	1.6771
	(400,0)	2.2917	1.8349	1.7245	1.6835	1.6641
	(400,4)	2.2917	1.8349	1.7245	1.6835	1.6641
M3	(0,0)	2.4689	2.3019	2.2949	2.2911	2.2890
	(0,2)	2.4683	2.3019	2.2943	2.2911	2.2890
	(0,4)	2.4678	2.3019	2.2943	2.2911	2.2890
	(200,0)	2.4042	2.2852	2.2782	2.2744	2.2723
	(200,2)	2.4042	2.2852	2.2776	2.2744	2.2723
	(400,0)	2.3369	2.2685	2.2610	2.2572	2.2550
	(400,4)	2.3364	2.2685	2.2604	2.2572	2.2550
M4	(0,0)	5.2483	4.9913	4.9412	4.9229	4.9143
	(0,2)	5.2477	4.9913	4.9412	4.9229	4.9143
	(0,4)	5.2477	4.9913	4.9407	4.9229	4.9143
	(200,0)	5.2176	4.9822	4.9358	4.9197	4.9116
	(200,2)	5.2176	4.9822	4.9358	4.9197	4.9116
	(400,0)	5.1863	4.9725	4.9310	4.9159	4.9089
	(400,4)	5.1858	4.9725	4.9310	4.9159	4.9089
M5	(0,0)	5.6021	5.5784	5.5704	5.5666	5.5644
	(0,2)	5.6021	5.5784	5.5704	5.5666	5.5644
	(0,4)	5.6021	5.5784	5.5704	5.5666	5.5644
	(200,0)	5.5930	5.5693	5.5617	5.5574	5.5553
	(200,2)	5.5930	5.5693	5.5612	5.5574	5.5553
	(400,0)	5.5838	5.5601	5.5521	5.5483	5.5461
	(400,4)	5.5838	5.5601	5.5521	5.5483	5.5456

Table 3.10. Effects of temperature/moisture changes on the variation of the non-dimensional wave phase velocity (v) with the circumferential wavenumber (n) for a $[0^\circ/45^\circ/90^\circ]_s$ laminated CNT-reinforced composite cylindrical shell coupled with the piezoelectric layers at the top and bottom surfaces ($\xi = 0.1$, $f_r = 0.6$, $r = 0.1$, $h/R = 1/30$).

Wave mode	$\Delta T(K), \Delta C(\%)$	Circumferential wavenumber (n)					
		0	2	4	6	8	10
M1	(0,0)	0.7533	0.7452	0.7468	0.7608	0.7883	0.8271
	(0,2)	0.7533	0.7452	0.7468	0.7608	0.7883	0.8271
	(0,4)	0.7533	0.7452	0.7463	0.7608	0.7878	0.8265
	(200,0)	0.7350	0.7258	0.7264	0.7393	0.7646	0.8018
	(200,2)	0.7350	0.7258	0.7264	0.7393	0.7646	0.8018
	(400,0)	0.71450	0.7043	0.7032	0.7145	0.7387	0.7738
	(400,4)	0.71450	0.7043	0.7027	0.7145	0.7382	0.7732
M2	(0,0)	2.2841	2.5157	2.8475	3.2224	3.6022	3.9663
	(0,2)	2.2836	2.5157	2.8475	3.2224	3.6022	3.9663
	(0,4)	2.2836	2.5157	2.8475	3.2224	3.6022	3.9663
	(200,0)	2.2669	2.5017	2.8357	3.2122	3.5925	3.9566
	(200,2)	2.2669	2.5017	2.8357	3.2117	3.5925	3.9566
	(400,0)	2.2496	2.4872	2.8233	3.2014	3.5828	3.9458
	(400,4)	2.2496	2.4872	2.8233	3.2014	3.5828	3.9458
M3	(0,0)	3.9884	4.0347	4.0972	4.1726	4.2593	4.3552
	(0,2)	3.9878	4.0342	4.0966	4.1721	4.2588	4.3547
	(0,4)	3.9873	4.0336	4.0956	4.1715	4.2582	4.3541
	(200,0)	3.8397	3.8887	3.9539	4.0325	4.1225	4.2216
	(200,2)	3.8392	3.8882	3.9534	4.032	4.1220	4.2205
	(400,0)	3.6803	3.7320	3.8004	3.8823	3.9760	4.0794
	(400,4)	3.6787	3.7309	3.7988	3.8812	3.9744	4.0783
M4	(0,0)	5.5558	5.7578	6.0029	6.2954	6.4182	6.5259
	(0,2)	5.5558	5.7578	6.0029	6.2954	6.4177	6.5254
	(0,4)	5.5558	5.7578	6.0024	6.2948	6.4177	6.5248
	(200,0)	5.5467	5.7492	5.9937	6.2259	6.3202	6.4284
	(200,2)	5.5467	5.7492	5.9937	6.2254	6.3196	6.4279
	(400,0)	5.5375	5.7400	5.9846	6.1241	6.2184	6.3272
	(400,4)	5.5370	5.7400	5.9846	6.1230	6.2173	6.3261
M5	(0,0)	6.1268	6.1801	6.2464	6.3277	6.6460	7.0500
	(0,2)	6.1262	6.1796	6.2458	6.3272	6.6460	7.0500
	(0,4)	6.1257	6.1790	6.2453	6.3266	6.6460	7.0495
	(200,0)	6.0271	6.0805	6.1473	6.2889	6.6369	7.0398
	(200,2)	6.0266	6.0799	6.1467	6.2889	6.6369	7.0398
	(400,0)	5.9232	5.9770	6.0444	6.2798	6.6272	7.0301
	(400,4)	5.9221	5.9760	6.0438	6.2792	6.6272	7.0295

Table 3.11. Effects of temperature/moisture changes and stacking sequence on the variation of the non-dimensional wave phase velocity (v) with the non-dimensional axial wavenumber (ξ) for a laminated CNT-reinforced composite cylindrical shell coupled with the piezoelectric layers at the top and bottom surfaces ($n = 1$, $f_r = 0.6$, $r = 0.1$, $h/R = 1/30$).

Wave mode	$\Delta T(K), \Delta C(\%)$	Stacking sequence	Non-dimensional axial wavenumber (ξ)				
			0.2	0.4	0.6	0.8	1
M3	(0,0)	$[45^\circ/-45^\circ]_s$	4.0783	3.9087	3.8295	3.7993	3.7837
		$[0^\circ/90^\circ]_s$	2.1058	1.3948	1.2181	1.1503	1.1174
		$[0^\circ/45^\circ/90^\circ]_s$	2.4689	2.3019	2.2949	2.2911	2.2890
	(200,2)	$[45^\circ/-45^\circ]_s$	4.0729	3.8952	3.8219	3.7928	3.7783
		$[0^\circ/90^\circ]_s$	2.0266	1.3544	1.1891	1.1255	1.0948
		$[0^\circ/45^\circ/90^\circ]_s$	2.4042	2.2852	2.2776	2.2744	2.2723
	(400,4)	$[45^\circ/-45^\circ]_s$	4.0665	3.8817	3.8139	3.7869	3.7729
		$[0^\circ/90^\circ]_s$	1.9426	1.3124	1.1589	1.1002	1.0716
		$[0^\circ/45^\circ/90^\circ]_s$	2.3364	2.2685	2.2604	2.2572	2.2550
M5	(0,0)	$[45^\circ/-45^\circ]_s$	4.4144	4.3719	4.3627	4.3590	4.3573
		$[0^\circ/90^\circ]_s$	5.9194	5.9194	5.9194	5.9194	5.9194
		$[0^\circ/45^\circ/90^\circ]_s$	5.6021	5.5784	5.5704	5.5666	5.5644
	(200,2)	$[45^\circ/-45^\circ]_s$	4.3994	4.3552	4.345	4.3417	4.3396
		$[0^\circ/90^\circ]_s$	5.9119	5.9119	5.9119	5.9119	5.9119
		$[0^\circ/45^\circ/90^\circ]_s$	5.5930	5.5693	5.5612	5.5574	5.5553
	(400,4)	$[45^\circ/-45^\circ]_s$	4.3843	4.3380	4.3277	4.3234	4.3218
		$[0^\circ/90^\circ]_s$	5.9043	5.9043	5.9043	5.9043	5.9043
		$[0^\circ/45^\circ/90^\circ]_s$	5.5838	5.5601	5.5521	5.5483	5.5456

3.2.10. Effect of Shell Geometry on Wave Dispersion Solutions

The effects of thickness to radius ratio of the host substrate laminated composite shell (h/R) on the variation of the non-dimensional wave phase velocity (v) with the non-dimensional axial wavenumber (ξ) and the circumferential wavenumber (n) are described, respectively, in Figs. 3.17 and 3.18 for a $[0^{\circ}/45^{\circ}/90^{\circ}]_s$ laminated CNT-reinforced composite cylindrical shell coupled with the piezoelectric layers at the top and bottom surfaces with $f_r = 0.6$ and $r = 0.1$ when $\Delta T = 200K$ and $\Delta C = 2\%$.

Fig. 3.17 displays the non-dimensional wave phase velocity curves versus the non-dimensional axial wavenumbers (ξ) for the first five wave modes ($M1, M2, M3, M4,$ and $M5$) at $n = 1$ for different h/R ratios. It is observed that at lower non-dimensional axial wavenumbers (ξ), higher h/R ratio leads to higher non-dimensional wave phase velocity, while this effect is not much significant at higher ξ and higher wave modes (see Fig. 3.17).

Fig. 3.18 shows the non-dimensional wave phase velocity curves versus the circumferential wavenumbers (n) for wave modes 2 and 5 ($M2$ and $M5$) at $\xi = 0.01, 0.1,$ and 1 for different h/R ratios. It can be seen that thicker shells (with higher h/R ratio) lead to higher wave phase velocities particularly at higher circumferential wavenumbers. This increase in the wave phase velocities with the increase of h/R ratio is because of an increase in the stiffness of the shell as a result of increase in the shell thickness, and this effect is more significant at higher circumferential wavenumbers due to increasing effect of circumferential wavenumber on the wave phase velocity. Furthermore, it is shown that the increment rate of the wave phase velocity with the increase of the circumferential wavenumber (n) at higher h/R ratio is higher than that at lower h/R ratio. In addition, this variation at lower non-dimensional axial wavenumbers ($\xi = 0.01$and 0.1) is more significant (see Fig. 3.18).

Another interesting finding is that at higher axial wavenumbers, axisymmetric wave motion independent of the circumferential direction (θ) and the circumferential wavenumber (n) can be considered, while at lower axial wavenumbers the increase of circumferential wavenumber leads to a sharp increase in wave phase velocities (see Fig. 3.18).

Therefore, based on the presented methodology in this research, we are also able to obtain the influence of shell geometry on structural dynamics by changing thickness to radius ratio (h/R) of the shell, where the results express that thicker shells with higher h/R ratio lead to higher wave phase velocities especially at lower axial wavenumbers and higher circumferential wavenumbers.

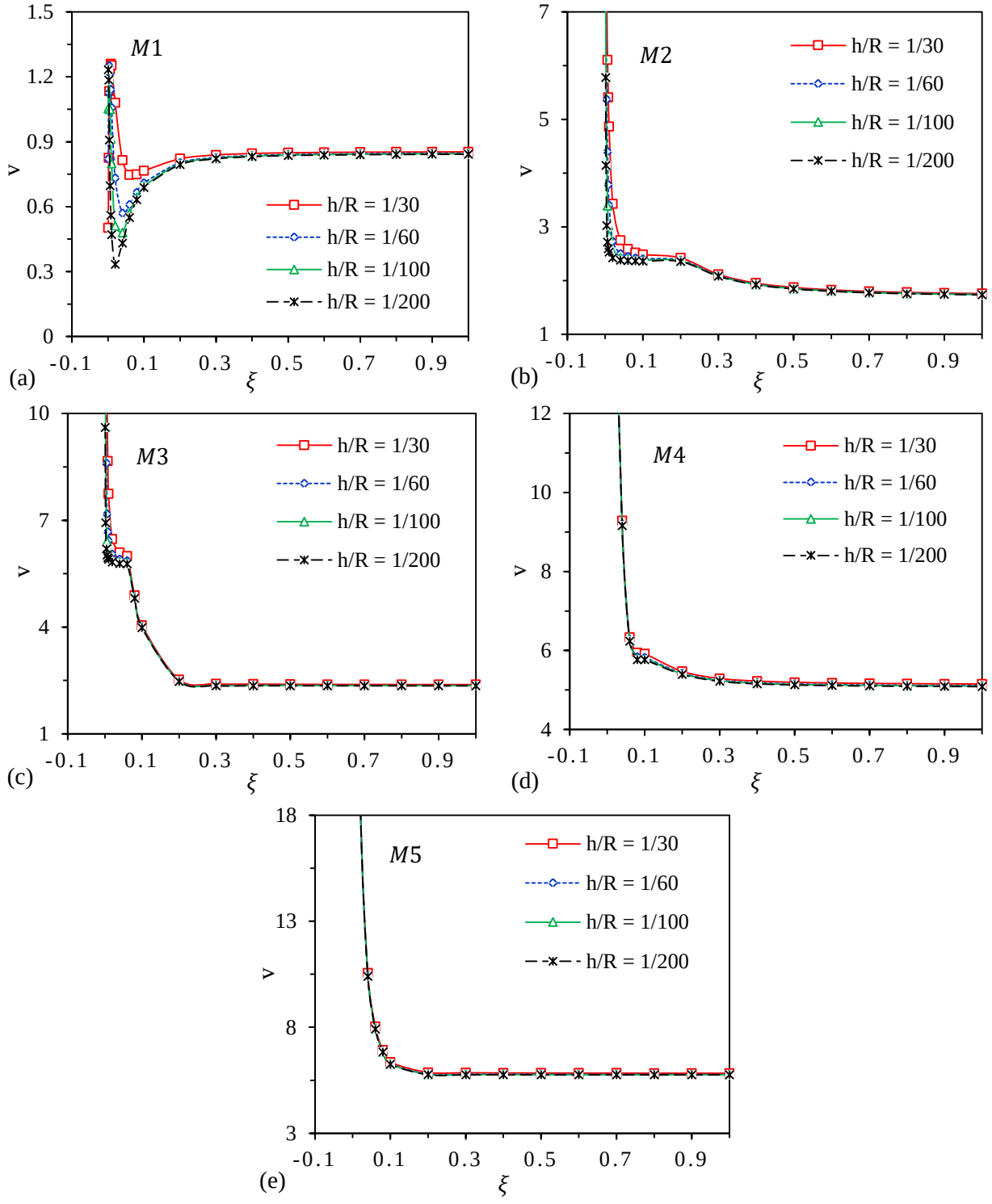

Figure 3.17. Effect of thickness to radius ratio of the host shell (h/R) on the dispersion curves of a $[0^{\circ}/45^{\circ}/90^{\circ}]_s$ laminated CNT-reinforced composite cylindrical shell coupled with the piezoelectric layers at the top and bottom surfaces with $r = 0.1$ and $f_r = 0.6$ for the first five wave modes ($M1$, $M2$, $M3$, $M4$, and $M5$) at $n = 1$ when $\Delta T = 200K$ and $\Delta C = 2\%$.

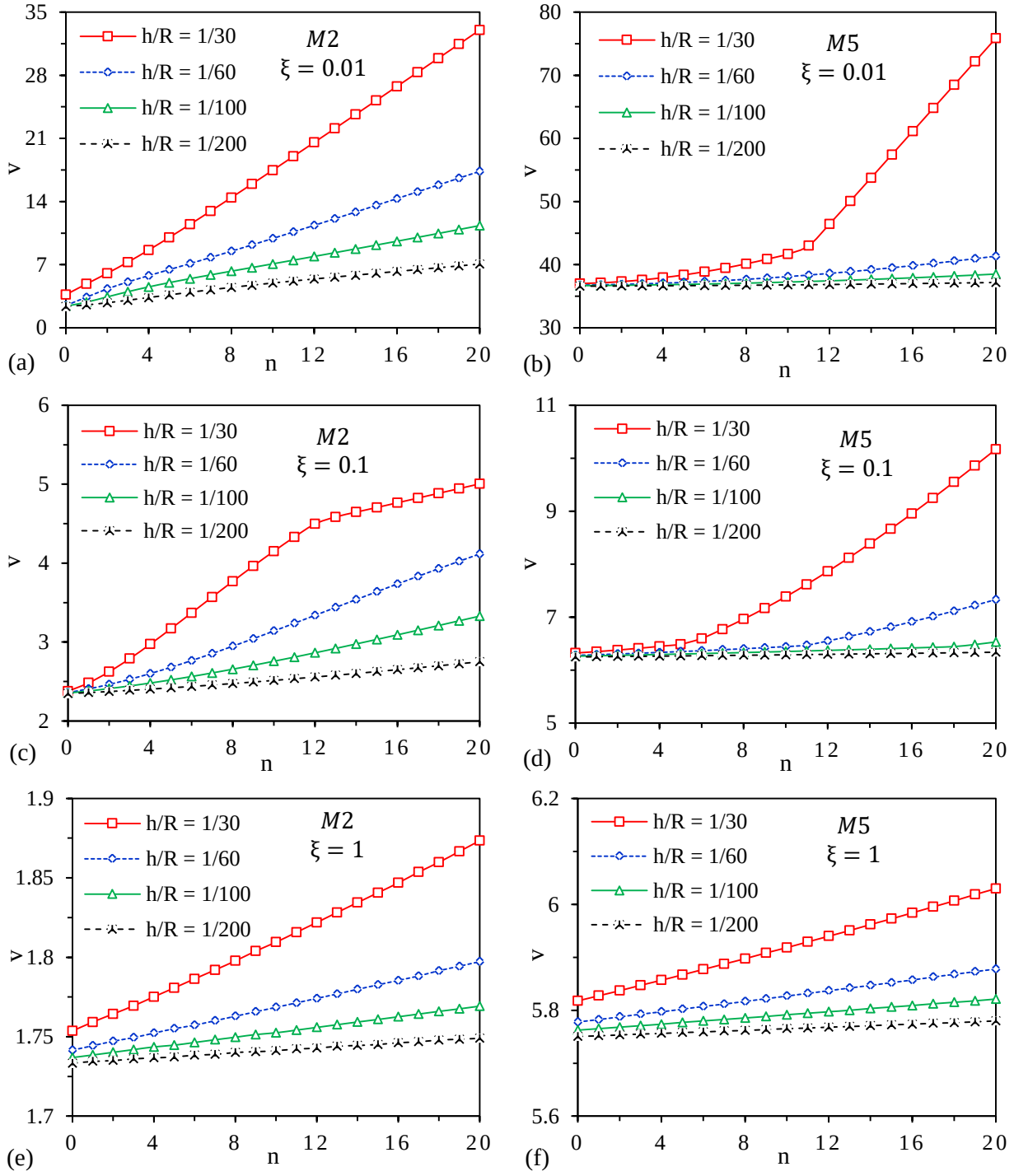

Figure 3.18. Effect of thickness to radius ratio of the host shell (h/R) on the variation of the non-dimensional phase velocity (v) with the circumferential wavenumber (n) for a $[0^{\circ}/45^{\circ}/90^{\circ}]_s$ laminated CNT-reinforced composite cylindrical shell coupled with the piezoelectric layers at the top and bottom surfaces with $r = 0.1$ and $f_r = 0.6$ for wave modes 2 and 5 ($M2$ and $M5$) at $\xi = 0.01, 0.1$, and 1 when $\Delta T = 200K$ and $\Delta C = 2\%$.

3.3. Parametric Studies on Vibration Characteristics of Smart Laminated Composite Cylindrical Shells

3.3.1. Effects of Hygrothermal Environmental Conditions on the Natural Frequencies with Various Boundary Conditions

The effects of hygrothermal environmental conditions on the change of the non-dimensional fundamental frequency parameter $\Omega = \omega H/\pi c_t$, corresponding to the first root of Eq. (2.124) $(M1)$, with the axial mode number m and the circumferential mode number n are described, respectively, in Tables 3.12 and 3.13 for C-C, C-SS, SS-SS, C-SL, and C-F boundary conditions. The non-dimensional frequencies are presented for axial modes $m = 0$, 1, …, 10 and circumferential mode $n = 1$ in Table 3.12, and for axial mode $m = 1$ and circumferential modes $n = 0, 1, \ldots, 10$ in Table 3.13. A $[0^\circ/45^\circ/90^\circ]_s$ laminated CNT-reinforced composite cylindrical shell integrated with the piezoelectric layers at the top and bottom surfaces with $r = 0.1$, $f_r = 0.6$, $h/R = 0.03$, and $L/R = 6$ is considered for these examples. Frequencies are calculated for seven series of hygrothermal conditions, i.e. $(\Delta T(K),\ \Delta C(\%)) = (0, 0)$, $(0, 2), (0, 4), (200, 0), (200, 2), (400, 0)$, and $(400, 4)$. As seen in Tables 3.12 and 3.13, an increase in temperature and/or moisture leads to a moderate decrease of the frequencies for various boundary conditions. This phenomenon again can be explained by the temperature-dependant and moisture-dependant material properties of the polymer matrix and the CNT reinforcing fiber, where an increase in temperature/moisture decreases the elastic moduli of the composites.

It is observed that the temperature variation has more significant effect on the frequencies than the moisture variation. It is seen from Tables 3.12 and 3.13 that at higher axial mode m and circumferential mode n, the temperature/moisture increase leads to more decrease of the

frequencies. For example, for C-C boundary condition, at $m = 1$, the non-dimensional frequency parameter Ω decreases from 0.0102 to 0.0101 $(\%0.98)$ by an increase of temperature and moisture set from $(0,0)$ to $(400,4)$, while for $m = 10$ under the same hygrothermal increase, the non-dimensional frequency parameter decreases from 0.0504 to 0.0497 $(\%1.388)$. This phenomenon can be explained that at higher axial mode m and circumferential mode n, considering the same particle motion, we have higher frequency than that at lower modes, hence, the material stiffness variation induced by an increase of temperature/moisture leads to more drop of the frequency at higher modes than lower ones.

Table 3.12. Effects of temperature/moisture variation and axial mode m on the non-dimensional fundamental frequency parameter $\Omega = \omega H/\pi c_t$ for a $[0^\circ/45^\circ/90^\circ]_s$ laminated CNT-reinforced composite cylindrical shell coupled with the piezoelectric layers at the top and bottom surfaces under various boundary conditions ($n = 1$, $f_r = 0.6$, $r = 0.1$, $h/R = 0.03$, $L/R = 6$).

Boundary conditions	$(\Delta T(K), \Delta C\%)$	Axial mode m										
		0	1	2	3	4	5	6	7	8	9	10
C-C	(0,0)	0.0021	0.0102	0.0180	0.0246	0.0301	0.0348	0.0386	0.0420	0.0449	0.0477	0.0504
	(200,2)	0.0021	0.0102	0.0178	0.0244	0.0299	0.0345	0.0383	0.0416	0.0446	0.0474	0.0501
	(400,4)	0.0021	0.0101	0.0176	0.0241	0.0296	0.0342	0.0380	0.0413	0.0443	0.0470	0.0497
C-SS	(0,0)	0.0006	0.0082	0.0161	0.0230	0.0288	0.0337	0.0377	0.0412	0.0442	0.0470	0.0497
	(200,2)	0.0006	0.0081	0.0160	0.0228	0.0286	0.0334	0.0374	0.0409	0.0439	0.0467	0.0494
	(400,4)	0.0006	0.0080	0.0158	0.0226	0.0283	0.0331	0.0371	0.0405	0.0436	0.0464	0.0490
SS-SS	(0,0)	0	0.0061	0.0142	0.0214	0.0275	0.0326	0.0368	0.0404	0.0435	0.0463	0.0491
	(200,2)	0	0.0060	0.0141	0.0212	0.0272	0.0323	0.0365	0.0400	0.0432	0.0460	0.0487
	(400,4)	0	0.0060	0.0140	0.0210	0.0270	0.0320	0.0362	0.0397	0.0428	0.0457	0.0484
C-SL	(0,0)	0.0007	0.0040	0.0123	0.0197	0.0261	0.0314	0.0358	0.0395	0.0427	0.0456	0.0484
	(200,2)	0.0007	0.0040	0.0122	0.0195	0.0258	0.0311	0.0355	0.0392	0.0424	0.0453	0.0480
	(400,4)	0.0007	0.0039	0.0121	0.0194	0.0256	0.0308	0.0352	0.0389	0.0421	0.0450	0.0477
C-F	(0,0)	0.0028	0.0021	0.0102	0.0180	0.0246	0.0301	0.0348	0.0386	0.0420	0.0449	0.0477
	(200,2)	0.0028	0.0021	0.0102	0.0178	0.0244	0.0299	0.0345	0.0383	0.0416	0.0446	0.0474
	(400,4)	0.0028	0.0021	0.0101	0.0176	0.0241	0.0296	0.0342	0.0380	0.0413	0.0443	0.0470

Table 3.13. Effects of temperature/moisture variation and circumferential mode n on the non-dimensional fundamental frequency parameter $\Omega = \omega H/\pi c_t$ for a $[0^\circ/45^\circ/90^\circ]_s$ laminated CNT-reinforced composite cylindrical shell coupled with the piezoelectric layers at the top and bottom surfaces under various boundary conditions ($m = 1$, $f_r = 0.6$, $r = 0.1$, $h/R = 0.03$, $L/R = 6$).

Boundary conditions	$(\Delta T(K), \Delta C\%)$	Circumferential mode n										
		0	1	2	3	4	5	6	7	8	9	10
C-C	(0,0)	0.0191	0.0102	0.0053	0.0045	0.0064	0.0096	0.0136	0.0182	0.0234	0.0291	0.0353
	(200,2)	0.0189	0.0102	0.0052	0.0045	0.0064	0.0096	0.0135	0.0181	0.0232	0.0288	0.0349
	(400,4)	0.0187	0.0101	0.0052	0.0044	0.0064	0.0095	0.0134	0.0179	0.0229	0.0284	0.0344
C-SS	(0,0)	0.0159	0.0082	0.0041	0.0039	0.0062	0.0094	0.0134	0.0180	0.0231	0.0288	0.0350
	(200,2)	0.0158	0.0081	0.0040	0.0039	0.0061	0.0093	0.0133	0.0178	0.0229	0.0285	0.0346
	(400,4)	0.0156	0.0080	0.0040	0.0039	0.0061	0.0093	0.0132	0.0176	0.0227	0.0282	0.0341
SS-SS	(0,0)	0.0128	0.0061	0.0029	0.0035	0.0059	0.0092	0.0131	0.0177	0.0229	0.0286	0.0347
	(200,2)	0.0126	0.0060	0.0029	0.0035	0.0059	0.0091	0.0130	0.0176	0.0227	0.0282	0.0343
	(400,4)	0.0125	0.0060	0.0029	0.0035	0.0058	0.0091	0.0129	0.0174	0.0224	0.0279	0.0339
C-SL	(0,0)	0.0096	0.0040	0.0020	0.0032	0.0057	0.0090	0.0129	0.0175	0.0226	0.0283	0.0345
	(200,2)	0.0095	0.0040	0.0020	0.0032	0.0057	0.0089	0.0128	0.0173	0.0224	0.0280	0.0341
	(400,4)	0.0094	0.0039	0.0020	0.0032	0.0056	0.0089	0.0127	0.0172	0.0222	0.0277	0.0336
C-F	(0,0)	0.0064	0.0021	0.0014	0.0030	0.0056	0.0088	0.0128	0.0173	0.0224	0.0281	0.0342
	(200,2)	0.0063	0.0021	0.0013	0.0030	0.0055	0.0088	0.0126	0.0171	0.0222	0.0278	0.0338
	(400,4)	0.0063	0.0021	0.0013	0.0030	0.0055	0.0087	0.0125	0.0170	0.0219	0.0274	0.0333

3.3.2. Effects of Axial and Circumferential Modes (m, n) on the Natural Frequencies for Various Boundary Conditions

The effects of the axial mode number m and the circumferential mode number n on the non-dimensional frequency parameters $\Omega = \omega H/\pi c_t$ corresponding to the first five roots of Eq. (2.124) ($M1$, $M2$, $M3$, $M4$, and $M5$) are shown, respectively, in Figs. 3.19 and 3.20 for C-C, C-SS, SS-SS, C-SL, and C-F boundary conditions of the shell. A $[0^\circ/45^\circ/90^\circ]_s$ laminated CNT-reinforced composite cylindrical shell integrated with the piezoelectric layers at the top and bottom surfaces with $r = 0.1$, $f_r = 0.6$, $h/R = 0.03$, and $L/R = 6$ when $\Delta T = 200K$ and $\Delta C = 2\%$ is considered for these examples. As shown in Fig. 3.19, the frequencies corresponding to all five roots and five boundary conditions increase with the increase of axial mode m, and C-F and C-C boundary conditions, respectively, lead to the lowest and the highest frequencies. From Fig. 3.20, it can be seen that the frequencies corresponding to the first root of Eq. (2.124) ($M1$) for the five boundary conditions C-C, C-SS, SS-SS, C-SL, and C-F decrease first and then increase with the circumferential mode n which may be related to the type of shell motion corresponding to $M1$. For higher circumferential mode numbers n, all five boundary conditions lead to similar frequencies, illustrating the effect of boundary conditions decreases at higher circumferential mode numbers n, while for lower circumferential mode numbers n, the effect of boundary conditions is significant and C-F boundary condition provides the lowest frequencies and C-C boundary condition has the highest ones (see Fig. 3.20a). For other roots ($M2$, $M3$, $M4$, and $M5$), the frequencies for the five boundary conditions C-C, C-SS, SS-SS, C-SL, and C-F increase as the circumferential mode n increases, and for $M2$ and $M5$, C-F and C-C boundary conditions lead to the lowest and the highest frequencies, respectively, within different circumferential modes n, while for $M3$ and $M4$, the influence of boundary condition is not significant (see Fig. 3.20b-e).

Therefore, it is resulted that the frequency normally increases with the increase of axial and circumferential mode numbers (m, n), and at higher vibration modes, higher frequencies are obtained for all five boundary conditions considered in this study. From the obtained results, it can also be concluded that more constraints at the edges of a smart laminated CNT-reinforced composite cylindrical shell increase its natural frequencies. This trend is due the fact that more constraints at the edges increase the flexural rigidity of the shell with stiffening the edge support, leading to higher frequencies. Hence, this phenomenon is to be expected that the clamped (C) edge is stronger and leads to higher frequencies than the simply supported (SS) edge, the sliding (SL) edge, and the free (F) edge without any constraint. It can also be concluded that the effect of boundary conditions on the natural frequencies is more observable by the variation of axial mode number m.

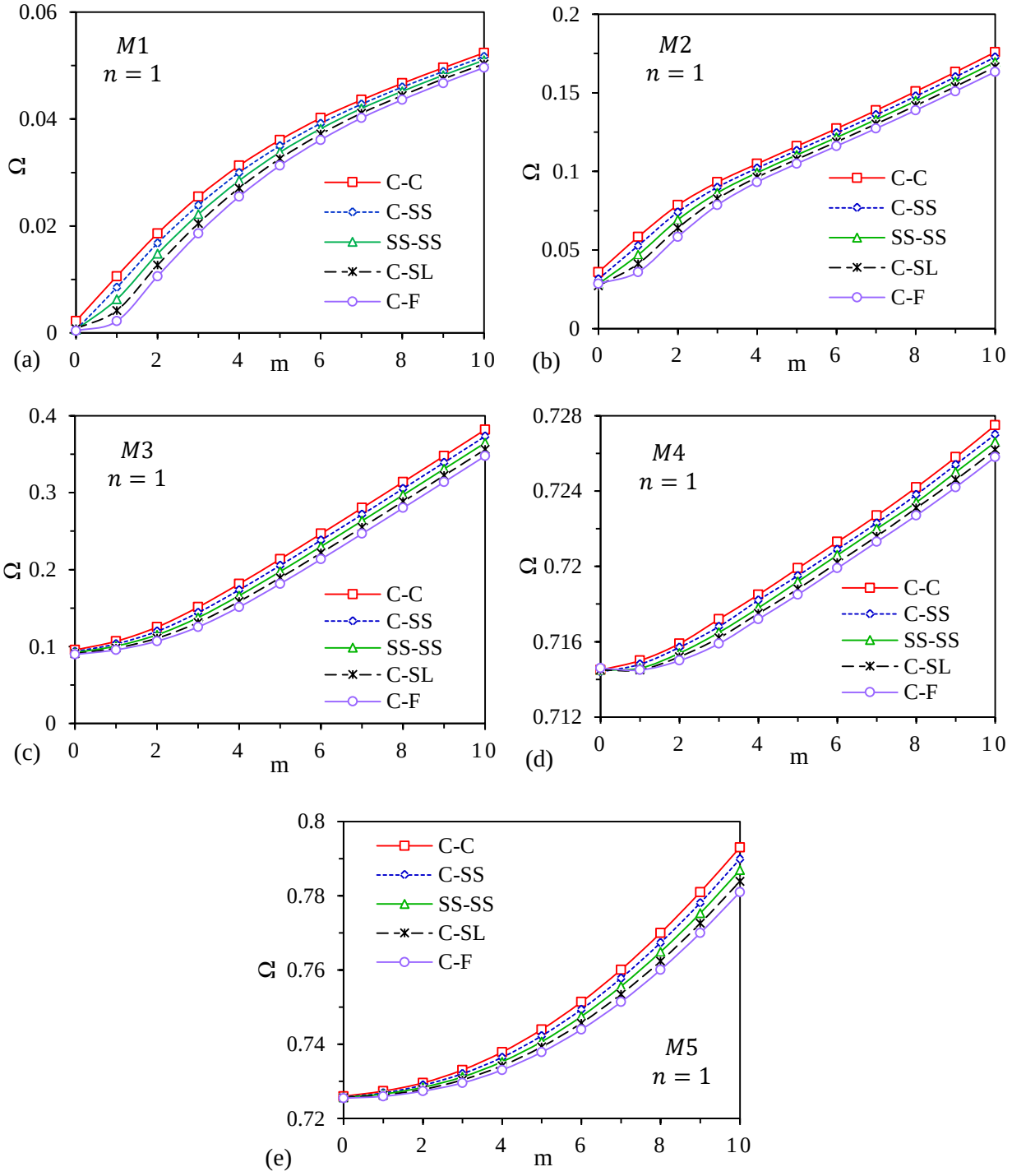

Figure 3.19. Effect of axial mode m on the non-dimensional frequency parameters $\Omega = \omega H/\pi c_t$ for $M1$, $M2$, $M3$, $M4$, and $M5$ at $n = 1$ for a $[0^{\circ}/45^{\circ}/90^{\circ}]_s$ laminated CNT-reinforced composite cylindrical shell coupled with the piezoelectric layers at the top and bottom surfaces with $r = 0.1$, $f_r = 0.6$, $h/R = 0.03$, and $L/R = 6$ when $\Delta T = 200K$ and $\Delta C = 2\%$ under C-C, C-SS, SS-SS, C-SL, and C-F boundary conditions.

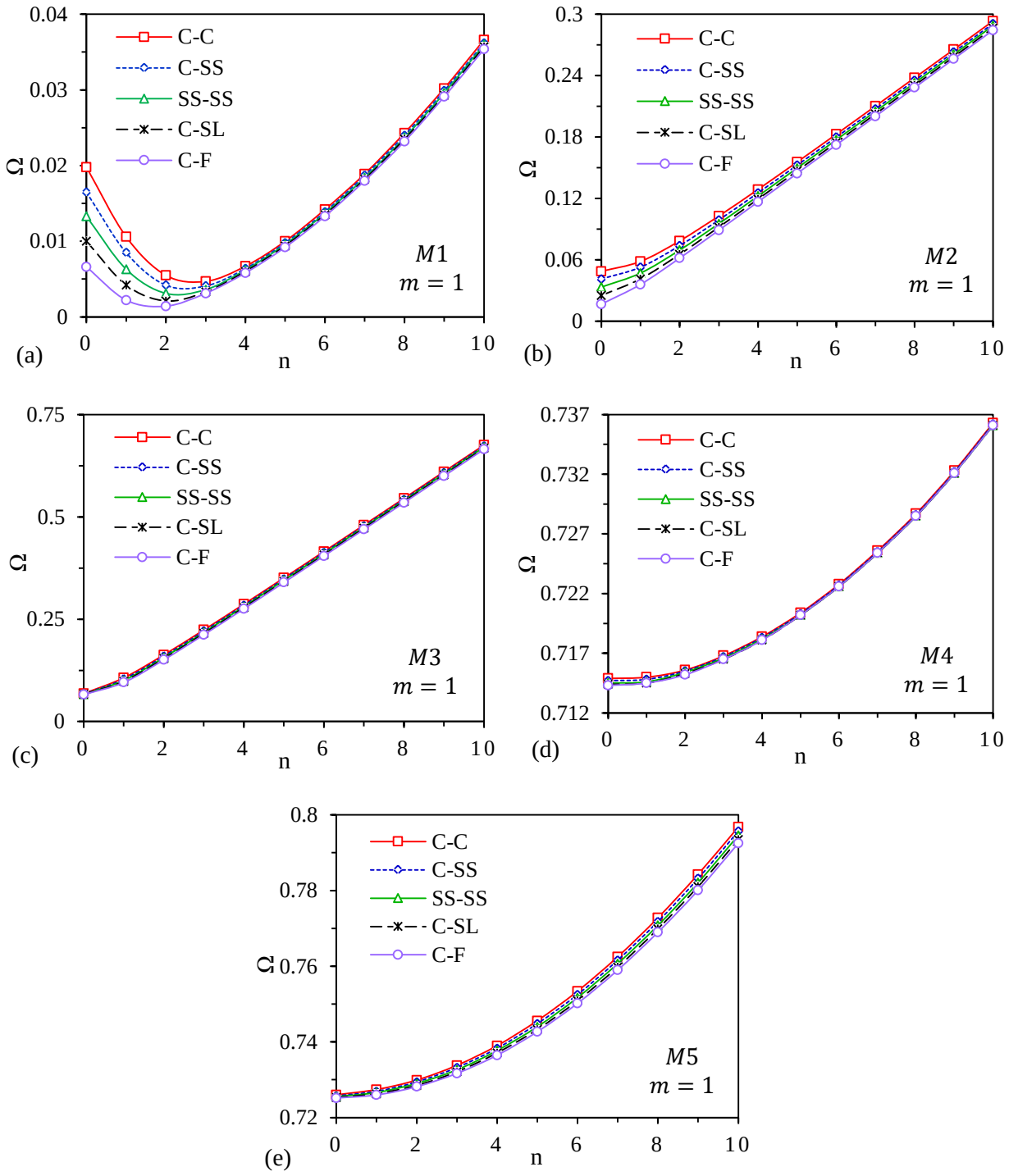

Figure 3.20. Effect of circumferential mode n on the non-dimensional frequency parameters $\Omega = \omega H/\pi c_t$ for $M1$, $M2$, $M3$, $M4$, and $M5$ at $m = 1$ for a $[0^{\circ}/45^{\circ}/90^{\circ}]_s$ laminated CNT-reinforced composite cylindrical shell coupled with the piezoelectric layers at the top and bottom surfaces with $r = 0.1$, $f_r = 0.6$, $h/R = 0.03$, and $L/R = 6$ when $\Delta T = 200K$ and $\Delta C = 2\%$ under C-C, C-SS, SS-SS, C-SL, and C-F boundary conditions.

3.3.3. Effect of CNT Volume Fraction on the Natural Frequencies for Various Boundary Conditions

Fig. 3.21 displays the influence of CNT volume fraction (f_r) on the non-dimensional frequency parameters $\Omega = \omega H/\pi c_t$ corresponding to the first five roots of Eq. (2.124) ($M1$, $M2$, $M3$, $M4$ and $M5$) for a $[0^\circ/45^\circ/90^\circ]_s$ laminated CNT-reinforced composite cylindrical shell integrated with the piezoelectric layers at the top and bottom surfaces with $r = 0.1$, $h/R = 0.03$, and $L/R = 6$ when $\Delta T = 200K$ and $\Delta C = 2\%$. Frequencies are calculated for the five boundary conditions C-C, C-SS, SS-SS, C-SL, and C-F and axial and circumferential modes $(m, n) = (1, 3)$. It is found that for the five boundary conditions, the frequencies increase as the CNT volume fraction increases in the polymer matrix. This increase in the frequencies with the CNT volume fraction can be explained by an increase in the stiffness and the strength of the CNT-reinforced composite cylindrical shell as a result of increase in the CNT volume fraction. For $M1$, $M2$, and $M3$, the influence of boundary conditions is more noticeable at higher CNT volume fraction due to the stiffening effect of boundary condition as well as CNT reinforcing effect, where C-C boundary condition has the highest frequencies and C-F boundary condition leads to the lowest ones, while for $M4$ and $M5$, for different CNT volume fractions the effect of boundary conditions is negligible (see Fig. 3.21a-e). Not only the frequency trend, but also the values of this result can be useful to guide the possible design of CNT-reinforced composites under vibration for various applications.

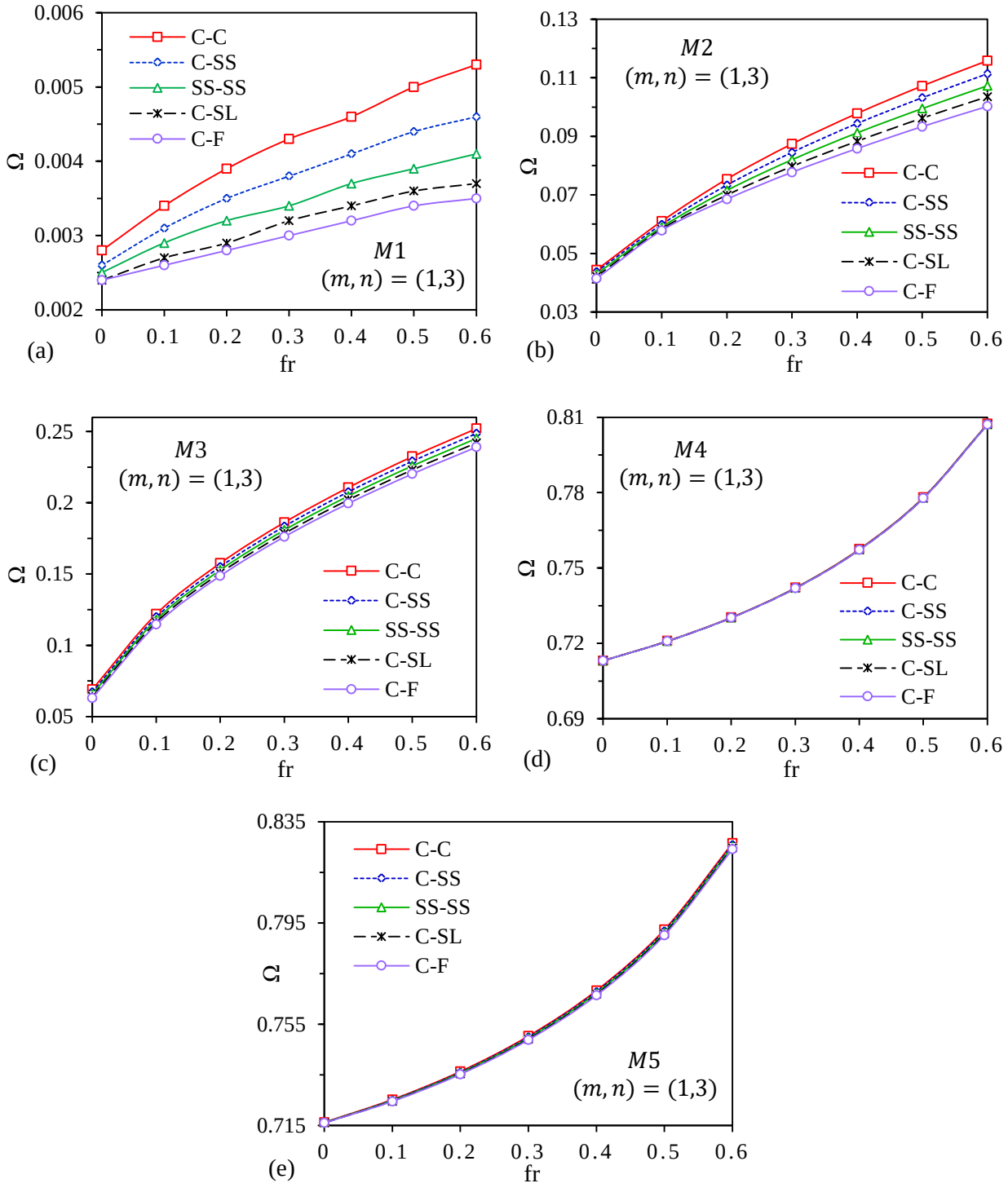

Figure 3.21. Effect of CNT volume fraction (f_r) on the non-dimensional frequency parameters $\Omega = \omega H/\pi c_t$ for $M1$, $M2$, $M3$, $M4$, and $M5$ at $(m, n) = (1, 3)$ for a $[0^\circ/45^\circ/90^\circ]_s$ laminated CNT-reinforced composite cylindrical shell coupled with the piezoelectric layers at the top and bottom surfaces with $r = 0.1$, $h/R = 0.03$, and $L/R = 6$ when $\Delta T = 200K$ and $\Delta C = 2\%$ under C-C, C-SS, SS-SS, C-SL, and C-F boundary conditions.

3.3.4. Effects of Shell Geometry Parameters on the Natural Frequencies for Various Boundary Conditions

To see the effect of the host laminated composite cylindrical shell geometry on the non-dimensional frequency parameters $\Omega = \omega H/\pi c_t$ corresponding to the first five roots of Eq. (2.124) ($M1$, $M2$, $M3$, $M4$, and $M5$), thickness to radius ratio of the host shell h/R and length to radius ratio of the host shell L/R are chosen as parameters of study. For this investigation, a $[0^\circ/45^\circ/90^\circ]_s$ CNT-reinforced composite cylindrical shell integrated with the piezoelectric layers at the top and bottom surfaces with $r = 0.1$ and $f_r = 0.6$ when $\Delta T = 200K$ and $\Delta C = 2\%$ is considered. The non-dimensional frequency parameters $\Omega = \omega H/2\pi c_t$ are plotted in Figs. 3.22 and 3.23, respectively, for different h/R and L/R ratios of the host shell with C-C, C-SS, SS-SS, C-SL, and C-F boundary conditions with given axial and circumferential modes $(m, n) = (1,3)$.

The variation of the frequency parameter Ω with the thickness to radius ratio of the shell (h/R) is shown in Fig. 3.22 when $L/R = 6$. It is observed that for thicker shells with higher h/R ratio, the frequencies corresponding to the first five roots ($M1$, $M2$, $M3$, $M4$, and $M5$) and the five boundary conditions are always higher than those with lower h/R ratio. This increase in the frequency parameter with the increment of h/R ratio is because of an increase in the shell stiffness as a result of increase in the shell thickness. It is also seen that the effect of boundary conditions at higher h/R ratio is relatively much significant where C-C boundary condition has the highest natural frequencies followed by C-SS, SS-SS, C-SL, and C-F boundary conditions. This phenomenon can be explained that an increase of shell thickness leads to the increase of shell rigidity and this property can be magnified with consideration of more constraints at the shell ends, where the difference between natural frequencies of different boundary conditions with different constraint levels is much significant for thicker shells (with higher h/R ratio).

Fig. 3.23 displays the frequency parameter Ω variation with the length to radius ratio of the shell (L/R) when $h/R = 0.03$. It is observed that for the first five roots ($M1$, $M2$, $M3$, $M4$, and $M5$) and the five boundary conditions, the frequencies first decrease noticeably for lower L/R ratio and then change smoothly for higher L/R ratio. Hence, we can say the natural frequency variations are much sensitive to the change of shell length when the host composite cylindrical shell is relatively short. The decrease of frequencies with the increase of L/R ratio is due to the smaller shell flexural rigidity at larger L/R ratio. Significant effect of boundary conditions on the frequencies is observed for lower L/R ratio, and discrepancies between the frequencies of C-C, C-SS, SS-SS, C-SL, and C-F boundary conditions are larger at lower L/R ratio (shorter cylindrical shells) where the C-C and C-F boundary conditions lead to the highest and lowest frequencies, respectively. While for long cylindrical shells (with higher L/R ratio), the influence of boundary condition is not noticeable and diminishes. This phenomenon can be explained that a decrease of shell length leads to the increase of shell rigidity and this property can be magnified with consideration of more constraints at the shell ends, where difference between natural frequencies of different boundary conditions with different constraint levels is much significant for shorter shells (with lower L/R ratio).

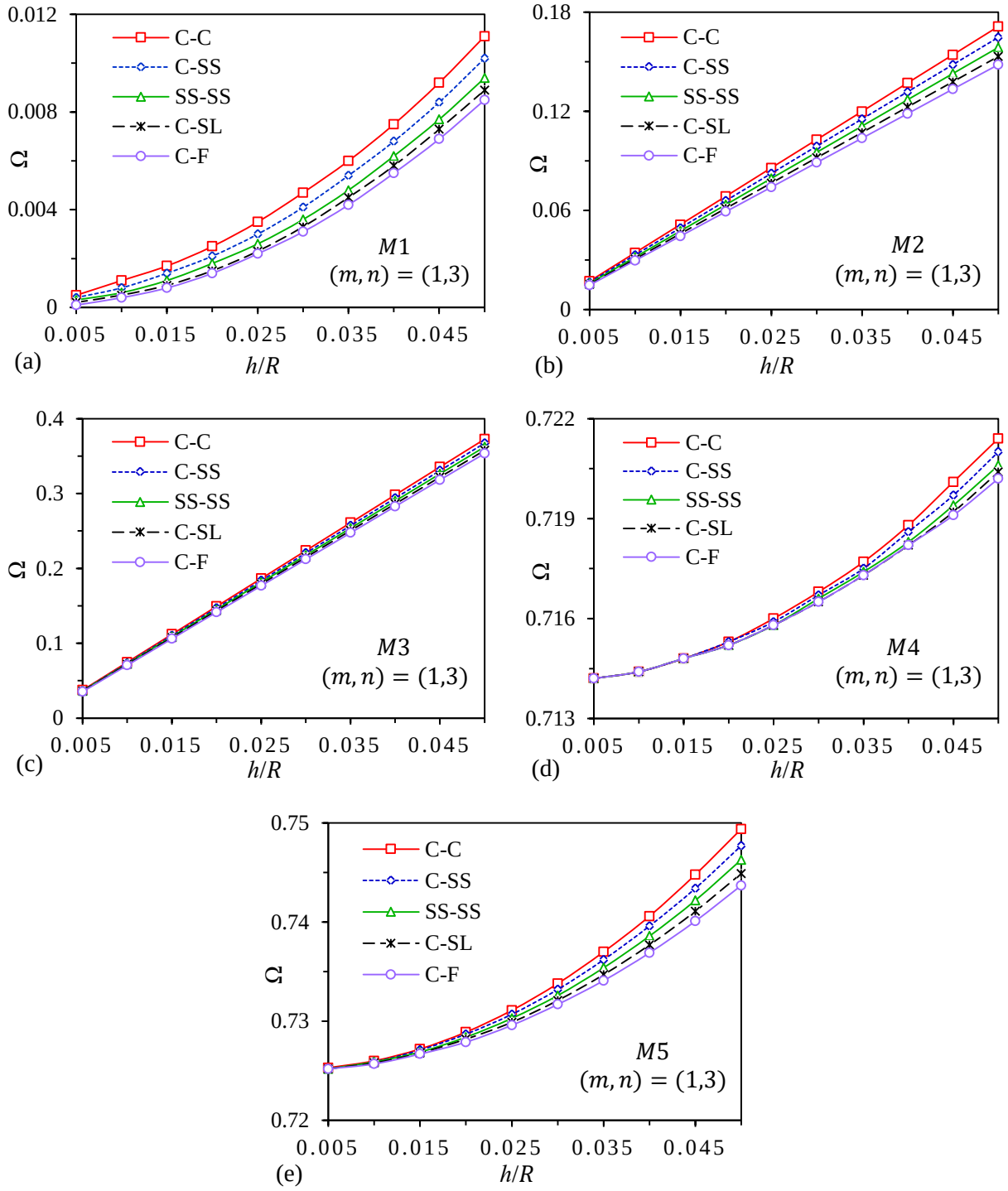

Figure 3.22. Effect of thickness to radius ratio of the host shell (h/R) on the non-dimensional frequency parameters $\Omega = \omega H/\pi c_t$ for $M1$, $M2$, $M3$, $M4$, and $M5$ at $(m,n) = (1,3)$ for a $[0^\circ/45^\circ/90^\circ]_s$ laminated CNT-reinforced composite cylindrical shell coupled with the piezoelectric layers at the top and bottom surfaces with $r = 0.1$, $f_r = 0.6$, and $L/R = 6$ when $\Delta T = 200K$ and $\Delta C = 2\%$ under C-C, C-SS, SS-SS, C-SL, and C-F boundary conditions.

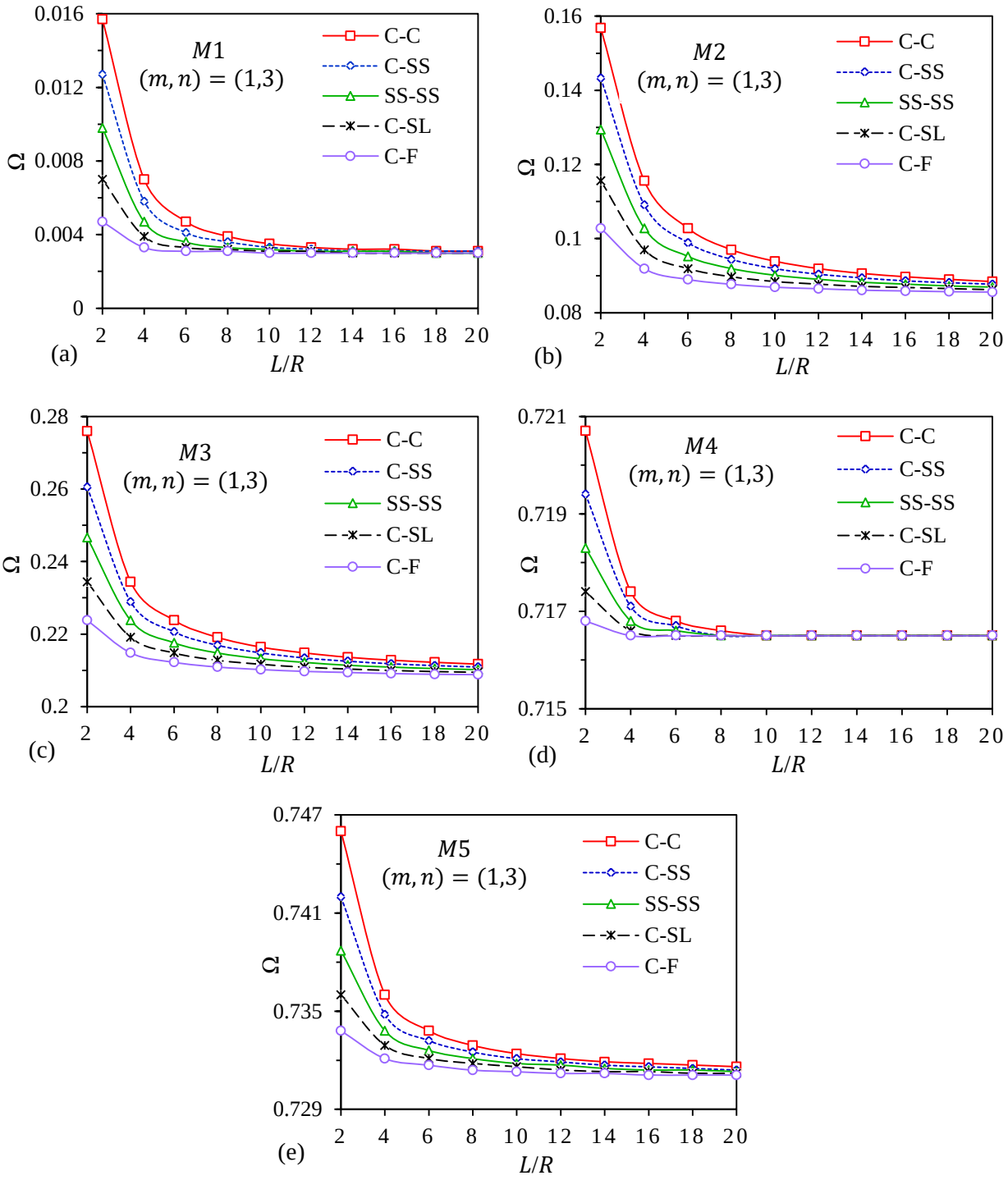

Figure 3.23. Effect of length to radius ratio of the host shell (L/R) on the non-dimensional frequency parameter $\Omega = \omega H/\pi c_t$ for $M1$, $M2$, $M3$, $M4$, and $M5$ at $(m, n) = (1, 3)$ for a $[0^\circ/45^\circ/90^\circ]_s$ laminated CNT-reinforced composite cylindrical shell coupled with the piezoelectric layers at the top and bottom surfaces with $r = 0.1$, $f_r = 0.6$, and $h/R = 0.03$ when $\Delta T = 200K$ and $\Delta C = 2\%$ under C-C, C-SS, SS-SS, C-SL, and C-F boundary conditions.

Chapter 4

Summary and Conclusions

A summary of the research presented in this thesis is given below. In addition, major findings and concluding remarks of this research are highlighted along with some suggested future research plans and directions.

4.1. Research Summary

Numerous research studies have been presented in the literature regarding analysis of wave propagation and vibration of laminated composite cylindrical shells using various numerical methods based on different shell theories. However, there is still a lack of research associated with analytical modeling and detailed analysis of wave propagation and vibration characteristics of smart laminated composite cylindrical shells with coupling effects of transverse shear, piezoelectricity, nanoparticles, hygrothermal environmental conditions, and mechanical boundary conditions where with FEA, it is difficult to study the effects of different composite designs on its wave propagation behaviors and vibration characteristics. The main objective of the present research is to establish a simple and comprehensive theoretical foundation and framework studying the structural dynamics of smart composite shells for possible NDE, structural enhancement or

energy harvesting applications by proposing and developing analytical models combining the existing theories to determine wave propagation and vibration characteristics of smart laminated composite cylindrical shell structures affected by various parameters such as the transverse shear, piezoelectric coupling, nanoparticles, hygrothermal environmental conditions, and mechanical boundary conditions. Analytical models were developed in the present research against the numerical simulation methods such as FEA. By the FEA, it is usually very difficult (or even impossible) to consider different CNT distributions as well as estimating the resulting composite hygrothermal properties in wave propagation and vibration modeling by the numerical approach where it requires extremely high calculation cost especially for the wave propagation analysis in infinite media.

A comprehensive theoretical foundation studying the structural dynamics of smart composite shells reinforced with different micro- and nano-sized fibers is established. The developed analytical models provide a valuable tool to derive more reliable and comprehensive correlations for predicting wave dispersion responses and vibration behaviors of smart laminated composite cylindrical shells with coupling effects of piezoelectricity, transverse shear and rotary inertia, nanoparticles, temperature and moisture variations, and boundary conditions. The predictions of the present micromechanics model and analytical solution of wave propagation and vibration problems for the effective elastic properties and structural dynamics of smart laminated composite cylindrical shells are compared with the existing results in the literature, where a good agreement is observed. Therefore, it can be concluded that the developed analytical models in the present research can be a useful tool contributing to obtain wave dispersion results and vibration characteristics for both smart isotropic and anisotropic multi-layered shells with coupling effects

of piezoelectric actuators and sensors, transverse shear and rotary inertia, nanoparticles, hygrothermal environmental conditions, and boundary conditions.

The analytical models developed in this thesis can be used for future research studies in determining wave propagation and vibration characteristics of smart laminated CNT-reinforced composites with different CNT distributions subjected to hygrothermal loading as well as mechanical loading for various engineering applications such as dynamic stability analysis, structural health monitoring, and energy harvesting.

However, the developed models in this thesis may not be appropriate for thick shells and nonlinear and large deformation problems, where we need to employ higher-order shell theories or the three-dimensional elasticity theory with higher accuracy.

4.2. Concluding Remarks

Major findings and concluding remarks of the accomplished research are listed as follows:

1) The effects of transverse shear and rotary inertia on structural dynamics of smart laminated composite shells are different from their effects on smart isotropic shells where it leads to higher wave phase velocities for smart laminated composite shells especially at higher wave modes. This is because of staked plies in which shear may occur between layers. Therefore, the model presented in this thesis is desired and capable to accurately consider the shear effects for smart laminated composite shells where its effects are more significant than on smart isotropic shells.

2) Since a piezoelectric layer is staked on the host laminated composite shell, it is very important to describe its coupling effects including shear, thickness, and polarization directions on wave propagation and vibration characteristics. Due to the importance of shear effects in smart laminated composites especially at higher wave modes, the effects

of coupled piezoelectric material on the wave propagation and vibration of a host laminated composite shell are more significant than its effects on the structural dynamics of a host isotropic shell.

3) The results from incorporating the micromechanics, wave, and shell theories indicate that the nanotubes aligned along the wave direction have more effects of the wave dynamics, where the effects of CNT volume fraction on the wave phase velocity considering CNTs along the direction of wave waviness are relatively higher than those with other CNT orientations. It is also found that the agglomeration of CNTs leads to the decrease of wave phase velocity in comparison to CNT fibers dispersed in the matrix along specific orientations. These findings cannot be obtained by the lamination theory considering for micro-sized fibers. Although CNT fibers generally lead to higher wave phase velocities than traditional fibers such as carbon and E-glass, but at higher wavenumbers of wave mod 1 ($M1$) and at a specific wavenumber ($\xi = 0.2$) of wave mode 2 ($M2$), the wave phase velocities of CNT fiber and carbon and E-glass fibers are almost the same.

4) Coupled hygrothermal strains considered in the constitutive equations allows us to include the effects of temperature and moisture variations on the wave dynamics of smart composite shells. A reduction in wave phase velocities and natural frequencies is observed when temperature/moisture increases in comparison to the case there is no temperature/moisture variation. Models ignoring hygrothermal strains are not able to describe the necessary influence of environmental conditions.

5) A formulation based on the first-order shear deformation shell theory and wave propagation approach with beam modal functions was developed to study the effects of various boundary conditions on the natural frequencies of smart laminated CNT-reinforced

composite cylindrical shells. The influence of mechanical boundary conditions on the natural frequencies is much significant for the composite shells with small circumferential modes, thick cylindrical shells (with large h/R ratio), and short cylindrical shells (with small L/R ratio).

4.3. Research Plans and Future Works

There are still many gaps in relation to structural dynamics of smart laminated composite shells, which requires further research studies. Suggestions for possible future works and directions are listed as follows:

- It was not possible to do experimental verification due the limitations of existing equipment and funding in our lab. Hence, as a future work, experimental validation is required to investigate the accuracy of the analytical models derived for analysis of wave dynamics and vibration of smart laminated composite shells with coupling effects of transverse shear, piezoelectricity, nanoparticles, hygrothermal environmental conditions, and mechanical boundary conditions. For this purpose, after fabrication of a smart composite sample, an acoustic wave via IDT can be applied on the surface of the sample to obtain wave propagation behaviors in the structure.
- Vibration analysis of smart fluid-filled laminated CNT-reinforced composite cylindrical shells resting on elastic foundation is still a gap in this research filed. Therefore, as a future work, a study can be conducted to solve this problem using the wave propagation approach. One application of this research can be in analysis of structural dynamics of smart laminated composite cylindrical shells used as clock spring sleeve in oil pipelines for the repair of damaged pipes.

- Considering the effects of electrical boundary conditions and actuations on wave propagation characteristics of smart CNT-reinforced composites is still an unsolved problem for the active control of smart composites and its NDE applications. Hence, a future study can be performed on dispersion solutions of piezoelectric coupled laminated CNT-reinforced composite cylindrical shells with various electrical boundary conditions and actuations.
- It is noted that the shell models (the ones used in this study and even the higher-order ones) developed to study the structural dynamics are only considered to be accurate for thin shell structures at lower dynamics modes. To understand the accuracy of the shell theories in estimating wave propagation and vibration characteristics of smart laminated composite thick shells (such as the ones with thickness to radius ratio larger than $1/10$ or even $1/5$), a future study can be conducted to model dynamics of wave motion and vibration using the general three-dimensional elasticity theory and compare the results with those obtained based on the shell theories.

Appendices

Appendix A

The components of the transformed reduced stiffness matrix $[Q_{ij}]$ $(i,j = x,\theta,s)$, relating the in-plane stresses $(\sigma_{xx},\sigma_{\theta\theta},\tau_{x\theta})$ to the in-plane strains $(\gamma_{xx},\gamma_{\theta\theta},\gamma_{x\theta})$, as a function of the components of the principal lamina stiffness matrix $[Q_{ij}]$ $(i,j = 1,2,6)$ are given by,

$$Q_{xx} = \acute{m}^4 Q_{11} + \acute{n}^4 Q_{22} + 2\acute{m}^2\acute{n}^2 Q_{12} + 4\acute{m}^2\acute{n}^2 Q_{66}$$

$$Q_{\theta\theta} = \acute{n}^4 Q_{11} + \acute{m}^4 Q_{22} + 2\acute{m}^2\acute{n}^2 Q_{12} + 4\acute{m}^2\acute{n}^2 Q_{66}$$

$$Q_{x\theta} = \acute{m}^2\acute{n}^2 Q_{11} + \acute{m}^2\acute{n}^2 Q_{22} + (\acute{m}^4 + \acute{n}^4) Q_{12} - 4\acute{m}^2\acute{n}^2 Q_{66}$$

$$Q_{xs} = \acute{m}^3\acute{n} Q_{11} - \acute{m}\acute{n}^3 Q_{22} - \acute{m}\acute{n}(\acute{m}^2 - \acute{n}^2) Q_{12} - 2\acute{m}\acute{n}(\acute{m}^2 - \acute{n}^2) Q_{66}$$

$$Q_{\theta s} = \acute{m}\acute{n}^3 Q_{11} - \acute{m}^3\acute{n} Q_{22} + \acute{m}\acute{n}(\acute{m}^2 - \acute{n}^2) Q_{12} + 2\acute{m}\acute{n}(\acute{m}^2 - \acute{n}^2) Q_{66}$$

$$Q_{ss} = \acute{m}^2\acute{n}^2 Q_{11} + \acute{m}^2\acute{n}^2 Q_{22} - 2\acute{m}^2\acute{n}^2 Q_{12} + (\acute{m}^2 - \acute{n}^2)^2 Q_{66} \qquad (A.1)$$

where

$$\acute{m} = cos\beta, \qquad \acute{n} = sin\beta \qquad (A.2)$$

The components of the principal lamina stiffness matrix $[Q_{ij}]$ $(i,j = 1,2,6)$ are function of material properties of the lamina as,

$$Q_{11} = C_{11} - \frac{C_{13}C_{13}}{C_{33}} = \frac{E_{11}}{1 - v_{12}v_{21}} \qquad Q_{12} = C_{12} - \frac{C_{13}C_{23}}{C_{33}} = \frac{v_{21}E_{11}}{1 - v_{12}v_{21}}$$

$$Q_{21} = C_{21} - \frac{C_{23}C_{13}}{C_{33}} = \frac{v_{12}E_{22}}{1 - v_{12}v_{21}} \qquad Q_{22} = C_{22} - \frac{C_{23}C_{23}}{C_{33}} = \frac{E_{22}}{1 - v_{12}v_{21}}$$

$$Q_{66} = C_{66} = G_{12} \qquad (A.3)$$

The components of the stiffness matrix $[C_{ij}]$ $(i,j = q,r)$ relating the transverse shear stresses $(\tau_{\theta z},\tau_{xz})$ to the transverse shear strains $(\gamma_{\theta z},\gamma_{xz})$ are given by,

$$C_{qq} = \acute{m}^2 C_{44} + \acute{n}^2 C_{55} \qquad C_{qr} = C_{rq} = -\acute{m}\acute{n} C_{44} + \acute{m}\acute{n} C_{55}$$

$$C_{rr} = \acute{n}^2 C_{44} + \acute{m}^2 C_{55} \qquad (A.4)$$

where $C_{44} = G_{23}$ and $C_{55} = G_{13}$. In above equations, $C_{ij}(1, \dots, 6)$, E_{11}, E_{22}, v_{12}, G_{12}, G_{13}, and G_{23} for a CNT-reinforced lamina are given by Eqs. (2.68) and (2.111), and $Q_{ij} = Q_{ji}$ and $C_{ij} = C_{ji}$.

Appendix B

$\bar{c}_{11}, \bar{c}_{12}, \bar{c}_{22}, \bar{c}_{66}, \bar{e}_{16}, \bar{e}_{21}, \bar{e}_{22},$ and $\bar{\epsilon}_{11}, \bar{\epsilon}_{22}, \bar{\epsilon}_{33}$ required for the constitutive equations of a piezoelectric cylindrical shell with the axial polarization based on the classical shell theory, Eq. (2.21), are obtained as,

$$\bar{c}_{11} = c_{11} - \frac{c_{13}^2}{c_{33}} \qquad \bar{c}_{12} = c_{12} - \frac{c_{13}c_{23}}{c_{33}} \qquad \bar{c}_{22} = c_{22} - \frac{c_{23}^2}{c_{33}} \qquad \bar{c}_{66} = c_{66}$$

$$\bar{e}_{16} = e_{16} \qquad \bar{e}_{21} = e_{21} - \frac{c_{13}e_{23}}{c_{33}} \qquad \bar{e}_{22} = e_{22} - \frac{c_{23}e_{23}}{c_{33}}$$

$$\bar{\epsilon}_{11}=\epsilon_{11} \qquad \bar{\epsilon}_{22}=\epsilon_{22}+\frac{e_{23}^2}{c_{33}} \qquad \bar{\epsilon}_{33}=\epsilon_{33}+\frac{e_{34}^2}{c_{44}} \qquad (B.1)$$

and $\bar{c}_{11}, \bar{c}_{12}, \bar{c}_{22}, \bar{c}_{44}, \bar{c}_{55}, \bar{c}_{66}, \bar{e}_{16}, \bar{e}_{21}, \bar{e}_{22}, \bar{e}_{34},$ and $\bar{\epsilon}_{11}, \bar{\epsilon}_{22}, \bar{\epsilon}_{33}$ required for the constitutive equations of a piezoelectric cylindrical shell with the axial polarization according to the first-order shear deformation shell theory, Eq. (2.23) are attained as,

$$\bar{c}_{11} = c_{11} - \frac{c_{13}^2}{c_{33}} \quad \bar{c}_{12} = c_{12} - \frac{c_{13}c_{23}}{c_{33}} \quad \bar{c}_{22} = c_{22} - \frac{c_{23}^2}{c_{33}} \quad \bar{c}_{44} = c_{44} \quad \bar{c}_{55} = c_{55} \quad \bar{c}_{66} = c_{66}$$

$$\bar{e}_{16} = e_{16} \qquad \bar{e}_{21} = e_{21} - \frac{c_{13}e_{23}}{c_{33}} \qquad \bar{e}_{22} = e_{22} - \frac{c_{23}e_{23}}{c_{33}} \qquad \bar{e}_{34} = e_{34}$$

$$\bar{\epsilon}_{11}=\epsilon_{11} \qquad \bar{\epsilon}_{22}=\epsilon_{22}+\frac{e_{23}^2}{c_{33}} \qquad \bar{\epsilon}_{33}=\epsilon_{33} \qquad (B.2)$$

Appendix C

$\bar{c}_{11}$, $\bar{c}_{12}$, $\bar{c}_{22}$, $\bar{c}_{66}$, $\bar{e}_{11}$, $\bar{e}_{12}$, $\bar{e}_{26}$, and $\bar{\epsilon}_{11}$, $\bar{\epsilon}_{22}$, $\bar{\epsilon}_{33}$ used in the constitutive relations of a piezoelectric cylindrical shell with the circumferential polarization based on the classical shell theory, Eq. (2.26), are given by,

$$\bar{c}_{11} = c_{11} - \frac{c_{13}^2}{c_{33}} \qquad \bar{c}_{12} = c_{12} - \frac{c_{13}c_{23}}{c_{33}} \qquad \bar{c}_{22} = c_{22} - \frac{c_{23}^2}{c_{33}} \qquad \bar{c}_{66} = c_{66}$$

$$\bar{e}_{11} = e_{11} - \frac{c_{13}e_{13}}{c_{33}} \qquad \bar{e}_{12} = e_{12} - \frac{c_{23}e_{13}}{c_{33}} \qquad \bar{e}_{26} = e_{26}$$

$$\bar{\epsilon}_{11} = \epsilon_{11} + \frac{e_{13}^2}{c_{33}} \qquad \bar{\epsilon}_{22} = \epsilon_{22} \qquad \bar{\epsilon}_{33} = \epsilon_{33} + \frac{e_{35}^2}{c_{55}} \qquad (C.1)$$

and $\bar{c}_{11}$, $\bar{c}_{12}$, $\bar{c}_{22}$, $\bar{c}_{44}$, $\bar{c}_{55}$, $\bar{c}_{66}$, $\bar{e}_{11}$, $\bar{e}_{12}$, $\bar{e}_{26}$, $\bar{e}_{35}$, and $\bar{\epsilon}_{11}$, $\bar{\epsilon}_{22}$, $\bar{\epsilon}_{33}$ used in the constitutive relations of a piezoelectric cylindrical shell with the circumferential polarization according to the first-order shear deformation shell theory, Eq. (2.28), are acquired as,

$$\bar{c}_{11} = c_{11} - \frac{c_{13}^2}{c_{33}} \qquad \bar{c}_{12} = c_{12} - \frac{c_{13}c_{23}}{c_{33}} \qquad \bar{c}_{22} = c_{22} - \frac{c_{23}^2}{c_{33}} \qquad \bar{c}_{44} = c_{44} \qquad \bar{c}_{55} = c_{55} \qquad \bar{c}_{66} = c_{66}$$

$$\bar{e}_{11} = e_{11} - \frac{c_{13}e_{13}}{c_{33}} \qquad \bar{e}_{12} = e_{12} - \frac{c_{23}e_{13}}{c_{33}} \qquad \bar{e}_{26} = e_{26} \qquad \bar{e}_{35} = e_{35}$$

$$\bar{\epsilon}_{11} = \epsilon_{11} + \frac{e_{13}^2}{c_{33}} \qquad \bar{\epsilon}_{22} = \epsilon_{22} \qquad \bar{\epsilon}_{33} = \epsilon_{33} \qquad (C.2)$$

Appendix D

$\bar{c}_{11}$, $\bar{c}_{12}$, $\bar{c}_{22}$, $\bar{c}_{66}$, $\bar{e}_{31}$, $\bar{e}_{32}$, and $\bar{\epsilon}_{11}$, $\bar{\epsilon}_{22}$, $\bar{\epsilon}_{33}$ required in the constitutive relations of a piezoelectric cylindrical shell with the radial polarization based on the classical shell theory, Eq. (2.31), are obtained as,

$$\bar{c}_{11} = c_{11} - \frac{c_{13}^2}{c_{33}} \qquad \bar{c}_{12} = c_{12} - \frac{c_{13}c_{23}}{c_{33}} \qquad \bar{c}_{22} = c_{22} - \frac{c_{23}^2}{c_{33}} \qquad \bar{c}_{66} = c_{66}$$

$$\bar{e}_{31} = e_{31} - \frac{c_{13}e_{33}}{c_{33}} \qquad \bar{e}_{32} = e_{32} - \frac{c_{23}e_{33}}{c_{33}}$$

$$\bar{\epsilon}_{11}=\epsilon_{11}+\frac{e_{15}^2}{c_{55}} \qquad \bar{\epsilon}_{22}=\epsilon_{22}+\frac{e_{24}^2}{c_{44}} \qquad \bar{\epsilon}_{33}=\epsilon_{33}+\frac{e_{33}^2}{c_{33}} \qquad (D.1)$$

and $\bar{c}_{11}$, $\bar{c}_{12}$, $\bar{c}_{22}$, $\bar{c}_{44}$, $\bar{c}_{55}$, $\bar{c}_{66}$, $\bar{e}_{15}$, $\bar{e}_{24}$, $\bar{e}_{31}$, $\bar{e}_{32}$, and $\bar{\epsilon}_{11}$, $\bar{\epsilon}_{22}$, $\bar{\epsilon}_{33}$ used in the constitutive relations of a piezoelectric cylindrical shell with the radial polarization according to the first-order shear deformation shell theory, Eq. (2.33), are determined by,

$$\bar{c}_{11} = c_{11} - \frac{c_{13}^2}{c_{33}} \qquad \bar{c}_{12} = c_{12} - \frac{c_{13}c_{23}}{c_{33}} \qquad \bar{c}_{22} = c_{22} - \frac{c_{23}^2}{c_{33}} \qquad \bar{c}_{44} = c_{44} \qquad \bar{c}_{55} = c_{55} \qquad \bar{c}_{66} = c_{66}$$

$$\bar{e}_{15} = e_{15} \qquad \bar{e}_{24} = e_{24} \qquad \bar{e}_{31} = e_{31} - \frac{c_{13}e_{33}}{c_{33}} \qquad \bar{e}_{32} = e_{32} - \frac{c_{23}e_{33}}{c_{33}}$$

$$\bar{\epsilon}_{11}=\epsilon_{11} \qquad \bar{\epsilon}_{22}=\epsilon_{22} \qquad \bar{\epsilon}_{33}=\epsilon_{33}+\frac{e_{33}^2}{c_{33}} \qquad (D.2)$$

Appendix E

The expression of coefficients of Eq. (2.36) are given by,

$A_1 = A_{xx} + \bar{c}_{22}h_p \qquad A_2 = A_{x\theta} + \bar{c}_{12}h_p \qquad A_3 = A_{xs} \qquad A_4 = B_{xx} + \frac{\bar{c}_{22}}{2}\left(hh_p + h_p^2\right)$

$A_5 = B_{x\theta} + \frac{\bar{c}_{12}}{2}\left(hh_p + h_p^2\right) \qquad A_6 = B_{xs}, \qquad A_7 = \bar{e}_{22}h_p$

$B_1 = A_{\theta x} + \bar{c}_{12}h_p \qquad B_2 = A_{\theta\theta} + \bar{c}_{11}h_p \qquad B_3 = A_{\theta s} \qquad B_4 = B_{\theta x} + \frac{\bar{c}_{12}}{2}\left(hh_p + h_p^2\right)$

$B_5 = B_{\theta\theta} + \frac{\bar{c}_{11}}{2}\left(hh_p + h_p^2\right) \qquad B_6 = B_{\theta s} \qquad B_7 = \bar{e}_{21}h_p$

$C_1 = A_{sx} \qquad C_2 = A_{s\theta} \qquad C_3 = A_{ss} + \bar{c}_{66}h_p \qquad C_4 = B_{sx}$

$C_5 = B_{s\theta} \qquad C_6 = B_{ss} + \frac{\bar{c}_{66}}{2}\left(hh_p + h_p^2\right) \qquad C_7 = \bar{e}_{16}h_p$

$D_1 = B_{xx} + \frac{\bar{c}_{22}}{2}\left(hh_p + h_p^2\right) \qquad D_2 = B_{x\theta} + \frac{\bar{c}_{12}}{2}\left(hh_p + h_p^2\right) \qquad D_3 = B_{xs}$

$D_4 = D_{xx} + \bar{c}_{22}\left(\frac{h_p h^2}{4} + \frac{hh_p^2}{2} + \frac{h_p^3}{3}\right) \qquad D_5 = D_{x\theta} + \bar{c}_{12}\left(\frac{h_p h^2}{4} + \frac{hh_p^2}{2} + \frac{h_p^3}{3}\right)$

$D_6 = D_{xs} \qquad D_7 = \frac{\bar{e}_{22}}{2}\left(hh_p + h_p^2\right)$

$E_1 = B_{\theta x} + \frac{\bar{c}_{12}}{2}\left(hh_p + h_p^2\right) \qquad E_2 = B_{\theta\theta} + \frac{\bar{c}_{11}}{2}\left(hh_p + h_p^2\right) \qquad E_3 = B_{\theta s}$

$E_4 = D_{\theta x} + \bar{c}_{12}\left(\frac{h_p h^2}{4} + \frac{hh_p^2}{2} + \frac{h_p^3}{3}\right) \qquad E_5 = D_{\theta\theta} + \bar{c}_{11}\left(\frac{h_p h^2}{4} + \frac{hh_p^2}{2} + \frac{h_p^3}{3}\right)$

$E_6 = D_{\theta s} \qquad E_7 = \frac{\bar{e}_{21}}{2}\left(hh_p + h_p^2\right)$

$F_1 = B_{sx} \qquad F_2 = B_{s\theta} \qquad F_3 = B_{ss} + \frac{\bar{c}_{66}}{2}\left(hh_p + h_p^2\right) \qquad F_4 = D_{sx} \qquad F_5 = D_{s\theta}$

$F_6 = D_{ss} + \bar{c}_{66}\left(\frac{h_p h^2}{4} + \frac{hh_p^2}{2} + \frac{h_p^3}{3}\right) \qquad F_7 = \frac{\bar{e}_{16}}{2}\left(hh_p + h_p^2\right)$

$G_1 = K_s\acute{A}_{rq} \qquad G_2 = K_s(\acute{A}_{rr} + \bar{c}_{44}h_p) \qquad H_1 = K_s(\acute{A}_{qq} + \bar{c}_{55}h_p) \qquad H_2 = K_s\acute{A}_{qr} \qquad (E.1)$

Appendix F

The expression of coefficients of Eq. (2.37) are given by,

$$\acute{A}_1 = A_{xx} + \bar{c}_{22}h_p \qquad \acute{A}_2 = A_{x\theta} + \bar{c}_{12}h_p \qquad \acute{A}_3 = A_{xs} \qquad \acute{A}_4 = -B_{xx} - \frac{\bar{c}_{22}}{2}\left(hh_p + h_p^2\right)$$

$$\acute{A}_5 = -B_{x\theta} - \frac{\bar{c}_{12}}{2}\left(hh_p + h_p^2\right) \qquad \acute{A}_6 = -2B_{xs} \qquad \acute{A}_7 = \bar{e}_{22}h_p$$

$$\acute{B}_1 = A_{\theta x} + \bar{c}_{12}h_p \qquad \acute{B}_2 = A_{\theta\theta} + \bar{c}_{11}h_p \qquad \acute{B}_3 = A_{\theta s} \qquad \acute{B}_4 = -B_{\theta x} - \frac{\bar{c}_{12}}{2}\left(hh_p + h_p^2\right)$$

$$\acute{B}_5 = -B_{\theta\theta} - \frac{\bar{c}_{11}}{2}\left(hh_p + h_p^2\right) \qquad \acute{B}_6 = -2B_{\theta s} \qquad \acute{B}_7 = \bar{e}_{21}h_p$$

$$\acute{C}_1 = A_{sx} \qquad \acute{C}_2 = A_{s\theta} \qquad \acute{C}_3 = A_{ss} + \bar{c}_{66}h_p \qquad \acute{C}_4 = -B_{sx}$$

$$\acute{C}_5 = -B_{s\theta} \qquad \acute{C}_6 = -2B_{ss} - \bar{c}_{66}\left(hh_p + h_p^2\right) \qquad \acute{C}_7 = \bar{e}_{16}h_p$$

$$\acute{D}_1 = B_{xx} + \frac{\bar{c}_{22}}{2}\left(hh_p + h_p^2\right) \qquad \acute{D}_2 = B_{x\theta} + \frac{\bar{c}_{12}}{2}\left(hh_p + h_p^2\right) \qquad \acute{D}_3 = B_{xs}$$

$$\acute{D}_4 = -D_{xx} - \bar{c}_{22}\left(\frac{h_p h^2}{4} + \frac{hh_p^2}{2} + \frac{h_p^3}{3}\right) \qquad \acute{D}_5 = -D_{x\theta} - \bar{c}_{12}\left(\frac{h_p h^2}{4} + \frac{hh_p^2}{2} + \frac{h_p^3}{3}\right)$$

$$\acute{D}_6 = -2D_{xs} \qquad \acute{D}_7 = \frac{\bar{e}_{22}}{2}\left(hh_p + h_p^2\right)$$

$$\acute{E}_1 = B_{\theta x} + \frac{\bar{c}_{12}}{2}\left(hh_p + h_p^2\right) \qquad \acute{E}_2 = B_{\theta\theta} + \frac{\bar{c}_{11}}{2}\left(hh_p + h_p^2\right) \qquad \acute{E}_3 = B_{\theta s}$$

$$\acute{E}_4 = -D_{\theta x} - \bar{c}_{12}\left(\frac{h_p h^2}{4} + \frac{hh_p^2}{2} + \frac{h_p^3}{3}\right) \qquad \acute{E}_5 = -D_{\theta\theta} - \bar{c}_{11}\left(\frac{h_p h^2}{4} + \frac{hh_p^2}{2} + \frac{h_p^3}{3}\right)$$

$$\acute{E}_6 = -2D_{\theta s} \qquad \acute{E}_7 = \frac{\bar{e}_{21}}{2}\left(hh_p + h_p^2\right)$$

$$\acute{F}_1 = B_{sx} \qquad \acute{F}_2 = B_{s\theta} \qquad \acute{F}_3 = B_{ss} + \frac{\bar{c}_{66}}{2}\left(hh_p + h_p^2\right) \qquad \acute{F}_4 = -D_{sx} \qquad \acute{F}_5 = -D_{s\theta}$$

$$\acute{F}_6 = -2D_{ss} - \bar{c}_{66}\left(\frac{h_p h^2}{2} + hh_p^2 + \frac{2h_p^3}{3}\right) \qquad \acute{F}_7 = \frac{\bar{e}_{16}}{2}\left(hh_p + h_p^2\right) \qquad (F.1)$$

Appendix G

The components of matrix $\left[L_{ij}\right]_{6\times6}$, Eq. (2.55), are given by,

$$L_{11} = I_0(c\gamma)^2 - A_1\gamma^2 - \frac{n\gamma}{R}(A_3 + C_1) - C_3\frac{n^2}{R^2} \qquad L_{12} = -\frac{n\gamma}{R}(A_2 + C_3) - A_3\gamma^2 - C_2\frac{n^2}{R^2}$$

$$L_{13} = A_2\frac{i\gamma}{R} + C_2\frac{in}{R^2} \qquad L_{14} = I_1(c\gamma)^2 - A_4\gamma^2 - \frac{n\gamma}{R}(A_6 + C_4) - C_6\frac{n^2}{R^2}$$

$$L_{15} = -\frac{n\gamma}{R}(A_5 + C_6) - A_6\gamma^2 - C_5\frac{n^2}{R^2} \qquad L_{16} = -A_7\gamma^2 - C_7\frac{n^2}{R^2}$$

$$L_{21} = -\frac{n\gamma}{R}(B_1 + C_3) - B_3\frac{n^2}{R^2} - C_1\gamma^2 \qquad L_{22} = I_0(c\gamma)^2 - B_2\frac{n^2}{R^2} - \frac{n\gamma}{R}(B_3 + C_2) - C_3\gamma^2 - \frac{H_1}{R^2}$$

$$L_{23} = \frac{in}{R^2}(B_2 + H_1) + \frac{i\gamma}{R}(C_2 + H_2) \qquad L_{24} = -\frac{n\gamma}{R}(B_4 + C_6) - B_6\frac{n^2}{R^2} - C_4\gamma^2 + \frac{H_2}{R}$$

$$L_{25} = I_1(c\gamma)^2 - \frac{n\gamma}{R}(B_6 + C_5) - B_5\frac{n^2}{R^2} - C_6\gamma^2 + \frac{H_1}{R} \qquad L_{26} = -\frac{n\gamma}{R}(B_7 + C_7)$$

$$L_{31} = -B_1\frac{i\gamma}{R} - B_3\frac{in}{R^2} \qquad L_{32} = -\frac{in}{R^2}(B_2 + H_1) - \frac{i\gamma}{R}(B_3 + G_1)$$

$$L_{33} = I_0(c\gamma)^2 - \frac{B_2}{R^2} - \frac{n\gamma}{R}(G_1 + H_2) - G_2\gamma^2 - H_1\frac{n^2}{R^2} \qquad L_{34} = -B_4\frac{i\gamma}{R} - B_6\frac{in}{R^2} + G_2 i\gamma + H_2\frac{in}{R}$$

$$L_{35} = -B_5\frac{in}{R^2} - B_6\frac{i\gamma}{R} + G_1 i\gamma + H_1\frac{in}{R} \qquad L_{36} = -B_7\frac{i\gamma}{R}$$

$$L_{41} = I_1(c\gamma)^2 - D_1\gamma^2 - \frac{n\gamma}{R}(D_3 + F_1) - F_3\frac{n^2}{R^2} \qquad L_{42} = -\frac{n\gamma}{R}(D_2 + F_3) - D_3\gamma^2 - F_2\frac{n^2}{R^2} + \frac{G_1}{R}$$

$$L_{43} = D_2\frac{i\gamma}{R} + F_2\frac{in}{R^2} - G_1\frac{in}{R} - G_2 i\gamma \qquad L_{44} = I_2(c\gamma)^2 - D_4\gamma^2 - \frac{n\gamma}{R}(D_6 + F_4) - F_6\frac{n^2}{R^2} - G_2$$

$$L_{45} = -\frac{n\gamma}{R}(D_5 + F_6) - D_6\gamma^2 - F_5\frac{n^2}{R^2} - G_1 \qquad L_{46} = -D_7\gamma^2 - F_7\frac{n^2}{R^2}$$

$$L_{51} = -\frac{n\gamma}{R}(E_1 + F_3) - E_3\frac{n^2}{R^2} - F_1\gamma^2 \qquad L_{52} = I_1(c\gamma)^2 - \frac{n\gamma}{R}(E_3 + F_2) - F_3\gamma^2 - E_2\frac{n^2}{R^2} + \frac{H_1}{R}$$

$$L_{53} = E_2\frac{in}{R^2} + F_2\frac{i\gamma}{R} - H_1\frac{in}{R} - H_2 i\gamma \qquad L_{54} = -\frac{n\gamma}{R}(E_4 + F_6) - F_4\gamma^2 - E_6\frac{n^2}{R^2} - H_2$$

$$L_{55} = I_2(c\gamma)^2 - \frac{n\gamma}{R}(E_6 + F_5) - F_6\gamma^2 - E_5\frac{n^2}{R^2} - H_1 \qquad L_{56} = -\frac{n\gamma}{R}(E_7 + F_7)$$

$$L_{61} = -\bar{e}_{16}\frac{n^2}{R^2} - \bar{e}_{22}\gamma^2 \qquad L_{62} = -\frac{n\gamma}{R}(\bar{e}_{16} + \bar{e}_{21}) \qquad L_{63} = \bar{e}_{21}\frac{i\gamma}{R}$$

$$L_{64} = -\frac{\bar{e}_{16}}{2R^2}(h + h_p)n^2 - \bar{e}_{22}\frac{(h + h_p)}{2}\gamma^2 \qquad L_{65} = -\frac{n\gamma}{2R}(h + h_p)(\bar{e}_{16} + \bar{e}_{21})$$

$$L_{66} = \bar{\epsilon}_{11}\frac{n^2}{R^2} + \bar{\epsilon}_{22}\gamma^2 \qquad (G.1)$$

Appendix H

The components of matrix $[S_{ij}]_{4\times4}$, Eq. (2.56), are given by,

$$S_{11} = I_0(c\gamma)^2 - A_1\gamma^2 - \frac{n\gamma}{R}(A_3 + C_1) - C_3\frac{n^2}{R^2} \qquad S_{12} = -\frac{n\gamma}{R}(A_2 + C_3) - A_3\gamma^2 - C_2\frac{n^2}{R^2}$$

$$S_{13} = A_2\frac{i\gamma}{R} - A_4 i\gamma^3 - \frac{i\gamma n^2}{R^2}(A_5 + C_6) - \frac{in\gamma^2}{R}(A_6 + C_4) + \frac{C_2}{R^2}in - C_5\frac{in^3}{R^3} \qquad S_{14} = -A_7\gamma^2 - C_7\frac{n^2}{R^2}$$

$$S_{21} = -\frac{n\gamma}{R}(B_1 + C_3) - B_3\frac{n^2}{R^2} - C_1\gamma^2 + F_1\frac{\gamma^2}{R} + \frac{n\gamma}{R^2}(E_1 + F_3) + E_3\frac{n^2}{R^3}$$

$$S_{22} = I_0(c\gamma)^2 - B_2\frac{n^2}{R^2} - \frac{n\gamma}{R}(B_3 + C_2) - C_3\gamma^2 + \frac{n\gamma}{R^2}(E_3 + F_2) + E_2\frac{n^2}{R^3} + F_3\frac{\gamma^2}{R}$$

$$S_{23} = \frac{B_2}{R^2}in - \frac{in\gamma^2}{R}(B_4 + C_6) - B_5\frac{in^3}{R^3} - \frac{i\gamma n^2}{R^2}(B_6 + C_5) + C_2\frac{i\gamma}{R} - C_4 i\gamma^3 - F_2\frac{i\gamma}{R^2} + F_4\frac{i\gamma^3}{R} +$$

$$\frac{i\gamma n^2}{R^3}(E_6 + F_5) + \frac{in\gamma^2}{R^2}(E_4 + F_6) - E_2\frac{in}{R^3} + E_5\frac{in^3}{R^4}$$

$$S_{24} = -\frac{n\gamma}{R}(B_7 + C_7) + \frac{n\gamma}{R^2}(E_7 + F_7)$$

$$S_{31} = -B_1\frac{i\gamma}{R} - B_3\frac{in}{R^2} - D_1 i\gamma^3 - \frac{in\gamma^2}{R}(D_3 + 2F_1) - E_3\frac{in^3}{R^3} - \frac{i\gamma n^2}{R^2}(E_1 + 2F_3)$$

$$S_{32} = -B_2\frac{in}{R^2} - B_3\frac{i\gamma}{R} - \frac{in\gamma^2}{R}(D_2 + 2F_3) - D_3 i\gamma^3 - \frac{i\gamma n^2}{R^2}(E_3 + 2F_2) - E_2\frac{in^3}{R^3}$$

$$S_{33} = I_0(c\gamma)^2 - \frac{B_2}{R^2} + \frac{\gamma^2}{R}(B_4 - D_2) + \frac{\gamma^2 n^2}{R^2}(D_5 + E_4 + 2F_6) + \frac{n\gamma^3}{R}(D_6 + 2F_4) + D_4\gamma^4 - \frac{n\gamma}{R^2}(2F_2 - B_6) +$$

$$\frac{\gamma n^3}{R^3}(E_6 + 2F_5) + \frac{n^2}{R^3}(B_5 - E_2) + E_5\frac{n^4}{R^4}$$

$$S_{34} = -B_7\frac{i\gamma}{R} - D_7 i\gamma^3 - \frac{i\gamma n^2}{R^2}(E_7 + 2F_7)$$

$$S_{41} = -\bar{e}_{16}\frac{n^2}{R^2} - \bar{e}_{22}\gamma^2 \qquad S_{42} = -\frac{n\gamma}{R}(\bar{e}_{16} + \bar{e}_{21})$$

$$S_{43} = \bar{e}_{21}\frac{i\gamma}{R} + \bar{e}_{22}\frac{(h+h_p)}{2}i\gamma^3 + \frac{(h+h_p)i\gamma n^2}{R^2}(\bar{e}_{16} + \bar{e}_{21}) \qquad S_{44} = \bar{\in}_{11}\frac{n^2}{R^2} + \bar{\in}_{22}\gamma^2 \qquad (H.1)$$

Appendix I

The components of matrix $[T_{ij}]_{4\times4}$, Eq. (2.57), are given by,

$$T_{11} = I_0(c\gamma)^2 - A_1\gamma^2 - \frac{n\gamma}{R}(A_3 + C_1) - C_3\frac{n^2}{R^2} \qquad T_{12} = -\frac{n\gamma}{R}(A_2 + C_3) - A_3\gamma^2 - C_2\frac{n^2}{R^2}$$

$$T_{13} = \frac{A_2}{R}i\gamma - A_4 i\gamma^3 - \frac{i\gamma n^2}{R^2}(A_5 + C_6) - \frac{in\gamma^2}{R}(A_6 + C_4) + C_2\frac{in}{R^2} - C_5\frac{in^3}{R^3} \qquad T_{14} = -A_7\gamma^2 - C_7\frac{n^2}{R^2}$$

$$T_{21} = -\frac{n\gamma}{R}(B_1 + C_3) - B_3\frac{n^2}{R^2} - C_1\gamma^2 \qquad T_{22} = I_0(c\gamma)^2 - B_2\frac{n^2}{R^2} - \frac{n\gamma}{R}(B_3 + C_2) - C_3\gamma^2$$

$$T_{23} = B_2\frac{in}{R^2} - \frac{in\gamma^2}{R}(B_4 + C_6) - B_5\frac{in^3}{R^3} - \frac{i\gamma n^2}{R^2}(B_6 + C_5) + C_2\frac{i\gamma}{R} - C_4 i\gamma^3 \qquad T_{24} = -\frac{n\gamma}{R}(B_7 + C_7)$$

$$T_{31} = -B_1\frac{i\gamma}{R} - B_3\frac{in}{R^2} \qquad T_{32} = -B_2\frac{in}{R^2} \qquad T_{33} = I_0(c\gamma)^2 - \frac{B_2}{R^2} + B_4\frac{\gamma^2}{R} + B_5\frac{n^2}{R^3} + B_6\frac{n\gamma}{R^2} \qquad T_{34} = -B_7\frac{i\gamma}{R}$$

$$T_{41} = -\bar{e}_{16}\frac{n^2}{R^2} - \bar{e}_{22}\gamma^2 \qquad T_{42} = -\frac{n\gamma}{R}(\bar{e}_{16} + \bar{e}_{21})$$

$$T_{43} = \bar{e}_{21}\frac{i\gamma}{R} + \bar{e}_{22}\frac{(h+h_p)}{2}i\gamma^3 + \frac{(h+h_p)i\gamma n^2}{R^2}(\bar{e}_{16} + \bar{e}_{21}) \qquad T_{44} = \bar{\in}_{11}\frac{n^2}{R^2} + \bar{\in}_{22}\gamma^2 \qquad (I.1)$$

Appendix J

Transformation matrix $[T_{ij}]$ and its inverse $[T_{ij}^{-1}]$, required for Eq. (2.69), are given by,

$$[T_{ij}] = \begin{bmatrix} \acute{m}^2 & \acute{n}^2 & 0 & 0 & 0 & 2\acute{m}\acute{n} \\ \acute{n}^2 & \acute{m}^2 & 0 & 0 & 0 & -2\acute{m}\acute{n} \\ 0 & 0 & 1 & 0 & 0 & 0 \\ 0 & 0 & 0 & \acute{m} & -\acute{n} & 0 \\ 0 & 0 & 0 & \acute{n} & \acute{m} & 0 \\ -\acute{m}\acute{n} & \acute{m}\acute{n} & 0 & 0 & 0 & \acute{m}^2 - \acute{n}^2 \end{bmatrix} \tag{J.1}$$

$$[T_{ij}^{-1}] = \begin{bmatrix} \acute{m}^2 & \acute{n}^2 & 0 & 0 & 0 & -2\acute{m}\acute{n} \\ \acute{n}^2 & \acute{m}^2 & 0 & 0 & 0 & 2\acute{m}\acute{n} \\ 0 & 0 & 1 & 0 & 0 & 0 \\ 0 & 0 & 0 & \acute{m} & \acute{n} & 0 \\ 0 & 0 & 0 & -\acute{n} & \acute{m} & 0 \\ \acute{m}\acute{n} & -\acute{m}\acute{n} & 0 & 0 & 0 & \acute{m}^2 - \acute{n}^2 \end{bmatrix} \tag{J.2}$$

where

$$\acute{m} = cos\beta, \qquad \acute{n} = sin\beta \tag{J.3}$$

The components of the stiffness matrix $[C]_{(x,\theta,z)}$ in the cylindrical coordinate system (x, θ, z) are given by,

$$C_{xx} = \acute{m}^4 C_{11} + 2\acute{m}^2\acute{n}^2 C_{12} + \acute{n}^4 C_{22} + 4\acute{m}^2\acute{n}^2 C_{66}$$

$$C_{x\theta} = \acute{m}^2\acute{n}^2 C_{11} + (\acute{m}^4 + \acute{n}^4) C_{12} + \acute{m}^2\acute{n}^2 C_{22} - 4\acute{m}^2\acute{n}^2 C_{66}$$

$$C_{xz} = \acute{m}^2 C_{13} + \acute{n}^2 C_{23}$$

$$C_{xs} = \acute{m}^3\acute{n} C_{11} - \acute{m}\acute{n}(\acute{m}^2 - \acute{n}^2) C_{12} - \acute{m}\acute{n}^3 C_{22} - 2\acute{m}\acute{n}(\acute{m}^2 - \acute{n}^2) C_{66}$$

$$C_{\theta\theta} = \acute{n}^4 C_{11} + 2\acute{m}^2\acute{n}^2 C_{12} + \acute{m}^4 C_{22} + 4\acute{m}^2\acute{n}^2 C_{66}$$

$$C_{\theta z} = \acute{n}^2 C_{13} + \acute{m}^2 C_{23}$$

$$C_{\theta s} = \acute{m}\acute{n}^3 C_{11} + \acute{m}\acute{n}(\acute{m}^2 - \acute{n}^2) C_{12} - \acute{m}^3\acute{n} C_{22} + 2\acute{m}\acute{n}(\acute{m}^2 - \acute{n}^2) C_{66}$$

$$C_{zz} = C_{33}$$

$$C_{zs} = \acute{m}\acute{n} C_{13} - \acute{m}\acute{n} C_{23}$$

$$C_{qq} = \acute{m}^2 C_{44} + \acute{n}^2 C_{55}$$

$$C_{rq} = -\acute{m}\acute{n} C_{44} + \acute{m}\acute{n} C_{55}$$

$$C_{rr} = \acute{n}^2 C_{44} + \acute{m}^2 C_{55}$$

$$C_{ss} = \acute{m}^2 \acute{n}^2 C_{11} - 2\acute{m}^2 \acute{n}^2 C_{12} + \acute{m}^2 \acute{n}^2 C_{22} + (\acute{m}^2 - \acute{n}^2)^2 C_{66} \qquad (J.4)$$

Appendix K

$\bar{C}_{\theta\theta}$, $\bar{C}_{\theta x}$, $\bar{C}_{\theta s}$, $\bar{C}_{xx}$, $\bar{C}_{xs}$, $\bar{C}_{rr}$, $\bar{C}_{rq}$, $\bar{C}_{qq}$, $\bar{C}_{ss}$, $\bar{e}_{16}$, $\bar{e}_{21}$, $\bar{e}_{22}$, $\bar{e}_{23}$, $\bar{e}_{34}$, and $\bar{\epsilon}_{11}$, $\bar{\epsilon}_{22}$, $\bar{\epsilon}_{33}$ for Eq. (2.71) are given by,

$$\bar{C}_{\theta\theta} = C_{\theta\theta} - \frac{C_{\theta z}^2}{C_{zz}} \qquad \bar{C}_{\theta x} = C_{\theta x} - \frac{C_{\theta z}C_{xz}}{C_{zz}} \qquad \bar{C}_{\theta s} = C_{\theta s} - \frac{C_{\theta z}C_{zs}}{C_{zz}} \qquad \bar{C}_{xx} = C_{xx} - \frac{C_{xz}^2}{C_{zz}}$$

$$\bar{C}_{xs} = C_{xs} - \frac{C_{xz}C_{zs}}{C_{zz}} \qquad \bar{C}_{rr} = C_{rr} \qquad \bar{C}_{rq} = C_{rq} \qquad \bar{C}_{qq} = C_{qq} \qquad \bar{C}_{ss} = C_{ss} - \frac{C_{zs}^2}{C_{zz}}$$

$$\bar{e}_{16} = e_{16} \qquad \bar{e}_{21} = e_{21} - e_{23}\frac{C_{\theta z}}{C_{zz}} \qquad \bar{e}_{22} = e_{22} - e_{23}\frac{C_{xz}}{C_{zz}} \qquad \bar{e}_{23} = -e_{23}\frac{C_{zs}}{C_{zz}}, \qquad \bar{e}_{34} = e_{34}$$

$$\bar{\epsilon}_{11}=\epsilon_{11} \qquad \bar{\epsilon}_{22}=\epsilon_{22}+\frac{e_{23}^2}{C_{zz}} \qquad \bar{\epsilon}_{33}=\epsilon_{33} \qquad (K.1)$$

and $\bar{C}_{\theta\theta}$, $\bar{C}_{\theta x}$, $\bar{C}_{xx}$, $\bar{C}_{rr}$, $\bar{C}_{qq}$, $\bar{C}_{ss}$, $\bar{e}_{16}$, $\bar{e}_{21}$, $\bar{e}_{22}$, $\bar{e}_{34}$, and $\bar{\epsilon}_{11}$, $\bar{\epsilon}_{22}$, $\bar{\epsilon}_{33}$ for Eq. (2.79) are given by,

$$\bar{C}_{\theta\theta} = C_{\theta\theta} - \frac{C_{\theta z}^2}{C_{zz}} \qquad \bar{C}_{\theta x} = C_{\theta x} - \frac{C_{\theta z}C_{xz}}{C_{zz}} \qquad \bar{C}_{xx} = C_{xx} - \frac{C_{xz}^2}{C_{zz}} \qquad \bar{C}_{rr} = C_{rr} \qquad \bar{C}_{qq} = C_{qq} \qquad \bar{C}_{ss} = C_{ss}$$

$$\bar{e}_{16} = e_{16} \qquad \bar{e}_{21} = e_{21} - e_{23}\frac{C_{\theta z}}{C_{zz}} \qquad \bar{e}_{22} = e_{22} - e_{23}\frac{C_{xz}}{C_{zz}} \qquad \bar{e}_{34} = e_{34}$$

$$\bar{\epsilon}_{11}=\epsilon_{11} \qquad \bar{\epsilon}_{22}=\epsilon_{22}+\frac{e_{23}^2}{C_{zz}} \qquad \bar{\epsilon}_{33}=\epsilon_{33} \qquad (K.2)$$

Appendix L

The expression of coefficients of Eq. (2.86) are given by,

$$A_1 = \bar{C}_{xx}h \qquad A_2 = \bar{C}_{xs}h \qquad A_3 = \bar{C}_{x\theta}h \qquad A_4 = \bar{e}_{22}h$$

$$B_1 = \bar{C}_{\theta x}h \qquad B_2 = \bar{C}_{\theta s}h \qquad B_3 = \bar{C}_{\theta\theta}h \qquad B_4 = \bar{e}_{21}h$$

$$C_1 = \bar{C}_{xs}h \qquad C_2 = \bar{C}_{ss}h \qquad C_3 = \bar{C}_{\theta s}h \qquad C_4 = \bar{e}_{23}h \qquad C_5 = \bar{e}_{16}h$$

$$D_1 = \bar{C}_{xx}\frac{h^3}{12} \qquad D_2 = \bar{C}_{\theta x}\frac{h^3}{12} \qquad D_3 = \bar{C}_{xs}\frac{h^3}{12}$$

$$E_1 = \bar{C}_{\theta x}\frac{h^3}{12} \qquad E_2 = \bar{C}_{\theta\theta}\frac{h^3}{12} \qquad E_3 = \bar{C}_{\theta s}\frac{h^3}{12}$$

$$F_1 = \bar{C}_{xs}\frac{h^3}{12} \qquad F_2 = \bar{C}_{\theta s}\frac{h^3}{12} \qquad F_3 = \bar{C}_{ss}\frac{h^3}{12}$$

$$G_1 = K_s\bar{C}_{rr}h \qquad G_2 = K_s\bar{C}_{rq}h$$

$$H_1 = K_s\bar{C}_{rq}h \qquad H_2 = K_s\bar{C}_{qq}h \tag{L.1}$$

The expression of coefficients of Eq. (2.87) are given by,

$$\acute{A}_1 = \bar{C}_{xx}h \qquad \acute{A}_2 = \bar{C}_{\theta x}h \qquad \acute{A}_3 = \bar{e}_{22}h \qquad \acute{B}_1 = \bar{C}_{\theta x}h \qquad \acute{B}_2 = \bar{C}_{\theta\theta}h \qquad \acute{B}_3 = \bar{e}_{21}h$$

$$\acute{C}_1 = \bar{C}_{ss}h \qquad \acute{C}_2 = \bar{e}_{16}h \qquad \acute{D}_1 = \bar{C}_{xx}\frac{h^3}{12} \qquad \acute{D}_2 = \bar{C}_{\theta x}\frac{h^3}{12} \qquad \acute{E}_1 = \bar{C}_{\theta x}\frac{h^3}{12} \qquad \acute{E}_2 = \bar{C}_{\theta\theta}\frac{h^3}{12}$$

$$\acute{F}_1 = \bar{C}_{ss}\frac{h^3}{12} \qquad \acute{G}_1 = K_s\bar{C}_{rr}h \qquad \acute{H}_1 = K_s\bar{C}_{qq}h \tag{L.2}$$

Appendix M

The components of characteristics matrix $[L_{ij}]$ $(i,j = 1,\dots,6)$ for a piezoelectric composite cylindrical shell reinforced with angled, straight CNTs (section 2.4.7) are obtained as,

$$L_{11} = I_0(c\gamma)^2 - A_1\gamma^2 - \frac{n\gamma}{R}(A_2 + C_1) - C_2\frac{n^2}{R^2} \qquad L_{12} = -A_2\gamma^2 - \frac{n\gamma}{R}(A_3 + C_2) - C_3\frac{n^2}{R^2}$$

$$L_{13} = A_3\frac{i\gamma}{R} + C_3\frac{in}{R^2} \qquad L_{14} = I_1(c\gamma)^2 \qquad L_{15} = 0 \qquad L_{16} = -A_4\gamma^2 - C_4\frac{n\gamma}{R} - C_5\frac{n^2}{R^2}$$

$$L_{21} = -\frac{n\gamma}{R}(B_1 + C_2) - B_2\frac{n^2}{R^2} - C_1\gamma^2 \qquad L_{22} = I_0(c\gamma)^2 - \frac{n\gamma}{R}(B_2 + C_3) - B_3\frac{n^2}{R^2} - C_2\gamma^2 - \frac{H_2}{R^2}$$

$$L_{23} = \frac{in}{R^2}(B_3 + H_2) + \frac{i\gamma}{R}(C_3 + H_1) \qquad L_{24} = \frac{H_1}{R} \qquad L_{25} = I_1(c\gamma)^2 + \frac{H_2}{R} \qquad L_{26} = -\frac{n\gamma}{R}(B_4 + C_5) - C_4\gamma^2$$

$$L_{31} = -B_1\frac{i\gamma}{R} - B_2\frac{in}{R^2} \qquad L_{32} = -\frac{i\gamma}{R}(B_2 + G_2) - \frac{in}{R^2}(B_3 + H_2)$$

$$L_{33} = I_0(c\gamma)^2 - \frac{B_3}{R^2} - G_1\gamma^2 - \frac{n\gamma}{R}(H_1 + G_2) - H_2\frac{n^2}{R^2} \qquad L_{34} = G_1 i\gamma + H_1\frac{in}{R}$$

$$L_{35} = G_2 i\gamma + H_2\frac{in}{R} \qquad L_{36} = -B_4\frac{i\gamma}{R}$$

$$L_{41} = I_1(c\gamma)^2 \qquad L_{42} = \frac{G_2}{R} \qquad L_{43} = -G_1 i\gamma - G_2\frac{in}{R}$$

$$L_{44} = I_2(c\gamma)^2 - D_1\gamma^2 - \frac{n\gamma}{R}(D_3 + F_1) - F_3\frac{n^2}{R^2} - G_1$$

$$L_{45} = -\frac{n\gamma}{R}(D_2 + F_3) - D_3\gamma^2 - F_2\frac{n^2}{R^2} - G_2 \qquad L_{46} = 0$$

$$L_{51} = 0 \qquad L_{52} = I_1(c\gamma)^2 + \frac{H_2}{R} \qquad L_{53} = -H_1 i\gamma - H_2\frac{in}{R}$$

$$L_{54} = -F_1\gamma^2 - \frac{n\gamma}{R}(F_3 + E_1) - E_3\frac{n^2}{R^2} - H_1$$

$$L_{55} = I_2(c\gamma)^2 - \frac{n\gamma}{R}(F_2 + E_3) - F_3\gamma^2 - E_2\frac{n^2}{R^2} - H_2 \qquad L_{56} = 0$$

$$L_{61} = -\bar{e}_{22}\gamma^2 - \bar{e}_{16}\frac{n^2}{R^2} - \bar{e}_{23}\frac{n\gamma}{R} \qquad L_{62} = -\frac{n\gamma}{R}(\bar{e}_{16} + \bar{e}_{21}) - \bar{e}_{23}\gamma^2 \qquad L_{63} = \bar{e}_{21}\frac{i\gamma}{R}$$

$$L_{64} = 0 \qquad L_{65} = 0 \qquad L_{66} = \bar{\in}_{11}\frac{n^2}{R^2} + \bar{\in}_{22}\gamma^2 \qquad (M.1)$$

The components of characteristics matrix $[L_{ij}]$ $(i,j = 1,\dots,6)$ for a piezoelectric composite cylindrical shell reinforced with randomly oriented (agglomerated), straight CNTs (section 2.4.7) are obtained as,

$$L_{11} = I_0(c\gamma)^2 - \acute{A}_1\gamma^2 - \acute{C}_1\frac{n^2}{R^2} \qquad L_{12} = -\frac{n\gamma}{R}\left(\acute{A}_2 + \acute{C}_1\right) \qquad L_{13} = \acute{A}_2\frac{i\gamma}{R} \qquad L_{14} = I_1(c\gamma)^2$$

$$L_{15} = 0 \qquad L_{16} = -\acute{A}_3\gamma^2 - \acute{C}_2\frac{n^2}{R^2}$$

$$L_{21} = -\frac{n\gamma}{R}\left(\acute{B}_1 + \acute{C}_1\right) \qquad L_{22} = I_0(c\gamma)^2 - \acute{B}_2\frac{n^2}{R^2} - \acute{C}_1\gamma^2 - \frac{\acute{H}_1}{R^2}$$

$$L_{23} = \frac{in}{R^2}\left(\acute{B}_2 + \acute{H}_1\right) \qquad L_{24} = 0 \qquad L_{25} = I_1(c\gamma)^2 + \frac{\acute{H}_1}{R} \qquad L_{26} = -\frac{n\gamma}{R}\left(\acute{B}_3 + \acute{C}_2\right)$$

$$L_{31} = -\acute{B}_1\frac{i\gamma}{R} \qquad L_{32} = -\frac{in}{R^2}\left(\acute{B}_2 + \acute{H}_1\right) \qquad L_{33} = I_0(c\gamma)^2 - \frac{\acute{B}_2}{R^2} - \acute{G}_1\gamma^2 - \acute{H}_1\frac{n^2}{R^2}$$

$$L_{34} = \acute{G}_1 i\gamma \qquad L_{35} = \acute{H}_1\frac{in}{R} \qquad L_{36} = -\acute{B}_3\frac{i\gamma}{R}$$

$$L_{41} = I_1(c\gamma)^2 \qquad L_{42} = 0 \qquad L_{43} = -\acute{G}_1 i\gamma$$

$$L_{44} = I_2(c\gamma)^2 - \acute{D}_1\gamma^2 - \acute{F}_1\frac{n^2}{R^2} - \acute{G}_1 \qquad L_{45} = -\frac{n\gamma}{R}\left(\acute{D}_2 + \acute{F}_1\right) \qquad L_{46} = 0$$

$$L_{51} = 0 \qquad L_{52} = I_1(c\gamma)^2 + \frac{\acute{H}_1}{R} \qquad L_{53} = -\acute{H}_1\frac{in}{R}$$

$$L_{54} = -\frac{n\gamma}{R}\left(\acute{F}_1 + \acute{E}_1\right) \qquad L_{55} = I_2(c\gamma)^2 - \acute{F}_1\gamma^2 - \acute{E}_2\frac{n^2}{R^2} - \acute{H}_1 \qquad L_{56} = 0$$

$$L_{61} = -\bar{e}_{22}\gamma^2 - \bar{e}_{16}\frac{n^2}{R^2} \qquad L_{62} = -\frac{n\gamma}{R}(\bar{e}_{16} + \bar{e}_{21}) \qquad L_{63} = \bar{e}_{21}\frac{i\gamma}{R}$$

$$L_{64} = 0 \qquad L_{65} = 0 \qquad L_{66} = \bar{\in}_{11}\frac{n^2}{R^2} + \bar{\in}_{22}\gamma^2 \qquad (M.2)$$

Appendix N

The expression of coefficients of Eq. (2.113) are given by,

$$A_1 = A_{xx} + 2\bar{c}_{22}h_p \qquad A_2 = A_{x\theta} + 2\bar{c}_{12}h_p \qquad A_3 = A_{xs} \qquad A_4 = B_{xx}$$

$$A_5 = B_{x\theta} \qquad A_6 = B_{xs} \qquad A_7 = 2\bar{e}_{22}h_p \qquad A_8 = -E_{xx} \qquad A_9 = -F_{xx}$$

$$B_1 = A_{\theta x} + 2\bar{c}_{12}h_p \qquad B_2 = A_{\theta\theta} + 2\bar{c}_{11}h_p \qquad B_3 = A_{\theta s} \qquad B_4 = B_{\theta x}$$

$$B_5 = B_{\theta\theta} \qquad B_6 = B_{\theta s} \qquad B_7 = 2\bar{e}_{21}h_p \qquad B_8 = -E_{\theta\theta} \qquad B_9 = -F_{\theta\theta}$$

$$C_1 = A_{sx} \qquad C_2 = A_{s\theta} \qquad C_3 = A_{ss} + 2\bar{c}_{66}h_p \qquad C_4 = B_{sx}$$

$$C_5 = B_{s\theta} \qquad C_6 = B_{ss} \qquad C_7 = 2\bar{e}_{16}h_p \qquad C_8 = -E_{x\theta} \qquad C_9 = -F_{x\theta}$$

$$D_1 = B_{xx} \qquad D_2 = B_{x\theta} \qquad D_3 = B_{xs} \qquad D_4 = D_{xx} + \bar{c}_{22}\left(\frac{h_p h^2}{2} + hh_p^2 + \frac{2h_p^3}{3}\right)$$

$$D_5 = D_{x\theta} + \bar{c}_{12}\left(\frac{h_p h^2}{2} + hh_p^2 + \frac{2h_p^3}{3}\right) \qquad D_6 = D_{xs} \qquad D_7 = -G_{xx} \qquad D_8 = -H_{xx}$$

$$E_1 = B_{\theta x} \qquad E_2 = B_{\theta\theta} \qquad E_3 = B_{\theta s} \qquad E_4 = D_{\theta x} + \bar{c}_{12}\left(\frac{h_p h^2}{2} + hh_p^2 + \frac{2h_p^3}{3}\right)$$

$$E_5 = D_{\theta\theta} + \bar{c}_{11}\left(\frac{h_p h^2}{2} + hh_p^2 + \frac{2h_p^3}{3}\right) \qquad E_6 = D_{\theta s} \qquad E_7 = -G_{\theta\theta} \qquad E_8 = -H_{\theta\theta}$$

$$F_1 = B_{sx} \qquad F_2 = B_{s\theta} \qquad F_3 = B_{ss} \qquad F_4 = D_{sx} \qquad F_5 = D_{s\theta}$$

$$F_6 = D_{ss} + \bar{c}_{66}\left(\frac{h_p h^2}{2} + hh_p^2 + \frac{2h_p^3}{3}\right) \qquad F_7 = -G_{x\theta} \qquad F_8 = -H_{x\theta}$$

$$G_1 = K_s\acute{A}_{rq} \qquad G_2 = K_s(\acute{A}_{rr} + 2\bar{c}_{44}h_p) \qquad H_1 = K_s(\acute{A}_{qq} + 2\bar{c}_{55}h_p) \qquad H_2 = K_s\acute{A}_{qr} \qquad (N.1)$$

Appendix O

The components of matrix $\left[L_{ij}\right]_{8\times 8}$, Eq. (2.120), are given by,

$$L_{11} = I_0(c\gamma)^2 - A_1\gamma^2 - \frac{n\gamma}{R}(A_3 + C_1) - C_3\frac{n^2}{R^2} \qquad L_{12} = -\frac{n\gamma}{R}(A_2 + C_3) - A_3\gamma^2 - C_2\frac{n^2}{R^2}$$

$$L_{13} = A_2\frac{i\gamma}{R} + C_2\frac{in}{R^2} \qquad L_{14} = I_1(c\gamma)^2 - A_4\gamma^2 - \frac{n\gamma}{R}(A_6 + C_4) - C_6\frac{n^2}{R^2}$$

$$L_{15} = -\frac{n\gamma}{R}(A_5 + C_6) - A_6\gamma^2 - C_5\frac{n^2}{R^2} \qquad L_{16} = -A_7\gamma^2 - C_7\frac{n^2}{R^2}$$

$$L_{17} = A_8 i\gamma + C_8\frac{in}{R} \qquad L_{18} = A_9 i\gamma + C_9\frac{in}{R}$$

$$L_{21} = -\frac{n\gamma}{R}(B_1 + C_3) - B_3\frac{n^2}{R^2} - C_1\gamma^2 \qquad L_{22} = I_0(c\gamma)^2 - B_2\frac{n^2}{R^2} - \frac{n\gamma}{R}(B_3 + C_2) - C_3\gamma^2 - \frac{H_1}{R^2}$$

$$L_{23} = \frac{in}{R^2}(B_2 + H_1) + \frac{i\gamma}{R}(C_2 + H_2) \qquad L_{24} = -\frac{n\gamma}{R}(B_4 + C_6) - B_6\frac{n^2}{R^2} - C_4\gamma^2 + \frac{H_2}{R}$$

$$L_{25} = I_1(c\gamma)^2 - B_5\frac{n^2}{R^2} - \frac{n\gamma}{R}(B_6 + C_5) - C_6\gamma^2 + \frac{H_1}{R} \qquad L_{26} = -\frac{n\gamma}{R}(B_7 + C_7)$$

$$L_{27} = B_8\frac{in}{R} + C_8 i\gamma \qquad L_{28} = B_9\frac{in}{R} + C_9 i\gamma$$

$$L_{31} = -B_1\frac{i\gamma}{R} - B_3\frac{in}{R^2} \qquad L_{32} = -\frac{in}{R^2}(B_2 + H_1) - \frac{i\gamma}{R}(B_3 + G_1)$$

$$L_{33} = I_0(c\gamma)^2 - \frac{B_2}{R^2} - \frac{n\gamma}{R}(G_1 + H_2) - G_2\gamma^2 - H_1\frac{n^2}{R^2} \qquad L_{34} = -B_4\frac{i\gamma}{R} - B_6\frac{in}{R^2} + G_2 i\gamma + H_2\frac{in}{R}$$

$$L_{35} = -B_5\frac{in}{R^2} - B_6\frac{i\gamma}{R} + G_1 i\gamma + H_1\frac{in}{R} \qquad L_{36} = -B_7\frac{i\gamma}{R} \qquad L_{37} = -\frac{B_8}{R} \qquad L_{38} = -\frac{B_9}{R}$$

$$L_{41} = I_1(c\gamma)^2 - D_1\gamma^2 - \frac{n\gamma}{R}(D_3 + F_1) - F_3\frac{n^2}{R^2} \qquad L_{42} = -\frac{n\gamma}{R}(D_2 + F_3) - D_3\gamma^2 - F_2\frac{n^2}{R^2} + \frac{G_1}{R}$$

$$L_{43} = D_2\frac{i\gamma}{R} + F_2\frac{in}{R^2} - G_1\frac{in}{R} - G_2 i\gamma \qquad L_{44} = I_2(c\gamma)^2 - D_4\gamma^2 - \frac{n\gamma}{R}(D_6 + F_4) - F_6\frac{n^2}{R^2} - G_2$$

$$L_{45} = -\frac{n\gamma}{R}(D_5 + F_6) - D_6\gamma^2 - F_5\frac{n^2}{R^2} - G_1 \qquad L_{46} = 0 \qquad L_{47} = D_7 i\gamma + F_7\frac{in}{R} \qquad L_{48} = D_8 i\gamma + F_8\frac{in}{R}$$

$$L_{51} = -\frac{n\gamma}{R}(E_1 + F_3) - E_3\frac{n^2}{R^2} - F_1\gamma^2 \qquad L_{52} = I_1(c\gamma)^2 - \frac{n\gamma}{R}(E_3 + F_2) - F_3\gamma^2 - E_2\frac{n^2}{R^2} + \frac{H_1}{R}$$

$$L_{53} = E_2\frac{in}{R^2} + F_2\frac{i\gamma}{R} - H_1\frac{in}{R} - H_2 i\gamma \qquad L_{54} = -\frac{n\gamma}{R}(E_4 + F_6) - F_4\gamma^2 - E_6\frac{n^2}{R^2} - H_2$$

$$L_{55} = I_2(c\gamma)^2 - \frac{n\gamma}{R}(E_6 + F_5) - F_6\gamma^2 - E_5\frac{n^2}{R^2} - H_1 \qquad L_{56} = 0$$

$$L_{57} = F_7 i\gamma + E_7\frac{in}{R} \qquad L_{58} = F_8 i\gamma + E_8\frac{in}{R}$$

$$L_{61} = -\bar{e}_{16}\frac{n^2}{R^2} - \bar{e}_{22}\gamma^2 \qquad L_{62} = -\frac{n\gamma}{R}(\bar{e}_{16} + \bar{e}_{21}) \qquad L_{63} = \bar{e}_{21}\frac{i\gamma}{R}$$

$$L_{64} = L_{65} = 0 \qquad L_{66} = \bar{\in}_{11}\frac{n^2}{R^2} + \bar{\in}_{22}\gamma^2 \qquad L_{67} = L_{68} = 0$$

$$L_{71} = L_{72} = L_{73} = L_{74} = L_{75} = L_{76} = 0 \qquad L_{77} = -\gamma^2 - \frac{n^2}{R^2} \qquad L_{78} = 0$$

$$L_{81} = L_{82} = L_{83} = L_{84} = L_{85} = L_{86} = L_{87} = 0 \qquad L_{88} = -\gamma^2 - \frac{n^2}{R^2} \qquad (O.1)$$

Appendix P

The components of matrix $\left[L_{ij}\right]_{8\times 8}$, Eq. (2.124), are given by,

$$L_{11} = I_0\omega^2 - A_1\gamma_m^2 - \frac{n\gamma_m}{R}(A_3 + C_1) - C_3\frac{n^2}{R^2} \qquad L_{12} = -\frac{n\gamma_m}{R}(A_2 + C_3) - A_3\gamma_m^2 - C_2\frac{n^2}{R^2}$$

$$L_{13} = A_2\frac{i\gamma_m}{R} + C_2\frac{in}{R^2} \qquad L_{14} = I_1\omega^2 - A_4\gamma_m^2 - \frac{n\gamma_m}{R}(A_6 + C_4) - C_6\frac{n^2}{R^2}$$

$$L_{15} = -\frac{n\gamma_m}{R}(A_5 + C_6) - A_6\gamma_m^2 - C_5\frac{n^2}{R^2} \qquad L_{16} = -A_7\gamma_m^2 - C_7\frac{n^2}{R^2}$$

$$L_{17} = A_8 i\gamma_m + C_8\frac{in}{R} \qquad L_{18} = A_9 i\gamma_m + C_9\frac{in}{R}$$

$$L_{21} = -\frac{n\gamma_m}{R}(B_1 + C_3) - B_3\frac{n^2}{R^2} - C_1\gamma_m^2 \qquad L_{22} = I_0\omega^2 - B_2\frac{n^2}{R^2} - \frac{n\gamma_m}{R}(B_3 + C_2) - C_3\gamma_m^2 - \frac{H_1}{R^2}$$

$$L_{23} = \frac{in}{R^2}(B_2 + H_1) + \frac{i\gamma_m}{R}(C_2 + H_2) \qquad L_{24} = -\frac{n\gamma_m}{R}(B_4 + C_6) - B_6\frac{n^2}{R^2} - C_4\gamma_m^2 + \frac{H_2}{R}$$

$$L_{25} = I_1\omega^2 - B_5\frac{n^2}{R^2} - \frac{n\gamma_m}{R}(B_6 + C_5) - C_6\gamma_m^2 + \frac{H_1}{R} \qquad L_{26} = -\frac{n\gamma_m}{R}(B_7 + C_7)$$

$$L_{27} = B_8\frac{in}{R} + C_8 i\gamma_m \qquad L_{28} = B_9\frac{in}{R} + C_9 i\gamma_m$$

$$L_{31} = -B_1\frac{i\gamma_m}{R} - B_3\frac{in}{R^2} \qquad L_{32} = -\frac{in}{R^2}(B_2 + H_1) - \frac{i\gamma_m}{R}(B_3 + G_1)$$

$$L_{33} = I_0\omega^2 - \frac{B_2}{R^2} - \frac{n\gamma_m}{R}(G_1 + H_2) - G_2\gamma_m^2 - H_1\frac{n^2}{R^2} \qquad L_{34} = -B_4\frac{i\gamma_m}{R} - B_6\frac{in}{R^2} + G_2 i\gamma_m + H_2\frac{in}{R}$$

$$L_{35} = -B_5\frac{in}{R^2} - B_6\frac{i\gamma_m}{R} + G_1 i\gamma_m + H_1\frac{in}{R} \qquad L_{36} = -B_7\frac{i\gamma_m}{R} \qquad L_{37} = -\frac{B_8}{R} \qquad L_{38} = -\frac{B_9}{R}$$

$$L_{41} = I_1\omega^2 - D_1\gamma_m^2 - \frac{n\gamma_m}{R}(D_3 + F_1) - F_3\frac{n^2}{R^2} \qquad L_{42} = -\frac{n\gamma_m}{R}(D_2 + F_3) - D_3\gamma_m^2 - F_2\frac{n^2}{R^2} + \frac{G_1}{R}$$

$$L_{43} = D_2\frac{i\gamma_m}{R} + F_2\frac{in}{R^2} - G_1\frac{in}{R} - G_2 i\gamma_m \qquad L_{44} = I_2\omega^2 - D_4\gamma_m^2 - \frac{n\gamma_m}{R}(D_6 + F_4) - F_6\frac{n^2}{R^2} - G_2$$

$$L_{45} = -\frac{n\gamma_m}{R}(D_5 + F_6) - D_6\gamma_m^2 - F_5\frac{n^2}{R^2} - G_1 \qquad L_{46} = 0$$

$$L_{47} = D_7 i\gamma_m + F_7\frac{in}{R} \qquad L_{48} = D_8 i\gamma_m + F_8\frac{in}{R}$$

$$L_{51} = -\frac{n\gamma_m}{R}(E_1 + F_3) - E_3\frac{n^2}{R^2} - F_1\gamma_m^2 \qquad L_{52} = I_1\omega^2 - \frac{n\gamma_m}{R}(E_3 + F_2) - F_3\gamma_m^2 - E_2\frac{n^2}{R^2} + \frac{H_1}{R}$$

$$L_{53} = E_2\frac{in}{R^2} + F_2\frac{i\gamma_m}{R} - H_1\frac{in}{R} - H_2 i\gamma_m \qquad L_{54} = -\frac{n\gamma_m}{R}(E_4 + F_6) - F_4\gamma_m^2 - E_6\frac{n^2}{R^2} - H_2$$

$$L_{55} = I_2\omega^2 - \frac{n\gamma_m}{R}(E_6 + F_5) - F_6\gamma_m^2 - E_5\frac{n^2}{R^2} - H_1 \qquad L_{56} = 0$$

$$L_{57} = F_7 i\gamma_m + E_7\frac{in}{R} \qquad L_{58} = F_8 i\gamma_m + E_8\frac{in}{R}$$

$$L_{61} = -\bar{e}_{16}\frac{n^2}{R^2} - \bar{e}_{22}\gamma_m^2 \qquad L_{62} = -\frac{n\gamma_m}{R}(\bar{e}_{16} + \bar{e}_{21}) \qquad L_{63} = \bar{e}_{21}\frac{i\gamma_m}{R}$$

$$L_{64} = L_{65} = 0 \qquad L_{66} = \bar{\epsilon}_{11}\frac{n^2}{R^2} + \bar{\epsilon}_{22}\gamma_m^2 \qquad L_{67} = L_{68} = 0$$

$$L_{71} = L_{72} = L_{73} = L_{74} = L_{75} = L_{76} = 0 \qquad L_{77} = -\gamma_m^2 - \frac{n^2}{R^2} \qquad L_{78} = 0$$

$$L_{81} = L_{82} = L_{83} = L_{84} = L_{85} = L_{86} = L_{87} = 0 \qquad L_{88} = -\gamma_m^2 - \frac{n^2}{R^2} \qquad (P.1)$$

Bibliography

[1] D. Chapelle, K.-J. Bathe, The Finite Element Analysis of Shells - Fundamentals, 2nd ed., Springer, Berlin, Germany, 2011.

[2] Parc olympique de Montréal, Parc Olymp. (n.d.). https://parcolympique.qc.ca.

[3] M. Amabili, Nonlinear Vibrations and Stability of Shells and Plates, Cambridge University Press, New York, 2008.

[4] Boeing: 777, (n.d.). https://www.boeing.com/commercial/777.

[5] Carnival Corporation & plc, Carnival Corp. Plc. (n.d.). https://www.carnivalcorp.com/index.

[6] I.M. Daniel, O. Ishai, Engineering Mechanics of Composite Materials, Second Edition, Oxford University Press, New York, 2006.

[7] S. Iijima, Helical microtubules of graphitic carbon, Nature. 354 (1991) 56. https://doi.org/10.1038/354056a0.

[8] M. Giulianini, N. Motta, Polymer Self-assembly on Carbon Nanotubes, in: S. Bellucci (Ed.), Self-Assem. Nanostructures INFN Lect. Vol III, Springer New York, New York, NY, 2012: pp. 1–72. https://doi.org/10.1007/978-1-4614-0742-3_1.

[9] J.A. Elliott, J.K.W. Sandler, A.H. Windle, R.J. Young, M.S.P. Shaffer, Collapse of Single-Wall Carbon Nanotubes is Diameter Dependent, Phys. Rev. Lett. 92 (2004) 095501. https://doi.org/10.1103/PhysRevLett.92.095501.

[10] Y. Jin, F.G. Yuan, Simulation of elastic properties of single-walled carbon nanotubes, Compos. Sci. Technol. 63 (2003) 1507–1515. https://doi.org/10.1016/S0266-3538(03)00074-5.

[11] T. Chang, J. Geng, X. Guo, Chirality- and size-dependent elastic properties of single-walled carbon nanotubes, Appl. Phys. Lett. 87 (2005) 251929. https://doi.org/10.1063/1.2149216.

[12] T. Vodenitcharova, L.C. Zhang, Bending and local buckling of a nanocomposite beam reinforced by a single-walled carbon nanotube, Int. J. Solids Struct. 43 (2006) 3006–3024. https://doi.org/10.1016/j.ijsolstr.2005.05.014.

[13] C.-L. Zhang, H.-S. Shen, Temperature-dependent elastic properties of single-walled carbon nanotubes: Prediction from molecular dynamics simulation, Appl. Phys. Lett. 89 (2006) 081904. https://doi.org/10.1063/1.2336622.

[14] C.Y. Wang, L.C. Zhang, A critical assessment of the elastic properties and effective wall thickness of single-walled carbon nanotubes, Nanotechnology. 19 (2008) 075705. https://doi.org/10.1088/0957-4484/19/7/075705.

[15] H.-S. Shen, Nonlinear bending of functionally graded carbon nanotube-reinforced composite plates in thermal environments, Compos. Struct. 91 (2009) 9–19. https://doi.org/10.1016/j.compstruct.2009.04.026.

[16] Z.X. Lei, K.M. Liew, J.L. Yu, Free vibration analysis of functionally graded carbon nanotube-reinforced composite plates using the element-free kp-Ritz method in thermal environment, Compos. Struct. 106 (2013) 128–138. https://doi.org/10.1016/j.compstruct.2013.06.003.

[17] M.-F. Yu, B.S. Files, S. Arepalli, R.S. Ruoff, Tensile Loading of Ropes of Single Wall Carbon Nanotubes and their Mechanical Properties, Phys. Rev. Lett. 84 (2000) 5552–5555. https://doi.org/10.1103/PhysRevLett.84.5552.

[18] M.-F. Yu, O. Lourie, M.J. Dyer, K. Moloni, T.F. Kelly, R.S. Ruoff, Strength and Breaking Mechanism of Multiwalled Carbon Nanotubes Under Tensile Load, Science. 287 (2000) 637–640. https://doi.org/10.1126/science.287.5453.637.

[19] M.M.J. Treacy, T.W. Ebbesen, J.M. Gibson, Exceptionally high Young's modulus observed for individual carbon nanotubes, Nature. 381 (1996) 678. https://doi.org/10.1038/381678a0.

[20] B.I. Yakobson, C.J. Brabec, J. Bernholc, Nanomechanics of Carbon Tubes: Instabilities beyond Linear Response, Phys. Rev. Lett. 76 (1996) 2511–2514. https://doi.org/10.1103/PhysRevLett.76.2511.

[21] C.F. Cornwell, L.T. Wille, Elastic properties of single-walled carbon nanotubes in compression, Solid State Commun. 101 (1997) 555–558. https://doi.org/10.1016/S0038-1098(96)00742-9.

[22] Z. Yao, C.-C. Zhu, M. Cheng, J. Liu, Mechanical properties of carbon nanotube by molecular dynamics simulation, Comput. Mater. Sci. 22 (2001) 180–184. https://doi.org/10.1016/S0927-0256(01)00187-2.

[23] S. Iijima, C. Brabec, A. Maiti, J. Bernholc, Structural flexibility of carbon nanotubes, J. Chem. Phys. 104 (1996) 2089–2092. https://doi.org/10.1063/1.470966.

[24] P. Kim, L. Shi, A. Majumdar, P.L. McEuen, Thermal Transport Measurements of Individual Multiwalled Nanotubes, Phys. Rev. Lett. 87 (2001) 215502. https://doi.org/10.1103/PhysRevLett.87.215502.

[25] R.H. Baughman, C. Cui, A.A. Zakhidov, Z. Iqbal, et al, Carbon nanotube actuators, Sci. Wash. 284 (1999) 1340–1344.

[26] J.N. Coleman, M. Cadek, R. Blake, V. Nicolosi, K.P. Ryan, C. Belton, A. Fonseca, J.B. Nagy, Y.K. Gun'ko, W.J. Blau, High Performance Nanotube-Reinforced Plastics: Understanding the Mechanism of Strength Increase, Adv. Funct. Mater. 14 (2004) 791–798. https://doi.org/10.1002/adfm.200305200.

[27] A. Wall, J.N. Coleman, M.S. Ferreira, Physical mechanism for the mechanical reinforcement in nanotube-polymer composite materials, Phys. Rev. B. 71 (2005) 125421. https://doi.org/10.1103/PhysRevB.71.125421.

[28] P.G. Collin, K. Bradley, M. Ishigami, A. Zettl, Extreme oxygen sensitivity of electronic properties of carbon nanotubes, Sci. Wash. 287 (2000) 1801–1804.

[29] C. Cantalini, L. Valentini, I. Armentano, J.M. Kenny, L. Lozzi, S. Santucci, Carbon nanotubes as new materials for gas sensing applications, J. Eur. Ceram. Soc. 24 (2004) 1405–1408. https://doi.org/10.1016/S0955-2219(03)00441-2.

[30] J. Kong, N.R. Franklin, C. Zhou, M.G. Chapline, et al, Nanotube molecular wires as chemical sensors, Sci. Wash. 287 (2000) 622–625.

[31] W. Zhu, C. Bower, O. Zhou, G. Kochanski, S. Jin, Large current density from carbon nanotube field emitters, Appl. Phys. Lett. 75 (1999) 873–875. https://doi.org/10.1063/1.124541.

[32] H. Murakami, M. Hirakawa, C. Tanaka, H. Yamakawa, Field emission from well-aligned, patterned, carbon nanotube emitters, Appl. Phys. Lett. 76 (2000) 1776–1778. https://doi.org/10.1063/1.126164.

[33] P. Kim, C.M. Lieber, Nanotube nanotweezers, Sci. Wash. 286 (1999) 2148–2150.

[34] J.H. Hafner, C.L. Cheung, C.M. Lieber, Growth of nanotubes for probe microscopy tips, Nature. 398 (1999) 761. https://doi.org/10.1038/19658.

[35] B.J. Hinds, N. Chopra, T. Rantell, R. Andrews, et al, Aligned Multiwalled Carbon Nanotube Membranes, Sci. Wash. 303 (2004) 62–5.

[36] J.N. Reddy, Mechanics of Laminated Composite Plates and Shells: Theory and Analysis, Second Edition, CRC Press, Boca Raton, 2003.

[37] I. Ahmad, Smart structures and materials, in: Proc. US Army Res. Off. Workshop Smart Mater. Struct. Mathemetacal Issues, 1988.

[38] J.J. Dosch, D.J. Inman, E. Garcia, A Self-Sensing Piezoelectric Actuator for Collocated Control, J. Intell. Mater. Syst. Struct. 3 (1992) 166–185. https://doi.org/10.1177/1045389X9200300109.

[39] Q. Wang, Wave propagation in a piezoelectric coupled cylindrical membrane shell, Int. J. Solids Struct. 38 (2001) 8207–8218. https://doi.org/10.1016/S0020-7683(01)00071-3.

[40] Interdigital transducer, Wikipedia. (2019). https://en.wikipedia.org/w/index.php?title=Interdigital_transducer&oldid=884499375.

[41] E. Carrera, S. Brischetto, P. Nali, Plates and Shells for Smart Structures, Wiley, New Delhi, India, 2011.

[42] T. Hehn, Y. Manoli, Piezoelectricity and Energy Harvester Modelling, in: T. Hehn, Y. Manoli (Eds.), CMOS Circuits Piezoelectric Energy Harvest. Effic. Power Extr. Interface Model. Loss

Anal., Springer Netherlands, Dordrecht, 2015: pp. 21–40. https://doi.org/10.1007/978-94-017-9288-2_2.

[43] G.R. Liu, Z.C. Xi, Elastic Waves in Anisotropic Laminates, CRC Press, Boca Raton, Florida, 2002.

[44] Frequency, Wikipedia. (2020). https://en.wikipedia.org/w/index.php?title=Frequency&oldid=950126009.

[45] Angular frequency, Wikipedia. (2020). https://en.wikipedia.org/w/index.php?title=Angular_frequency&oldid=946329357.

[46] Wavelength, Wikipedia. (2020). https://en.wikipedia.org/w/index.php?title=Wavelength&oldid=953748107.

[47] Wavenumber, Wikipedia. (2020). https://en.wikipedia.org/w/index.php?title=Wavenumber&oldid=956419837.

[48] Phase velocity, Wikipedia. (2020). https://en.wikipedia.org/w/index.php?title=Phase_velocity&oldid=953241025.

[49] A.E.H. Love, A treatise on the mathematical theory of elasticity, Dover Publication, New York, 1944. http://archive.org/details/atreatiseonmath01lovegoog.

[50] L.H. Donnell, Stability of Thin-Walled Tubes Under Torsion, California Institute of Technology, United States, 1935. http://ntrs.nasa.gov/search.jsp?R=19930091553.

[51] D.-I.W. Flügge, Die Stabilität der Schalen, in: Statik Dyn. Schalen, Springer Berlin Heidelberg, 1957: pp. 214–263. https://doi.org/10.1007/978-3-642-52728-9_8.

[52] V.Zacharovič. Vlasov, General Theory of Shells and Its Application in Engineering, National Aeronautics and Space Administration, Washington, 1964.

[53] J.L. Sanders, An Improved First-approximation Theory for Thin Shells, U.S. Government Printing Office, Washington, 1960.

[54] E. Reissner, A New Derivation of the Equations for the Deformation of Elastic Shells, Am. J. Math. 63 (1941) 177–184. https://doi.org/10.2307/2371288.

[55] I. Mirsky, G. Herrmann, Nonaxially Symmetric Motions of Cylindrical Shells, J. Acoust. Soc. Am. 29 (1957) 1116–1123. https://doi.org/10.1121/1.1908716.

[56] T.C. Lin, G.W. Morgan, A study axi-symmetric vibrations of cylindrical shells as affected by rotary inertia and transverse shear, Journal of Applied Mechanics. 23 (1956) 255–261.

[57] R.M. Cooper, P.M. Naghdi, Propagation of Nonaxially Symmetric Waves in Elastic Cylindrical Shells, J. Acoust. Soc. Am. 29 (1957) 1365–1373. https://doi.org/10.1121/1.1908812.

[58] J.E. Greenspon, Vibrations of a Thick-Walled Cylindrical Shell—Comparison of the Exact Theory with Approximate Theories, J. Acoust. Soc. Am. 32 (1960) 571–578. https://doi.org/10.1121/1.1908148.

[59] K.J. Bathe, Finite element procedures, Prentice Hall, 1996.

[60] I. Harari, A survey of finite element methods for time-harmonic acoustics, Comput. Methods Appl. Mech. Eng. 195 (2006) 1594–1607. https://doi.org/10.1016/j.cma.2005.05.030.

[61] R. Lee, A.C. Cangellaris, A study of discretization error in the finite element approximation of wave solutions, IEEE Trans. Antennas Propag. 40 (1992) 542–549. https://doi.org/10.1109/8.142629.

[62] M.N. Guddati, B. Yue, Modified integration rules for reducing dispersion error in finite element methods, Comput. Methods Appl. Mech. Eng. 193 (2004) 275–287. https://doi.org/10.1016/j.cma.2003.09.010.

[63] F. Ihlenburg, I. Babuška, Finite element solution of the Helmholtz equation with high wave number Part I: The h-version of the FEM, Comput. Math. Appl. 30 (1995) 9–37. https://doi.org/10.1016/0898-1221(95)00144-N.

[64] F. Ihlenburg, I. Babuska, Finite Element Solution of the Helmholtz Equation with High Wave Number Part II: The h-p Version of the FEM, SIAM J. Numer. Anal. 34 (1997) 315–358.

[65] A. Deraemaeker, I. Babuška, P. Bouillard, Dispersion and pollution of the FEM solution for the Helmholtz equation in one, two and three dimensions, Int. J. Numer. Methods Eng. 46 (1999) 471–499. https://doi.org/10.1002/(SICI)1097-0207(19991010)46:4<471::AID-NME684>3.0.CO;2-6.

[66] K.J. Bathe, E.L. Wilson, Stability and accuracy analysis of direct integration methods, Earthq. Eng. Struct. Dyn. 1 (1972) 283–291. https://doi.org/10.1002/eqe.4290010308.

[67] W. Zhong, W.P. Howson, F.W. Williams, Precise Solutions for Surface Wave Propagation in Stratified Material, J. Vib. Acoust. 123 (2000) 198–204. https://doi.org/10.1115/1.1350567.

[68] J. Cho, U. Lee, An FFT-Based Spectral Analysis Method for Linear Discrete Dynamic Systems with Non-Proportional Damping, Shock Vib. (2006). https://doi.org/10.1155/2006/537523.

[69] A. Chakraborty, S. Gopalakrishnan, A Spectral Finite Element Model for Wave Propagation Analysis in Laminated Composite Plate, J. Vib. Acoust. 128 (2006) 477–488. https://doi.org/10.1115/1.2203338.

[70] T. Mazúch, WAVE DISPERSION MODELLING IN ANISOTROPIC SHELLS AND RODS BY THE FINITE ELEMENT METHOD, J. Sound Vib. 198 (1996) 429–438. https://doi.org/10.1006/jsvi.1996.0580.

[71] D. Datta, N.N. Kishore, Features of ultrasonic wave propagation to identify defects in composite materials modelled by finite element method, NDT E Int. 29 (1996) 213–223. https://doi.org/10.1016/S0963-8695(96)00016-3.

[72] A. Chakraborty, D. Roy Mahapatra, S. Gopalakrishnan, Finite element analysis of free vibration and wave propagation in asymmetric composite beams with structural discontinuities, Compos. Struct. 55 (2002) 23–36. https://doi.org/10.1016/S0263-8223(01)00130-1.

[73] D.R. Mahapatra, S. Gopalakrishnan, A spectral finite element for analysis of wave propagation in uniform composite tubes, J. Sound Vib. 268 (2003) 429–463. https://doi.org/10.1016/S0022-460X(02)01539-0.

[74] E. Manconi, B.R. Mace, Wave characterization of cylindrical and curved panels using a finite element method, J. Acoust. Soc. Am. 125 (2009) 154–163. https://doi.org/10.1121/1.3021418.

[75] D. Xiao, Q. Han, T. Jiang, Guided wave propagation in a multilayered magneto-electro-elastic curved panel by Chebyshev spectral elements method, Compos. Struct. 207 (2019) 701–710. https://doi.org/10.1016/j.compstruct.2018.09.031.

[76] Y. Liang, Y. Li, Y. Liu, Q. Han, D. Liu, Investigation of wave propagation in piezoelectric helical waveguides with the spectral finite element method, Compos. Part B Eng. 160 (2019) 205–216. https://doi.org/10.1016/j.compositesb.2018.09.083.

[77] C.T. Tsai, A.N. Palazotto, On the finite element analysis of non-linear vibration for cylindrical shells with high-order shear deformation theory, Int. J. Non-Linear Mech. 26 (1991) 379–388. https://doi.org/10.1016/0020-7462(91)90067-4.

[78] T.C. Ramesh, N. Ganesan, Finite Element Analysis of Cylindrical Shells With a Constrained Viscoelastic Layer, J. Sound Vib. 172 (1994) 359–370. https://doi.org/10.1006/jsvi.1994.1180.

[79] D. Chakravorty, J.N. Bandyopadhyay, P.K. Sinha, Finite element free vibration analysis of point supported laminated composite cylindrical shells, J. Sound Vib. 181 (1995) 43–52. https://doi.org/10.1006/jsvi.1995.0124.

[80] H. Li, Y. Yang, Dynamic response and active control of a composite cylindrical shell with piezoelectric shear actuators, Smart Mater. Struct. 16 (2007) 909. https://doi.org/10.1088/0964-1726/16/3/041.

[81] Y. Jiangong, W. Bin, C. Guoqiang, Wave characteristics in functionally graded piezoelectric hollow cylinders, Arch. Appl. Mech. 79 (2009) 807–824. https://doi.org/10.1007/s00419-008-0255-0.

[82] S.T. Quek, Q. Wang, On dispersion relations in piezoelectric coupled-plate structures, Smart Mater. Struct. 9 (2000) 859. https://doi.org/10.1088/0964-1726/9/6/317.

[83] S.V. Gopinathan, V.V. Varadan, V.K. Varadan, A review and critique of theories for piezoelectric laminates, Smart Mater. Struct. 9 (2000) 24. https://doi.org/10.1088/0964-1726/9/1/304.

[84] M.-L. Zhu, S.-W.R. Lee, H.-L. Li, T.-Y. Zhang, P. Tong, Modeling of torsional vibration induced by extension-twisting coupling of anisotropic composite laminates with piezoelectric actuators, Smart Mater. Struct. 11 (2002) 55. https://doi.org/10.1088/0964-1726/11/1/306.

[85] C. Ossadzow-David, M. Touratier, A multilayered piezoelectric shell theory, Compos. Sci. Technol. 64 (2004) 2121–2137. https://doi.org/10.1016/j.compscitech.2004.03.005.

[86] W. Chen, C. Lu, J. Yang, J. Wang, A circular cylindrical, radially polarized ceramic shell piezoelectric transformer, IEEE Trans. Ultrason. Ferroelectr. Freq. Control. 56 (2009) 1238–1245. https://doi.org/10.1109/TUFFC.2009.1165.

[87] C.F. Lü, J.S. Yang, J. Wang, W.Q. Chen, Power transmission through a hollow cylinder by acoustic waves and piezoelectric transducers with radial polarization, J. Sound Vib. 325 (2009) 989–999. https://doi.org/10.1016/j.jsv.2009.04.002.

[88] S. Kapuria, P. Kumari, Three-dimensional piezoelasticity solution for dynamics of cross-ply cylindrical shells integrated with piezoelectric fiber reinforced composite actuators and sensors, Compos. Struct. 92 (2010) 2431–2444. https://doi.org/10.1016/j.compstruct.2010.02.016.

[89] G.G. Sheng, X. Wang, Response and control of functionally graded laminated piezoelectric shells under thermal shock and moving loadings, Compos. Struct. 93 (2010) 132–141. https://doi.org/10.1016/j.compstruct.2010.06.007.

[90] MR. Saviz, Dynamic analysis of a laminated cylindrical shell with piezoelectric layer and clamped boundary condition, Finite Elem. Anal. Des. 104 (2015) 1–15. https://doi.org/10.1016/j.finel.2015.05.004.

[91] H.-L. Dai, H.-Y. Zheng, Buckling and post-buckling analyses for an axially compressed laminated cylindrical shell of FGM with PFRC in thermal environments, Eur. J. Mech. - ASolids. 30 (2011) 913–923. https://doi.org/10.1016/j.euromechsol.2011.05.009.

[92] M. Nasihatgozar, V. Daghigh, M. Eskandari, K. Nikbin, A. Simoneau, Buckling analysis of piezoelectric cylindrical composite panels reinforced with carbon nanotubes, Int. J. Mech. Sci. 107 (2016) 69–79. https://doi.org/10.1016/j.ijmecsci.2016.01.010.

[93] M. Hussein, P.R. Heyliger, DISCRETE LAYER ANALYSIS OF AXISYMMETRIC VIBRATIONS OF LAMINATED PIEZOELECTRIC CYLINDERS, J. Sound Vib. 192 (1996) 995–1013. https://doi.org/10.1006/jsvi.1996.0230.

[94] G.G. Sheng, X. Wang, Thermoelastic vibration and buckling analysis of functionally graded piezoelectric cylindrical shells, Appl. Math. Model. 34 (2010) 2630–2643. https://doi.org/10.1016/j.apm.2009.11.024.

[95] S.M. Hasheminejad, V. Rabbani, Active Transient Sound Radiation Control from a Smart Piezocomposite Hollow Cylinder, Arch. Acoust. 40 (2015) 359–381. https://doi.org/10.1515/aoa-2015-0039.

[96] S.M. Hasheminejad, V. Rabbani, M. Alaei-Varnosfaderani, Active transient elasto-acoustic response damping of a thick-walled liquid-coupled piezolaminated cylindrical vessel, Mech. Based Des. Struct. Mach. 44 (2016) 189–211. https://doi.org/10.1080/15397734.2015.1048461.

[97] Q. Wang, Axi-symmetric wave propagation in a cylinder coated with a piezoelectric layer, Int. J. Solids Struct. 39 (2002) 3023–3037. https://doi.org/10.1016/S0020-7683(02)00233-0.

[98] Q. Wang, K.M. Liew, Analysis of wave propagation in piezoelectric coupled cylinder affected by transverse shear and rotary inertia, Int. J. Solids Struct. 40 (2003) 6653–6667. https://doi.org/10.1016/S0020-7683(03)00422-0.

[99] K. Dong, X. Wang, Influences of large deformation and rotary inertia on wave propagation in piezoelectric cylindrically laminated shells in thermal environment, Int. J. Solids Struct. 43 (2006) 1710–1726. https://doi.org/10.1016/j.ijsolstr.2005.05.044.

[100] K. Dong, X. Wang, Wave propagation characteristics in piezoelectric cylindrical laminated shells under large deformation, Compos. Struct. 77 (2007) 171–181. https://doi.org/10.1016/j.compstruct.2005.06.011.

[101] K. Dong, X. Wang, The Effect of Transverse Shear, Rotary Inertia on Wave Propagation in Laminated Piezoelectric Cylindrical Shells in Thermal Environment, J. Reinf. Plast. Compos. 26 (2007) 1523–1538. https://doi.org/10.1177/0731684407079519.

[102] S.M. Hasheminejad, M. Alaei-Varnosfaderani, Vibroacoustic response and active control of a fluid-filled functionally graded piezoelectric material composite cylinder, J. Intell. Mater. Syst. Struct. 23 (2012) 775–790. https://doi.org/10.1177/1045389X12439637.

[103] S.M. Hasheminejad, M. Alaei-Varnosfaderani, Acoustic radiation and active control from a smart functionally graded submerged hollow cylinder, J. Vib. Control. 20 (2014) 2202–2220. https://doi.org/10.1177/1077546313483787.

[104] T. Mori, K. Tanaka, Average stress in matrix and average elastic energy of materials with misfitting inclusions, Acta Metall. 21 (1973) 571–574. https://doi.org/10.1016/0001-6160(73)90064-3.

[105] Y. Han, J. Elliott, Molecular dynamics simulations of the elastic properties of polymer/carbon nanotube composites, Comput. Mater. Sci. 39 (2007) 315–323. https://doi.org/10.1016/j.commatsci.2006.06.011.

[106] L.W. Zhang, B.A. Selim, Vibration analysis of CNT-reinforced thick laminated composite plates based on Reddy's higher-order shear deformation theory, Compos. Struct. 160 (2017) 689–705. https://doi.org/10.1016/j.compstruct.2016.10.102.

[107] D.-L. Shi, X.-Q. Feng, Y.Y. Huang, K.-C. Hwang, H. Gao, The Effect of Nanotube Waviness and Agglomeration on the Elastic Property of Carbon Nanotube-Reinforced Composites, J. Eng. Mater. Technol. 126 (2004) 250–257. https://doi.org/10.1115/1.1751182.

[108] B. Sobhani Aragh, A.H. Nasrollah Barati, H. Hedayati, Eshelby–Mori–Tanaka approach for vibrational behavior of continuously graded carbon nanotube-reinforced cylindrical panels, Compos. Part B Eng. 43 (2012) 1943–1954. https://doi.org/10.1016/j.compositesb.2012.01.004.

[109] S. Kamarian, A. Pourasghar, M.H. Yas, Eshelby-Mori-Tanaka approach for vibrational behavior of functionally graded carbon nanotube-reinforced plate resting on elastic foundation, J. Mech. Sci. Technol. 27 (2013) 3395–3401. https://doi.org/10.1007/s12206-013-0861-9.

[110] H.-S. Shen, C.-L. Zhang, Thermal buckling and postbuckling behavior of functionally graded carbon nanotube-reinforced composite plates, Mater. Des. 31 (2010) 3403–3411. https://doi.org/10.1016/j.matdes.2010.01.048.

[111] H.-S. Shen, Y. Xiang, Postbuckling of axially compressed nanotube-reinforced composite cylindrical panels resting on elastic foundations in thermal environments, Compos. Part B Eng. 67 (2014) 50–61. https://doi.org/10.1016/j.compositesb.2014.06.020.

[112] M.M. Keleshteri, H. Asadi, Q. Wang, Postbuckling analysis of smart FG-CNTRC annular sector plates with surface-bonded piezoelectric layers using generalized differential quadrature method, Comput. Methods Appl. Mech. Eng. 325 (2017) 689–710. https://doi.org/10.1016/j.cma.2017.07.036.

[113] Y. Kiani, Thermal post-buckling of FG-CNT reinforced composite plates, Compos. Struct. 159 (2017) 299–306. https://doi.org/10.1016/j.compstruct.2016.09.084.

[114] M.M. Keleshteri, H. Asadi, Q. Wang, On the snap-through instability of post-buckled FG-CNTRC rectangular plates with integrated piezoelectric layers, Comput. Methods Appl. Mech. Eng. 331 (2018) 53–71. https://doi.org/10.1016/j.cma.2017.11.015.

[115] Y. Heydarpour, M.M. Aghdam, P. Malekzadeh, Free vibration analysis of rotating functionally graded carbon nanotube-reinforced composite truncated conical shells, Compos. Struct. 117 (2014) 187–200. https://doi.org/10.1016/j.compstruct.2014.06.023.

[116] A. Alibeigloo, Free vibration analysis of functionally graded carbon nanotube-reinforced composite cylindrical panel embedded in piezoelectric layers by using theory of elasticity, Eur. J. Mech. - ASolids. 44 (2014) 104–115. https://doi.org/10.1016/j.euromechsol.2013.10.002.

[117] M. Mirzaei, Y. Kiani, Free vibration of functionally graded carbon nanotube reinforced composite cylindrical panels, Compos. Struct. 142 (2016) 45–56. https://doi.org/10.1016/j.compstruct.2015.12.071.

[118] Q. Wang, X. Cui, B. Qin, Q. Liang, Vibration analysis of the functionally graded carbon nanotube reinforced composite shallow shells with arbitrary boundary conditions, Compos. Struct. 182 (2017) 364–379. https://doi.org/10.1016/j.compstruct.2017.09.043.

[119] Y. Kiani, Free vibration of FG-CNT reinforced composite spherical shell panels using Gram-Schmidt shape functions, Compos. Struct. 159 (2017) 368–381. https://doi.org/10.1016/j.compstruct.2016.09.079.

[120] J. Torabi, R. Ansari, Nonlinear free vibration analysis of thermally induced FG-CNTRC annular plates: Asymmetric versus axisymmetric study, Comput. Methods Appl. Mech. Eng. 324 (2017) 327–347. https://doi.org/10.1016/j.cma.2017.05.025.

[121] Y. Kiani, Free vibration of functionally graded carbon nanotube reinforced composite plates integrated with piezoelectric layers, Comput. Math. Appl. 72 (2016) 2433–2449. https://doi.org/10.1016/j.camwa.2016.09.007.

[122] M. Mohammadzadeh-Keleshteri, H. Asadi, M.M. Aghdam, Geometrical nonlinear free vibration responses of FG-CNT reinforced composite annular sector plates integrated with piezoelectric layers, Compos. Struct. 171 (2017) 100–112. https://doi.org/10.1016/j.compstruct.2017.01.048.

[123] H. Razavi, A.F. Babadi, Y. Tadi Beni, Free vibration analysis of functionally graded piezoelectric cylindrical nanoshell based on consistent couple stress theory, Compos. Struct. 160 (2017) 1299–1309. https://doi.org/10.1016/j.compstruct.2016.10.056.

[124] S. Kamarian, M. Salim, R. Dimitri, F. Tornabene, Free vibration analysis of conical shells reinforced with agglomerated Carbon Nanotubes, Int. J. Mech. Sci. 108–109 (2016) 157–165. https://doi.org/10.1016/j.ijmecsci.2016.02.006.

[125] F. Tornabene, N. Fantuzzi, M. Bacciocchi, E. Viola, Effect of agglomeration on the natural frequencies of functionally graded carbon nanotube-reinforced laminated composite doubly-curved shells, Compos. Part B Eng. 89 (2016) 187–218. https://doi.org/10.1016/j.compositesb.2015.11.016.

[126] Q. Wang, Wave propagation in carbon nanotubes via nonlocal continuum mechanics, J. Appl. Phys. 98 (2005) 124301. https://doi.org/10.1063/1.2141648.

[127] K. Dong, X. Wang, Wave propagation in carbon nanotubes under shear deformation, Nanotechnology. 17 (2006) 2773. https://doi.org/10.1088/0957-4484/17/11/009.

[128] K. Dong, B.Y. Liu, X. Wang, Wave propagation in fluid-filled multi-walled carbon nanotubes embedded in elastic matrix, Comput. Mater. Sci. 42 (2008) 139–148. https://doi.org/10.1016/j.commatsci.2007.07.007.

[129] M. Janghorban, M.R. Nami, Wave propagation in functionally graded nanocomposites reinforced with carbon nanotubes based on second-order shear deformation theory, Mech. Adv. Mater. Struct. 24 (2017) 458–468. https://doi.org/10.1080/15376494.2016.1142028.

[130] D.F. Adams, A.K. Miller, Hygrothermal Microstresses in a Unidirectional Composite Exhibiting Inelastic Material Behavior, J. Compos. Mater. 11 (1977) 285–299. https://doi.org/10.1177/002199837701100304.

[131] D.E. Bowles, S.S. Tompkins, Prediction of Coefficients of Thermal Expansion for Unidirectional Composites, J. Compos. Mater. 23 (1989) 370–388. https://doi.org/10.1177/002199838902300405.

[132] B.F. Boukhoulda, E. Adda-Bedia, K. Madani, The effect of fiber orientation angle in composite materials on moisture absorption and material degradation after hygrothermal ageing, Compos. Struct. 74 (2006) 406–418. https://doi.org/10.1016/j.compstruct.2005.04.032.

[133] R.D. Blevins, Formulas for natural frequency and mode shape, Van Nostrand Reinhold, New York, 1979.

[134] A.E. Armenkas, D.C. Gazis, G. Herrmann, Free Vibrations of Circular Cylindrical Shells, Pergamon Press, Oxford, 1969.

[135] A.A. Khdeir, J.N. Reddy, Influence of edge conditions on the modal characteristics of cross-ply laminated shells, Comput. Struct. 34 (1990) 817–826. https://doi.org/10.1016/0045-7949(90)90352-3.

[136] C.T. Loy, K.Y. Lam, Vibrations of rotating thin cylindrical panels, Appl. Acoust. 46 (1995) 327–343. https://doi.org/10.1016/0003-682X(96)81499-X.

[137] A. Nosier, J.N. Reddy, Vibration and stability analyses of cross-ply laminated circular cylindrical shells, J. Sound Vib. 157 (1992) 139–159. https://doi.org/10.1016/0022-460X(92)90571-E.

[138] A.A. Khdeir, J.N. Reddy, D. Frederick, A study of bending, vibration and buckling of cross-ply circular cylindrical shells with various shell theories, Int. J. Eng. Sci. 27 (1989) 1337–1351. https://doi.org/10.1016/0020-7225(89)90058-X.

[139] L. Librescu, A.A. Khdeir, D. Frederick, A shear deformable theory of laminated composite shallow shell-type panels and their response analysis I: Free vibration and buckling, Acta Mech. 76 (1989) 1–33. https://doi.org/10.1007/BF01175794.

[140] A. Ludwig, R. Krieg, An analytical quasi-exact method for calculating eigenvibrations of thin circular cylindrical shells, J. Sound Vib. 74 (1981) 155–174. https://doi.org/10.1016/0022-460X(81)90501-0.

[141] K.P. Soldatos, V.P. Hadjigeorgiou, Three-dimensional solution of the free vibration problem of homogeneous isotropic cylindrical shells and panels, J. Sound Vib. 137 (1990) 369–384. https://doi.org/10.1016/0022-460X(90)90805-A.

[142] K. Forsberg, Influence of Boundary Conditions on the Modal Characteristics of Thin Cylindrical Shells, J. Acoust. Soc. Am. 35 (1963) 1898–1899. https://doi.org/10.1121/1.2142740.

[143] K.Y. Lam, C.T. Loy, EFFECTS OF BOUNDARY CONDITIONS ON FREQUENCIES OF A MULTI-LAYERED CYLINDRICAL SHELL, J. Sound Vib. 188 (1995) 363–384. https://doi.org/10.1006/jsvi.1995.0599.

[144] K.Y. Lam, C.T. Loy, Vibration characteristics of thin cylindrical panels, Appl. Acoust. 42 (1994) 347–359. https://doi.org/10.1016/0003-682X(94)90102-3.

[145] C.T. Loy, K.Y. Lam, C. Shu, Analysis of Cylindrical Shells Using Generalized Differential Quadrature, Shock Vib. 4 (1997) 193–198. https://doi.org/10.3233/SAV-1997-4305.

[146] X.M. Zhang, G.R. Liu, K.Y. Lam, Frequency analysis of cylindrical panels using a wave propagation approach, Appl. Acoust. 62 (2001) 527–543. https://doi.org/10.1016/S0003-682X(00)00059-1.

[147] T.Y. Ng, H. Li, K.Y. Lam, Generalized differential quadrature for free vibration of rotating composite laminated conical shell with various boundary conditions, Int. J. Mech. Sci. 45 (2003) 567–587. https://doi.org/10.1016/S0020-7403(03)00042-0.

[148] P. Malekzadeh, M. Farid, P. Zahedinejad, A three-dimensional layerwise-differential quadrature free vibration analysis of laminated cylindrical shells, Int. J. Press. Vessels Pip. 85 (2008) 450–458. https://doi.org/10.1016/j.ijpvp.2008.02.005.

[149] G. Jin, T. Ye, Y. Chen, Z. Su, Y. Yan, An exact solution for the free vibration analysis of laminated composite cylindrical shells with general elastic boundary conditions, Compos. Struct. 106 (2013) 114–127. https://doi.org/10.1016/j.compstruct.2013.06.002.

[150] Q. Wang, V.K. Varadan, Vibration of carbon nanotubes studied using nonlocal continuum mechanics, Smart Mater. Struct. 15 (2006) 659. https://doi.org/10.1088/0964-1726/15/2/050.

[151] R. Ansari, B. Arash, H. Rouhi, Vibration characteristics of embedded multi-layered graphene sheets with different boundary conditions via nonlocal elasticity, Compos. Struct. 93 (2011) 2419–2429. https://doi.org/10.1016/j.compstruct.2011.04.006.

[152] B. Arash, Q. Wang, A review on the application of nonlocal elastic models in modeling of carbon nanotubes and graphenes, Comput. Mater. Sci. 51 (2012) 303–313. https://doi.org/10.1016/j.commatsci.2011.07.040.

[153] R. Ansari, S. Ajori, B. Arash, Vibrations of single- and double-walled carbon nanotubes with layerwise boundary conditions: A molecular dynamics study, Curr. Appl. Phys. 12 (2012) 707–711. https://doi.org/10.1016/j.cap.2011.10.007.

[154] R. Ansari, B. Arash, Nonlocal Flügge Shell Model for Vibrations of Double-Walled Carbon Nanotubes With Different Boundary Conditions, J. Appl. Mech. 80 (2013) 021006-021006–12. https://doi.org/10.1115/1.4007432.

[155] P. Zhu, Z.X. Lei, K.M. Liew, Static and free vibration analyses of carbon nanotube-reinforced composite plates using finite element method with first order shear deformation plate theory, Compos. Struct. 94 (2012) 1450–1460. https://doi.org/10.1016/j.compstruct.2011.11.010.

[156] M.H. Yas, A. Pourasghar, S. Kamarian, M. Heshmati, Three-dimensional free vibration analysis of functionally graded nanocomposite cylindrical panels reinforced by carbon nanotube, Mater. Des. 49 (2013) 583–590. https://doi.org/10.1016/j.matdes.2013.01.001.

[157] L.W. Zhang, Z.X. Lei, K.M. Liew, Free vibration analysis of functionally graded carbon nanotube-reinforced composite triangular plates using the FSDT and element-free IMLS-Ritz method, Compos. Struct. 120 (2015) 189–199. https://doi.org/10.1016/j.compstruct.2014.10.009.

[158] L.W. Zhang, Y. Zhang, G.L. Zou, K.M. Liew, Free vibration analysis of triangular CNT-reinforced composite plates subjected to in-plane stresses using FSDT element-free method, Compos. Struct. 149 (2016) 247–260. https://doi.org/10.1016/j.compstruct.2016.04.019.

[159] Q. Wang, X. Cui, B. Qin, Q. Liang, Vibration analysis of the functionally graded carbon nanotube reinforced composite shallow shells with arbitrary boundary conditions, Compos. Struct. 182 (2017) 364–379. https://doi.org/10.1016/j.compstruct.2017.09.043.

[160] Z. Qin, F. Chu, J. Zu, Free vibrations of cylindrical shells with arbitrary boundary conditions: A comparison study, Int. J. Mech. Sci. 133 (2017) 91–99. https://doi.org/10.1016/j.ijmecsci.2017.08.012.

[161] Z. Qin, Z. Yang, J. Zu, F. Chu, Free vibration analysis of rotating cylindrical shells coupled with moderately thick annular plates, Int. J. Mech. Sci. 142–143 (2018) 127–139. https://doi.org/10.1016/j.ijmecsci.2018.04.044.

[162] B. Safaei, R. Moradi-Dastjerdi, Z. Qin, F. Chu, Frequency-dependent forced vibration analysis of nanocomposite sandwich plate under thermo-mechanical loads, Compos. Part B Eng. 161 (2019) 44–54. https://doi.org/10.1016/j.compositesb.2018.10.049.

[163] A.M. Zenkour, M. Sobhy, Thermal buckling of various types of FGM sandwich plates, Compos. Struct. 93 (2010) 93–102. https://doi.org/10.1016/j.compstruct.2010.06.012.

[164] M.K. Rath, S.K. Sahu, Vibration of woven fiber laminated composite plates in hygrothermal environment, J. Vib. Control. 18 (2012) 1957–1970. https://doi.org/10.1177/1077546311428638.

[165] A.M. Zenkour, Hygrothermal effects on the bending of angle-ply composite plates using a sinusoidal theory, Compos. Struct. 94 (2012) 3685–3696. https://doi.org/10.1016/j.compstruct.2012.05.033.

[166] H.S. Panda, S.K. Sahu, P.K. Parhi, Hygrothermal effects on free vibration of delaminated woven fiber composite plates – Numerical and experimental results, Compos. Struct. 96 (2013) 502–513. https://doi.org/10.1016/j.compstruct.2012.08.057.

[167] M. Zidi, A. Tounsi, M.S.A. Houari, E.A. Adda Bedia, O. Anwar Bég, Bending analysis of FGM plates under hygro-thermo-mechanical loading using a four variable refined plate theory, Aerosp. Sci. Technol. 34 (2014) 24–34. https://doi.org/10.1016/j.ast.2014.02.001.

[168] M. Sobhy, An accurate shear deformation theory for vibration and buckling of FGM sandwich plates in hygrothermal environment, Int. J. Mech. Sci. 110 (2016) 62–77. https://doi.org/10.1016/j.ijmecsci.2016.03.003.

[169] M.S. Atanasov, D. Karličić, P. Kozić, G. Janevski, THERMAL EFFECT ON FREE VIBRATION AND BUCKLING OF A DOUBLE-MICROBEAM SYSTEM, Facta Univ. Ser. Mech. Eng. 15 (2017) 45–62. https://doi.org/10.22190/FUME161115007S.

[170] F. Farhatnia, M. Ghanbari-Mobarakeh, S. Rasouli-Jazi, S. Oveissi, THERMAL BUCKLING ANALYSIS OF FUNCTIONALLY GRADED CIRCULAR PLATE RESTING ON THE PASTERNAK ELASTIC FOUNDATION VIA THE DIFFERENTIAL TRANSFORM METHOD, Facta Univ. Ser. Mech. Eng. 15 (2017) 545–563. https://doi.org/10.22190/FUME170104004F.

[171] H.-S. Shen, Y. Xiang, F. Lin, Nonlinear vibration of functionally graded graphene-reinforced composite laminated plates in thermal environments, Comput. Methods Appl. Mech. Eng. 319 (2017) 175–193. https://doi.org/10.1016/j.cma.2017.02.029.

[172] N.V.S. Naidu, P.K. Sinha, Nonlinear free vibration analysis of laminated composite shells in hygrothermal environments, Compos. Struct. 77 (2007) 475–483. https://doi.org/10.1016/j.compstruct.2005.08.002.

[173] S.N. Wosu, D. Hui, L. Daniel, Hygrothermal effects on the dynamic compressive properties of graphite/epoxy composite material, Compos. Part B Eng. 43 (2012) 841–855. https://doi.org/10.1016/j.compositesb.2011.11.045.

[174] P. Malekzadeh, Y. Heydarpour, Free vibration analysis of rotating functionally graded cylindrical shells in thermal environment, Compos. Struct. 94 (2012) 2971–2981. https://doi.org/10.1016/j.compstruct.2012.04.011.

[175] H.S. Panda, S.K. Sahu, P.K. Parhi, Effects of moisture on the frequencies of vibration of woven fibre composite doubly curved panels with strip delaminations, Thin-Walled Struct. 78 (2014) 79–86. https://doi.org/10.1016/j.tws.2014.01.010.

[176] H.-S. Shen, D.-Q. Yang, Nonlinear vibration of functionally graded fiber-reinforced composite laminated cylindrical shells in hygrothermal environments, Appl. Math. Model. 39 (2015) 1480–1499. https://doi.org/10.1016/j.apm.2014.09.010.

[177] M. Biswal, S.K. Sahu, A.V. Asha, Experimental and numerical studies on free vibration of laminated composite shallow shells in hygrothermal environment, Compos. Struct. 127 (2015) 165–174. https://doi.org/10.1016/j.compstruct.2015.03.007.

[178] M. Biswal, S.K. Sahu, A.V. Asha, Vibration of composite cylindrical shallow shells subjected to hygrothermal loading-experimental and numerical results, Compos. Part B Eng. 98 (2016) 108–119. https://doi.org/10.1016/j.compositesb.2016.05.037.

[179] A. Venkatachari, S. Natarajan, M. Haboussi, M. Ganapathi, Environmental effects on the free vibration of curvilinear fibre composite laminates with cutouts, Compos. Part B Eng. 88 (2016) 131–138. https://doi.org/10.1016/j.compositesb.2015.10.017.

[180] H.-S. Shen, Y. Xiang, Y. Fan, Nonlinear vibration of functionally graded graphene-reinforced composite laminated cylindrical shells in thermal environments, Compos. Struct. 182 (2017) 447–456. https://doi.org/10.1016/j.compstruct.2017.09.010.

[181] H.-S. Shen, Y. Xiang, Y. Fan, D. Hui, Nonlinear vibration of functionally graded graphene-reinforced composite laminated cylindrical panels resting on elastic foundations in thermal environments, Compos. Part B Eng. 136 (2018) 177–186. https://doi.org/10.1016/j.compositesb.2017.10.032.

[182] X. Wang, K. Dong, X.Y. Wang, Hygrothermal effect on dynamic interlaminar stresses in laminated plates with piezoelectric actuators, Compos. Struct. 71 (2005) 220–228. https://doi.org/10.1016/j.compstruct.2004.10.004.

[183] P.K. Mahato, D.K. Maiti, Aeroelastic analysis of smart composite structures in hygro-thermal environment, Compos. Struct. 92 (2010) 1027–1038. https://doi.org/10.1016/j.compstruct.2009.09.050.

[184] N. Nanda, Non-linear free and forced vibrations of piezoelectric laminated shells in thermal environments, IES J. Part Civ. Struct. Eng. 3 (2010) 147–160. https://doi.org/10.1080/19373260.2010.490329.

[185] G. Shankar, S. Keshava Kumar, P.K. Mahato, Vibration analysis and control of smart composite plates with delamination and under hygrothermal environment, Thin-Walled Struct. 116 (2017) 53–68. https://doi.org/10.1016/j.tws.2017.03.013.

[186] R. Haggenmueller, H.H. Gommans, A.G. Rinzler, J.E. Fischer, K.I. Winey, Aligned single-wall carbon nanotubes in composites by melt processing methods, Chem. Phys. Lett. 330 (2000) 219–225. https://doi.org/10.1016/S0009-2614(00)01013-7.

[187] H. Bisheh, N. Wu, Wave propagation characteristics in a piezoelectric coupled laminated composite cylindrical shell by considering transverse shear effects and rotary inertia, Compos. Struct. 191 (2018) 123–144. https://doi.org/10.1016/j.compstruct.2018.02.010.

[188] H.Kh. Bisheh, N. Wu, Analysis of wave propagation characteristics in piezoelectric cylindrical composite shells reinforced with carbon nanotubes, Int. J. Mech. Sci. 145 (2018) 200–220. https://doi.org/10.1016/j.ijmecsci.2018.07.002.

[189] H. Bisheh, N. Wu, Wave propagation in piezoelectric cylindrical composite shells reinforced with angled and randomly oriented carbon nanotubes, Compos. Part B Eng. 160 (2019) 10–30. https://doi.org/10.1016/j.compositesb.2018.10.001.

[190] H. Bisheh, N. Wu, Wave propagation in smart laminated composite cylindrical shells reinforced with carbon nanotubes in hygrothermal environments, Compos. Part B Eng. 162 (2019) 219–241. https://doi.org/10.1016/j.compositesb.2018.10.064.

[191] H. Bisheh, N. Wu, D. Hui, Polarization effects on wave propagation characteristics of piezoelectric coupled laminated fiber-reinforced composite cylindrical shells, Int. J. Mech. Sci. 161–162 (2019) 105028. https://doi.org/10.1016/j.ijmecsci.2019.105028.

[192] H. Bisheh, N. Wu, On dispersion relations in smart laminated fiber-reinforced composite membranes considering different piezoelectric coupling effects, J. Low Freq. Noise Vib. Act. Control. 38 (2019) 487–509. https://doi.org/10.1177/1461348418821773.

[193] H. Bisheh, N. Wu, T. Rabczuk, Free vibration analysis of smart laminated carbon nanotube-reinforced composite cylindrical shells with various boundary conditions in hygrothermal environments, Thin-Walled Struct. 149 (2020) 106500. https://doi.org/10.1016/j.tws.2019.106500.

[194] H. Bisheh, T. Rabczuk, N. Wu, Effects of nanotube agglomeration on wave dynamics of carbon nanotube-reinforced piezocomposite cylindrical shells, Compos. Part B Eng. 187 (2020) 107739. https://doi.org/10.1016/j.compositesb.2019.107739.

[195] A.C. Eringen, Elastodynamics, New York, 1974.

[196] J.N. Reddy, Mechanics of Laminated Composite Plates and Shells: Theory and Analysis, Second Edition, CRC Press. (2003). https://www.crcpress.com/Mechanics-of-Laminated-Composite-Plates-and-Shells-Theory-and-Analysis/Reddy/p/book/9780849315923.

[197] I. Mirsky, Vibrations of Orthotropic, Thick, Cylindrical Shells, J. Acoust. Soc. Am. 36 (1964) 41–51. https://doi.org/10.1121/1.1918910.

[198] K.F. Graff, Wave Motion in Elastic Solids, Dover Publication, New York, 1991. https://www.abebooks.com/9780486667454/Wave-Motion-Elastic-Solids-Dover-0486667456/plp.

[199] R.L. Burden, J.D. Faires, Numerical Analysis, 3rd ed., PWS Publishers, 1985.

[200] R. Hill, A self-consistent mechanics of composite materials, J. Mech. Phys. Solids. 13 (1965) 213–222. https://doi.org/10.1016/0022-5096(65)90010-4.

[201] V.N. Popov, V.E. Van Doren, M. Balkanski, Elastic properties of crystals of single-walled carbon nanotubes, Solid State Commun. 114 (2000) 395–399. https://doi.org/10.1016/S0038-1098(00)00070-3.

[202] F. Tornabene, N. Fantuzzi, M. Bacciocchi, Linear static response of nanocomposite plates and shells reinforced by agglomerated carbon nanotubes, Compos. Part B Eng. 115 (2017) 449–476. https://doi.org/10.1016/j.compositesb.2016.07.011.

[203] M.S.P. Shaffer, A.H. Windle, Fabrication and Characterization of Carbon Nanotube/Poly(vinyl alcohol) Composites, Adv. Mater. 11 (1999) 937–941. https://doi.org/10.1002/(SICI)1521-4095(199908)11:11<937::AID-ADMA937>3.0.CO;2-9.

[204] B. Vigolo, A. Pénicaud, C. Coulon, C. Sauder, R. Pailler, C. Journet, P. Bernier, P. Poulin, Macroscopic Fibers and Ribbons of Oriented Carbon Nanotubes, Science. 290 (2000) 1331–1334. https://doi.org/10.1126/science.290.5495.1331.

[205] A.H. Akbarzadeh, Z.T. Chen, Magnetoelectroelastic behavior of rotating cylinders resting on an elastic foundation under hygrothermal loading, Smart Mater. Struct. 21 (2012) 125013. https://doi.org/10.1088/0964-1726/21/12/125013.

[206] X.M. Zhang, Vibration analysis of cross-ply laminated composite cylindrical shells using the wave propagation approach, Appl. Acoust. 62 (2001) 1221–1228. https://doi.org/10.1016/S0003-682X(01)00014-7.

[207] X.M. Zhang, G.R. Liu, K.Y. Lam, VIBRATION ANALYSIS OF THIN CYLINDRICAL SHELLS USING WAVE PROPAGATION APPROACH, J. Sound Vib. 239 (2001) 397–403. https://doi.org/10.1006/jsvi.2000.3139.

[208] X.M. Zhang, G.R. Liu, K.Y. Lam, Coupled vibration analysis of fluid-filled cylindrical shells using the wave propagation approach, Appl. Acoust. 62 (2001) 229–243. https://doi.org/10.1016/S0003-682X(00)00045-1.

[209] X.M. Zhang, Parametric analysis of frequency of rotating laminated composite cylindrical shells with the wave propagation approach, Comput. Methods Appl. Mech. Eng. 191 (2002) 2057–2071. https://doi.org/10.1016/S0045-7825(01)00368-1.

[210] E. Ventsel, T. Krauthammer, Thin Plates and Shells: Theory: Analysis, and Applications, 1st ed., Marcel Dekker, Inc., New York, 2001.

[211] L. Bing-ru, W. Xuan-yin, G. Hui-liang, D. Yuan-ming, Study on applicability of modal analysis of thin finite length cylindrical shells using wave propagation approach, J. Zhejiang Univ.-Sci. A. 6 (2005) 1122–1127. https://doi.org/10.1007/BF02842236.

[212] K.Y. Lam, C.T. Loy, Analysis of rotating laminated cylindrical shells by different thin shell theories, J. Sound Vib. 186 (1995) 23–35. https://doi.org/10.1006/jsvi.1995.0431.

[213] K.Y. Lam, T.Y. Ng, W. Qian, Vibration Analysis of Thick Laminated Composite Cylindrical Shells, AIAA J. 38 (2000) 1102–1107. https://doi.org/10.2514/2.1077.

List of Publications in Ph.D. Research

Journal Papers

1. **Hossein Bisheh**, Timon Rabczuk, Nan Wu, **Effects of nanotube agglomeration on wave dynamics of carbon nanotube-reinforced piezocomposite cylindrical shells**, *Composites Part B: Engineering*, Vol. 187, April 2020, 107739. https://doi.org/10.1016/j.compositesb.2019.107739.
2. **Hossein Bisheh**, Nan Wu, Timon Rabczuk, **Free vibration analysis of smart laminated carbon nanotube-reinforced composite cylindrical shells with various boundary conditions in hygrothermal environments**, *Thin-Walled Structures*, Vol. 149, April 2020, 106500. https://doi.org/10.1016/j.tws.2019.106500.
3. **Hossein Bisheh**, Nan Wu, David Hui, **Polarization effects on wave propagation characteristics of piezoelectric coupled laminated fiber- reinforced composite cylindrical shells**, *International Journal of Mechanical Sciences*, Vol. 161, October 2019, 105028. https://doi.org/10.1016/j.ijmecsci.2019.105028.
4. **Hossein Bisheh**, Nan Wu, **Wave propagation in smart laminated composite cylindrical shells reinforced with carbon nanotubes in hygrothermal environments,** *Composites Part B: Engineering*, Vol. 162, 219-241, 2019. https://doi.org/10.1016/j.compositesb.2018.10.064.
5. **Hossein Bisheh**, Nan Wu, **Wave propagation in piezoelectric cylindrical composite shells reinforced with angled and randomly oriented carbon nanotubes**, *Composites Part B: Engineering*, Vol. 160, 10-30, 2019. https://doi.org/10.1016/j.compositesb.2018.10.001.

6. **Hossein Bisheh**, Nan Wu, **On dispersion relations in smart laminated fiber-reinforced composite membranes considering different piezoelectric coupling effects**, *Journal of Low Frequency Noise, Vibration & Active Control*, Vol. 38(2), 487–509, 2019. https://doi.org/10.1177/1461348418821773.
7. **Hossein Kh. Bisheh**, Nan Wu, **Analysis of wave propagation characteristics in piezoelectric cylindrical composite shells reinforced with carbon nanotubes**, *International Journal of Mechanical Sciences*, Vol. 145, 200-220, 2018. https://doi.org/10.1016/j.ijmecsci.2018.07.002
8. **Hossein Bisheh**, Nan Wu, **Wave propagation characteristics in a piezoelectric coupled laminated composite cylindrical shell by considering transverse shear effects and rotary inertia**, *Composite Structures*, Vol. 191, 123-144, 2018. https://doi.org/10.1016/j.compstruct.2018.02.010.
9. **Hossein Bisheh**, Mojtaba Bisheh, Nan Wu, **An investigation into laminated composite automotive drive shafts**, *International Journal of Mechanical and Production Engineering*, Vol. 8(5), 2020.

Conference Papers

10. **Hossein Bisheh,** Nan Wu, **Effects of transverse shear and rotary inertia on wave propagation in a smart laminated composite cylindrical shell**, *26th Annual International Conference on Composites/Nano Engineering (ICCE-26)*, July 15-21, 2018, Paris, France.
11. **Hossein Bisheh**, Mojtaba Bisheh, Nan Wu, **An investigation into laminated composite automotive drive shafts**, *IASTEM - 784th International Conference on Mechanical and Aerospace Engineering (ICMAE)*, February 28- 29, 2020, Toronto, Canada (**Winner of the Excellent Paper Award**).

12. Hossein Bisheh, Nan Wu, **Design and analysis of a laminated composite automotive drive shaft**, *20th International Conference on Aerospace, Mechanical, Automotive and Materials Engineering (ICAMAME 2018)*, August 9-10, 2018, Vancouver, Canada.